Electrical radial flux machine design focusing on magnet recycling and reuse : Application to hybrid or electric vehicles

Ziwei Li

Communauté
UNIVERSITÉ Grenoble Alpes

THÈSE

Pour obtenir le grade de

DOCTEUR DE LA COMMUNAUTÉ UNIVERSITÉ GRENOBLE ALPES
Spécialité : **GENIE ELECTRIQUE**

Arrêté ministériel : 25 mai 2016

Présentée par

Ziwei LI

Thèse dirigée par **Afef KEDOUS-LEBOUC**, Directeur de recherche, CNRS et codirigée par **Lauric GARBUIO,** MCF, G-INP
préparée au sein du **Laboratoire de Génie Electrique de Grenoble (G2Elab)**
dans **l'École Doctorale Electronique, Electrotechnique, Automatique et Traitement du Signal (EEATS)**

Dimensionnement de machines électriques à flux radial facilitant le recyclage des aimants permanents : application aux véhicules hybrides ou électriques

Electrical radial flux machine design focusing on magnet recycling and reuse: Application to hybrid or electric vehicles

Thèse soutenue publiquement le **2 mai 2019**,
devant le jury composé de :

Madame. AFEF KEDOUS-LEBOUC
DIRECTRICE DE RECHERCHE, CNRS DELEGATION ALPES, Directeur de thèse
Monsieur ANOUAR BELAHCEN
PROFESSEUR UNIVERSITE AALTO - FINLANDE, Rapporteur
Monsieur ABDELMOUNAIM TOUNZI
PROFESSEUR, UNIVERSITE LILLE 1, Rapporteur
Monsieur CHRISTOPHE ESPANET
PROFESSEUR, UNIVERSITE DE FRANCHE-COMTE, Président
Monsieur VLADIMIR LAZAROV
PROFESSEUR EMERITE, UNIVERSITE TECHNIQUE DE SOFIA - BULGARIE, Examinateur
Monsieur LAURIC GARBUIO
MAITRE DE CONFERENCES, GRENOBLE INP, Examinateur
Monsieur JEAN-MARC DUBUS
INGENIEUR DE RECHERCHE, VALEO, Examinateur
Monsieur DR. RADU FRATILA
INGENIEUR, VALEO, Examinateur

Acknowledgement

This doctor thesis concludes my work which is funded by an EU project named DEMETER. My work started in 2016. I have mainly stayed at Valeo electrical equipment department, Créteil, France, and have a close collaboration with Electrical Engineering Laboratory G2Elab, Grenoble, France. This thesis indeed born in a revolution period of the automotive industry. During these three years, the automotive electrification has gained profound changes. For instance, in the middle term of the thesis, Toyota developed a new magnet with a huge reduction of key rare earth elements usage. A new emission regulation named WLTP entered into force. Thus, former works based on old knowledge and regulations were soon out of date. These are the challenges of the thesis, but it is also exciting to be part of this revolution.

There are many people I need to thank. First of all, I would like to thank the thesis jury members - Mr. Belahcen and Mr. Tounzi, the reporters of the jury; and Mr. Espanet, the president of the jury ,for their constructive comments on the thesis.

Then, back to 2015, I went to Leuven for the PhD interview of DEMETER. There I met Mr. Dubus, the senior expert from Valeo, and professor. Mrs. Kedous-Lebouc from G2ELAB. I still remember the question they asked "Why do you want to participate in this project?" and my answer was "This is a global challenge. New technology is the best way to solve the crisis. Not only Europe benefits, but all over the world." I got this opportunity and soon moved to France from Sweden. At the beginning in France, life is from a scratch. However, Mr. Dubus gave me tremendous help without any remuneration, I feel so grateful for his selfless dedication. Also professor Kedous-Lebouc was always helpful whenever I visited Grenoble. She treated me and her students just like her family.

My gratitude also goes to all the Valeo colleagues who involved in this project. Since the beginning of my work in Valeo, I have been supervised by Dr. Legranger and Dr. Fratila. I thank gratefully for their guidance, technical support and thesis reviewing! Thank you to my friend Lihao Wang and Mr. Mazarin for the assistance of tests; Thank you to Mr. Charles for the work of mock-up fabrication; Thank you to Mr. Reynouard and Mr. Lahiani for the work of hybrid system simulations. Thank you to Dr. Mipo, the senior expert of Valeo, and Dr. Personnaz, the director of E-machine team, as well as Dr. Farah, the former director of E-machine team, for their advices and firm supports of this project.

Furthermore, I would like to thank all my DEMETER colleagues and friends. You make this journey full of joy! Pranshu, my closest friend in Valeo, thank you for all your timely supports. Also life in France is easier to have a friend who is willing to speak English at the beginning. Thank you to my "motor gang"- Amit and Dr Garbuio from G2Elab, Adolfo and Professor. Rasmussen from Aalborg university, professor Hebert from CRISMAT Laboratory. Thank you for your secondment hosting at Grenoble, Aalborg and Caen respectively. They were such wonderful experiences! There are countless thank you for all my friends and colleagues in the DEMETER project, I will miss you all.

Finally, my heart goes to my parents. Thank you for your endless love, trust and support. You have done great work and have given incredible dedication. For both economically and spiritually, supporting me to stay in Europe for nearly 6 years is such a heavy burden. Luckily, we have gone through the journey. You made me who I am today, and now it is time for me to let you enjoy the life!

Demeter The research leading to these results has received funding from European Community's Horizon 2020 Programme ([H2020/2014-2019)] under Grant Agreement no. 674973 (MSCA-ETN DEMETER). This publication reflects only the authors view, exempting the Community from any liability. Project website: http://etn-demeter.eu/.

Contents

List of Figures

List of Tables

List of Acronyms

GHG	Green House Gases
ICE	Internal Combustion Engine
REEs	Rare earth elements
PM	Permanent Magnet
Ce	Cerium
Sm	Samarium
Gd	Gadolinium
Pr	Praseodymium
Nd	Neodymium
Dy	Dysprosium
NdFeB	Neodymium-Iron-Boron
MOs	Magnetic Objects
SE	Steinmetz Equation
PMSM	Permanent Magnet Synchronous Machine
SPMSM	Surface mounted Permanent Magnet Synchronous Machine
IPMSM	Interior Permanent Magnet Synchronous Machine
SRM	Switch Reluctance Machine
SynRM	Synchronous Reluctance Machine
IM	Induction Machine
WRM	Wound Rotor Machine
PMASynRM	PM Assisted Synchronous Reluctance Machine
FSPM	Flux Switch Permanent Magnet machine
SMC	Soft Magnet Composite
EoL	End of Life
HDDs	Hardware Drive Disks
WEEE	Waste Electrical & Electronic Equipments
(H)EV	(Hybrid) Electrical Vehicle
Back-EMF	Counter -ElectroMotive Force
HDDR	Hydrogenation Desproportionation-Desorption Recombination
HPMS	Hydrogen Process of Magnet Scrap
PPS	Polyphenolyne Sulfide
PTFE	Poly Tetra Fluoro Ethylene
SPP	Slot per Pole per Phase
MMF	MagnetoMotive Forces
FW	Flux-Weakening
RMS	Root Mean Square
MTPA	Max Torque Per Ampere
MTPV	Max Torque Per Voltage
WIRE	Weighted Index of Recycling and Energy
NEDC	New European Driving Cycle
WLTP	World Harmonized Light Vehicles Test Procedure

List of Notations

ω_s	Electrical angular speed
ω_{mech}	mechanical speed (Rotor rotation angular speed)
k_{w1}	Fundamental winding factor
y_{sp}	Coil pitch in slots
q	Slots per pole per phase
p	Pole pairs
s	Total slots number
δ	Airgap length
D_{in}	Inner diameter of stator
ϑ	Electrical degree on rotor
S_1	Current loading
T	Torque
B	Flux density
L	Active machine length
θ	Electrical degree of the rotor
J_{rms}	Slot current density in root mean square value
A_{Cu}	Copper area in one slot
U_{line_Y}	Line voltage in Y connection
U_{phase_Y}	Phase voltage in Y connection
I_{line_Y}	Line current in Y connection
I_{phase_Y}	Phase current in Y connection
R_Y	Equivalent resistance of Y connection
N_Y	Equivalent turn number per phase of Y connection
U_{line_Δ}	Line voltage in Delta connection
U_{phase_Δ}	Phase voltage in Delta connection
I_{line_Δ}	Line current in Delta connection
I_{phase_Δ}	Phase current in Delta connection
R_Δ	Equivalent resistance of Delta connection
N_Δ	Equivalent turn number per phase of Delta connection
$i_{s\alpha}$	Current of α-axis on stator reference frame
$i_{s\beta}$	Current of β –axis on stator reference frame
I_d	Current of d-axis on rotor reference frame
I_q	Current of q-axis on rotor reference frame
Ψ_s	flux linkage of each phase on the stator reference frame
Ψ_m	flux linkage of PM
I_N	Maximum allowed current of a motor drive
U_N	Maximum allowed voltage of a motor drive
V_{DC}	DC side voltage limit
k_m	Modulation factor
$\mathbf{R_s}$	Stator resistance
L_d	Inductance of d-axis on rotor reference frame
L_q	Inductance of q-axis on rotor reference frame
$cos(\varphi)$	Power factor

I_{cc}	Short circuit current (three-phase short)
E	E-machine efficiency
P_{copper}	Copper loss (Joule loss)
P_{iron}	Iron loss
P_{mech}	Mechanical loss
T_{iron}	Iron core temperature
T_{coil}	Coil temperature

General introduction

Nowadays the world is facing a serious climate changes, due to the excessive Green House Gases (GHG) emissions from human activities. It is imperative to reduce the CO_2 emission of automotive. One of the essential strategies to further achieve that is to use new energy vehicle. New energy vehicle includes various sub-group. The most important branch is Hybrid and Electrical Vehicles ((H)EVs). (H)EVs can be powered either by Lithium battery or Fuel cell battery. However, no matter what the energy storage devices they have, (H)EVs always need electrical machines to transfer electrical energy into mechanical energy. Therefore, electrical machines are the key component for (H)EVs.

Valeo is a leading company in the field of electrical machine productions for automotive applications. It also has the ambition to be the leader of (H)EVs powertrain systems. Therefore, it is very essential for Valeo to produce high performance electrical machines for (H)EVs applications. In this case Permanent Magnet (PM) electrical machines seem to be the best candidates. To keep the cost of productions as low as possible, it is essential to investigate the cost of PMs in electrical machines. The strongest rare earth PM was invented in 1982- Neodymium-Iron-Boron ($Nd_2Fe_{14}B$) type magnet, or simply written as NdFeB. Commonly, in order to improve the temperature stability as well as resistant demagnetization of magnets, small portion of heavy rare earth element, Dysprosium (Dy) or Terbium (Tb), is added to the alloy.

However, with a high demand of high grade NdFeB magnets, the supplies of several key rare earth elements have serious problems, especially for Europe. Unfortunately, elements like Nd, Dy and Tb faced this high supply risk. In 2011, the global market for rare earth materials experienced a crisis that was reflected in a sharp rise in prices. Therefore, it is imperative to find a new way to exploit rare earth elements, or even replace REE magnets. For Europe, possible solutions to tackle the rare earth supply risks include

1. Prospecting new REE mines inside Europe,

2. Developing REE-free magnets with performances aim to NdFeB magnets,

3. recycling rare earth magnets.

However, the first two solutions seem to meet their bottlenecks. Hence, it is necessary to investigate the third solution. **Demeter -European Training Network for the Design and Recycling of Rare-Earth Permanent Magnet Motors and Generators in Hybrid and Full Electric Vehicles,** is an Europe Union registered project. DEMETER envisaged three routes for the recovery of rare earth PM from these devices, which are so called **direct re-use**, **direct recycling** and **indirect recycling**. Valeo is one of the principal partners in this project, and it mainly focuses on the route of PM **direct re-use**. The aim of this route is to achieve easy way of removing magnets from End of Life (EoL) motors/generators and then been used again in new motors/generators. This doctor thesis mainly focuses on radial flux type PM electrical machines, which are the most widely used type of electrical machines nowadays. The applications include Mild Hybrid Electric Vehicles (MHEV) or small Electric Vehicles (EV). The new motor design not only needs to be recycled friendly for PMs, but also needs to meet all the strict requirements for the applications.

The first chapter presents the background of the thesis and introduction of the bibliography. The conventional PM e-machines mainly refer to radial flux PM Synchronous e-Machines (PMSM). Two common types of PMSM are highlighted - Surface mounted Permanent Magnet Synchronous Machines (SPMSM) and Interior Permanent Magnet Synchronous Machines (IPMSM).

The second chapter presents several designs of SPMSMs and IPMSMs that attempt to satisfy the requirement of EV and HEV applications, such as performances, cost, reliability and series production. Meanwhile, magnet reuse and recycling concept should be followed. With the studies of both SPMSM and IPMSM designs, it was found that an IPMSM design can fairly fulfill all the requirements and constraints.

The third chapter presents the design, fabrication and test validation of the IPMSM with new magnet materials and assembly methods ready for recycling. A kind of bonded magnet was used for the IPMSM. This bonded magnet was made from a Hydrogenation Desproportionation-Desorption Recombination (HDDR) anisotropic NdFeB magnet powder, with Sulfide (PPS) binder. Although the energy product is lower than sintered NdFeB magnets, it is still higher than Ferrites. The bonded magnet could be directly assembled to the rotor by injection molding, and with magnetization at the same time. Hence the assembly of the machine became much easier than the assembly with sintered magnets. Besides, no matter what shape the magnets needs to be, the assembly method is always the same. The disassembly of the magnets became easy as well - Because there was no glue, and the magnetic force of the bonded NdFeB was less strong than traditional sintered NdFeB, they could be easily pushed out from the rotor. Besides, no segmentation was needed for bonded magnets due to their large resistivity. For the scaled recycling process, the rotors could be heated up together to melt down the bonded magnets for extraction. After taking out the magnets, they can be mixed with a certain percent of virgin magnets compound to make new bonded magnets without remarkable changes on *BH* performances. In summary, the entire recycling process is relatively easy and ecologically sustainable. Thus, based on this new concept, an IPMSM with bonded NdFeB magnets could be fabricated. Series benchmark tests were carried out, for instance no-load tests, short circuit tests and load tests.

The last chapter presents a methodology to evaluate e-machines with respect to the recyclability. Here the definition of the recyclability has two aspects :

- If the e-machine can be easily disassembled, and if the material can be easily recycled?
- If the e-machine can utilize the recycled materials without or with acceptable performance degradation?

At present no tool was found to evaluate this recyclability for e-machine designs. No experiment had been conducted for benchmark. Based on the two aspects of the recyclability, in this thesis two methods are presented to analyze and evaluate the recycling of PM e-machines for EVs:

- The first method evaluates recyclability of the production and recycling phases of a PM e-machine, regarding its assembly, disassembly and standardization of series production.
- The second method evaluates the recyclability at the user-phase. Mainly the impacts of utilizing recycled materials (in this case is recycled PM only) on the energy consumption of an e-machine over the complete user phase is analyzed.

The results of both methods are represented by two indexes. These indexes together can be named Weighted Index of Recycling and Energy (WIRE). By using WIRE, the recyclability between different machines can be comparable, even with different dimension or power.

In this chapter, WIRE was first validated on a commercial PM HUB motor used for a small golf car. Then the validated WIRE methods were used to evaluate the IPMSM with bonded magnets. The formerly obtained efficiency maps were used to calculate the energy index for both EV and HEV applications. It was found that by assuming 20% remanence flux density degradation on recycled magnets [79], and with WLTP drive cycle, the energy consumptions of the e-machine with recycled magnets for both HEV and EV applications had small degradation but in acceptable level. However, by taking into account the whole life cycle cost of rare earth mining and magnet production, it is very promising that the magnet reuse and recycling can gain environment benefit.

Chapter 1- Bibliography

1.1 Background

Nowadays the world is facing a serious climate changes, due to the excessive GreenHouse Gases (GHG) emissions from human activities. Based on a study [1], one of the important GHG emission sources is automotive. Therefore, it is imperative to reduce the CO_2 emission in this case. As Fig. 1 shows, the CO_2 emissions of cars are continuously decreasing. Meanwhile the fuel saving and CO2-cut-down technologies of Internal Combustion Engine (ICE) will soon hit their upper limits [2].

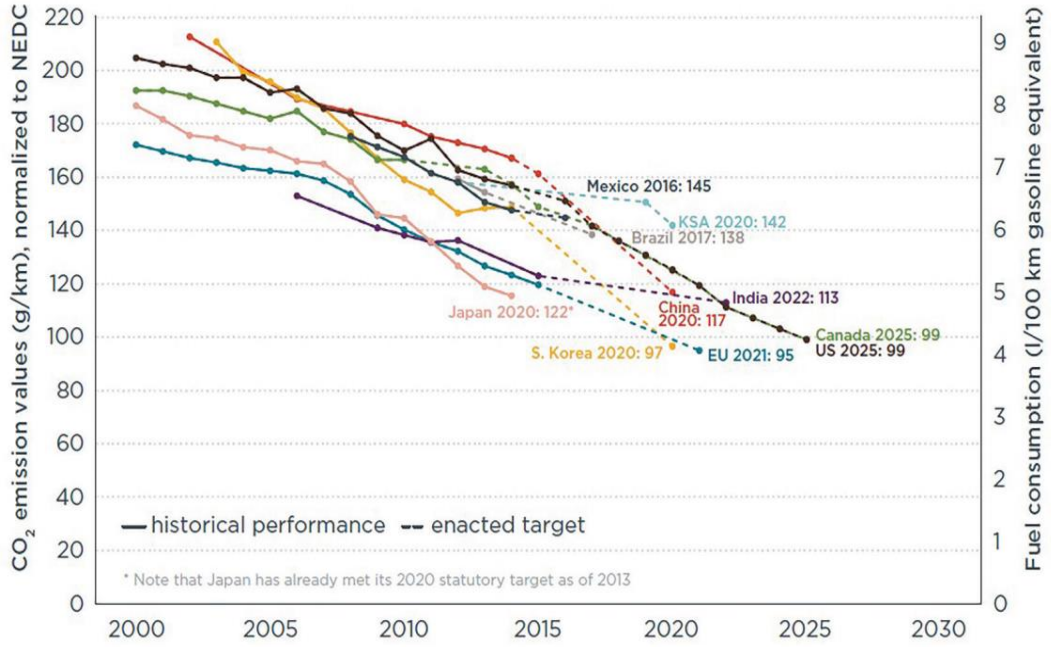

Fig. 1 Historical fleet CO_2 average emissions performance and current standards (g CO_2/km normalized to New European Driving Cycle (NEDC)) for passenger cars

Therefore, one of the essential strategies to further reduce automotive CO2 emission is to use new energy vehicle. New energy vehicle is a large group. Among the group, the most important branch is Hybrid and Electrical Vehicles ((H)EVs). They can be powered either by Lithium battery or Fuel cell battery. However, no matter what the energy storage devices they have, (H)EVs always need electrical machines to transfer electrical energy into mechanical energy. Therefore, electrical machines are one of the key component for (H)EVs.

It can be foreseen in the near future that the (H)EVs growth will boom. Roland Berger [3], strategy consultants based in Munich, calculated that the share of all electrical powertrains will be increased from less than 2% at 2015, to around 18% at 2030, even under the assumption that conventional powertrains continuous to dominate the market. Bloomberg New Energy also predicted the EV adoption in long-term [4]. They claimed "*by 2040, 54% of new car sales and 33% of the global car fleet will be electric*", as shown in Fig. 2. In addition, another important point is that EVs become economic competitive with ICE cars by 2025, without the scenario of subsidization. Thus with the increase of (H)EVs market share, the demand of electrical machines for (H)EVs will also be dramatically increased along with.

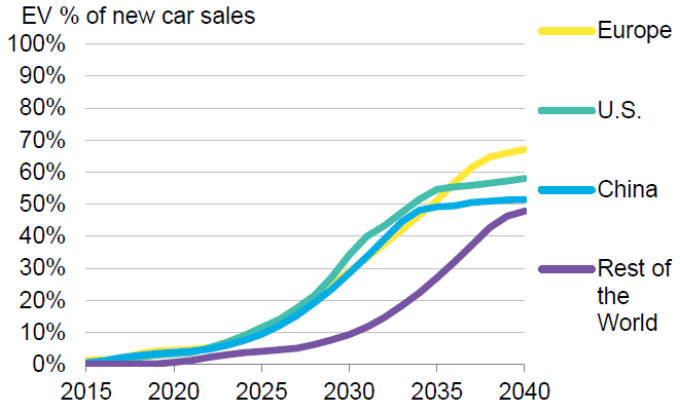

Fig. 2 Long-term EV sales penetration by country [4]

Valeo is a leading company in the field of electrical machine productions for automotive applications. It has one of the biggest market shares for starter and alternator [5], the number of the mass production of electrical machines is tremendous. Valeo also has the ambition to be the leader of (H)EVs powertrain systems. Therefore, it is very essential for Valeo to produce high performance electrical machines for (H)EVs applications, such as machines with high torque density, high efficiency and low noise and vibration. In this case Permanent Magnet (PM) electrical machines seem to be the best candidates. Indeed, nowadays most of EVs on market are equipped with PM electrical machines [6]. Therefore, for PM electrical machines, PM is naturally their most important part. Although the weight percentage of PMs is relatively small among the whole weight of the machine, the cost of PMs may go up to half of the total cost of a PM electrical machine [7]. Thus, to keep the cost of productions as low as possible, it is essential to investigate the cost of PMs in electrical machines.

PM is "*an object made from a material that is magnetized and creates its own persistent magnetic field*" [8]. Natural PMs have been found since ancient time. While with the development of electro-magnetic theories since the beginning of 20th century, the PM materials had gained huge progress –PM materials evolved from ferrite and Alnico magnets, to rare earth PMs, with several important scientific breakthroughs [8] [9]. Therefore, nowadays the mainstream PM materials contain rare earth elements, their magnetic energy products become much stronger than ferrite magnets. As Fig. 3 shows, after ferrite and Alnico, SmCo came out to be a much stronger magnet. It is made of alloys of samarium (**Sm**, rare earth element) and cobalt (**Co**). There are two typical samarium–cobalt magnet alloys – $SmCo_5$ and Sm_2Co_{17} (In Fig. 3, Sm_2TM_{17} is equivalent to Sm_2Co_{17}, TM means Transition Metal, the TM content is rich in cobalt). Soon after SmCo magnets, the strongest rare earth PM was invented in 1982- Neodymium-Iron-Boron ($Nd_2Fe_{14}B$) type magnet. Generally, their energy densities can be twice of SmCo magnets. Commonly, in order to improve the temperature stability as well as resistant demagnetization of magnets, small portion of heavy rare earth element, Dysprosium (**Dy**) or Terbium (**Tb**), is added to the alloy.

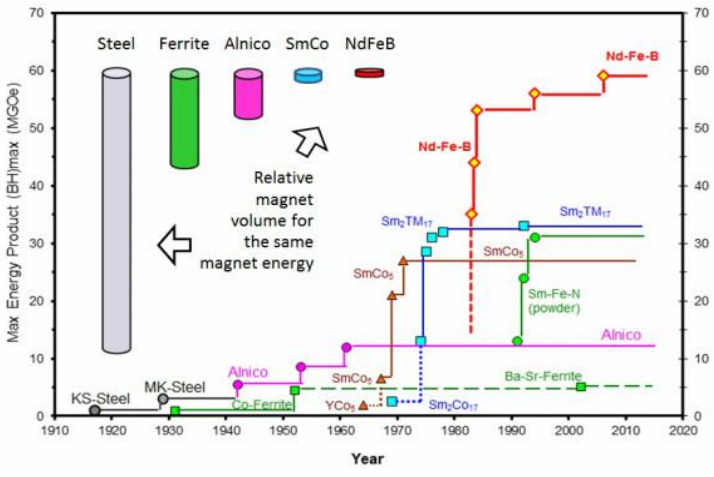

Fig. 3 Energy product comparison of different types of magnet [9]

Therefore, due to the superiority of energy density, PM electrical machines with NdFeB magnet are widely used in emerging high-tech industries, such as Hard Disc Drives (HDDs), wind turbines and (H)EVs etc. However, with such a high demand, the supply of rare earth element becomes a serious problem.

The rare-earth elements (REEs) comprise seventeen elements that are part of fifteen lanthanides, as well as scandium and yttrium in the periodic table [10], as shown in Fig. 4. Then rare earth elements are divided into Light Rare Earth Elements (LREE), and Heavy Rare Earth Elements (HREE), as shown in Fig. 5. In fact, not all rare earth elements are "rare"; the crust contents of rare earth elements are pretty abundant. The difficulty of extraction and separation makes them "rare". Besides, not all rare earth elements are in supply risk. For instance, [11] [12] clarified that Cerium (Ce) is oversupply. Samarium (Sm), Gadolinium (Gd) and Praseodymium (Pr) are not in supply risk. Unfortunately, deposits of heavy rare earth elements, such as Dy and Tb are rare indeed. The costs of Dy and Tb are extremely high (Dy is 10 times more expensive than Nd and Pr). While due to the huge demand, part of light rare earth elements, such as Nd, is also in a high supply risk [12]. These elements are massively used in high performance NdFeB magnets productions. The general supply risk of Critical Raw Materials (CRMs) is shown in Fig. 6.

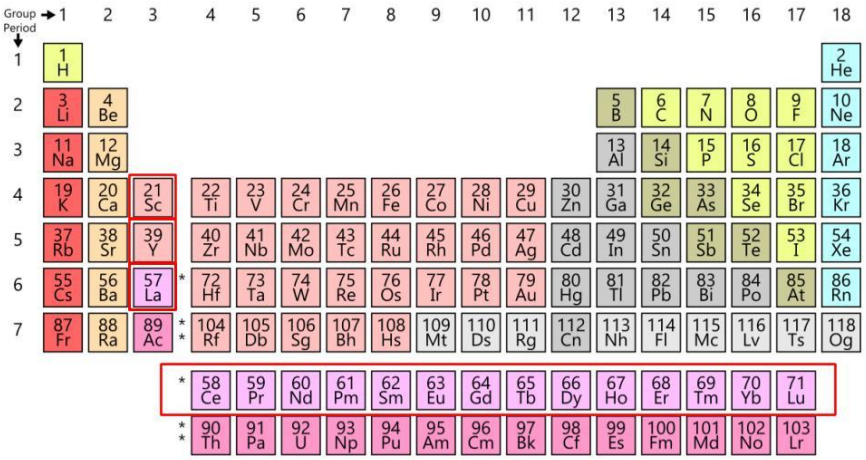

Fig. 4 Periodic table, rare earth elements are highlighted with red boxes [10]

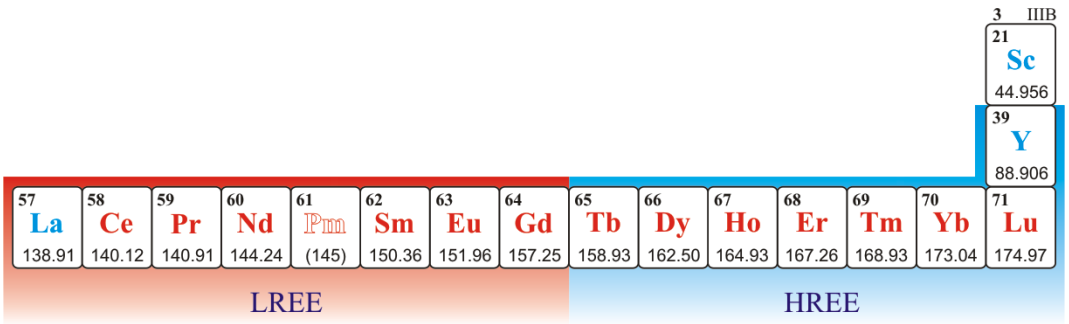

Fig. 5 Groups of light and heavy rare earth elements

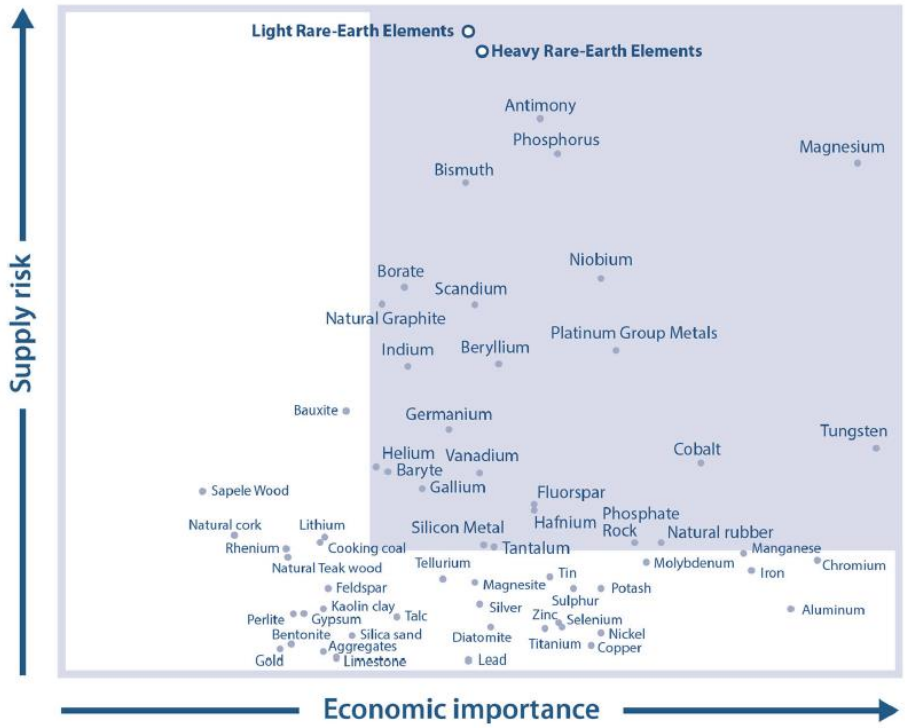

Fig. 6 CRMs from 2017 report of EU Commission [13]

In 2011, the global market for rare earth materials experienced a crisis that was reflected in a sharp rise in prices. For instance, on the most critical days of this crisis, the price of Nd increased approximately six times of itself at 2010, nearly 10 times of gold price, as Fig. 7 shows. During the last 4 years, the prices of Dy and Nd also had a small fluctuation. There was a forecast that over the next 25 years the rise of the demand for neodymium and dysprosium will be 700% and 2600% respectively [15]. The scenario of 2011 crisis had lightly appeared once more in 2017 [16]. There is no sign to see the crisis completely stop in the near future.

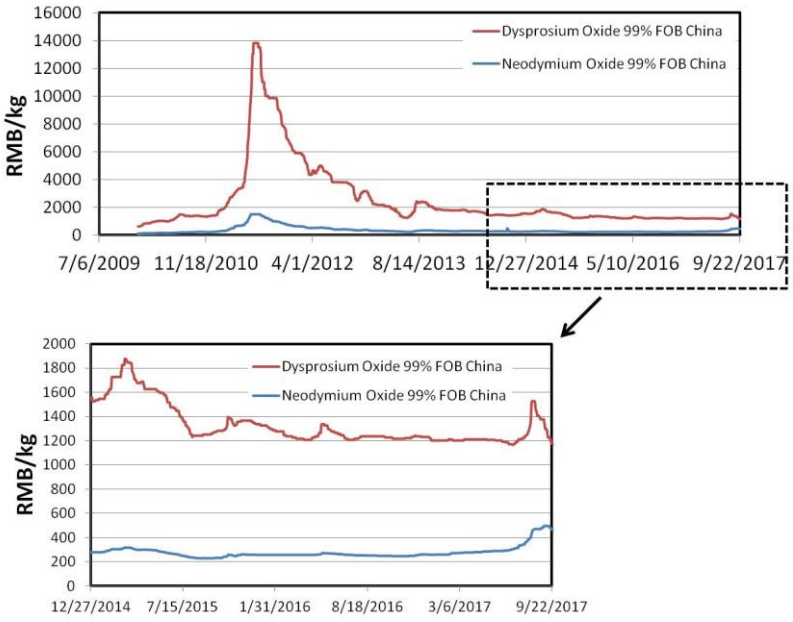

Fig. 7 The prices oscillation of rare earth Nd and Dy from 2009 to 2017 [14]

Besides the expense of rare earth elements, rare earth mining is always a filthy process. Usually the mining ore is in large scale, many toxic chemicals have to be dumped to soils. Therefore, the soil of the ore is heavily damaged. For instance, the leaching process needs to pour acid on soil, which destroys the original pH balance of the soil. In addition, the statistics indicate that producing one ton of rare earths creates 2,000 tons of mine tailings and 12,000 tons of wastewater [17].

People may think SmCo magnets could be an alternative solution to replace NdFeB magnet. Since SmCo magnets have relative high energy products. Although Samarium also belong to rare earth element, their deposits are not so rare. However, Co supply is another serious problem - Most of Co is mined in Democratic Republic of the Congo (DRC). However, due to the poverty and civil wars of the country, the mining industry is in troubles [18]– The way of mining is still very primitive. The health of mining workers has no security. Women and child labors are common in the mining, which result in huge humanitarian crisis. Finally, for (H)EVs, Lithium batteries also have large demands on Co, due to their cathode materials. Thus, it is not a good idea to largely replace NdFeB magnets with SmCo magnets.

Therefore, it is imperative to find a new way to exploit rare earth elements, or even replace REE magnets. For Europe, possible solutions to tackle the rare earth supply risks include (1) searching for new REE mines inside Europe [19], (2) developing REE-free magnets whose performances should be as good as NdFeB magnets [20], and (3) recycling rare earth magnets [11]. However, solution (1) is still at exploratory stage, while (2) is still a niche technology that has not been yet in practical use. After all this new magnet still contains quite a portion of Nd. Thus, it is necessary to investigate solution (3).

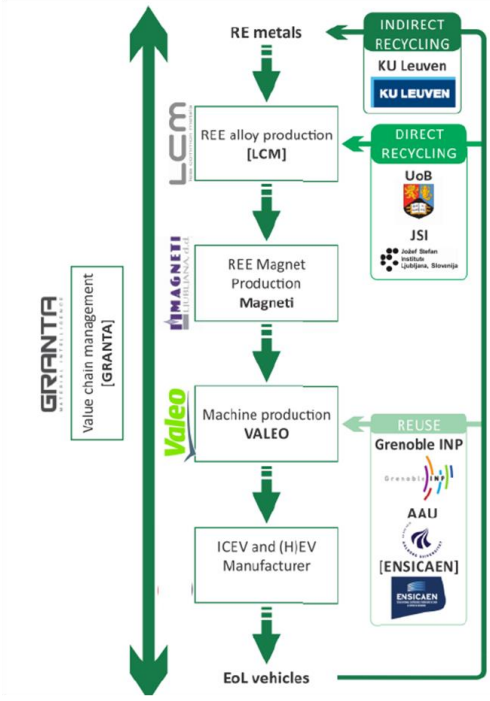

Fig. 8 DEMETER project structure and full value chain approach [22].

Rare earth recycling is a grand concept. For the sources of REEs recycling, they can be pre-consumer scrap, industrial residues or REE-containing End-of-Life (EoL) products. Besides, there are many ways to recycle the REEs. Based on different recycling object, the recycling circles are different. Since the automotive industry moves towards more (H)EVs, they are likely to become the main consumer of REE magnets [21] . **Demeter -European Marie Slowska Curie Action MSCA Training Network for the Design and Recycling of Rare-Earth Permanent Magnet Motors and Generators in Hybrid and Full Electric Vehicles,** is an European Union registered project focusing on the rare earth magnet recycling from electrical machines that used in (H)EVs, the project structure is shown in Fig. 8.

The sources for the recycling are considered as EoL products, which are traction motors of (H)EVs in this project. General recycling route of electrical motors had been established. Basically, it is to shred the entire motors and using magnetic and eddy current separator to separate different metals (mainly iron, aluminum and copper) [22]. However, current method cannot protect and separate magnets. Because the shredding process totally damages the structure of magnets and disperses the magnet swarf. Meanwhile for the strong PM like NdFeB, they can stick to the shredder assembly and can lead to the degradation of recycling efficiency [24].

Therefore, PMs need to be treated individually. Based on this background, [7] envisaged three routes for the recovery of rare earth PM from these devices, which are so called **direct re-use**, **direct recycling** and **indirect recycling**, as shown in Fig. 9. Valeo is one of the principal partners in this project, and it mainly focuses on the route of PM **direct re-use**. The aim of this route is to achieve easy way of removing magnets from EoL motors/generators and then use them again in new motors/generators. The other two ways hence use complex physical or chemical treatments for recycling. Direct and indirect recycling chains are correspondingly longer than that of direct re-use, as shown in Fig. 10. Thus once the loop of direct re-use can be realized, it will be the most economical way to recycle magnets.

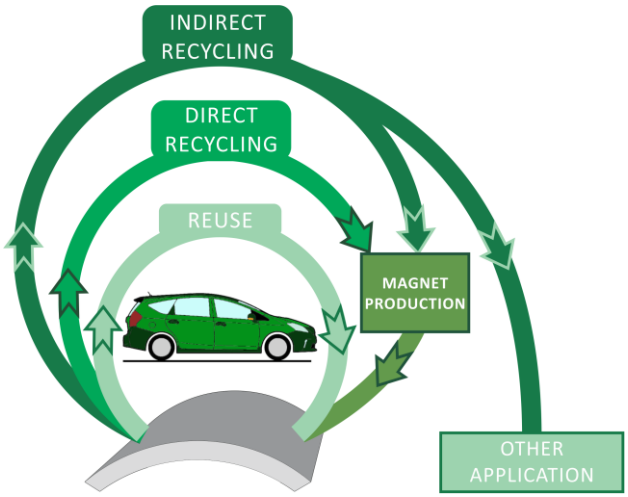

Fig. 9 Three magnet recycling options of traction motors/generators [22].

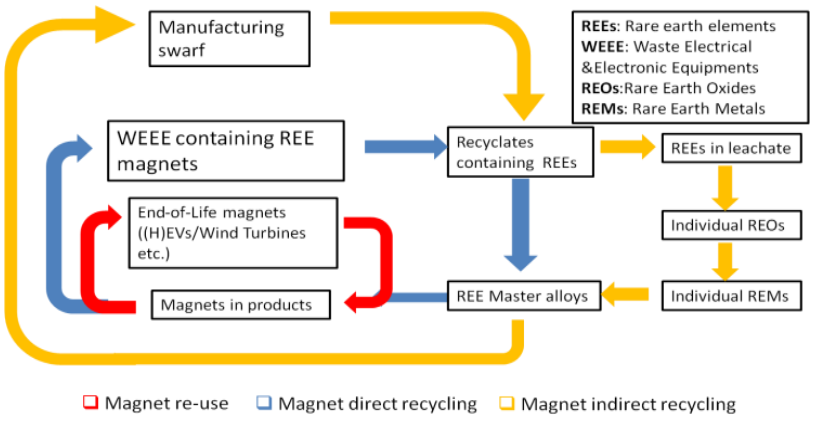

Fig. 10 Three recycling routes for REE permanent magnets from End-of-Life Waste Electrical &Electronic Equipments (WEEEs) [11]

One of the packages in Demeter project is to develop strategies based on Design-for-Reuse. As there are many different types of PM electrical machines, this thesis mainly focuses on radial flux type PM electrical machines, which are the most widely used type of electrical machines nowadays. Details of these radial flux machines will be presented in the following sections.

1.2 Magnetic materials for electrical machines

The introduction of electrical machines starts with the materials they utilize. Apart from the conductor material, such as copper, an E-machine uses different kinds of magnetic materials. Thus, first of all it is necessary to look into the theories of magnetism. Then, ferromagnetism materials are highlighted. Two groups of ferromagnetism material – soft magnetic materials and hard magnetic materials are introduced. Iron loss is the main focus of soft magnetic materials, while demagnetization curves and different types of magnet are introduced for the hard magnetic materials.

1.2.1 Magnetism

The magnetization is characterized by the magnetization vector which is denoted M [A/m]. It represents the distribution of magnetic moment in a per unit volume. Normally M need to be transfer to magnetic polarization, which is denoted as J [T], the relationship between M and J is shown in Eq. 1.

$$J=\mu_o M \qquad \text{Eq. 1}$$

where μ_o is the vacuum permeability or magnetic constant, $\mu_o = 4\pi 10^{-7}$ [H/m].

Normally for electrical machine analysis, flux density B [T] is the observation parameter. The relationship between B and J can be written as Eq. 2,

$$B=\mu_o H+J \qquad \text{Eq. 2}$$

where H is the auxiliary magnetic field with unit [A/m]. Eq. 2 can also be rewritten as Eq. 3 with a relative permeability μ_r.

$$B=\mu_o\mu_r H,\ M=\chi H \qquad \text{Eq. 3}$$

where χ is called volume magnetic susceptibility. So μ_r is expressed as Eq. 4

$$\mu_r=1+\chi \qquad \text{Eq. 4}$$

Therefore, based on μ_r, the magnetism can be mainly categorized in three groups:

- Diamagnetism, for $\mu_r \leqslant 1$. Diamagnetism materials generate an opposite magnetic field inside themselves when an external magnetic field is applied to them. Thus their susceptibility is negative (but larger than -1). Diamagnetism occurs in all common materials, such as Cu, Ag and water. Superconductivity is an example of diamagnetism.

- Paramagnetism, for $\mu_r \geqslant 1$. Paramagnetism materials induce weak magnetic field which direction is the same with applied external magnetic field. Thus their susceptibility is a small positive value. However, when the external field is removed, the magnetic field of paramagnetism material disappears at the same time. Materials such as Al, Ni, Cr and Mn present paramagnetism.
- Ferromagnetism, for $\mu_r >> 1$. Ferromagnetism is a kind of magnetism by materials that can acquire strong magnetization from external magnetic fields. When the external field is removed, the materials can still retain a significant magnetization, which is so called remanence. Normally with a certain level of reverse magnetic field, the remanence can still be kept, which indicates the coercivity of the material.

The schematic diagram for these three types of magnetism is shown in Fig. 11.

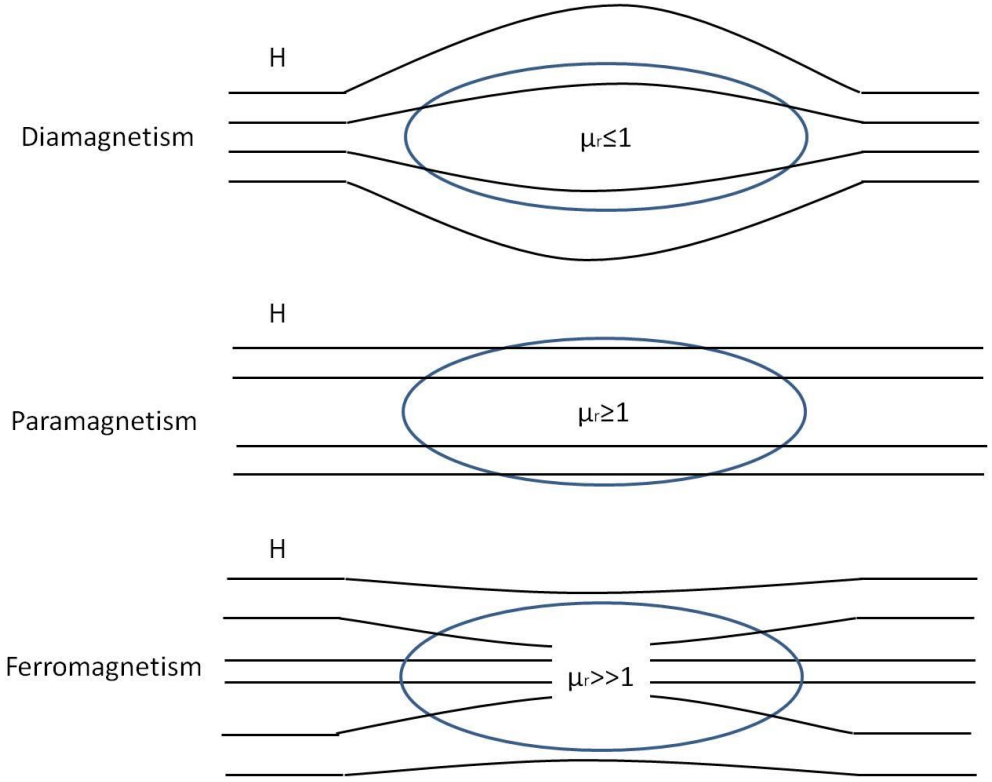

Fig. 11 Three types of magnetism with external magnetic fields

There are two other types of magnetism, the ferrimagnetism and the antiferromagnetism. However, their discussion is out of the scope of this thesis.

1.2.2 Ferromagnetic materials

1.2.2.1 Magnetic domain and domain wall

The material research of PM machines mainly focuses on ferromagnetism materials. It is found by Pierre Weiss in 1900s that ferromagnetism materials are composed of magnetic domains. Each domain is separated by a domain wall. The magnetic domain and domain walls can be shown as Fig. 12. It is found that even without external field, each magnetic domain is still magnetized to saturation. At the demagnetization state, and from a macro perspective, the material magnetization is neutral. However, when the external field is applied, the domain walls are moved with the domains and the magnetic moments start to rotate. With stronger and stronger external field, the magnetization of each domain is more and more aligned with the external field direction. Finally, when the

magnetizations of all domains are parallel to the external field, the magnetization of the material is saturated. This magnetization process is illustrated in Fig. 13, where S is the saturation point.

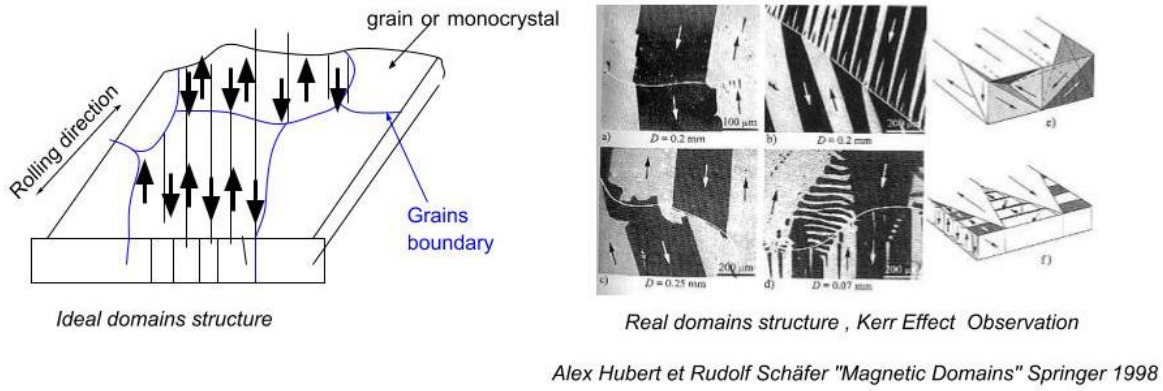

Fig. 12 Domains structure in a polycrystalline Grain oriented SiFe steel

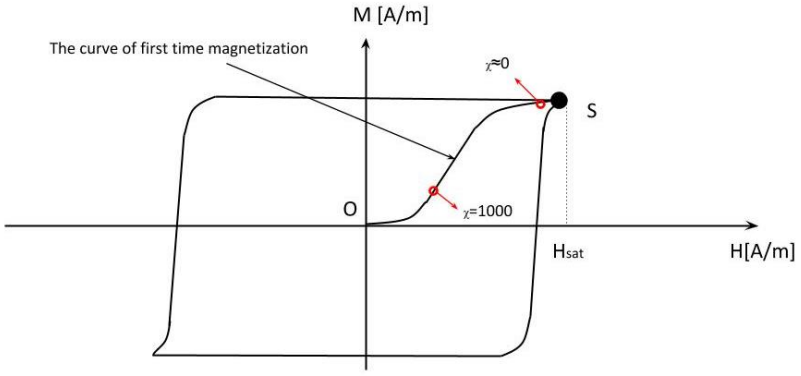

Fig. 13 A hysteresis curve and the curve of first-time magnetization of a typical ferromagnetism material with relative permeability highlighted.

It is necessary to highlight that the relative permeability is not a constant value during the magnetization. As Fig. 13 shows, at the beginning of the magnetization, there is a linear part of M-H curve. Thus, initially χ =1000, which makes the relative permeability very high. However, when the magnetization is near the saturation point S, χ is approximate to 0, which makes the relative permeability approaching to 1.

Depending on the required magnetic field strength to vary easily or not the magnetization, these materials can also be divided into soft magnetic materials, such as electrical steels, and hard magnetic materials, such as PMs. This required magnetic field strength can be expressed as coercivity. As Fig. 14 shows, two types of hysteresis loops are depicted, where *iHc* denotes intrinsic coercivity; black loop represents a hard magnetic material; red loop represents a soft magnetic material. Normally the intrinsic coercivities of soft magnetic materials are within hundreds of A/m, while the intrinsic coercivities of hard magnetic materials are between several kA/m to MA/m. Thus, the hard magnetic material has much higher absolute coercivity iHc_2 than the soft magnetic material coercivity iHc_1.

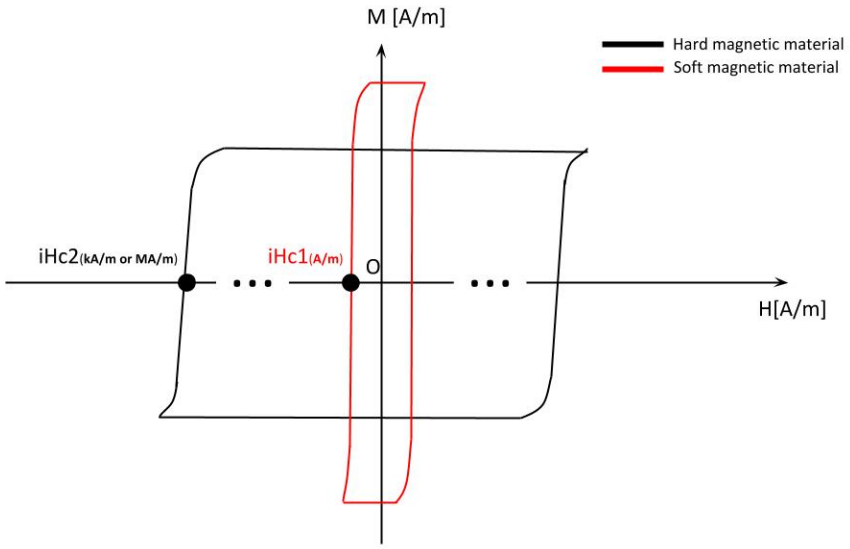

Fig. 14 Hysteresis loops of soft and hard materials with their coercivities.

1.2.2.2 Soft magnetic materials

Soft magnetic materials, such as electrical steels, have high permeability as well as low coercivity. They are used for guiding magnetic field in an electrical machine. The most common electrical steel is Silicon-iron (SiFe), other electrical steels are Cobalt-iron (CoFe), Nikel-iron (NiFe), Soft Magnetic Composite (SMC), etc.

Iron loss is generated from iron cores of both stator and rotor. It is created by the alternating magnetic field that acts on soft ferromagnetic materials. Macroscopically, many models have been established to describe the phenomenon. In the following, we shorty presents two well-known magnetic loss models: The Steinmetz model and the Bertotti's model.

The Steinmetz Equation (SE) was first proposed in 1884. Afterwards there were many modified SE models for the improvement of accuracy. Nevertheless, the basic form of SE is shown as Eq. 5.

$$P_{iron} = k.(f)^{\alpha}\hat{B}^{\beta} \qquad \text{Eq. 5}$$

where f is the frequency of the waveform, $\hat{B}$ is the peak value of a flux density. k, α and β are constant coefficients determined by the material properties. Normally these coefficients can be either supplied from iron sheet manufacturers, or acquired through Epstein frame measurements, which is an IEC standard method for measuring magnetic properties of electrical steel sheets [102].

To simplify, the Eq.5 can be considered as the sum of two terms: **hysteresis loss** and **eddy current loss.** Hysteresis loss can be obtained through quasi-static measurement. they are proportional to the hysteresis loop at very low frequency. Normally the hysteresis loss in a per unit volume soft magnetic material can be expressed as Eq. 6.

$$P_{hyst} = f\int_{f\to 0} HdB \qquad \text{Eq. 6}$$

Then correlating Eq. 6 with iron material properties, it can be found that H is a function of B. Thus, hysteresis loss is a linear function of $\hat{B}^{\zeta}$ ($1<\zeta<2$) and f. Eq. 6 can be rewritten as Eq. 7,

$$P_{hyst} = k_h f \hat{B}^{\zeta} \quad \text{Eq. 7}$$

where k_h is a constant of hysteresis loss determined by the material hysteresis property.

The next part is eddy current loss, sometimes also called dynamic loss. Eddy current loss in a per unit volume soft magnetic material can be expressed as Eq. 8, assuming a linear material and a quasi-homogeneous flux density (sinusoidal alternating flux density) in the cross section of the sheet,

$$P_{eddy} = k_e f^2 \hat{B}^2 \quad \text{Eq. 8}$$

where k_e is a constant of eddy current loss determined by the magnetic material resistivity as well as eddy current distribution (skin effect).

Therefore, Eq. 7 and Eq. 8 together can be added up to derive the total iron losses. The form of the total iron losses is written as Eq. 5.

However, the aforementioned classical SE equations are only practical with a perfect sinusoidal waveform excitation. Nowadays most of the AC machines are driven by power electronics with non-sine waveforms. Moreover, due to the non-linear effect of the iron core, such as saturation, the flux density in the core is neither sinusoidal. In order to process the waveform with multiple harmonics, FFT needs to be implemented first to the waveform. Then both equations need to solve the losses for each harmonic component. Therefore, the calculation process is not practical to solve the iron loss of an e-machine.

A better way to calculate the iron loss with non-sine waveform is proposed in [103]. The hysteresis loss can be expressed as Eq. 9,

$$P_{hyst} = k_H f (\frac{B_{max} - B_{min}}{2})^{\zeta} \quad \text{Eq. 9}$$

where B_{max} and B_{min} are the max and minimum values of the flux density waveform respectively, f is still the alternating frequency. Besides, it requires the flux density waveform symmetric, which results in symmetrical major loop of the hysteresis curve.

The eddy current loss can be expressed as Eq. 10,

$$P_{eddy} = k_E \frac{1}{T} \int_0^T (\frac{dB}{dt})^2 dt \quad \text{Eq. 10}$$

where $\frac{dB}{dt}$ is the changing rate of the flux density. Thus, any flux waveform can be calculated for iron losses in a practical way. The total iron losses can be expressed as Eq. 11.

$$P_{iron} = k_H f (\frac{B_{max} - B_{min}}{2})^{\zeta} + k_E \frac{1}{T} \int_0^T (\frac{dB}{dt})^2 dt \quad \text{Eq. 11}$$

The drawback of using this modified SE is that the history of the flux waveform variation needs to be recalled. Besides, minor loops of the hysteresis curve cannot be included, which may underestimate the hysteresis loss.

Apart from SE, nowadays another commonly used iron losses model is Bertotti's model. Bertotti's model uses the segregated iron losses into hysteresis loss, eddy current loss and excess loss. In this Model, Bertotti applies his statistical theory of domains motion, introduces the concepts of Magnetic Objects (MOs) which is a number of correlated domains and express the excess loss as a function of MOs. A simplified formula of the total loss based on this model is expressed as Eq. 12 for a sinusoidal waveform of the flux density.

$$P_{iron} = k_{hyst} f \hat{B}^2 + k_{ec} f^2 \hat{B}^2 + k_{exc} f^{1.5} \hat{B}^{1.5} \quad \text{Eq. 12}$$

In the equation, the first part describes the hysteresis loss, which is simply proportional to the square of flux density peak value, and linear to the frequency. Theoretically, k_{hyst} is derived from the characterization of the hysteresis curve of the material.

The second part is eddy current loss. It is simply proportional to both squares of flux density peak value and frequency. Theoretically the eddy current loss coefficient can be derived from [104], as Eq. 13 shown,

$$k_{ec} = \frac{\pi^2 d^2}{6 \rho_{sheet} D} \quad \text{Eq. 13}$$

where d is the thickness of iron sheet; ρ_{sheet} is the resistivity of the iron sheet; D is the density of the iron. As mentioned before, this equation does not consider the influence of skin effect in laminations.

Except SMC, all electrical steels are commonly in lamination form. Because it is electrically insulated between two laminations, large induced eddy current in the axial direction of the laminations can be effectively eliminated. Eddy current is only constrained in each lamination, which becomes much smaller, as Fig. 15 shows. Thus, for the sake of eddy current loss reduction, it is necessary to use laminated steels.

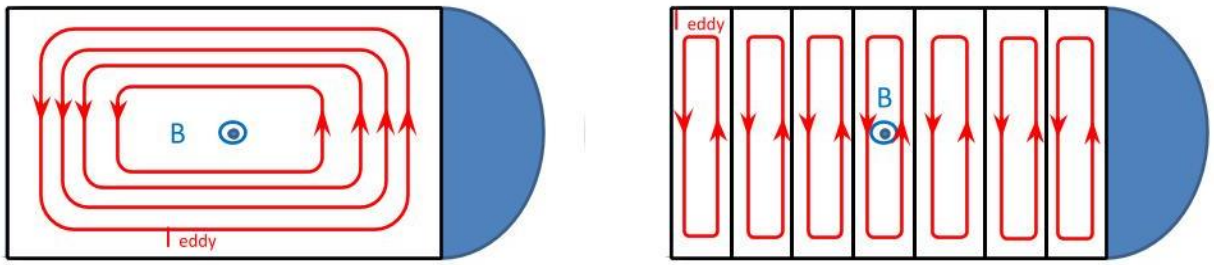

Fig. 15 Eddy currents in a solid iron core (left) and in a laminated iron core (right) respectively, view of axial cross section.

Different electrical steels have their own lamination thickness norms. For instance, the common SiFe non-oriented laminations have 0.35mm thickness. Generally, from Eq. 13, smaller the lamination thickness, lower the eddy current loss. However, the manufacture difficulty, as well as the cost will be higher for the thinner lamination. Fig. 16 illustrates B-H curves of three different laminations. The gauges of M600-50A, M270-35A and NO30-16 are 0.5 mm, 0.35 mm and 0.30 mm respectively. It can be observed that with smaller lamination thickness, the saturation level of the lamination becomes lower as well because it contains in practice higher silicon or other additional non- magnetic elements content to enhance the decrease of the magnetic loss.

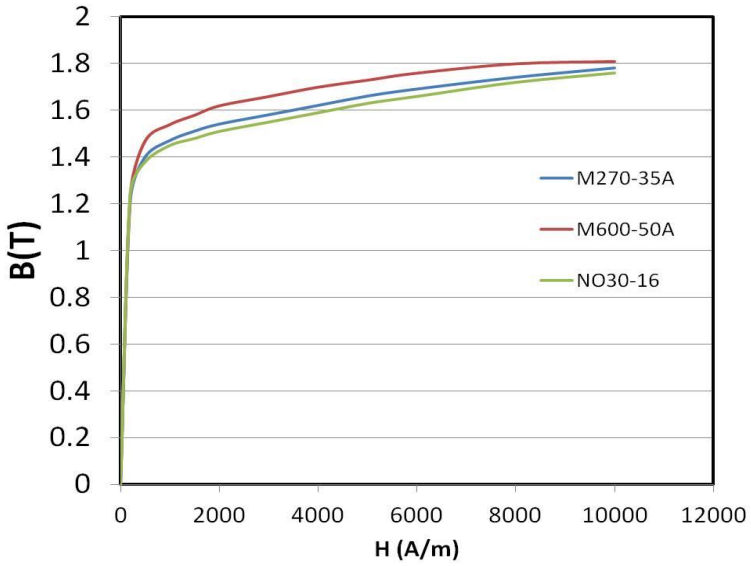

Fig. 16 B-H curves of laminations M270-35A, M600-50A and NO 30-16 respectively @ 50 Hz

Then, Fig. 17 shows the iron loss density of these three laminations at 4 different excitation frequencies. It is obvious to find that with higher frequency and higher flux density, the iron loss of each lamination is higher also. With smaller lamination thickness, the iron loss becomes lower at the same excited frequency and flux density. From gauge 0.5 mm to 0.35 mm, there is a huge reduction on iron loss. However, from gauge 0.35 mm to 0.30 mm, the iron loss reduction is not such significant at low frequency. While at high frequency and high flux density, the iron loss of these two gauges have an apparent difference.

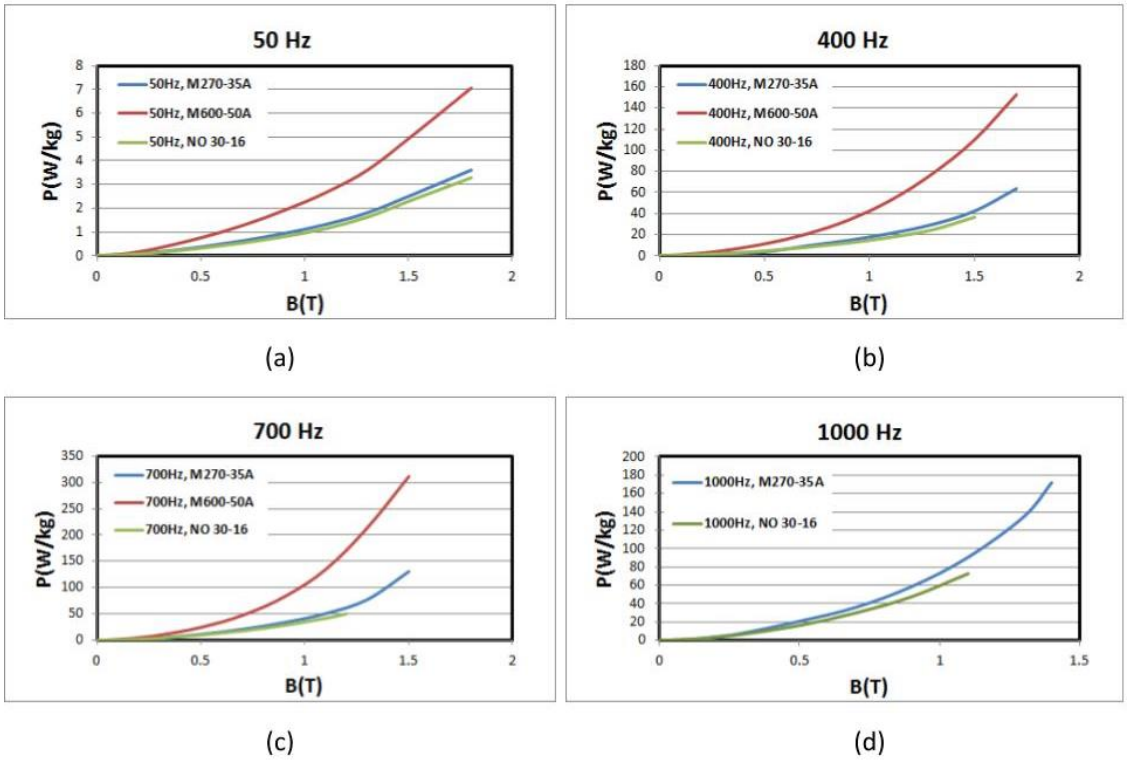

Fig. 17 Epstein frame measured iron loss densities of M270-35A, M600-50A and NO 30-16 respectively at 4 different electrical frequencies [128]

For SMC, their iron core is directly pressed together by metallic powder. As every metallic particle is electrically insulated, eddy currents in all dimensions are reduced; the eddy current loss is considerably small. However, SMC has relatively low permeability [49], and the iron loss of SMC at low frequency region is higher than SiFe lamination.

Come back to Bertotti's model, the special part of it is the excess loss. Excess loss is used to fill the gap between the sum of hysteresis loss plus eddy current loss, and the measurement losses. To explain the excess loss microscopically, it is a kind of Joule heating that generated by magnetic domain walls of soft magnetic materials under the excitation of an alternating magnetic field. A typical theoretical expression for k_{exc} is Eq. 14,

$$k_{exc} = \sqrt{SV_0\sigma G} \qquad \text{Eq. 14}$$

Where S denotes the cross section area of the lamination; V_0 denotes the statistical distribution of the local coercive fields; σ denotes the electric conductivity of the lamination; $G \approx 0.136$, is a constant related to the eddy current damping.

Although it seems to be difficult to derive all these coefficients theoretically, a practical way is to use curve fit-in method with the given iron loss curves from the supplier of iron laminations. Thus it totally becomes a numerical process.

From the experiments, it was found that the simplified Bertotti's model has medium accuracy. It is necessary to adjust Eq. 12 to Eq. 15 for better accuracy [105].

$$P_{iron} = k_{hyst} f \hat{B}^{\beta} + k_{ec} f^2 \hat{B}^2 + k_{exc} f^{1.5} \hat{B}^{1.5} \qquad \text{Eq. 15}$$

where β is a new coefficient for curve fit in. In this case, Eq. 15 is similar to Eq. 11, but with an additional part - excess loss.

However, even with Eq. 15, the accuracy still cannot be guaranteed if the skin effect of the lamination is not negligible. Nevertheless, Bertotti's model is relatively simple to be implemented, as long as the coefficients - k_{hyst}, k_{ec} and k_{exc} and even β are obtained. The searching of these coefficients is a one-time job. Unlike SE methods, the coefficients are correlated to the history of the flux waveforms. The physical meaning of Bertotti's model is rather easy to understand.

There are many other iron loss models that can improve the calculation accuracy. These models are mainly built on Preisach hysteresis model [106]. Minor loops of the hysteresis curve can be well emulated. However, naturally they also need more knowledge of material and flux waveform. For instance, full hysteresis curves at different frequencies normally need to be taken into account. Rotational magnetic field need to be recorded. Thus, calculation will become very sophisticated.

It needs to be highlighted that iron loss is highly sensitive the manufacturing process, such as cutting, punching and welding, etc. Also for some soft magnetic materials, their iron losses are very sensitive to changes of temperature. For instance, NiFe alloys can be easily deteriorated by impropriate manufacturing process. Their BH curves changes with temperature variation, which result in different iron losses. The details of each model and its advantages and disadvantages can be found in [107]. This thesis had done a comprehensive study of iron losses models as well as soft magnetic materials.

In this thesis, in terms of the limit of the knowledge on the iron lamination, only classic SE model is implemented. Some discussion will be done in Chapter 2 Section 2.2.4 Efficiency. An experience coefficient (large than 1) will be multiplied to the iron loss results from the classic SE model, to represent manufacturing impacts. Temperature impacts are ignored in this thesis.

1.2.2.3 Hard magnetic materials

Magnetically hard materials mainly include ferrite, Alnico, SmCo, NdFeB, and some new alloys such as SmFeN or NdFeN.

To implement these PM materials in electrical machines, first they need to be magnetized. The magnetization is characterized by their *M-H* curves. PM materials have isotropic and anisotropic types. For the crystalline structure of an anisotropic PM, there are directions of easy magnetization for magnetic domains (easy axis) and of hard magnetization (hard axis). For isotropic PM, no matter what magnetization direction is, there is no difference. So every magnetization direction can be seen as easy axis. Anisotropic materials are more interesting than the isotropic ones from the performance point of view. The drawback is additional process step that increases the cost. Nevertheless, taking the anisotropic material as an example, the M-H curves of the PM material under a certain temperature are shown in Fig. 18.

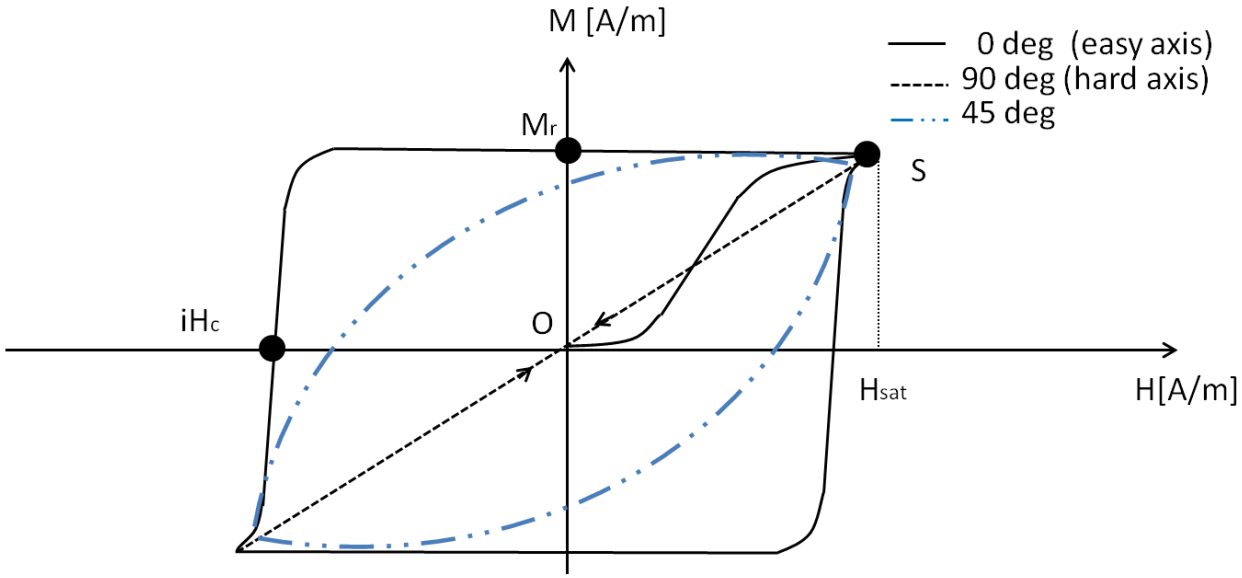

Fig. 18 M-H curves of an anisotropic PM material with different magnetization angles

Here only parallel magnetization is assumed. Hence, the magnetization direction is defined by the angle between the magnetic field direction and the easy axis. For instance, if the magnetic field is aligned with the easy axis, the magnetization direction is 0°. The angle between the magnetic field and the easy axis can be also 45°, just as the blue *M-H* curve shows. However, the limit of magnetization direction is 90 °, which indicates the magnetic field is aligned with hard axis.

Magnetization with 0° is analyzed first. When the PM is magnetized for the first time, the *M-H* curve follows an initial curve from *O* to *S*. Point *S* represents the saturation level of the PM. Even with the magnetic field strength larger than H_{sat}, the level of *M* is not increased. Afterwards, with the decrease of the field *H*, *M-H* curve will not follow the original curve. Instead, magnetic hysteresis is appeared; *M* will be kept at a relatively constant level. When *H=0*, the level of *M* is called remanent magnetization M_r. This relative constant level of *M* can be maintained even with a reverse field strength (*-H*). However, up to the knee point of *M-H* curve, *M* level starts to drop rapidly with the increase of the reverse field. When the strength of reverse field reach iH_c, which is known as intrinsic coercivity, the level of *M* becomes zero. Therefore, for magnetization aligned with easy axis, the shape of the hysteresis curve is symmetric with the origin point *O*, and the shape of the closure curve is similar to a rectangle.

Then for 90° magnetization direction, *M* is simply increased and decreased with *H*, no matter how many times the PM is magnetized. Thus, the remanent magnetization and intrinsic coercivity for hard axis magnetization is close to zero. 45° magnetization direction is also studied. The shape of *M-H* curve is similar to a spindle. Both levels of

remanent magnetization and intrinsic coercivity are between 90° and 0° magnetization. Thus it is found that to fully utilize PM material, the magnetization direction has to be aligned with easy axis.

Assuming the PM material is ideally magnetized, the PM can be put into a magnetic circuit of an electrical machine. An example of the *B-H* curves of a NdFeB N41 is shown in Fig. 19. Meanwhile, the working points, which are the intersections of the load lines and the B-H curves of the magnets, are also shown.

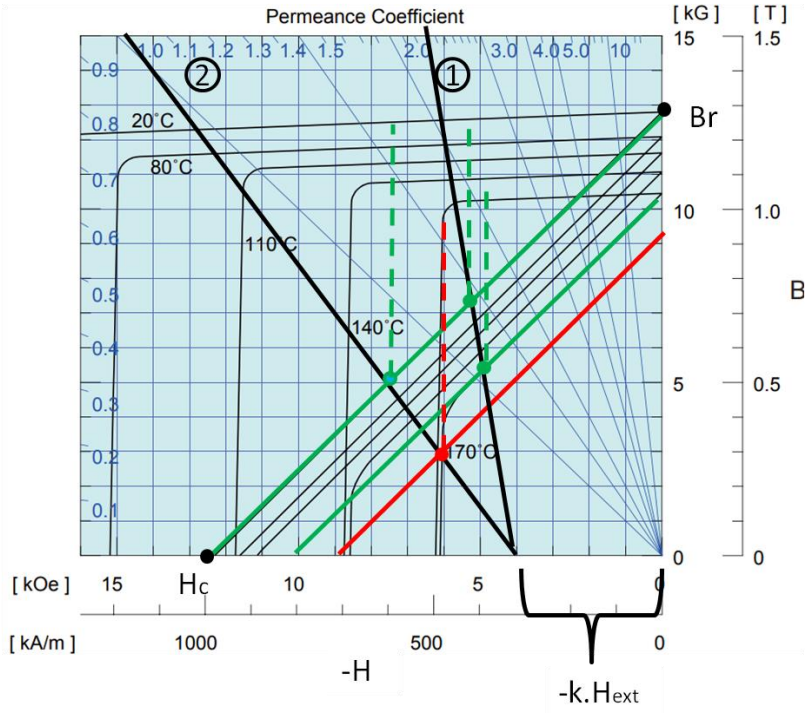

Fig. 19 *B-H* and *J-H* curves of a PM material *vs* machine loading lines with different slopes in second quadrant

In the figure, Both *B-H* and *J-H* curves are displayed with changing temperatures. *B* denotes flux density [T]. *J* denotes magnetic polarization [T]. The shape of *J-H* closure curves is close to rectangular shape. The knee points are very easy to locate. However, the shape of *B-H* curves is close to a diamond. The knee points are not clear to recognize. In Fig. 19, only second quadrant is focused. The remanence flux density *Br* and coercivity H_c of a *B-H* curve are shown in Fig. 19. For electrical machine designs, *B-H* curves need to be used rather than *M-H* curves. In the figure, two set of units can be found. Besides Tesla [T] and field strength [A/m], Gauss [G] can also be used as the unit of *J* and *B*, while Oersted [Oe] can be used as the unit of H. The convert factor (multiply) from [G] to [T] is 10^{-4}, and from [Oe] to [A/m] is $10^3/4\pi$.

Then, the machine loading lines can be derived from magnetic circuit. Based on Ampere's Law, if assuming the permeability of magnet is the same with air permeability, and leakage flux is ignored, the line can be drawn on the *B-H* plane by using Eq. 16,

$$B_m = -\mu_o \frac{A_\delta h}{A_m \delta} H_m - \mu_o \frac{A_\delta}{A_m \delta} NI \text{ [90]} \qquad \text{Eq. 16}$$

where B_m and H_m is the flux density and field strength on magnet respectively. A_δ and A_m is the airgap area and magnet area respectively. h and δ is the magnet height and the airgap length respectively. *N* and *I* are the number of turns and current amplitude respectively. *NI* represents the external field from armature reaction of the electrical machine. Thus Eq. 16 can be simplified as Eq. 17,

$$B_m = -k.h.H_m - k.H_{ext} \quad \text{Eq. 17}$$

where k is a constant correlated to the airgap and magnet area. Due to the power and torque requirements of an electrical machine, normally k is a constant. k and h together decides the slope of the loading line.

Thus, the easiest way to change the slope is to change the height of the magnet (assume the magnet is in the air). With larger h, the slope will be steeper as well. As Fig. 19 shows, there are two loading lines. Line 1 has larger slope than line 2, which means the magnet height of line 1 is higher than line 2. Then intersection points between loading lines and *B-H* curves are the working points of magnets.

Taking the *B-H* curves of 20 ℃ and 170 ℃ for examples, 4 intersection points are obtained.

2 intersection points on 20 ℃ *B-H* curve are far beyond the corresponding knee point of *M-H* curve. This indicates the PM will not be demagnetized at 20 ℃.

However, when the temperature is 170 ℃, both H_c and B_r are reduced, and *B-H* curve moves forward to origin point. It can be found that for the 2 intersection points on 170 ℃ *B-H* curve, the point with line 1 is still beyond the corresponding knee point of *M-H* curve.

However, the point with line 2 is beneath the knee point. Thus, the working point is not on the linear segment of *B-H* curve. This working condition leads to irreversible demagnetization of the PM. Even if PM temperature goes back to 20℃, the working point will not go back to the original position. Instead, both amplitudes of H_m and B_m will be lower than original values.

Therefore, in order to avoid the risk of irreversible demagnetization, it is better to increase the height of the magnet.

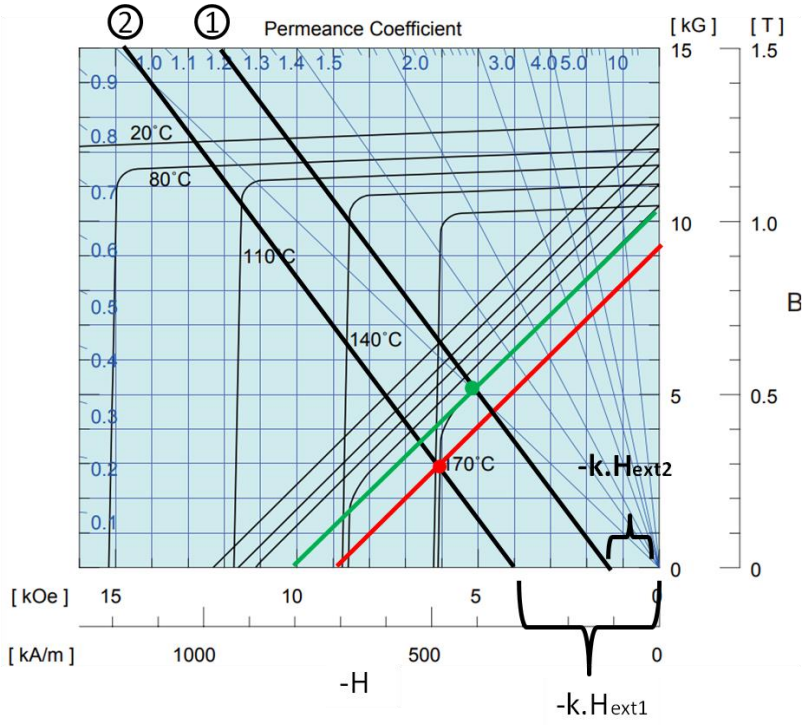

Fig. 20 *B-H* and *J-H* curves of a PM material *vs* machine loading lines with different impacts of external magnetic field

Another scenario is shown in Fig. 20. The loading line may not only be influenced by the magnet height (slope), but also by the external field, which decides the displacement of the loading line. Two loading lines are shown in Fig. 20. The displacement of line 2 is larger than line 1, due to larger H_{ext} of line 2 than line 1. Nevertheless, still taking *B-H* curve with 170°C for example, the intersection point of line 1 and *B-H* curve is safe from irreversible demagnetization. However, the intersection point of line 2 is beneath the knee point, which indicates irreversible demagnetization.

Next, different types of hard magnetic materials are discussed. Normally they include Ferrite, Alnico, SmCo, NdFeB and SmFeN magnets.

Ferrite magnet is made of oxidized iron, such as Fe_2O_3, and metallic particles, such as $SrCO_3$. With certain portion mixing, the compound is subjected to calcination (a thermal treatment), crushing, milling, and some wet or dry process. Finally, the magnet product is made. One interesting property about ferrites is their unique temperature effect. Not like other magnets, whose magnetic field strength decreases with the increased temperature, the magnetic strength of ferrites is proportional to the increase of temperature. Thus, ferrite magnets applications are benefit from temperature rising. Nevertheless, ferrite still have very low *Br* and *Hc*.

Alnico magnet is made of iron, aluminum, nickel and cobalt, sometimes copper and titanium can also be added. Before rare earth PMs came out, alnico was the strongest magnet. The magnets are produced by casting or sintering processes. Proper heat treatment is very important to develop optimal magnetic properties, no matter isotropy or anisotropy. To produce anisotropic Alnico magnet, an external magnetic field needs to be applied when the alloy is cooling from 900 °C to 800 °C, near its Curie point *Tc*. Curie point is the temperature above which PMs lose their magnetic properties. Above this temperature, the ordered magnetic moments of a PM are disordered. Due to the low *Hc*, Alnico is not commonly used on E-Machine applications

For SmCo magnets, no matter they are $SmCo_5$ or Sm_2Co_{17}, the production processes are basically the same. They all need to go through melting, cooling, milling and finally either sintering or bonding. Sintered SmCo magnets exhibit anisotropy magnetic orientation. While bonded SmCo magnets can be both anisotropy and isotropy. SmCo magnets have advantages such as good temperature stability, high coercivity and anti-corrosion.

Nowadays the strongest magnet is NdFeB type magnets, as Fig. 21 shown. The most common type of NdFeB magnet is sintering. Traditional sintering production process has the following steps - melting, crushing, jet milling, pressing/alignment, sintering, annealing and machining. Recently some novel sintering processes have been invented. For instance, Sagawa has invented a new process based on traditional sintering NdFeB magnet process, but without pressing step. This is so called Press-Less Process (PLP). In this case, the corecivity of the magnet can be improved without the increase of Dy content, due to the air interception [54]. Besides, due to the corrosion problem, coating is a compulsory step at the end. The coating material can be either metallic, such as nickel, or polymer, like epoxy, or a mixture of these two.

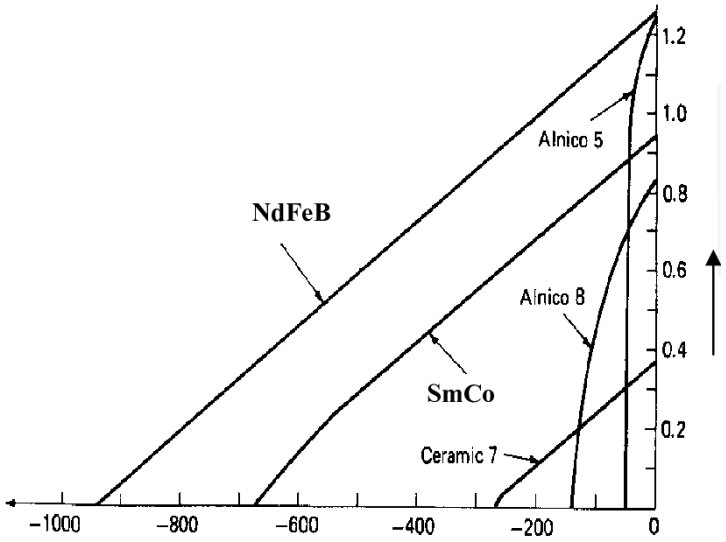

Fig. 21 Typical B-H curves of different types of permanent magnets [55].

Another group of NdFeB magnets are made by bonding process. Bonded NdFeB magnets have less flux product than sintered NdFeB magnets. Because sintered magnet is fully dense magnet powder, while bonded magnet is a mixture of binder and magnet powder. However, the advantage of bonded magnets is that they can easily form into complex shaped part. Moreover, bonded magnets have no corrosion issue, thus no coating is needed. Due to the polymer binder, bonded magnets have much higher electrical resistivity than sintered magnets, leading to much less risk of eddy current heat-up. Bonded NdFeB magnets are normally produced by three crafts –compression molding, injection molding and extrusion molding [56].

- Compression molding is most widely used. Magnet powders with binder are directly compressed together. The process goes through compound mixing, seizing, compacting and machining.
- Injection molding basically uses the same process with compression molding. But instead of compacting, an injection machine is used to inject compound into the mold. Thus it has more shape flexibility than compression molding. The steps of the process are shown in Fig. 22. However, bonded magnets made by injection molding normally have slightly lower energy product than compression molding.
- Extrusion molding uses an extrusion mold machine after seizing step. It is mainly used for producing ring shape bonded magnets. It has very high productivity, while the shape flexibility is lower.
- Based on different molding methods, different binders need to be used correspondingly. For instance, commonly compression molding uses epoxy binder, while injection molding uses Nylon or Polyphenolyne Sulfide (PPS) binder.

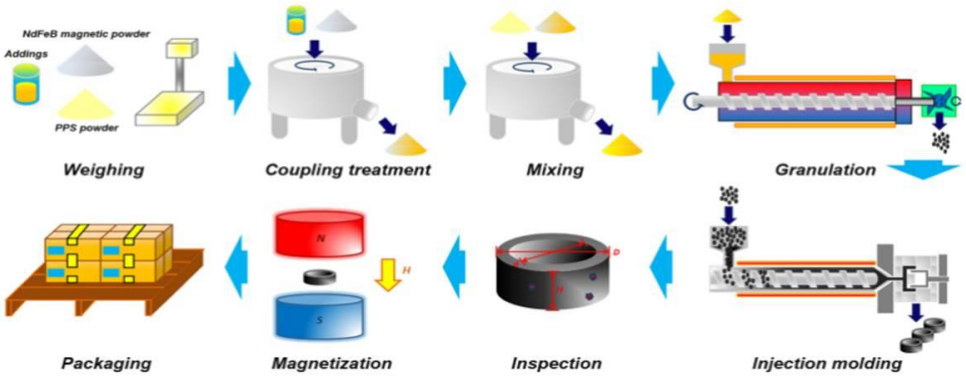

Fig. 22 Traditional process steps for making injection bonded NeFeB magnet [85]

Traditionally, the magnet powder for bonded magnet is isotropic, as the normal crystal particles size of the magnet powder are around 100 μm. While with the development of new magnet powder processes, such as Hydrogenation Desproportionation-Desorption Recombination (HDDR) [57], or the melt spinning process developed by Magnequench [58], the crystal particles sizes of magnet powder become much smaller than 100 μm. Thus, with an orientation field during the molding, the bonded magnet can be anisotropic. Also due to the particle size reduction, there is no need to add heavy rare earth element to increase coercivity, such as the Dy-free HDDR bonded NdFeB magnet invented by Aichi Steel [57]. Anisotropic NdFeB bonded magnets have higher energy products than isotropic ones. As shown in Fig. 23, the energy products of anisotropic bonded magnets (25MGOe/ 200 kJ/m^3) are just in the middle of ferrite magnets (5MGOe/40 kJ/m^3) and sintered NdFeB magnets (45MGOe/360 kJ/m^3), which perfectly fill the gap of the permanent magnets market.

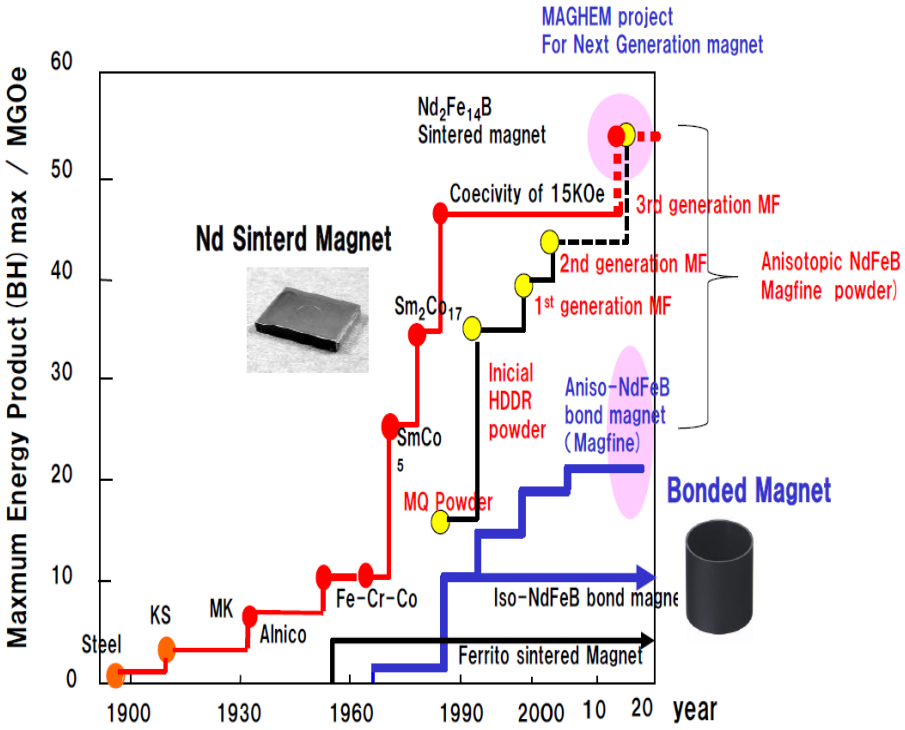

Fig. 23 The development of NdFeB anisotropic magnet powder and bonded magnet [57]

Finally, there are some newly developed types of NdFeB magnets. For instance, Daido [50] invented hot deformed process, which uses hot press and extrusion methods during the pressing step. In this case grain size is highly reduced, which results in a larger heat resistance with less Dy. [51] even made an improvement on hot-deformed NdFeB magnet by doping Nb to enhance the remanence. Another example is Grain Boundary Diffusion (GBD) technology initiated by Shin-estu [52]. It is another way to reduce the usage of Dy, while maintaining the heat resistance of the magnet. Normally GBD treatment is added between the steps of machining and coating [53]. Recently Toyota further pushed the limit of GBD technology, as mentioned in [20]. Their new sintered NdFeB magnet has no Dy nor Tb, and reduced Nd content, while the heat resistance of the magnet is well maintained. Besides the improvement of GBD treatment, lanthanum (La) and cerium (Ce) are used to replace part of Nd content. They claimed the amount of Nd reduction is between 20%-50%. While the process for mass production is still on the way of development.

Besides the PM composites aforementioned, there are some new PM alloys that need to take special attention. For instance, PM alloys such as SmFeN and NdFeN [59] [60] have good anisotropy characteristic, and contain much less rare earth elements due to their crystal structure. However, the main problem is that due to their unstable magnetic properties at high temperature [61]. it is impossible to have sintering process with high temperature. In this case the magnet powder has to be bonded, which leads to low energy products.

The main characteristics of different types of PM are shown in the Table I.

Table I. MAIN MATERIALS PROPERTIES COMPARISON OF DIFFERENT PMs

Materials property	Ferrite	Alnico	Sintered SmCo		Bonded NdFeB		Sintered NdFeB **with Dy/Tb**	**Hot deformed/GBD NdFeB**	Bonded SmFeN/NdFeN
			SmCo5	Sm2Co17	Compression molding	Injection molding			
BH product	Very low	Very low	Middle	High	Middle	Low	Very high	Very high	Middle
Br	Very low	High	Middle	High	Middle	Low	High	Very high	Middle
iHc	Low	Very low	Very high	High	Middle	Middle	Very high	High	Middle
Tc	High	Very high	high	Very high	Middle	Middle	Middle	Middle	Low
Thermal stability	Middle *	Very high	High	Very high	Middle	Middle	Middle	Middle	Very low
Electrical conductivity	Very low	High	High	High	Middle	Middle	Very high	Very high	Middle
Grinding needed	Yes	Yes	Yes	Yes	No	No	Yes	Yes	No
Easy corrosion	Yes	Yes	No	No	No	No	Yes	Yes	No
Raw material cost	Very low	Middle	high	Very high	Middle	Middle	Very high	High	Low
Process cost	Very low	Very low	Middle	Middle	Middle	High	Middle	Very high	High

* Ferrite coercivity is proportional to the change of temperature.

1.3 Overview of electrical machines

1.3.1 DC and AC electrical machines

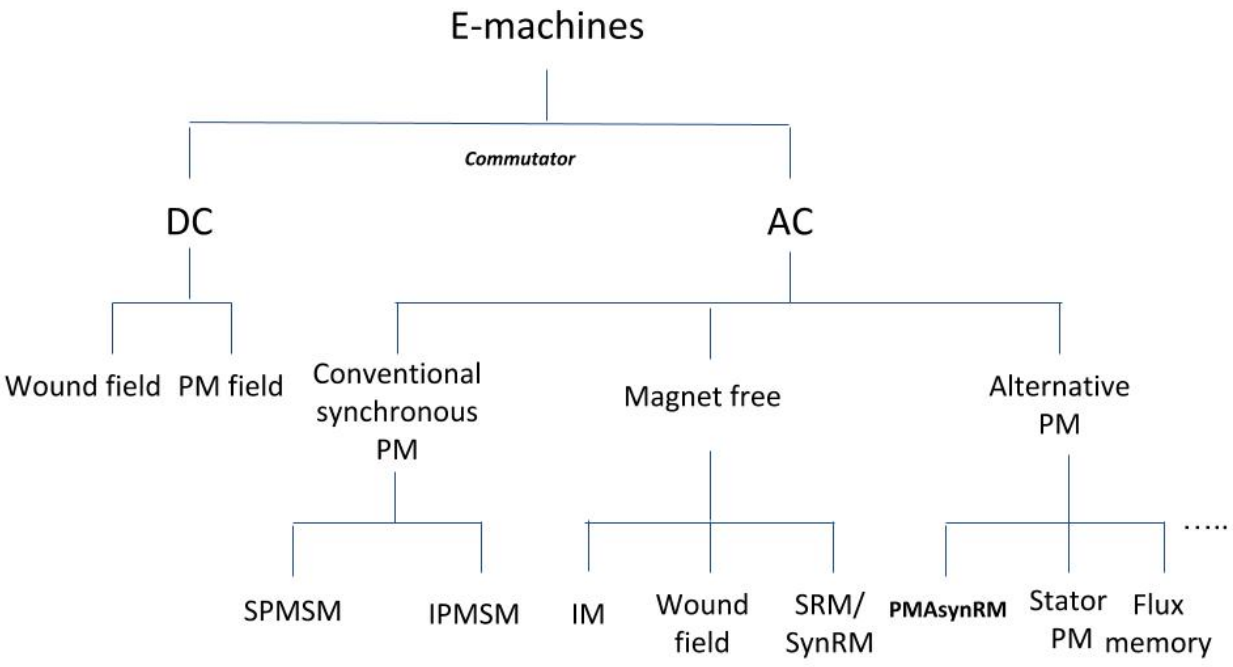

Fig. 24 E-machines family tree

Electrical machines are energy conversion devices between electrical energy and mechanical energy. As Fig. 24 shown, depending on the existence of commutator, which is a mechanical switch, the electrical energy can be the form of either DC or Alternative current (AC). For DC machines, DC directly goes through a commutator. Thus DC can be transferred to AC to generate rotating force. The disadvantage is that wear and tear happens to the mechanical switch, which results in a risk of commutator break down and frequent maintenance. Thus, DC motors are nearly eliminated in (H)EVs traction. While for AC machines, instead of commutator, drive system with power electronics inside is used to transfer the DC of battery into AC supply. AC machines have advantages such as excellent variable speed control and high reliability. Therefore, in this thesis, AC machines are the only interest.

It is necessary to know the existing products and potential electrical machines used for electrical vehicle. The overall compared motors are divided into three categories, which are conventional PM e-machines, magnet free e-machines and alternative magnet e-machines. The pros and cons of each type of motor are investigated with comparison. Thus, new possibilities about electrical machine designs can be illustrated.

1.3.2 Conventional PM synchronous e-machines

Here the conventional PM e-machines mainly refer to radial flux PM Synchronous e-Machines (PMSM). Two types of PMSM are highlighted - Surface mounted Permanent Magnet Synchronous Machines (SPMSM) and Interior Permanent Magnet Synchronous Machines (IPMSM). The stators of these two types of e-machine are normally similar. Thus the main differences are on the rotors. Typical rotors of SPMSM and IPMSM are shown in Fig. 35.

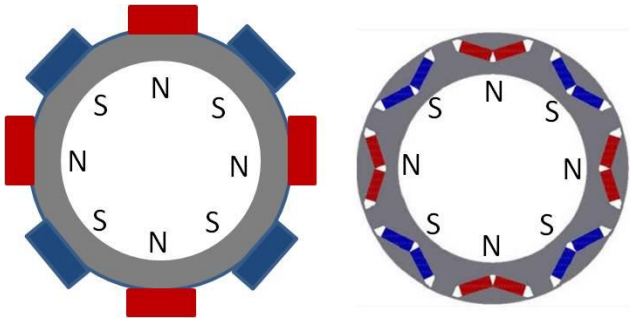

Fig. 25 Typical rotors of SPMSM (left) and IPMSM (right)

For a SPMSM, the torque is named magnet torque. As the rotor can spontaneously generate magnetic flux, all the current of the stator can be used for torque generation. For an IPMSM, as there are PMs inside the rotor, part of the torque is also magnet torque. For the other part of the torque, it is generated by the variation of the reluctance, due to the saliency of the rotor. Therefore, this part of the torque is named reluctance torque. There is one position for the rotor that the reluctance is the minimum, and at this time no reluctance torque is generated. However, for other rotor positions, the reluctance torques are generated in the direction that always trying to reduce reluctance to minimum. Typical torque curves vs. rotor position of an IPMSM with the separation of magnet torque and reluctance torque are demonstrated in Fig. 26. The details about reluctance torque calculation as well as formulas will be shown in Section 2.2.3.

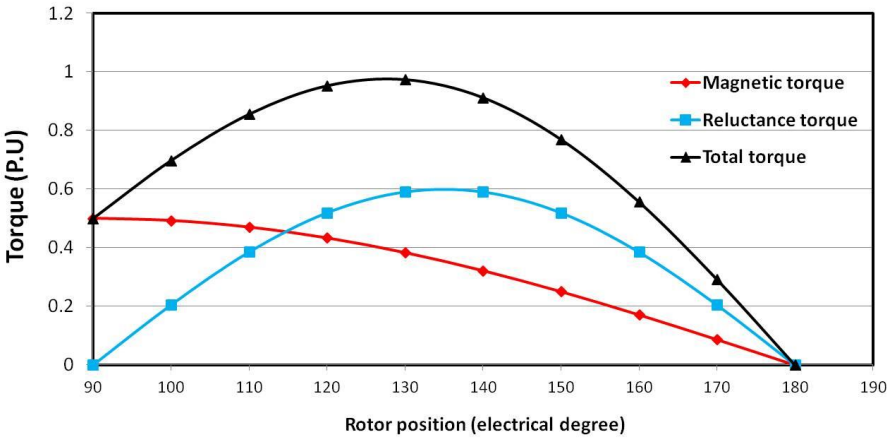

Fig. 26 Total torque and its separation of magnetic and reluctance torques of an IPMSM (motor mode)

It can be found that the positions for the max magnet torque and the max reluctance torque are different. Thus, it is necessary to calculate the optimal position for the max total torque. However, for SPMSM, the max torque position is always the same, which is 90° in the plot. More torque curves analysis will be discussed in Chapter 2.

Nowadays these two types of e-machines are widely used in automotive industry. However, due to the PMs supply risk, it is necessary to reduce or even remove the PMs usage. Thus, in the following studies, other types of e-machines with less PMs are investigated.

1.3.3 Magnet-free e-machines

Typical magnet free machines include Induction Machine (IM), Switch Reluctance Machine (SRM), Synchronous reluctance machine (SynRM) and Wound Rotor Motor (WRM).

- IM, or so called asynchronous electrical machine, is an AC E-machine, which using electromagnetic induction between stator and rotor to produce torque and rotation. This induction is caused by the speed difference, or so called “slip”, between the rotor and stator. The slip induces currents inside the rotor conductors, which are commonly squirrel-cage type. These currents in turn create the magnetic field that together with the stator magnetic field to produce the torque. The advantage of the IM is that no electric connection is needed to the rotor.
- SRM is a type of stepper motor which divides a full rotation of the rotor into a number of steps equally. The torque is produced through the attraction between stator and rotor by using rotor saliency. Thus it also uses reluctance torque. SRM needs special motor drive system, which generates step pulse waveforms instead of sinusoidal waveforms to control the voltage and current.
- SynRM also uses reluctance torque. Actually if the PMs of an IPMSM are removed, it will become a SynRM. Therefore, the drives of SynRM are similar to traditional PM synchronous machines or IMs, which use sinusoidal waveforms to control the voltage and current.
- WRM is also a type of synchronous machine, the main difference between WRMs and PM machines is the flux generation - WRMs use rotor wound coils with DC current to generate flux, instead of PMs. Thus, the efficiencies of WRMs are certainly lower than PMSM

The most significant advantages of these magnet-free machines are their low cost. As a case study shown in Table II, with the same performances (the same torque/speed profile) and outer dimensions, three electrical machines were compared – an IPMSM, a SRM and an IM. These three electrical machines are shown in Fig. 27. It was found that once permanent magnets are removed from electrical machines, the materials cost drops dramatically.

Table II. MATERIALS COST IN A 30 KW TRACTION MOTOR FOR A MOTOR WITH RARE EARTH MAGNETS ('INTERIOR PERMANENT MAGNET MOTOR') AND TWO OPTIONS WITHOUT RARE EARTH MAGNET [34]

Motor type	Materials	Laminated steel	Copper	NdFeB magnet	Totals [kg/USD]
	USD/kg	1.3	6.6	132	
IPMSM	Weight	23.9	6.0	1.30	31.2
	Cost	31.0	39.5	171.6	242.2
SRM	Weight	19.3	7.4	0	26.7
	Cost	25.1	49.1	0	74.2
IM	Weight	18.0	18.2	0	36.3
	Cost	23.4	120.4	0	143.8

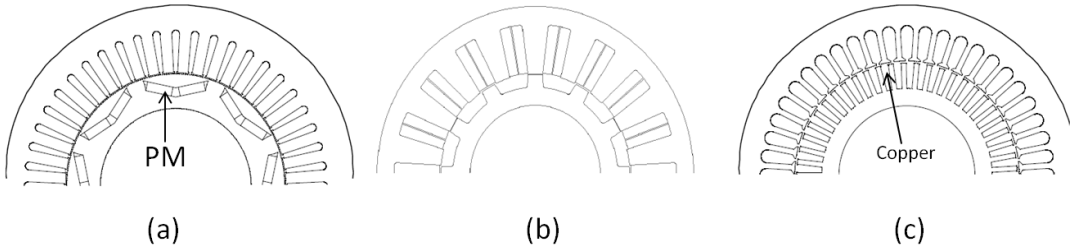

Fig. 27 The cross sections of three e-machines for comparisons: (a) IPMSM, (b) SRM, (c) IM, redrawn from [34]

Besides, currently a few magnet-free machines are equipped on commercial vehicles already [30]. For instance, Automaker Tesla has used IM on their products, as the rotor shown in Fig. 28; Renault has used WRM in their vehicles, as the rotor shown in Fig. 29.

Fig. 28 Tesla induction motor rotors with copper squirrel cage and end cup [7]

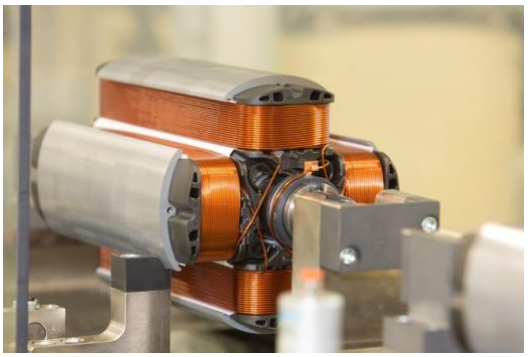

Fig. 29 Renault WRM rotor with copper wound winding [35]

However, magnet-free machines also face several serious problems. The common issues are their low power or torque density and lower efficiency compared to PM machines. These two points are extremely important to (H)EVs applications. The space for traction motors installation of HEVs usually is very limited. Also a small drop of efficiency may result in large cost increasing in a long term, as Fig. 30 shown, most of the energy consumption is in the user phase. The common pros and cons, as well as improvement methods of each magnet-free machine are listed in Table III.

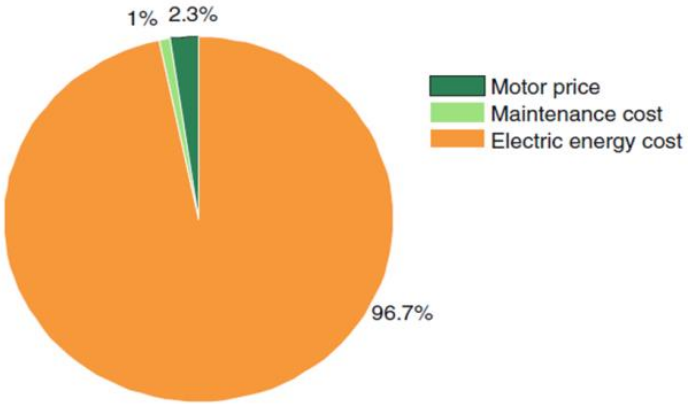

Fig. 30 Life cycle cost breakdown for an 11kW motor operated 4000h per year [33]

Table III. COMPARISON OF MAGNET-FREE MOTORS [34] [7]

Motor types	**Advantages**	**Disadvantages**	**Improvement**
IM	-Design and control techniques are well developed	-High losses produced by rotor conductors, hard to cool down rotor -Thermal variation highly influence performances	-Replacing Aluminum by Copper for the rotor conductors
SRM	-Low cost -Robust rotor	-Large noise and torque ripple -Low torque density -Low efficiency -Special controller is required	- Optimized machine design to reduce torque ripple & noise, and increase torque density. -Implement good iron materials to reduce iron loss, thus improve efficiency.
SynRM	-Low cost - Common synchronous drive system	-Low power factor -Low torque density -Weak mechanical strength of the rotor due to thin bridges	- Optimize rotor cavities to increase saliency and reduce mechanic stress.
WRM	-Variable flux control	-Slip ring is required to provide conducting path, as well as additional switch components for converter. -Low torque density -Low efficiency	- Improve the material properties of the slip ring - Switch slip ring to contactless transformer

Some novel designs to improve the torque density and efficiency of SRM and SynRM are found recently. For instance, A. Chiba, et al [36] - [38] attempted to increase the torque density of a SRM by three means:

- Increasing stator and rotor pole number to increase torque density.
- Most importantly, a lamination of high silicon (6.5%) steel with only 0.1 mm thickness is applied in order to significantly reduce iron losses at high speed.
- The machine is designed for high speed operation. Because the losses during the high speed operation is dominated by iron loss. The SRM with thin lamination has advantage on iron loss over conventional IPMSM. Besides, by coupling a reducer with a large speed reduction ratio, large torque outputs can still be achieved.
- Then to avoid large windage loss at high speed, the radius of the rotor should be kept relatively small.

In this case, the torque density and efficiency of SRM can be comparable with IPMSM used in the second generation Toyota Prius. However, as mentioned in the material studies, the common gauge of silicon steel is around 0.35 mm. 0.1 mm thickness lamination is still a niche technology. Thus the cost is very high, not to mention other technique challenges such as the influence of punching and cutting. Moreover, it is possible to increase the complexity of other powertrain components, such as converters - due to the increase of switch frequency for high pole number, as well as high rotation speed, the converter complexity escalates, so does the cost.

Other efforts have been spent on SynRM with axial laminations to increase the saliency [39]-[43]. With higher saliency, the torque density will be higher as well. Fig. 31 shows an example of axially laminated rotor. Each pole comprises 5 pieces laminations in radial direction.

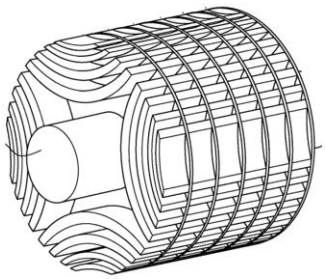

Fig. 31 Schematic diagram of an axially laminated rotor with a modular structure [42]

Sometimes in order to further increase the saliency, the lamination material is even anisotropic. In this case, the machine is called Axial Laminated Anisotropic (ALA) SynRM. From some prototypes experiment [40] it was found that at the rotation speed 500 rpm, and with the same given peak torque, the efficiency of an ALA- SynRM is higher than an IM, with similar configurations such as drive system and stator ampere turns. While the efficiency of a traditional transversal laminated SynRM was lower than the IM.

However, as Fig. 31 also demonstrated, the mechanical assembly is extremely difficult. The assembly needs to be done by brackets or binder, not to mention their mechanical strength. Thus, ALA-SynRM may only suit for low speed applications.

Therefore, from the study above, there are still many challenges to replace PM machines with magnet-free machines.

1.3.4 Alternative PM e-machines

Secondly, alternative magnet electrical machines are investigated. These kinds of e-machines still use magnets to produce flux, but different from conventional PMSMs.

PM assisted Synchronous Reluctance motors (PMAsynRMs) has similar topology with IPMSMs. However, the essential difference between these two e-machines is the dominant torque. For IPMSM, the dominant torque is still magnet torque. While for PMAsynSMs, PMs tend to work as a power factor corrector. Thus, the dominant torque is reluctance torque [43].

Another group of alternative magnet e-machines uses magnets that are REEs free, which significantly reduces the cost of magnets. For instance, a newly designed ferrite magnet motor was used for tractions in [7] [45]. However, these kinds of motors face the problems such as difficulty of manufactures or demagnetization.

For other alternative magnet e-machines, usually the structures are more complicated, such as flux switch PM e-machines [46] and flux memory e-machines [47].

A schematic plot of a simple flux switch PM e-machine is shown in Fig. 47. It is found that PMs are positioned in the stator instead of the rotor. Both stator and rotor have saliency. The torque is generated by both PMs and reluctance. Based on the control theory of the machine, it is similar to SRM. However, the magnet strengthens the flux linkage, thus the torque density is higher than SRM.

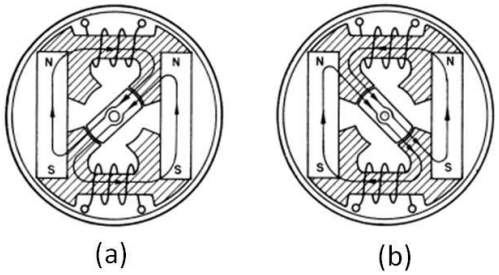

Fig. 32 schematic plot of a single phase PM flux-switch machine (a) armature with positive current magnitude; (b) armature with negative current magnitude [48].

A schematic plot of a simple flux memory e-machine is shown in Fig. 33. The machine normally uses PMs with lower coercivity and high remanence, such as AlNiCo, for the flux memory. Thus, by using the magnetization coil to control the PM magnetization states, the flux can be varied, which is similar to a WRM. While with the help of PM, the flux generated from the rotor can be larger than what in WRMs. Besides, compared to PMSM, the flux weakening does not demand high current. The torque speed range can be extended, and the efficiency can be improved as well. However, from the Fig it can be found that operations of demagnetization and remagnetization need to run at linear recoil loop region. This requirement makes the control very difficult. Thus, other PM materials with better linear hysteresis properties, such as Ferrite or SmCo need to be considered.

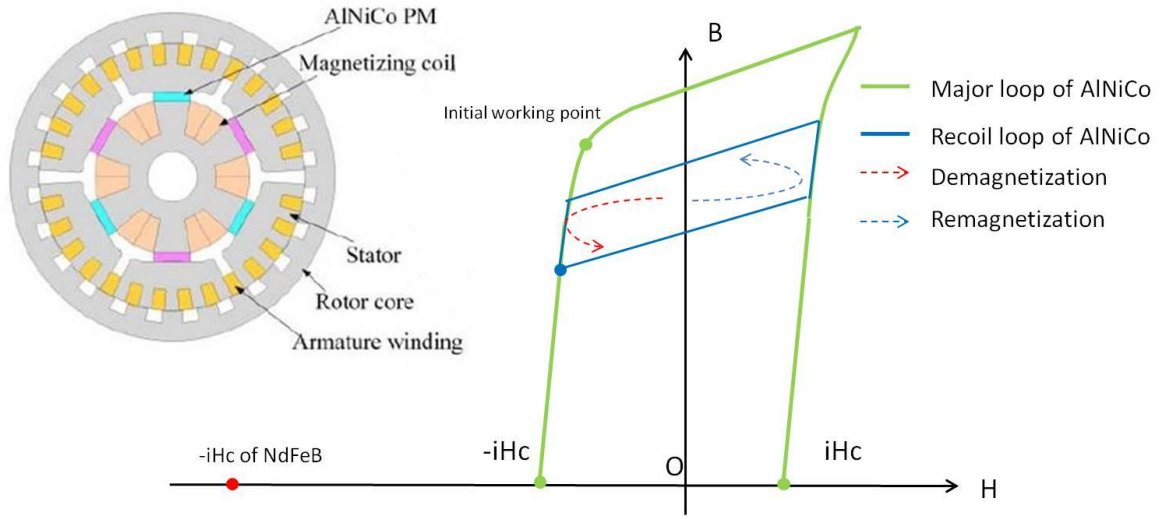

Fig. 33 A demonstration of a memory flux machine model and the control of the hysteresis loops of an AlNiCo PM [47].

In summary, the specific pros and cons of each motor are listed in Table IV. Typical model or prototype of each alternative magnet electrical machine is shown in Fig. 34.

Table IV. COMPARISON OF ALTERNATIVE MAGNET ELECTRICAL MACHINES

Motor types	Advantages	Disadvantages	Improvement
PM assisted Synchronous Reluctance motor (PMASynRM) [7], [43], [44]	-Reduced magnets usage -Offer a wide constant-power operation meanwhile achieve the controllable generator mode operation	-Difficult manufacture -Mechanical weakness at high speed -Demagnetization -Torque ripple -Low power factor	-Simplify manufacture process -Add more iron bridges -Increase magnet thickness -Barrier optimization
Ferrite magnet motor [7], [45]	-Low cost -Negative temperature coefficient of Ferrite magnet	-Ease of demagnetization -Low torque density	-Careful electromagnetic design
Flux-switching PM e-Machine (FSPM) [46]	-Magnet in stator, a more reliable rotor structure, suit for high speed operation -Easy to control magnet temperature rise -Enable module assembly	-Heavy saturation lead to weak over-load capacity -High magnet volume	-Using E-core or C-core topologies -Replacing part of magnet with coil for magnetic field production
Flux memory e-machine [47]	-Using Alnico magnet, relatively high torque density. - Online magnetizing (Similar to wound rotor motor), flux variable, enabling large efficient area. -Free of Dy element, cost reduction.	-Complex structure. - Hard to control the nonlinear hysteresis curves during online magnetizing. -Demand new control theory. -Risk of irreversible demagnetization -Contain Cobalt	-Applying new hysteresis algorithm such as Preisach model combined with FEM study. -Hybrid PMs strategy – using DC magnetized poles or using new magnets with less Cobalt

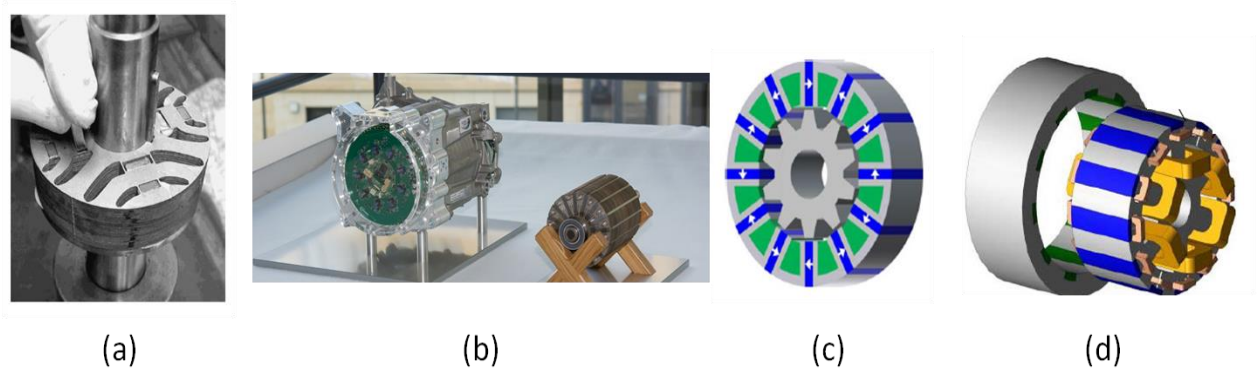

Fig. 34 Examples of alternative magnet electrical machines (a) a rotor prototype of a PMASynRM and its magnet insertion process [44], (b) a prototype of ferrite magnet electrical machine with its rotor [45], (c) a 3D model of a typical FSPM [46], (d) a 3D model of a dual-sided PM variable flux memory machine [47].

In summary, for magnet free motors, although the production cost is lower than PM motors, their inadequate performances as well as different problems make them hard to be commercialized. Therefore, PMSMs are indispensable at present. Next, to understand the requirements of the e-machines in (H)EVs, as well as how they operate, the following sections will discuss electric and hybrid powertrain systems mainly focusing on electrical machines.

1.4 Electrical and Hybrid powertrain systems

Compared to ICE vehicles, (H)EVs have many benefits such as fuel efficient, Zero Emission Vehicle (ZEV) mode and noise reduction, etc. Thus (H)EVs have a large positive impact on social environment and personal drive experience.

For pure EVs, their powertrains are mainly comprised of energy storage system (mainly lithium battery nowadays), electrical machines and electrical control drives. Battery transfers chemical energy to electrical energy, but only direct current (DC) can be produced.

For hybrid electrical vehicles, the complete powertrain systems are the combination of ICE and electrical system. There is a large diversity on hybrid powertrain systems. First, depending on the degree of hybridization, it can be categorized as mild hybrid, full (or heavy) hybrid and plug-in hybrid. A typical mild hybrid system has a 48V DC battery and an electrical machine with power less than 20 kW [25]. Most of mild hybrid vehicles cannot be solely driven by motors due to their limited power (except few A-segment cars). Otherwise if the voltage is way higher than 48V (normally in the range 200 – 300 V DC), the power of electrical machines can be higher than 20 kW. In this case, it is called full hybrid systems, which is enough to propel the vehicle solely. Finally, if the battery of a hybrid vehicle can be charged through charging station, it is a plug-in hybrid vehicle. Normally plug-in hybrid vehicles have more power and higher voltage than full hybrid. Also, not like plug-in hybrid, the battery of full hybrid vehicle cannot be charged by external charge station. A general classification of hybridization according to power level is shown in Fig. 35.

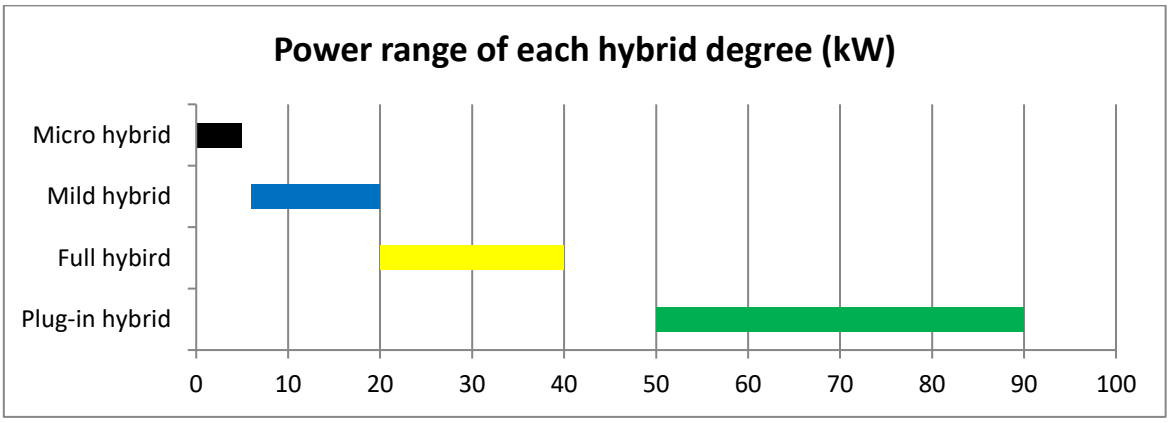

Fig. 35 General classification of hybrid degree from power level [27]

Second, the hybrid powertrain systems can be categorized by the architecture of the coupling between electrical machine and ICE powertrain. Generally, the systems can be divided to series, parallel and power-split hybridizations.

Series hybrid uses engine to drive an electrical generator to charge the battery, instead of propelling the wheel directly. While one more electrical motor is used to drive the vehicle solely. Thus, it has advantages such as good mechanical decoupling between wheel and engine, enabling the same drive experience with pure EV. The disadvantages are that ICE needs to be converted twice to reach the wheels. Thus, the whole system is not such efficient. Also it needs two electrical machines at least. A good commercial example of series hybrid is BMW i3.

Parallel hybrid combines the power of ICE and electrical machine together to propel the wheels. Thus it has advantages such as flexibility of power choices between electrical machine and ICE. Generally, the power plants can be also smaller than series hybrid, as only one electrical machine is able to realize the system. Thus regardless of manufacturing issues, the system can be more efficient than series hybrid. However, a parallel hybrid system is naturally more complex than a series hybrid system, since the joint between electrical machine and ICE is complicated. Moreover, the energy management system making the power splits also needs to be more intelligent than series hybrid.

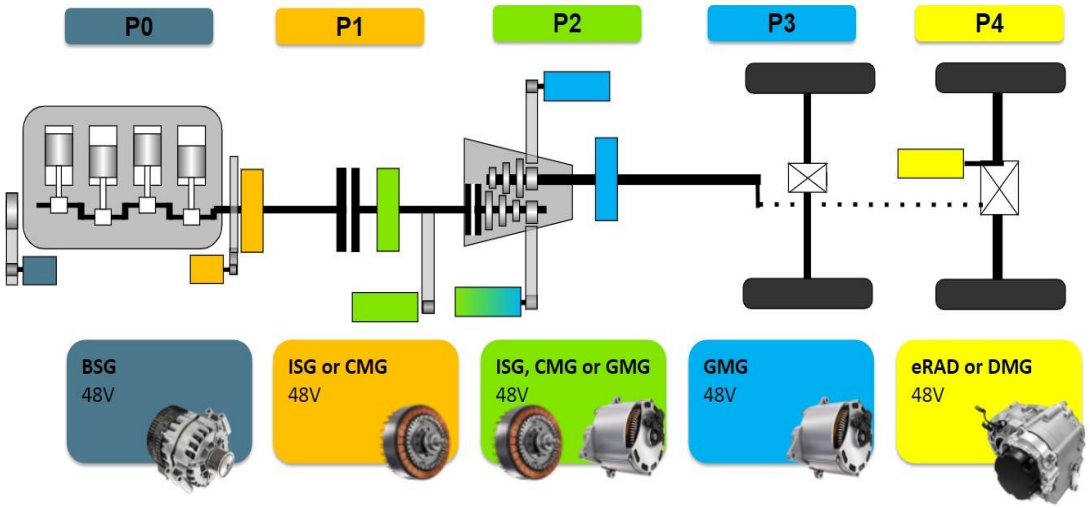

Fig. 36 Hybrid electrical vehicle powertrain structure schematic plot

In a parallel hybrid powertrain system, there are mainly 5 different positions for the coupling of electrical machine and ICE. They are named from P0 to P4, which are shown in Fig. 36. The summary of P0~P4 are shown below:

P0: A belt system directly couples an electric motor with ICE on the front end auxiliary drive, as Fig. 37 shows. The assembly is simple and cheap. But the impossibility of turning off ICE interferes with the hybrid functionalities such as recuperation, and prevents Zero Emission Mode (ZEV). Thus, the potential to cut CO2 emission is low.

Fig. 37 A prototype of P0 belt drive system (left) and its coupled e-machine (right), filmed by author

P1: An electrical machine is directly coupled with the ICE crankshaft on the back end auxiliary drive, as Fig. 38 shows. The functionality is the same with P0. Thus, same disadvantages with P0 may have in P1.

Fig. 38 A prototype of P1 mild hybrid system and its e-machine made by Mercedes [26]

P2: The electric machine is placed between the engine and the transmission. The electric machine can be decoupled from the engine for zero emission drive thanks to the disconnecting clutch. There are two types of P2 coupling. The first one is called P2 inline, where the machine is placed at the main drive axis, it has the same speed than the engine. The second one is called P2 offline, where the machine is placed parallel to the main axis and is connected with a chain of reducer. Besides the functions of P0/P1, P2 has additional function of (ZEV). The regenerative braking can also be more efficient, which increases the potential of CO2 emission cut down.

P3: An electrical machine is integrated at the gearbox output with an additional reducer. It has the same functionalities as P2. However, P3 needs to be associated with a P0 machine for specific situation, such as generation mode only.

P4: The electric machine or several are directly integrated in the rear axle, with one or two speed gearbox or just in-wheel. This unit guarantee All-Wheel Drive (AWD). It has all functionalities like P2 and P3, except that the

generation mode is prohibited due to safety concerns (vehicle dynamic instability). Thus a P0 generator is also needed.

The positions of hybrid can suit for all degrees of hybridization, such as mild hybrid, full hybrid and plug-in hybrid. Here taking mild hybrid 48V system for example, the assembly difficulty, functionality, fuel saving and CO_2 reduction compared to combustion vehicles are listed in Table V, where the data was collected from tier 1 suppliers.

Table V SUMMARY OF CHARACTERISTICS OF P0 TO P4 PARALLEL HYBRIDS

Architecture	Assembly	Functionality	Fuel saving(48V) [28]	CO2 reduction[27]
P0: ICE coupling with belt	Easy	Simple	3-7%	7.4%
P1: ICE coupling with crankshaft	Middle	Simple	3-7%	8.7%
P2: ICE decoupling with crankshaft	Hard	Rich	10-12%	10.7% or (20%-21.7% [29])
P3: Gearbox coupling	Hard	Rich	12%	-
P4: Axles coupling	Medium	Very rich	10-12%	13.2% (+P0)

Finally, to combine the advantages of series and parallel hybrid systems, power-split hybrid is invented, as Fig. 55 shows. Power-split hybrid has all functionalities of both series and parallel hybrids. It can utilize the entire power more efficiently than other hybrid architectures. However, the complexity of the system rises up on all levels. The most distinguished example of power-split hybrid is Toyota Prius.

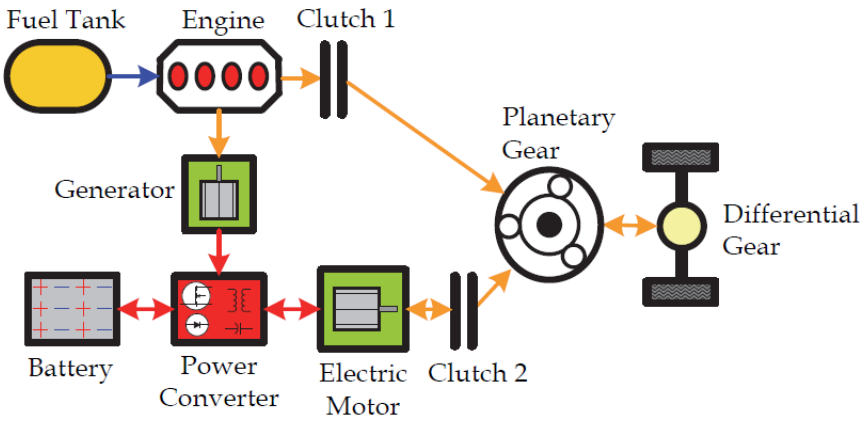

Fig. 39 Architecture of a typical series- parallel HEV [31]

While no matter what hybrid structure is, it always requests the electrical machine with high power and torque density, as well as high efficiency. As discussed in the last section, there are different vital disadvantages for other e-machines apart of conventional PM e-machines. Therefore, currently HEVs cannot get rid of conventional PMs electrical machines. In practical this is also true, as in the market most of HEVs use PM e-machines [32].

In this case, magnets reuse method for conventional PMs e-machines becomes a promising way to relieve the PMs supply risk. The following section will show the state-of- the-art research on PM machine designs related to PM reuse and recycling.

1.5 Literature review of PM e-machine magnets reuse

1.5.1 Magnets reuse problems of PM e-machines

Recent magnet disassembly technologies of PM electrical machines are investigated in this section. The purpose is to summarize the previous methods and experiences in this field.

There was a well-known project during 2011 to 2014 named MORE (MOtor REcycling) [62][63]. It was led by Germany research institute Fraunhofer ISI, and numerous industrial giants such as Siemens AG and Daimler AG. The project had explored several measurements of magnet disassembly from EoL traction motors of EVs and HEVs.

The EoL electrical machines they investigated were Surface mounted Permanent Magnet Synchronous Machine (SPMSM) and IPMSM, which are the mainstream radial flux PM electrical machines that had been widely used in (H)EVs. For the disassembly process of SPM motors, thermal and chemical treatments have mainly been used. At the beginning, the researchers attempted to directly use mechanical methods to remove the magnet from SPM motors. However, it was found that the magnets can be easily damaged due to their brittleness and the inappropriate tools the researchers applied. Hence, the researchers switched to thermal treatments. The idea was to heat up the rotor in order to decompose the adhesive that used to fix the magnets. However, the problem appeared that the glue started to dissolve at 200 ° C, while the demagnetized temperature for the NdFeB magnet is around 350° C (Different kinds of NdFeB magnets have different demagnetized temperatures, but generally it should be higher than 300° C). Thus, the individual magnet may uncontrollably fly out from the rotor due to leftover magnetic forces. This might damage the magnet itself, as well as the heating stove. In this case, a temperature resistant fixation is required for the magnets. A heat resistance metal sleeve over the rotor surface was used by the researchers, as Fig. 40 shows. Besides, the decomposition process of the glue can lead to heavy smoke. A more environment friendly extraction method for the decomposition products is therefore necessary.

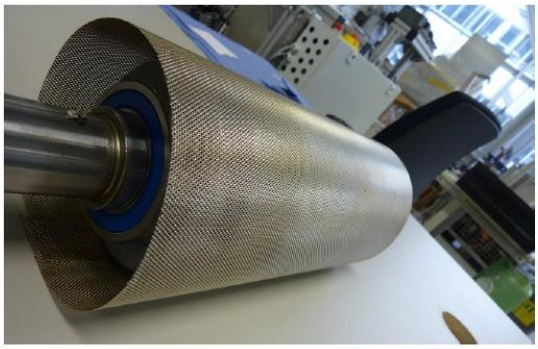

Fig. 40 The temperature resistance metal sleeve over rotor surface to fix magnets [62]

After the thermal treatment, complicated chemical treatments have to be implemented. In order to remove the leftover bandage and adhesive materials, some chemicals such as NaOH, boiling dimethylformamide and acetone need to be sprayed on the magnets surface. However, the effect of the treatment was not always ideal. Contaminations of penetration adhesive were still found on the magnets under the microscope after thermal and chemical treatments.

For the disassembly process of IPM motor, thermal and mechanical treatments have mainly been used. As the rotor consists of several skewed rings, the rotor needed to be separated into several pieces first. Then each piece was sent to furnaces for glue melting. Following as Fig. 41 shows, punching and pressing devices are utilized to extract magnets. In order to prevent the damage caused by the attraction or repulsion forces of adjacent magnets, the magnets were forced to pass through separated tubes to a conveyor belt during the extraction.

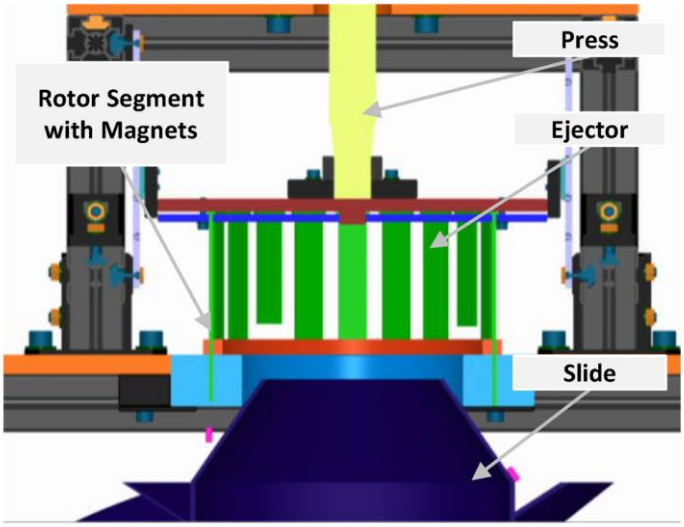

Fig. 41 Magnets dismantling concept of IPMs [62]

However, the feasibility of this method for real products is suspicious, as the magnets are not fully demagnetized, strong attractive forces between magnets and laminations still remains, it is very hard to directly push out magnets. Besides, many rotors also need resins casting during assembly process to make the structure robust. The fixation of resin can be extremely firm; it is almost impossible to remove them. How to solve this problem still left a question mark.

Therefore, according to the aforementioned magnet disassembly methods, researchers face several difficulties:

1. High level of plant investment and long disassembly process. Such as complex magnet mechanical removal devices, heat-up stove, chemical treatment facilities. What worse, even if high investment has been made, it can only process very limited types of electrical machine. Once the techniques of electrical machine altered, the disassembly plant might no longer be valid. Thus, mass production is an issue.
2. Non-relevant aide materials, such as glue or plastic, cause additional cost. Besides, due to contamination or leaching from these aide materials, the recycling of the magnet is impeded. Moreover, the chemical treatments are usually health hazards. For instance, dimethylformamide has been classified in Group 2A carcinogen list by International Agency of Research on Cancer (IARC).
3. NdFeB magnets are always brittle. However, there is no effective way to protect them from damages. Metal sleeve might not be enough for the protection. Moreover, the qualities of the magnets after disassembly remain unknown. For instance, thermal treatment in air might make the surface of the magnet oxidizes, even if there is a nickel jacket on the surface of the magnet. Besides, thermal treatment may decrease the mechanical stiffness of NdFeB magnets. Regarding the magnet inserting process [64], [65], [66] of current IPM electrical machines, there are many difficulties to pull out magnets without damage, such as the control of pull-out forces, glue removal, demagnetization and automation process.
4. The magnets shape needs additional machining steps to fit in a new rotor design once the cavities shape changes.

These difficulties must be carefully considered in the next phase electrical machine design. Thus, in order to find an ideal solution, alternative electrical machine designs and techniques have to be reviewed besides conventional SPM and IPM electrical machines. The pros and cons of each type of electrical machine that related to magnets disassembly and recycling should be clearly known.

1.5.2 State-of –the- art of magnets reuse methods for PM e-machines

From the discussion above, it is still necessary to apply PM traction motors for (H)EVs. Hence, two approaches are proposed for PM reuse and recycling - one approach focuses on magnets reuse and machine easy disassembly. The other one focuses on using recycled magnet products.

For the ease of disassembly, 4 novel design strategies were proposed in recent studies –Complete magnet reusing, Modular magnet pole design, Magnet powder reusing and Modularity design. Fig. 42 shows these 4 design strategies with their pros and cons regarding the four magnet reuse difficulties listed in the last section.

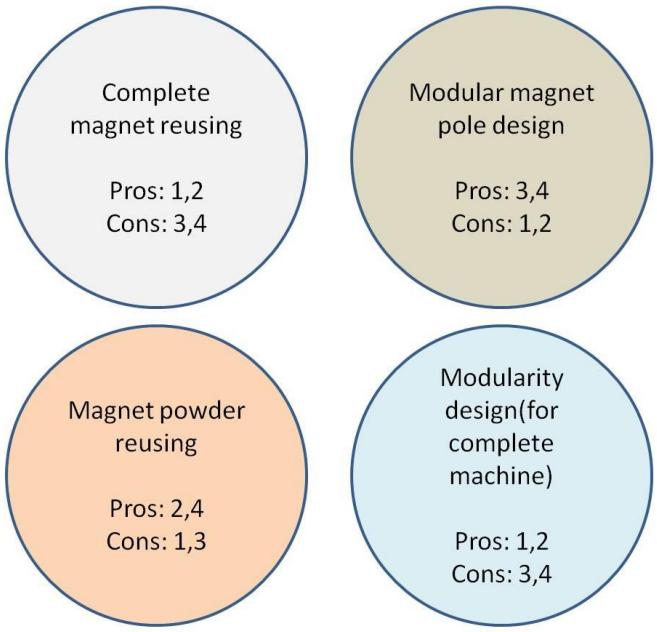

1. High level of plant investment and long disassembly process.
2. Non-relevant aide materials, such as glue or plastic, cause additional cost.
3. No effective way to protect magnets from damages.
4. Magnets shapes need additional machining steps to fit in a new rotor designs.

Fig. 42 Pros and cons of 4 different electrical machine design strategies regarding magnet reuse (pros indicates difficulty can be overcome, cons means not).

For recycled magnet usage, it is important to know the commercial possibility regarding the cost and performances of the corresponding PM machines. The details of these strategies are shown below.

1.5.2.1 Complete magnet reusing

The most straight forward way of reusing permanent magnets is to reuse the whole magnet piece, such as a magnet ring or magnet bulks. For instance, as [67] presented, the rotor is basically a magnet ring made by bonded NdFeB magnets. The magnet ring is magnetized as a continuous Halbach array, which makes the airgap flux sinusoidal concentrated, as Fig. 59 shows. As for the reason of using bonded magnets instead of sintered magnets, it is mainly due to the high cost and large difficulties of magnetization for sintered magnets. Also unlike sintered magnet, which always needs adhesive agent for fixing, bonded magnets do not require it, which results in easy extraction process.

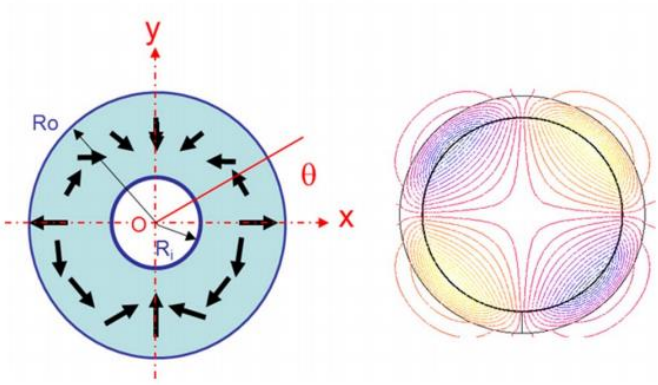

Fig. 43 An example of 4 pole internal field Halbach Cylinder (left) and magnetic orientation field distribution (right) [67]

The authors compared the results of the rotors with and without rotor iron back, it is found that due to the shield effect of Halbach array, the iron back has tiny influence on the motor electromagnetic performances, regardless of its mechanical function. Thus, the rotor can be simply a magnet ring and might be directly reused.

Thus, regarding the disassembly difficulties, difficulties "1 - cost and scale" and "2 - aide materials" can be solved. Difficulty "3 - magnet protection" is uncertained depending on the design of rotor bracket. However, difficulty "4 – magnet shape" is still a problem - To reuse the ring for the next new motor design, it has no choice but to keep the rotor shape all the same. However, this is not always feasible in reality. So at the end, the magnet ring always needs to be smashed for new magnet production.

Besides, there are some other issues regarding the machine design. The magnet ring designs can only be applied on few scenarios in order to gain large airgap area and good mechanical strength - normally they are outer rotor design. To sufficiently take the advantages of Halbach array, it always goes to high pole number to obtain high flux concentration on the airgap. In this case, it is better to choose concentrated winding configurations. However, this combination leads to several issues: due to the high pole number, the top speed is limited to relatively low range. There is a high chance to induce large eddy current in the magnet ring due to high sub-harmonics [68]. Only if the resistivity of magnet is high, such as bonded magnet, or segmented magnets, the eddy current can be inhibited. Thus, there are huge limitations on the application scenarios of complete magnet reusing.

1.5.2.2 Modular magnet pole design ("Lego design")

The first strategy is modular magnet pole design or so called "Lego design". As Fig. 44 shown, from (a) to (d), a solid shaped magnet pole can be continuously divided into small and standardized segments. Thus, the small magnet segments can be reused for future generations, no matter what the magnets shape will be.

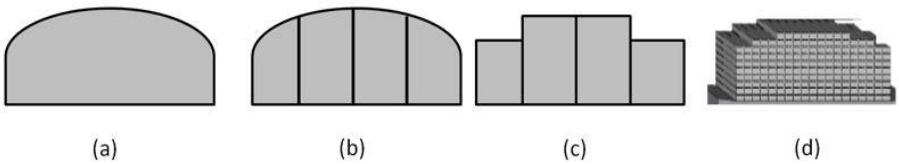

Fig. 44 (a) A solid piece of bread loaf magnet. (b) Segmented bread loaf magnet. (c) Combined rectangular shape magnet. (d) Magnet pole with standard segments for reusing [69].

A related project was carried by S. Hogberg, et al. [70] [71] in Denmark recently. They have demonstrated a way of reusing magnets from wind turbine, from both aspects of machine design and disassembly process. For the new machine design, they have chosen SPM machine for their fundamental design as well. The idea was to use

segmented magnets with standard size. The magnet poles were then formed by these magnet segments with massive glue. Considering the severe working environment of wind turbines, the magnet poles could be covered by stainless steel containers. Thus, difficulty "4 – magnet shape" is solved. Then for the disassembly process, they have mainly chosen thermal treatment for glue melting and magnet demagnetization. The heating temperature was well controlled around the Curie point of the magnet. The degradation of the magnets was also studied. They found that by choosing proper magnet coating, magnets degradation after thermal treatment could be well limited. For sintered NdFeB magnets, the best coating to prevent degradation was NiCu+Epoxy. Thus, the difficulty "3 – magnet protection" is solved.

The main problems of this design are the increased cost due to the segmentation and additional glue, as well as the concern if the disassembly is really energy saving and environmentally friendly. Thus difficulties "1 - cost and scale" and "2- aide materials" still have many question marks.

Besides, as the active space of magnet pole is occupied by the massive glue, average torque is reduced. In order to compensate the lost torque, the machine has to be slightly over-dimensioned. For this case, the length of the machine was increased by 3.5% comparing to the original one. After all, this design was for wind turbine application. Compared to (H)EV applications, the requirements such as torque, speed and operating temperatures are considerably different. Therefore, this strategy may not perfectly suit for motors used for (H)EVs traction.

1.5.2.3 Magnet powder reusing

Following the "Lego" concept, the magnet segment can be further divided into magnet powder. Thus, this is called magnet powder reusing. P. Kjeldsteen et al. [72] have developed a novel manufacturing method called Ingress Protection (IP) magnet. The idea is to directly press and seals a kind of isotropic NdFeB magnet into a hermitically stainless steel container prior to magnetization. The magnet has no bind agent or coating. Fig. 45 shows the schematic of production.

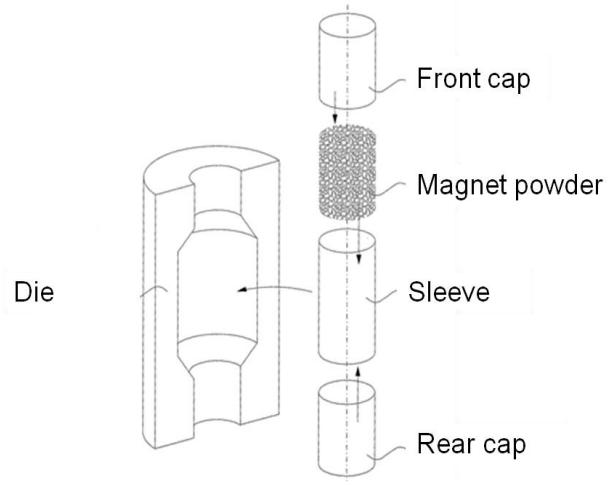

Fig. 45 IP magnet rotor production schematic diagram [72]

The advantages are that random magnet shape is able to be formed and glue-free production is used for easy extraction. Thus, difficulties "2- aide materials" and "4 - magnet shape" can be solved. While no matter how simply it looks to extract magnets, demagnetization is always the first step for disassembly. Moreover the demagnetized chunks which taken out from the rotor still need to be mechanically crushed again, just as Fig. 46 shows. Thus, the authors investigated the recycled magnets quality after these thermal and mechanical treatments.

Fig. 46 Left: The cutting cross section of IP magnet for recycling; right: magnet chunk collected for further crushing process [73]

From [73], it was found that temperature of demagnetization highly influenced the performance of the recycled magnet powder. Multiple demagnetizing temperatures were used, such as 350°C, 400°C and 650°C. It was observed that 350°C gave the best BH product after re-magnetizing. But still no matter what the demagnetization temperature was, there was always around 10% reduction of *Br* and 20% reduction of *iHc*, still in acceptable level. Thus, difficulty "3 - magnet protection" is solved. Currently the water pump company Grundfos has already applied the patent for the IP magnet [72]. They have commercialized a motor with mass production. They have even built up the whole recycling lines [74]. Thus, difficulty "1 – cost and scale" seems to be solved.

Notwithstanding, currently the direct magnet powder compression method is only for small motor applications (axial length < 5cm, outer diameter < 5cm). Demonstrations are required for more powerful applications in the future, such as traction motors in (H)EVs.

1.5.2.4 Modularity design

Finally, some general methods about easy disassembly are demonstrated. The main idea is modularity design. Unlike the method of "modular magnet pole" design, which only focuses on magnet segmentation, these modularity designs can be applied to the entire rotor, winding, entire stator and etc. Thus they can naturally improve magnet disassembly rate.

For instance, I. Stamenkovic et al. [75] have proposed an ironless motor, which can be easily assembled and disassembled, due to the flexibility of the structure and easy accessibility of permanent magnets. Moreover, the total weight is also reduced due to the absence of iron. S. T. Lundmark et al. [76] and M. Alatalo [77] have proposed a segmented motor with SMC materials and magnet glue free assembly, as Fig. 47 shows. It can easily extract the copper winding, since the stator core made by SMC materials can be easily crushed. Also the rotor core is segmented and the magnet is a complete piece of ring, thus similar to complete magnet reuse, the magnet can be taken out from the rotor at one step. Other classical modularity designs are exhausted by Z. Q. Zhu et al. [78]. Although the paper has listed the advantages and challenges of modularity designs for electrical machines from the points of assembly, it also suits for disassembly aspects, as disassembly is the inversed process of assembly. In general, due to the "smart design" of the structure, the assembly and disassembly becomes easier than convention machines, once automatic processes are involved. Thus difficulty "1 – cost and scale" can be overcome. With some joint structures, each module can be combined together without binder or glue. Thus, difficulty "2 - aide materials" can be solved.

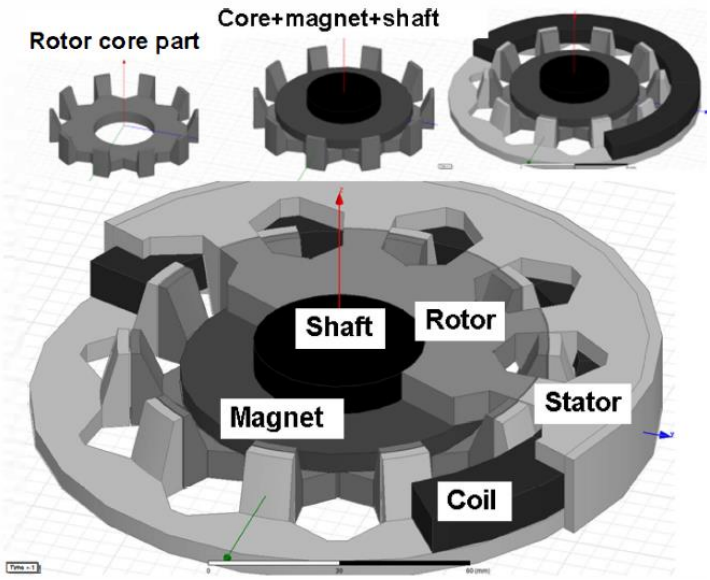

Fig. 47 The modularity design of a claw-pole motor [76]

However, similar to the disadvantages of complete magnet reusing, difficulty "3 - magnet protection" and difficulty "4 – magnet shape" cannot be solved, since the magnets are still kept in the machine with the conventional way. Besides these typical difficulties, another huge problem is that the performances of the machine can be largely affected by modular designs. For instance, [75] also highlighted that without iron core, the flux linkages were much weaker than convention PM machines. This led to torque reduction. Thus, with the limit space for (H)EV traction motor, the torque performance may not meet the requirements. In [78], the authors pointed out that improper manufacture tolerance gap between each module may have a negative impact on the results of winding factor, average torque and cogging torque. Mechanical weakness is also a common problem for modular design, since a complex mechanic structure need to be designed for holding each segment.

1.5.3 Using recycled magnet

Apart from the new design strategies, it is also necessary to verify if recycled rare earth permanent magnets can be used on electrical machines that meet all requirements. M. Kimiabeigi et al. [79] used the recycled NdFeB magnets made from WEEE. Currently the largest single input of NdFeB in WEEE is Hard Drive Disks (HDDs), due to their large amount on the market and also their short life cycle (normally 5 years). With Hydrogen Process of Magnet Scrap (HPMS), and auxiliary processes such as milling and sieving, the rare earth element can be recovered. Finally, with molding process - using 20% (Poly Tetra Fluoro Ethylene) PTFE binder and compression molding, keeping molding temperature 360 °C for 5 mins, the bonded magnet can be formed. Compared to sintered magnet, bonded magnet has the advantages of forming complex shape without machining, moreover, no need for coating.

It is found from commercialization point of view, despite more complex process than virgin magnets, it is likely that the society will benefit from this recycling process – as Fig. 48 shows, these techniques are in fact more environment friendly than the primary mining productions. Moreover, once the cost of rare earth raw material rises again (as the scenario of rare earth crisis), the recycled magnet might become profitable.

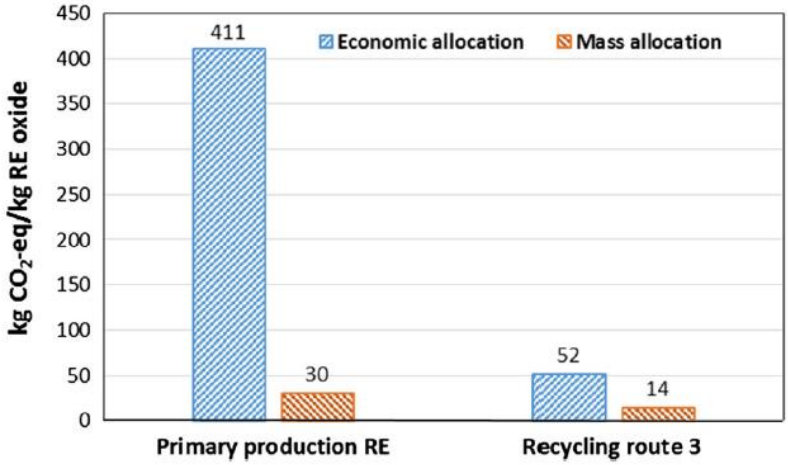

Fig. 48 Global warming potential, recovery of pure neodymium and dysprosium oxides [62]

However, the main problem of the strategy is that the properties of recycled bonded magnets are much weaker than sintered magnet, especially for the remanence Br, which is only slightly stronger than ferrite magnets. Thus, the motor design needs to be revised to meet the performances. For instance, using more reluctance torque, or increase the axial length to compensate the torque loss. Besides in this paper, the bonded magnet is still standard rectangular shape, which did not fully take advantage of the shaping superiority of bonded magnet. Finally, for the spoke type IPM, although the rotor is a quite simple structure, they have the inherent disadvantages of small reluctance torque, large torque ripple [80] [81], as well as poor performance of mechanical stress for high speed operation [82].

From the study above, it can be found that there are many difficulties of PM machine disassembly considering PM reuse. However, PM machines have unparalleled advantages than magnet free electrical machines regarding (H)EVs applications. Therefore, it is important to reduce the cost of PM machines by applying new magnet reuse techniques. Recent studies reveal that it is possible applying new machine designs to overcome PM disassembly difficulties. However, it is still a question mark if these designs can still fulfill the requirements of (H)EV applications. Thus this thesis not only proposes new designs for PM reuse, but also validates the performances of PM machine if they can meet the requirements of (H) EVs. Besides, it is not enough to only think over new design methods for disassembly. It is also important to evaluate the recyclability between different machines for the ease of comparison, where recyclability means how easy and how costly the disassembly process can be done; and how much does the recycle method influence the performances of the machine. Based on this idea, the thesis proposes special indexes to quantify their recyclability of magnets. Thus, some novel methodologies which help measuring the recyclability of electrical machines are introduced.

1.6 Conclusion

From both economical and ecological point of views, recycling rare earth permanent magnet is necessary. Direct reuse PMs can be a substantial recycling path. In this case, new designs for PM electrical machines might be required. The magnetic materials used on electrical machines were reviewed in this chapter. It was found NdFeB PMs have been the best hard magnetic materials until now, thus PM e-machines cannot avoid using rare earth elements. An overview study on the family of electrical machines were carried out. It was concluded that PM e-machines are indispensable for the (H)EVs applications, due to their superior performances. In this case, four key magnet reuse strategies were summarized for PM e-machines from literature studies.

Chapter 2- Methodology and results

2.1 Machine designs for magnet reuse

From literature study, it is known that using SPMSM at least can partly solve the magnet reuse problems. For SPMSM, magnets are exposed on the surface of the rotor, thus they can be easily accessed for disassembly. In this case, SPMSM with "Lego" design philosophy will be attempted on the electrical machines designed for (H)EVs.

As [71] suggested, standard magnet segments are supposed to be used for the magnet pole construction. Sintered NdFeB magnets will be used for segments. A heat resistance retention sleeve needed to be covered on the surface of the magnet poles. On one hand, the sleeve can fix the magnets in place during the thermal treatment of disassembly. On the other hand, the sleeve can fix the magnets during the high rotation of machine operation. The material of the retain sleeve can be carbon fiber or some composite fibers [83], as shown in Fig. 49. Metallic sleeve is not preferred, such as Titanium, due to the risk of eddy current generation inside the sleeve during the high speed operation of the machine. However, the material of the sleeve normally is expensive, which inevitably increase the cost of the whole machine.

Fig. 49 An example of retention sleeve made by composite fibers [83]

Another solution is to apply the philosophy of magnet powder reusing. Hence, an IPMSM is designed for magnet reusing. The magnet inside the rotor of IPMSM will be a kind of bonded NdFeB magnet with anisotropic magnet powder (made by d-HDDR process). Inspired by IP magnet technology, the rotor of IPMSM will be assembled together with the bonded magnets production. A brief idea is to use rotor cavities directly as the mold for the injection molding of bonded magnets. In this case, the shape of bonded magnets can be aligned with the shape of rotor cavities. Besides, PPS will be used as the binder. As the melting point of PPS is near 300°C, the injection molding has to be carried out around 300°C. Coincidentally, this is also close to the temperature of NdFeB magnet powder Curie's point T_c. Thus it is possible to magnetize the magnet easily during the injection molding, even with the magnets inside the rotor iron core. This is so called Post-Assembly Magnetization (PAM) [84]. To provide the magnetic field, permanent magnets or an electro-magnetizer will be circled around the rotor core. The magnetic field generated will be well tuned to meet the requirement of magnets magnetization direction. The schematic map of this process is shown in Fig. 50. Therefore, the rotor assembly process becomes easier compared to the traditional magnets insertion process for IPMSM.

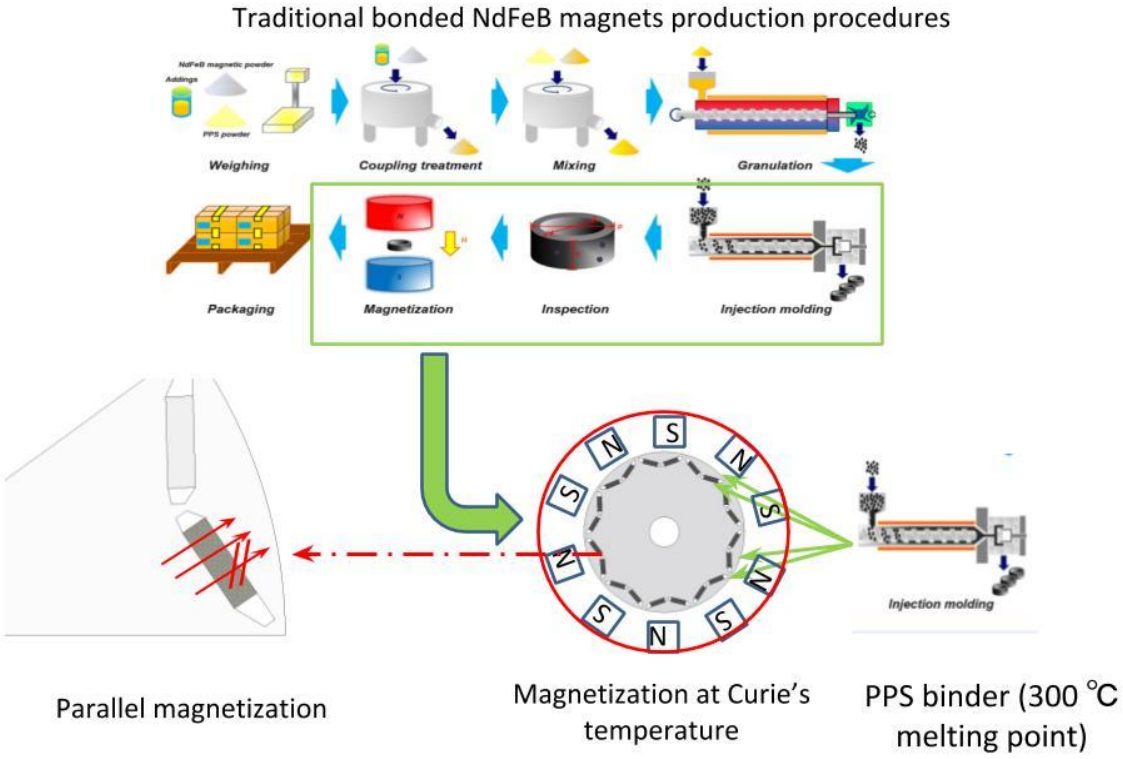

Fig. 50 Schematic map of the proposed manufacture process for the IPMSM rotor, with the integration of magnet powder injection molding and magnetization (picture of traditional bonded magnet procedure refers [85]).

As for disassembly, thermal treatment can be implemented. PPS binder is thermoplastic, which means it can be repeatedly melted and condensed. The rotor thus can be heated up (induction or furnace heating) to T_c for demagnetization and melting. Afterwards magnets can be extracted in a gummy state. It was investigated by the magnet supplier that when 70% virgin magnet powder is mixed with 30% of these recycled bonded magnets, the quality of the final magnet can be well maintained. As shown in Fig. 51, recycled magnet experiments were done to identify the performances of mixed magnets. Compounds with 30% and 50% recycled magnets were studied. Taking the 30% recycled compound as an example - For the recycled part, it can be recycled once, namely R1, or recycled twice, namely R2, etc, up to R5, as Fig. 51 (a) shows. Then the performances of remanence Br, energy product BH_{max} and intrinsic coercivity iH_c were compared. It was found that Br tends to be stable all the time, and no loss appeared, regardless of how many times the compound recycled. BH_{max} tends to be stable after R1, and only showed 1% loss for the 30% recycled part, and 1.5% loss for the 50% recycled part. Intrinsic coercivity iH_c tends to be stable after R2, and only showed 2% loss for the 30% recycled part, and 4% loss for the 50% recycled part. Therefore, the recycling strategy is totally acceptable for the industry. No matter on the aspect of assembly process simplification, or the aspect of disassembly feasibility and recycled magnets quality.

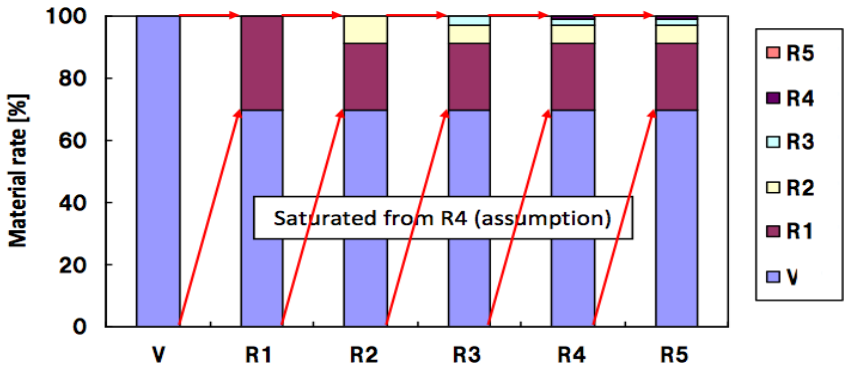

(a)

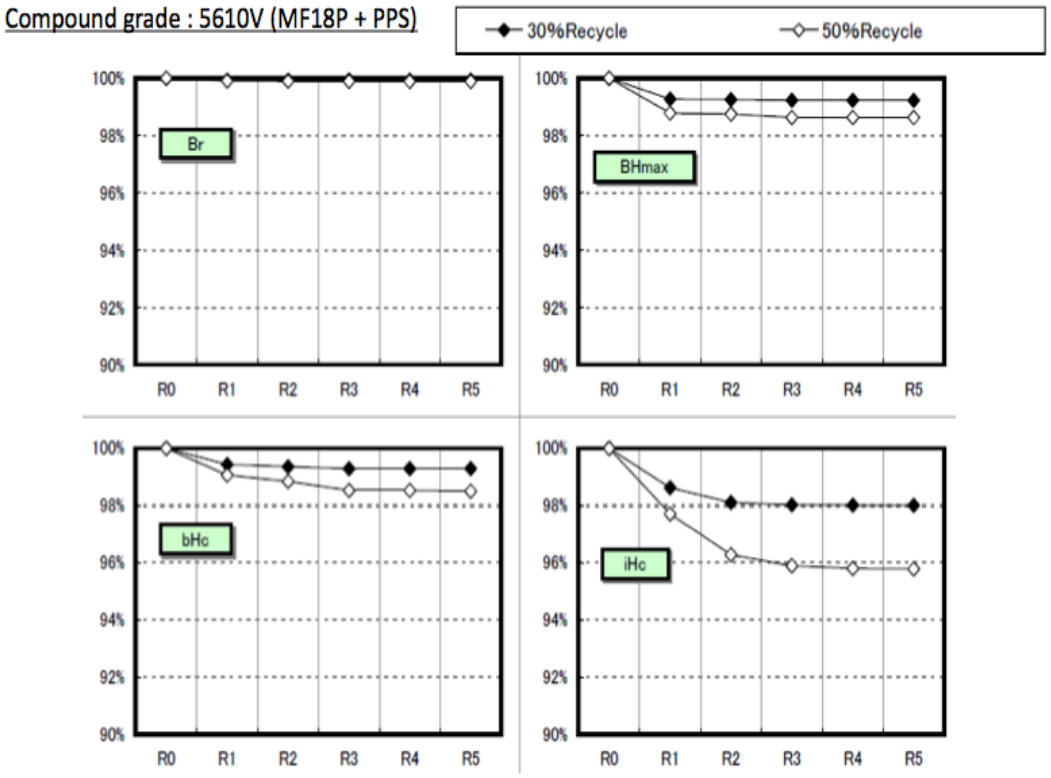

(b)

Fig. 51 (a) Percentage of different recycled magnet batches mixing for new magnet production (diagram of 30% recycled magnets) (b) Performances of different mixed compound with 30% recycled magnet and 50% recycled magnet respectively [87]

Then, the only question mark is that if the new designed electrical machine can fulfill the requirements of (H)EV applications, regarding the torque, speed and efficiency, etc? The following sections will investigate the performances of these two machine designs of SPMSM and IPMSM.

2.2 Sizing and formulas

In order to design an electrical machine, basic physical theories and mathematical models need to be established. This section introduces the analytical methods for the electrical machine design. Radial flux PMSMs are the main focus.

Electrical machines are based on the theories of Maxwell equation set and Lorentz force. For PMSM, the magnetic field is generated by PMs. A PM provides a constant magnetic field under a constant temperature. Here the position of PMs is limited to a rotor. By Lorentz force, it is known that current-carrying conductors can generate magnetic forces under the magnetic field. Thus, a stator with certain arrangement of windings is needed. The direction of the forces can be judged by the right hand law. It is found that the forces are tangential to the conductors. As the conductors are fixed, the reaction forces act on the rotor and thus create a torque to rotate it.

2.2.1 Windings arrangement

There are mainly two types of windings for e-machines. One is called distributed winding. The other one is called fractional slot winding, or sometimes also called concentrated winding. Fig. 52 shows examples of theoretical connections and also real prototypes of these two windings.

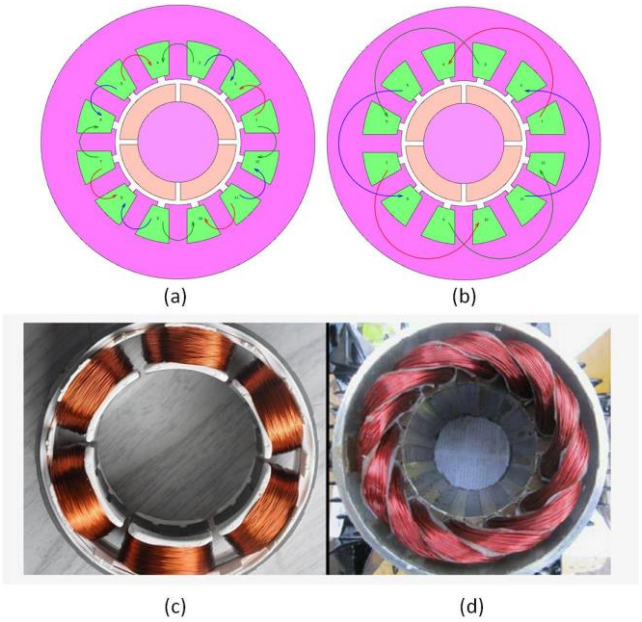

Fig. 52 Comparisons of distributed winding and concentrated winding (a,c) concentrated winding schematic plot and with stator prototype top view; (b,d) distributed winding schematic plot and with stator prototype top view [88].

This section will mainly investigate the characteristics of these two types of windings. It also needs to be highlighted that only series winding is considered. Parallel winding or parallel strand will not be discussed. Parallel windings and strands are normally applied to help increase the copper areas, which lead to resistances decrease. Also they can help reduce the skin effect at certain degree. However, it may raise some serious issues. For example, circulating current may appear due to inappropriate strand placement, or fault conditions. This additional circulating current may magnify the proximity effect, which results in higher copper loss than series winding configuration, as well as severe thermal condition. These topics related to parallel windings can be found in [112]-[114].

2.2.1.1 Winding factor

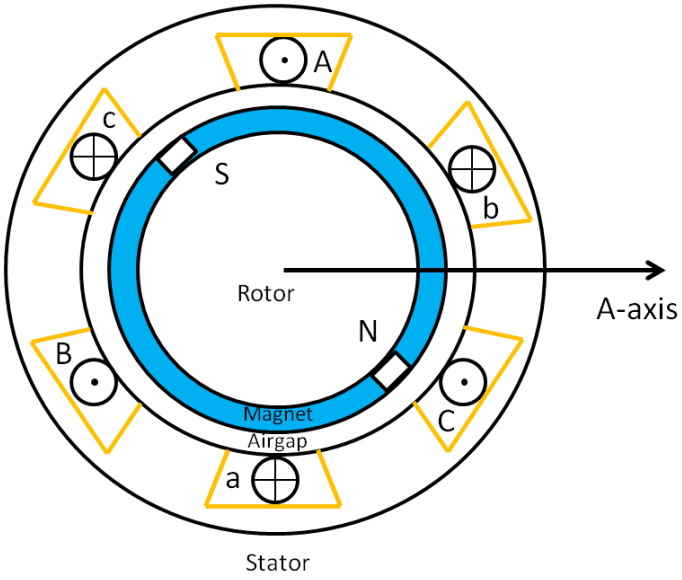

Fig. 53 A simple model that represent a 2-pole, three phases, inner rotor SPMSM

A simple model of a SPMSM with 2-pole, three phases, inner rotor is shown in Fig. 53. This model has a single layer winding. The coil pitch in slots y_{sp} refers to how many slots one phase crosses. Thus in Fig. 53, for phase A positive to phase A negative, y_{sp} =3, which are characterized as full pitch winding.

The number of slots per pole per phase q is equal to 1. When q is an integer, the winding is classified as integer winding. Otherwise when q is lower than 1, the winding is classified as fractional winding. For integer windings, the fundamental winding factor k_{w1} can be derived by Eq. 18 [90]:

$$k_{w1} = \frac{1}{q} . \frac{sin\frac{\pi}{6}}{sin\frac{\pi}{6q}} . sin\frac{y_{sp}.\pi}{6q} \qquad \text{Eq. 18}$$

Thus with the known y_{sp} and q, k_{w1} is calculated which equals to 1. High winding factor is always preferred, as the airgap Magneto-Motive Forces (MMF) is proportional to the fundamental winding factor (assuming using the same magnetic materials and currents). Higher MMF results in higher torque.

Another situation is that in each slot, there might be two or even more layers, as shown in Fig. 54 (b). Then a new arrangement for the winding is to make y_{sp} =2 instead of 3. Thus with the same q and Eq. 18, k_{w1}= 0.866. This winding is characterized as a short pitch winding. Although the winding factor of short pitch is lower than full pitch, sometimes the harmonics MMF are reduced by short pitch. This can lead to fewer losses than full pitch winding.

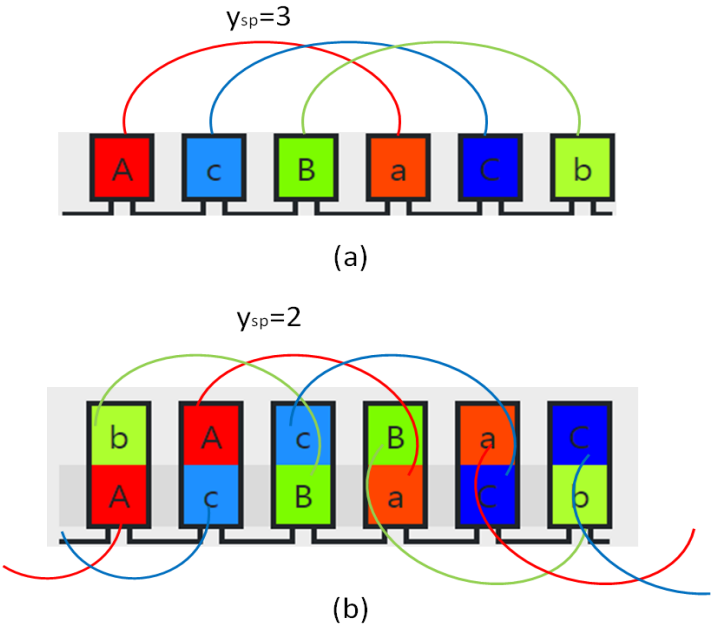

Fig. 54 Schematics of 2 poles, 6 slots machines with (a) single layer full pitch winding; (b) double layer short pitch winding

If *q* is smaller than 1, then the winding is classified as fractional slot winding. For instance, Fig. 55 shows two kinds of fractional slot winding with *q*=0.5. (a) is called single layer concentrated winding; (b) is called double layers concentrated winding.

The winding factor calculations for fractional slot winding are more complicated than integral winding. Eq. 18 cannot be used directly for fractional slot winding. Analytical methods need to be applied. For instance, Fig. 55 (a) is a 4 poles, 6 slots machine with single layer concentrated winding and equal tooth size. To calculate the winding factor, a phasor diagram needs to be used, as shown in Fig. 56.

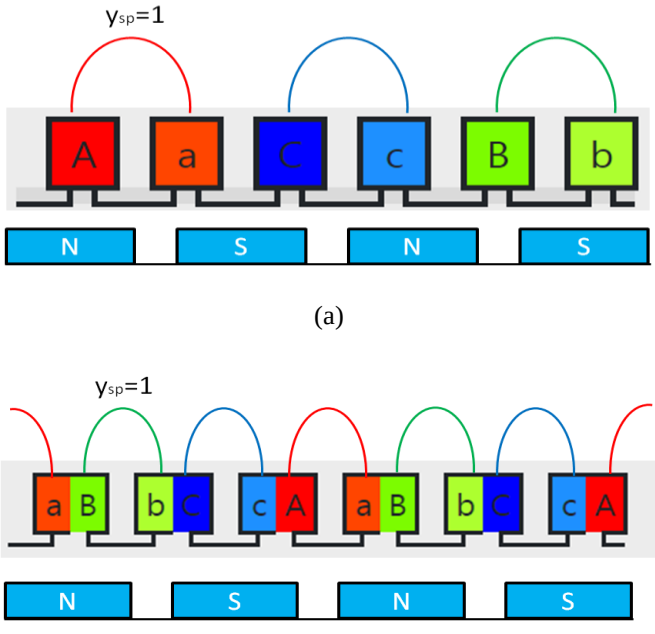

Fig. 55 Schematics of concentrated windings with 4 poles, 6 slots (a) single layer, (b) double layers

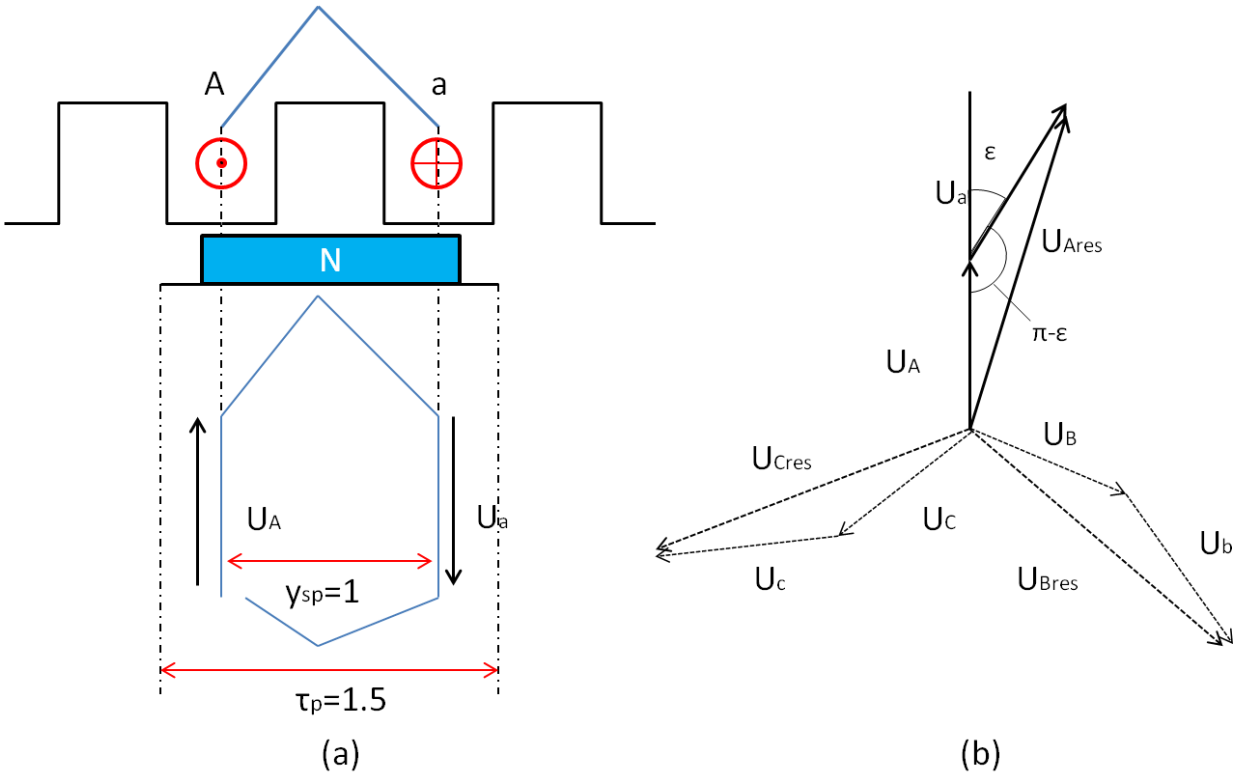

Fig. 56 (a) Induced voltages in a coil with concentrated winding (b) Phasor diagram

Here takes one phase for example. Because the winding of the phase is always wound around a tooth, the coil pitch in slot is always y_{sp}=1. Assume p denotes pole pair number, s denotes slot number, thus the motor has $2p$=4, s=6. Then the pole pitch in slot can be derived τ_p=$s/2p$=1.5. U is the induced voltage. As the number of turns for A and a are the same, U_A=U_a. Thus Eq. 19 can be used for the winding factor calculation:

$$k_{w1} = \frac{geometric\ sum\ of\ U_A\ and\ U_a}{algebraic\ sum\ of\ U_A\ and\ U_a} \qquad \text{Eq. 19}$$

It can be found from Fig. 56 (b), U_{Ares} is the geometric sum, while U_A+U_a=$2U_A$ is the algebraic sum. As the angle π-ε can be derived by Eq. 20.

$$\pi - \varepsilon = \frac{y_{sp}}{\tau_p}\pi \qquad \text{Eq. 20}$$

Hence winding factor k_{w1} can be calculated by Eq. 21.

$$k_{w1} = sin\left(\frac{\pi y_{sp}}{2\tau_p}\right) = sin\left(\frac{\pi}{3}\right) \qquad \text{Eq. 21}$$

Therefore, the winding factor of the 2p6s motor with concentrated winding is k_{w1} = 0.866.

However, this method is only suited for simple concentrated windings. For motors with high pole and slot numbers, or with unequal size teeth, it is better to use Fourier Transfer for the derivation of MMF harmonic that corresponding to the number of pole pair.

Still taking the 2p6s machine as an example, the MMF waveform of one moment can be drawn as Fig. 57.

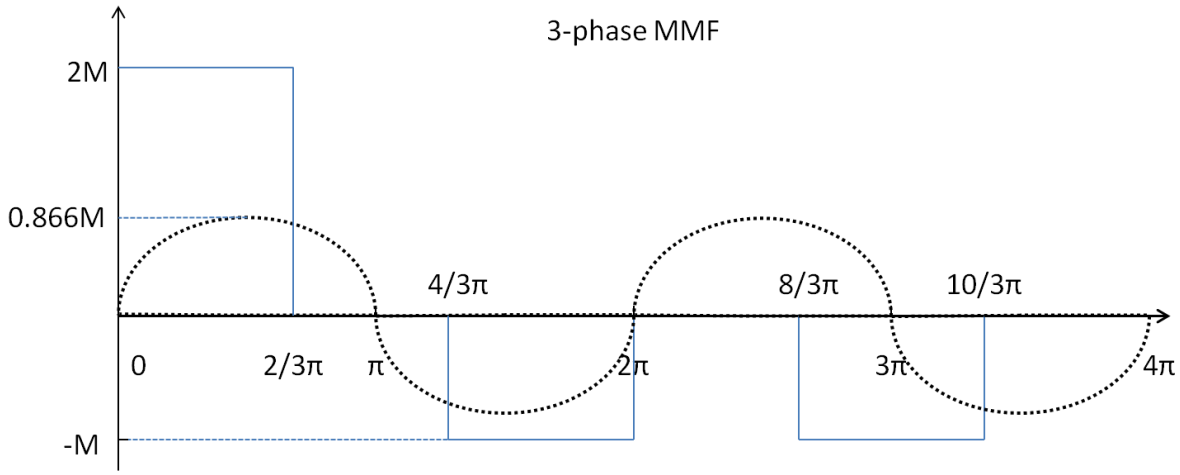

Fig. 57 3-phase MMF of 2p6s motor at the moment I_A=Î, I_B=−Î/2, I_C=−Î/2

For this moment, the current in phase A reaches to its peak $\hat{I}$. At the same time, currents in phases B and C are both $-\hat{I}/2$. Thus, the MMF amplitude for each phase is expressed as Eq. 22.

$$M_A=qn_s\hat{I}=2M;\ M_B=M_C=qn_s.(-\hat{I}/2)=-M\ ; \qquad \text{Eq. 22}$$

Thus, by doing Fast Fourier Transfer for the MMF waveform, the spectrum can be found in Fig. 58.

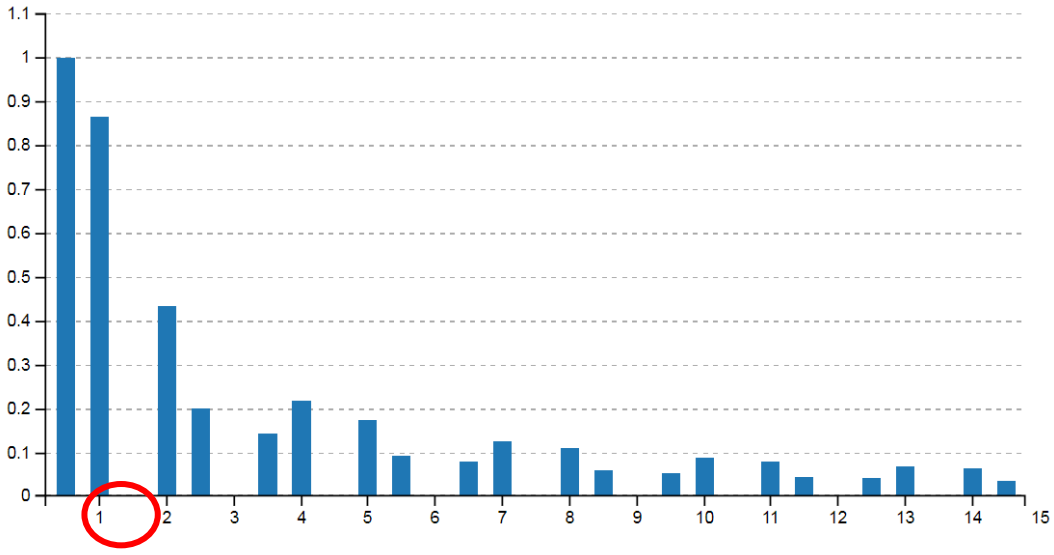

Fig. 58 Harmonics spectrum of 2p6s motor MMF by using FFT

The harmonic corresponding to the number of pole pairs is defined as order 1. It can be noticed the amplitude of order 1 is 0.866, which is the winding factor k_{w1}. The result is the same with what is obtained from the phasor diagram analysis. Besides, all the other harmonic components can be observed by Fourier Transfer. For instance, there is a sub-harmonic component in the spectrum with large amplitude, which is even larger than 1st order harmonic. Large sub-harmonics give many disadvantages of machine design, such as high rotor losses, high torque ripple and unbalanced pull forces [91], [94]. Sub-harmonics do not exist in distributed winding. Thus, when concentrated winding is used for the machine design, it would be better to avoid large sub-harmonics.

The winding factors of other pole slot combinations, as well as double layer windings, can be found in [95], [96]. Here only the highest winding factor of each pole pair is screened out, as shown in Fig. 59.

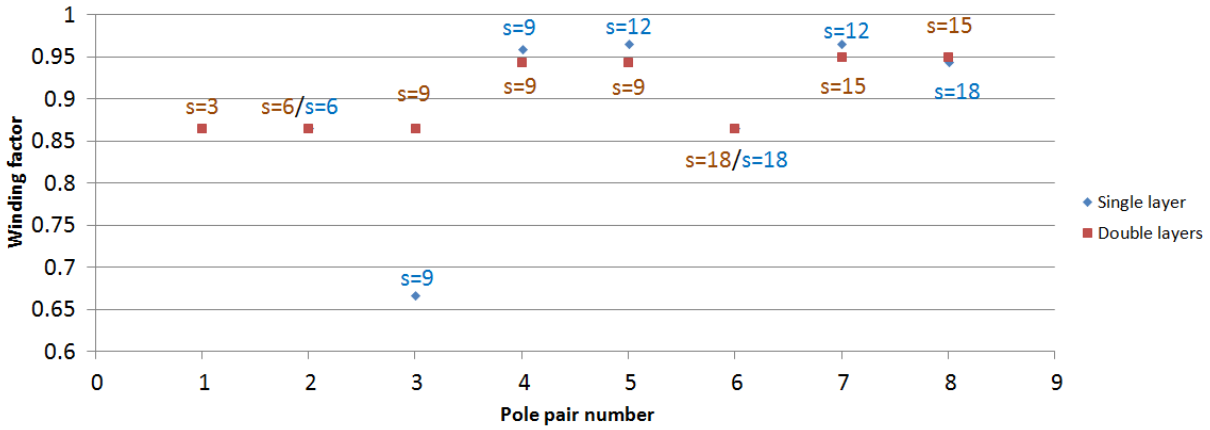

Fig. 59 The maximum winding factor of each pole pair number and corresponding slot number, up to 8 pole pairs.

It can be observed that with the increase of pole number, the max winding factor also tends to increase. Besides, it seems that the winding factors of single layer are slightly higher than double layers, especially when the pole number is high. However, this does not mean that the single layer windings are always better choices than the double layer windings, regarding other harmonics content.

With the help of online machine design tool EMETOR FEM [97], the sub-harmonic contents can be obtained for these windings with max winding factors. Here only the sub-harmonic with the highest amplitude is screened out, as shown in Fig. 60.

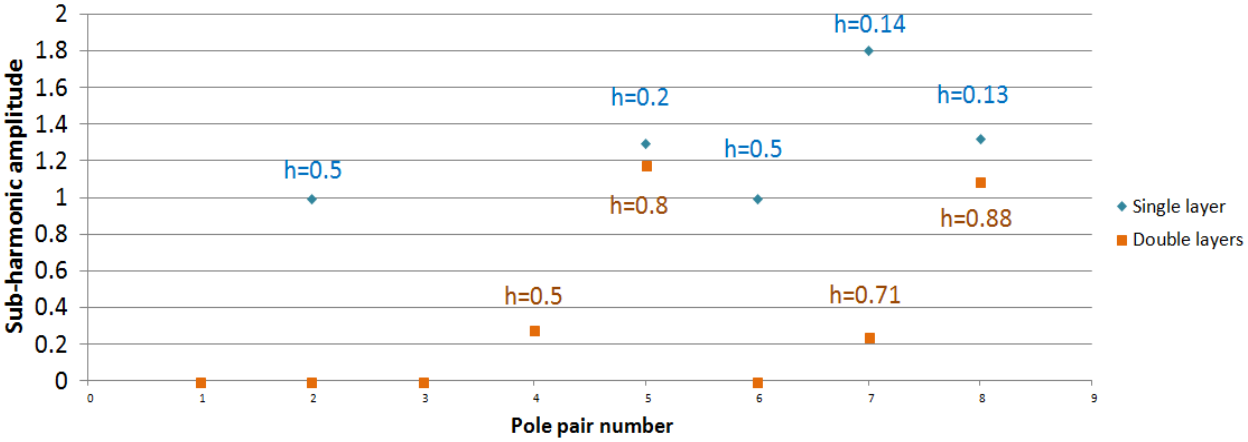

Fig. 60 The maximum sub-harmonic amplitude of each pole-slot combination with the max winding factor and corresponding its harmonic order (h<1), up to 8 pole pairs.

It is found that single layer windings have much higher possibility to obtain large sub-harmonic component than double layers windings. Thus, to reduce sub-harmonic, it is better to choose double layers windings. Moreover, it can be observed that for the order of each sub-harmonic, single layer windings tend to have low order close to 0, while double-layer windings tend to have high order close to 1.

2.1.1.2 End-windings

One more significant difference between distributed windings and concentrated windings is their end winding structures. The end winding lengths of distributed windings have to be longer than concentrated winding. Because the coil pitch of distributed winding is larger than concentrated winding. In Fig. 61, schematics of distributed winding and concentrated winding are shown respectively for end winding length calculations.

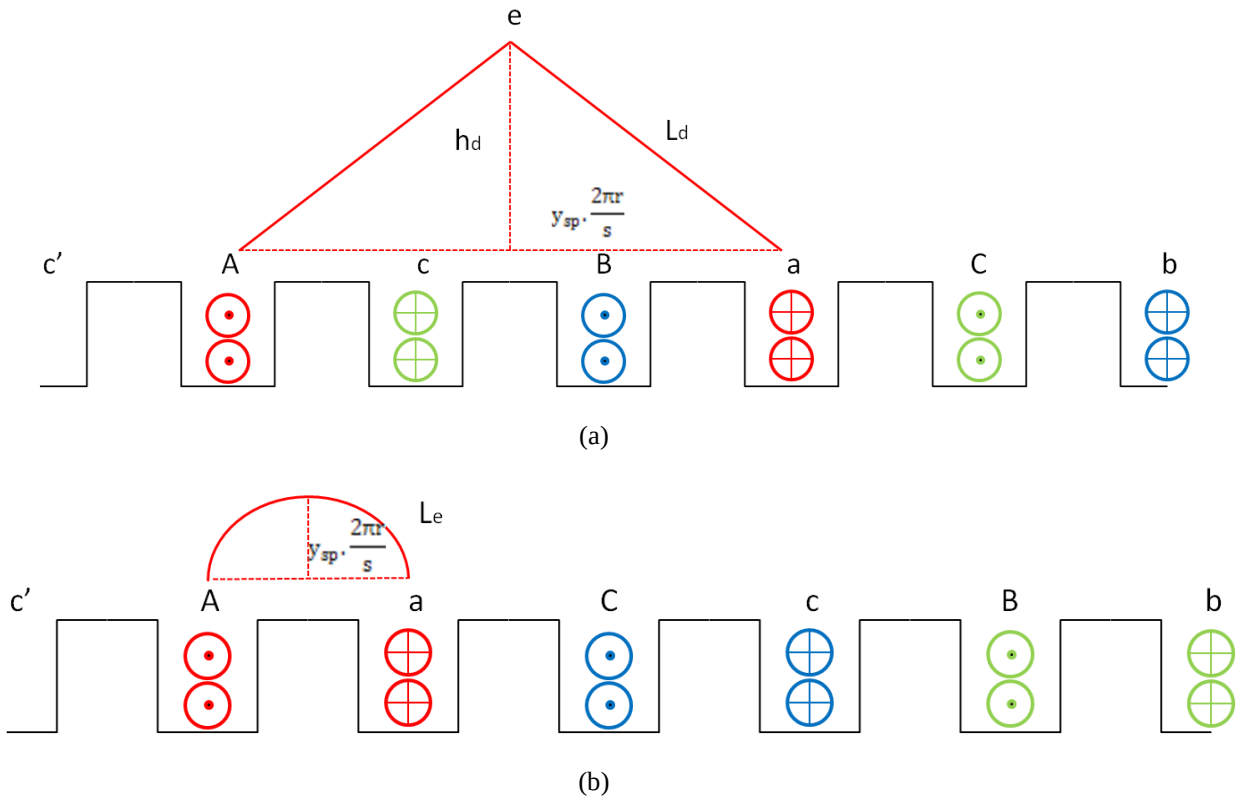

Fig. 61 Schematics of one turn and one side end winding length of (a) distributed winding; (b) concentrated winding.

In (a), the end winding shape of the distributed winding is close to a triangle. The length of bottom edge of the triangle, which is denoted as L_{Aa}, depends on the coil pitch of one phase. It can be calculated in Eq. 23,

$$L_{Aa} = y_{sp}.\frac{2\pi r}{s} \qquad \text{Eq. 23}$$

where y_{sp} is still coil pitch in slot. s is still slot number. r is the sum of stator inner radius (inner rotor) and stator teeth height.

Then the height of end winding is denoted as h_d. h_d value depends on many factors, such as coil pitch, turn number, manufacture process and even conductor materials properties. Normally it is close to a half of L_{Aa}. Thus, half of one turn and one side end winding length of distributed winding L_d is expressed in Eq. 24.

$$L_d = \sqrt{{h_d}^2 + (0.5L_{Aa})^2} \quad \text{Eq. 24}$$

If assumes that $h_d = 0.5\ L_{Aa}$, then Eq. 24 can be expressed as Eq. 25.

$$L_d = 0.707.y_{sp}.\frac{2\pi r}{s} \quad \text{Eq. 25}$$

Fig. 61 (a) is just an ideal case for distributed winding. As the coil of one phase has to cross coils of other phases, the collision between each phase is easy to happen. Moreover, insulation can also occupy some space. Thus, the end windings length of distributed winding needs to be even longer than ideal situation.

In Fig. 61 (b), the end winding shape of the concentrated winding is close to a semicircle. The bottom edge can be also calculated by Eq. 23. The only difference is that for concentrated winding, the coil pitch y_{sp} is always 1. Thus, half of one turn and one side end winding length of concentrated winding L_c is Eq. 26.

$$L_c = 0.25\pi.\frac{2\pi r}{s} \quad \text{Eq. 26}$$

Comparing Eq. 25 and Eq. 26, with the same size of stator and teeth, it can be found the proportion between L_d and L_c is Eq. 27,

$$\frac{L_d}{L_c} = \frac{0.707.y_{sp}}{0.25\pi} \approx 0.9y_{sp} \quad \text{Eq. 27}$$

where y_{sp} of distributed winding is greater or equal to 2 (short pitch). Thus the minimum end winding length of distributed winding is 1.8 times longer than concentrated winding. Moreover, concentrated windings have more compact size than distributed windings, due to the height of end winding. However, as mentioned above, this conclusion has many assumptions. Each end winding length needs a specific calculation for each case. Besides, it is not saying that concentrated windings surely have lower Joules losses than distributed windings. Because if the winding factor is also considered, then concentrated windings normally have lower winding factors than distributed winding, which leads to higher current for the same torque production. Therefore, it is hard to say which type of winding gives better efficiency, not to mention the issues of iron losses.

2.2.1.3 Three phases winding Y -Δ connections

Three phases winding gives an advantage of keeping total power constant, which is not the case for single or two phases winding. Thus, nowadays three phase winding is always preferred.

From the system level, there are two ways of connection for three phases winding - Star connection Y and Delta connection Δ. They are shown in Fig. 62.

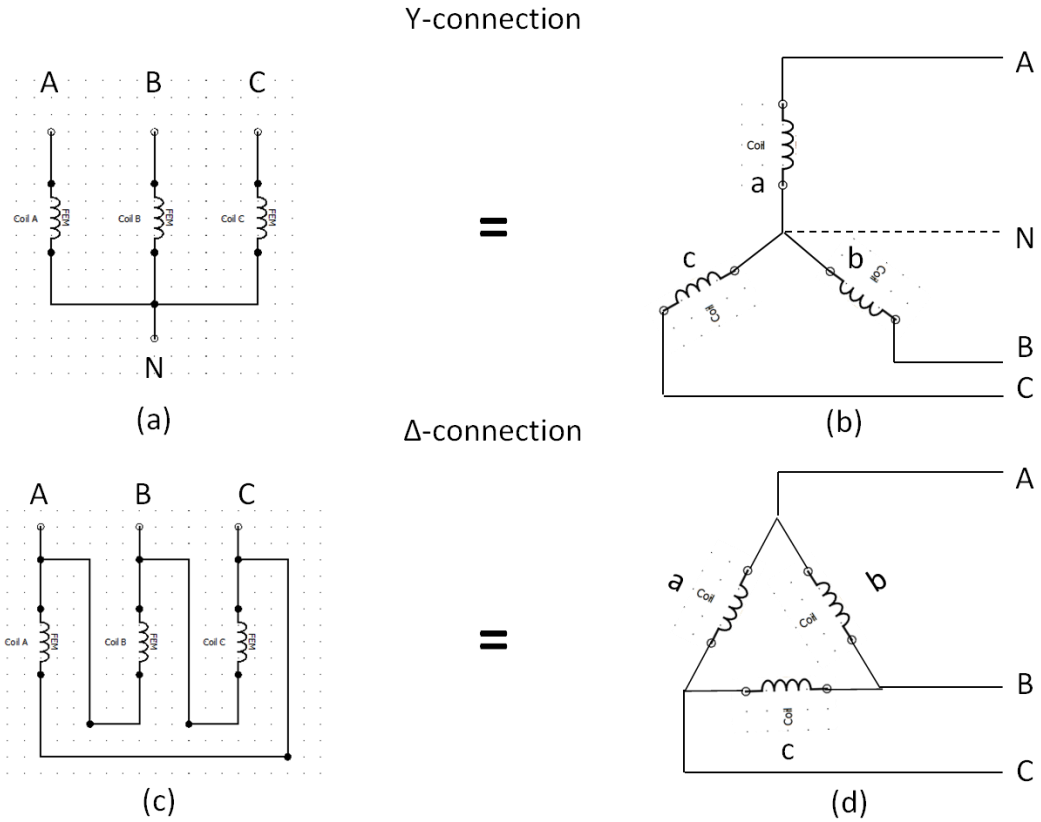

Fig. 62 Schematics of three phases Y and Δ connections

In Fig. *A*, *B* and *C* exhibit the connections of three phases, for Y connection, *N* is the connection point of one phase terminal with other phases. It ideally has a zero voltage. Thus *N* denotes the neutral point. Thus, it can be observed that for star connection, the coil ends of three phases are connected together with the neutral point. While for Δ connection, one end of a coil is connected with one start of another coil, thus the coils form a triangle shape from the circuit view. There is no neutral point anymore.

For multi-phase system, there are two types of voltage and current – line voltage, line current and phase voltage, phase current. Line voltage means the voltage difference between different phases, and the same thing apply to line current. Phase voltage means the voltage on each phase coil (Electrical potential between phase terminal and neutral point), and the same thing apply to phase current. The definitions can be indicated by the phasor diagram shown in Fig. 63, which is corresponding to the circuits of Fig. 62 (b) and (d) respectively.

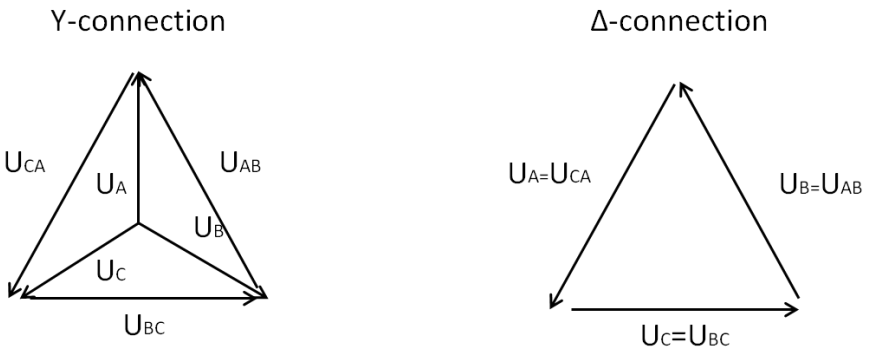

Fig. 63 Voltage phasor diagram of Y and Δ connection respectively

For the Y connection with balanced voltages, it can be found that line voltages U_{AB}, U_{CA} and U_{BC} are $\sqrt{3}$ times of phase voltages U_A, U_B and U_C. While the line currents I_{AB}, I_{CA} and I_{BC} keep the same with the phase currents I_A, I_B and I_C. For Δ connection with balance voltages, it can be found that phase line voltages U_{AB}, U_{CA} and U_{BC} are the same with phase voltages U_A, U_B and U_C. Thus in turn, the line current I_{AB}, I_{CA} and I_{BC} are $\sqrt{3}$ times of the phase currents I_A, I_B and I_C, due to the equivalent power between Δ and Y connections. Thus, the relationships can be summarized in Eq. 28 formula set:

$$\begin{gathered} \mathrm{U_{line\_Y}} = \sqrt{3}.\,\mathrm{U_{phase\_Y}} \\ \mathrm{I_{line\_Y}} = \mathrm{I_{phase\_Y}} \\ \mathrm{U_{Line\_\Delta}} = \mathrm{U_{phase\_\Delta}} \\ \mathrm{I_{Line\_\Delta}} = \sqrt{3}.\,\mathrm{I_{phase\_\Delta}} \\ \mathrm{P} = \sqrt{3}.\,\mathrm{U_{line}I_{line}cos\Phi} \\ \mathrm{P} = 3.\,\mathrm{U_{phase}I_{phase}\ cos\Phi} \\ \mathrm{R_\Delta} = 3.\,\mathrm{R_Y} \end{gathered} \qquad \text{Eq. 28}$$

where $cos\Phi$ is the power factor. Thus, assuming the turn number per phase of Δ connection is N_d, and in order to convert Δ to Y connection with the same power, the turn number per phase N_Y for Y connection will be Eq. 29.

$$N_Y = \frac{N_d}{\sqrt{3}} \qquad \text{Eq. 29}$$

In this case, if N_d is integer, N_Y might be fraction, and vice versa. Thus, by playing different connection methods, more possibilities of turn number per phase can be found, instead of only integer turn number. This trick may help to optimize the machine design, especially when the power of the machine is highly sensitive to the number of turns per phase.

2.2.2 Electromagnet torque calculation

Electromagnet torque is generated by Lorentz force. The general equation of torque by Lorentz force for a line shape conductor is Eq. 30,

$$dT = r.di.L.B \text{ [N.m]} \qquad \text{Eq. 30}$$

where r is the rotor radius, which is also the arm of Lorentz force. L is the length of the line shape conductor, which is the same length of machine active length. B is flux density around the conductor. di is one piece of current on the circumference of stator. di can be expressed by Eq. 31, where I_1 is the fundamental current sin wave. D_{in} is the inner diameter of stator. δ is the airgap length. θ is the electrical angle of the rotor.

$$di = I_1.\frac{D_{in}-\delta}{2p}.d\,\theta \text{ [A]} \qquad \text{Eq. 31}$$

For an electrical machine, as Fig. 53 shows, the conductors are arranged around the rotor circumference, and with p electrical periodicities. Thus the total torque can be written as Eq. 32.

$$T = p.\int_{\theta=0}^{2\pi} dT \text{ [N.m]} \qquad \text{Eq. 32}$$

Then, several assumptions are made for currents and flux density:

1. The input currents for conductors are sinusoidal, and only one phase is considered.
2. Each slot has conductors with N_s turns. The fundamental winding factor is still k_{w1}.
3. The magnetic flux density is generated by the magnets on rotor, and the flux waveform is also sinusoidal.
4. The phase difference between current sine wave and flux sin wave is γ_d.

Thus, with assumptions 1 and 2, a new parameter named current loading S_1 can be given in Eq. 33,

$$\widehat{S_1} = N_s \frac{\widehat{I_1}.}{(\pi\frac{(D_{in}-\delta)}{s})} \text{ [A/mm]} \quad \text{Eq. 33}$$

where $\widehat{S_1}$ is the peak value of the current loading. $\widehat{I_1}$ is also the peak value of the current. s is still the total stator slots number. Thus, the equation in denominator is the slot pitch in length.

With the assumption 3, B can be written as Eq. 34, where B_δ denotes the airgap flux density.

$$B = \widehat{B_\delta} cos\ \theta_r \text{ [T]} \quad \text{Eq. 34}$$

With the assumption 4, the waveforms of S and B can be drawn on the rotor circumference coordinate. Fig. 64 shows the moment when phase current reach its maximum.

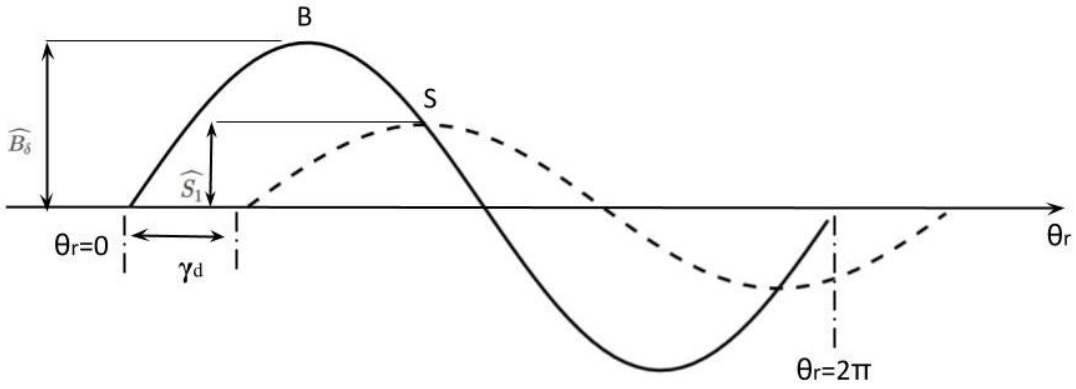

Fig. 64 Sinusoidal waveforms of airgap flux density and current loading with phase shift.

Thus, considering the phase shift, the expression of waveform S can be written as Eq. 35, where S_1 denotes the fundamental component of current loading.

$$S = \widehat{S_1} sin\ (\theta_r - \gamma_d) \text{ [A/mm]} \quad \text{Eq. 35}$$

where γ_d denotes the angle between current waveform I_m and the airgap flux density B_δ. Taking into account the winding factor, Eq. 30 and Eq. 31 hence can be rewritten as Eq. 36.

$$T = \frac{(D_{in}-\delta)}{2}.p.\int_{\theta_r=0}^{2\pi}\frac{(D_{in}-\delta)}{2p}.L.\widehat{S_1}.\widehat{B_\delta}.k_{w1}.sin\ \theta_r.sin(\theta_r-\gamma_d)d\theta_r \text{ [N.m]} \quad \text{Eq. 36}$$

Finally, Eq. 36 can be equivalent to Eq. 37.

$$T = \pi.\frac{(D_{in}-\delta)^2}{4}.L.\widehat{S_1}.\widehat{B_\delta}.k_{w1}.sin(\gamma_d) \text{ [N.m]} \quad \text{Eq. 37}$$

Eq. 37 shows that the torque is linear proportional to the active length, current loading, airgap flux density and winding factor. The torque is also proportional to the square of rotor diameter, and the sine value of phase shift angle between *S* and *B*.

Thus, without the considerations of magnetic saturation or flux leakage, the torque of a radial flux electrical machine can be linear scale up with the increases of active length, current loading and airgap flux density. In turn, all these parameters can constraint the torque value. For instance, current loading is constrained by slot current density *J*, which can be expressed as Eq. 38,

$$J_{rms} = \frac{N_s\widehat{I_1}}{\sqrt{2}A_{Cu}} = \frac{\widehat{S_1}.(\pi\frac{(D_{in}-\delta)}{s})}{\sqrt{2}A_{Cu}} \text{ [Arms/mm}^2\text{]} \quad \text{Eq. 38}$$

where J_{rms} is the root mean square [RMS] value of current density. A_{Cu} is the copper area in one slot. The maximum slot current density is correlated to the thermal condition of the machine. The slot current densities of typical e-machines are listed in Table VI. The ratio A_{Cu} / A_{slot} of is called filling factor.

Table VI TYPICAL SLOT CURRENT DENSITY OF ELECTRICAL MACHINES WITH SOLID COPPER WIRES UNDER DIFFERENT COOLING METHODS

Cooling system	**Current density J_{rms} [Arms/mm^2]**
Air cooling [92]	3 ~ 8
Fins and heat sinks [93]	5 ~ 8
Water or oil jacket [93]	10 ~15
Spray oil-cooled end turns of rotor winding [93]	>28
Cold plates between poles and rectangular wire rotor winding [93]	≈22

There are different types of winding regarding the cross section shape of the conductor and the winding process. Typical cross section shape can be round or rectangular. Common winding process can be random wound with strand conductors, or form wound with flat conductor [98]. Classical filling factors for random wound round shape winding are lower than 0.6, while are between 0.5 to 0.7 for form wound rectangular winding [99]. The windings with mechanical pre-compressed treatment can even achieve better filling factor [100] .

Besides, for other constraints such as airgap length, a default value of 0.5 mm is used, due to the production process in factories. Thus, with the constraints like cooling method and filling factor, current loading can be defined. Then with the given dimensions of the machine, as well as magnet flux density, the electromagnet torque can be estimated.

2.2.3 Park transformation and flux weakening

2.2.3.1 Three phase windings

Based on Section 2.2.2, the vector methods as well as their transformation will be systematically introduced in this section, as the vector form can make the instantaneous values look very compact.

First of all, a phasor diagram shown in Fig. 66 can be utilized to interpret Fig. 65 (aligned with Fig. 53) with *dq* axis.

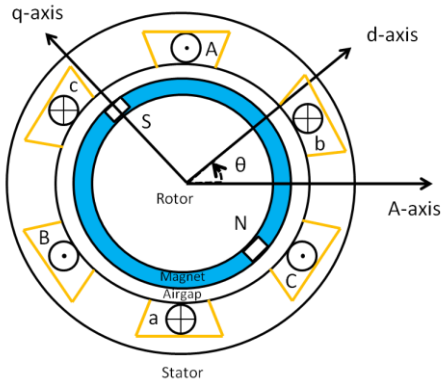

Fig. 65 *d* and *q* axis express in space with a simple SPMSM model

In Fig. 65 and Fig. 66, θ indicates the angle between rotor d-axis and phase A-axis, where d-axis is chosen so as to be aligned with the PM flux axis, while the q-phase axis leads the d-phase axis of π/2 electrical radians. θ is linked to the electrical angular speed $\omega_s$of the rotor, it can be expressed as, where $\omega_{mech}$is the rotor mechanical angular speed.

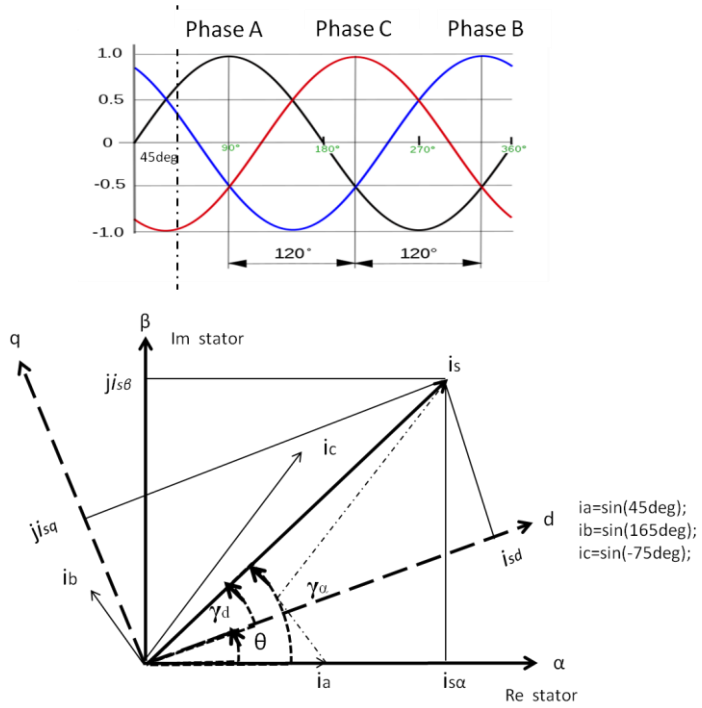

Fig. 66 Vector plot of an instantaneous current with respect to the stator and rotor reference frames

$$\theta = \omega_s t, \qquad \omega_s = p\omega_{mech} \qquad \text{Eq. 39}$$

The positive rotation direction is counter-clockwise. Here an instantaneous current is taken for example. For a moment, the angular position of the three-phase currents is 45°. Thus, i_a, i_b and i_c can be illustrated by arrows on the phasor plot with direction and length. At the beginning, a fixed frame $\alpha\beta$-coordinate is applied. This is based on the stator reference frame, and it represents a complex plane. α-axis is the real axis and β-axis is the imaginary axis. α-axis is also aligned with phase A-axis.

Thus, vectors i_a, i_b and i_c can be synthesized as a single current vector, with angle γ_α between is and α-axis. Vector is can also be projected on α-axis and β-axis as $i_{s\alpha}$ and $i_{s\beta}$. This projection can be expressed by

Eq. 40.

$$\begin{bmatrix} i_{s\alpha} \\ i_{s\beta} \end{bmatrix} = \underbrace{\begin{bmatrix} \frac{2}{3} & -\frac{1}{3} & -\frac{1}{3} \\ 0 & \frac{1}{\sqrt{3}} & -\frac{1}{\sqrt{3}} \end{bmatrix}}_{T_{23}} \begin{bmatrix} i_a \\ i_b \\ i_c \end{bmatrix} \qquad \text{Eq. 40}$$

The matrix used for $\alpha\beta$ transformation is named T_{23}. The inverse transformation can be expressed by

$$\begin{bmatrix} i_a \\ i_b \\ i_c \end{bmatrix} = \underbrace{\begin{bmatrix} 1 & 0 \\ -\frac{1}{2} & \frac{\sqrt{3}}{2} \\ -\frac{1}{2} & -\frac{\sqrt{3}}{2} \end{bmatrix}}_{T_{32}} \begin{bmatrix} i_{s\alpha} \\ i_{s\beta} \end{bmatrix} \qquad \text{Eq. 41}$$

Then i_s can be further transferred to rotor reference frame, or so called synchronous rotating reference frame, which is dq-axis. For the transformation, angle θ is taken into account, as Eq. 42 shows.

$$\begin{bmatrix} i_d \\ i_q \end{bmatrix} = \underbrace{\begin{bmatrix} \cos(\theta) & \sin(\theta) \\ -\sin(\theta) & \cos(\theta) \end{bmatrix}}_{T_{dq}(\theta)} \begin{bmatrix} i_{s\alpha} \\ i_{s\beta} \end{bmatrix} \qquad \text{Eq. 42}$$

Where the matrix used for dq transformation is named $T_{dq}(\theta)$. The inverse transformation can be expressed by Eq. 43.

$$\begin{bmatrix} i_{s\alpha} \\ i_{s\beta} \end{bmatrix} = \underbrace{\begin{bmatrix} \cos(\theta) & -\sin(\theta) \\ \sin(\theta) & \cos(\theta) \end{bmatrix}}_{T_{dq}^{-1}(\theta)} \begin{bmatrix} i_d \\ i_q \end{bmatrix} \qquad \text{Eq. 43}$$

Thus, together with

Eq. 40 and Eq. 42, the transformation from stator reference frame to rotor reference frame is called Park Transformation. By doing Park transformation, the varied three phase currents can be transferred to two constant values on d and q axis respectively. The machine will be controlled like a DC machine with the constant value of currents. Thus this transformation brings huge convenience in the calculations of torque and power, as well as

control. Besides, by using matrix T_{23}, the amplitude of the current can be preserved. This kind of Park Transformation is also called Clarke's Transformation [101].

Besides current, voltage can use the same transformation. The voltage of each phase on the stator reference frame can be expressed as Eq. 44,

$$u_s = R_s i_s + \frac{d}{dt}(\Psi_s) \quad \text{Eq. 44}$$

where Ψ_s is the flux linkage of each phase on the stator reference frame. By using Park transformation (Clarke form),Eq. 44 can be expressed with *dq* frame as Eq. 45,

$$\begin{aligned} T_{32}.T_{dq}^{-1}(\theta).\begin{bmatrix} u_d \\ u_q \end{bmatrix} &= R_s.T_{32}.T_{dq}^{-1}(\theta).\begin{bmatrix} i_d \\ i_q \end{bmatrix} + \frac{d}{dt}(T_{32}.T_{dq}^{-1}(\theta).\begin{bmatrix} \Psi_d \\ \Psi_q \end{bmatrix}) \\ =R_s.T_{32}.T_{dq}^{-1}(\theta).\begin{bmatrix} i_d \\ i_q \end{bmatrix} &+ T_{32}.\frac{d}{dt}\left(T_{dq}^{-1}(\theta)\right).\begin{bmatrix} \Psi_d \\ \Psi_q \end{bmatrix} + T_{32}.T_{dq}^{-1}(\theta)\frac{d}{dt}(\begin{bmatrix} \Psi_d \\ \Psi_q \end{bmatrix}) \end{aligned} \quad \text{Eq. 45}$$

As there is Eq. 46,

$$\begin{aligned} \theta &= \omega_s t \\ \frac{d}{dt}\left(T_{dq}^{-1}(\omega_s t)\right) &= \omega_s.T_{dq}^{-1}(\omega_s t).T_{dq}^{-1}(\frac{\pi}{2}) \end{aligned} \quad \text{Eq. 46}$$

Substitute Eq. 46 into Eq. 45 there is Eq. 47.

$$T_{32}.T_{dq}^{-1}(\theta).\begin{bmatrix} u_d \\ u_q \end{bmatrix} = R_s.T_{32}.T_{dq}^{-1}(\theta).\begin{bmatrix} i_d \\ i_q \end{bmatrix} + T_{32}.\omega.T_{dq}^{-1}(\theta).\begin{bmatrix} 0 & -1 \\ 1 & 0 \end{bmatrix}.\begin{bmatrix} \Psi_d \\ \Psi_q \end{bmatrix} + T_{32}.T_{dq}^{-1}(\theta)\frac{d}{dt}(\begin{bmatrix} \Psi_d \\ \Psi_q \end{bmatrix}) \quad \text{Eq. 47}$$

Matrixes T_{32},T_{dq}^{-1}can be removed from both sides of the equation. Finally, the expression can be simplified as Eq. 48.

$$\begin{bmatrix} u_d \\ u_q \end{bmatrix} = R_s \begin{bmatrix} i_d \\ i_q \end{bmatrix} + \omega_s \begin{bmatrix} -\Psi_q \\ \Psi_d \end{bmatrix} + \frac{d}{dt}(\begin{bmatrix} \Psi_d \\ \Psi_q \end{bmatrix}) \quad \text{Eq. 48}$$

Thus, from Eq. 48 it can be observed that voltage in the d-direction is partly contributed by a flux in *q*-direction, so the same for the voltage in the *q*-direction. This is so called cross-coupling phenomenon.

It is well known for the relationship between flux linkage and current, which is $\boldsymbol{\Psi} = \boldsymbol{L}.\boldsymbol{i}$, where L is the inductance. Meanwhile, the flux linkage on d-axis is partly contributed by permanent magnet flux $\boldsymbol{\Psi_m}$. Thus Eq. 48 can be rewritten as Eq. 49.

$$\begin{aligned} u_d &= R_s i_d + L_d \frac{di_d}{dt} - \omega_s L_q i_q \\ u_q &= R_s i_q + L_q \frac{di_q}{dt} + \omega_s L_d i_d + \omega_s \Psi_m = R_s i_q + L_q \frac{di_q}{dt} + \omega_s L_d i_d + E \end{aligned} \quad \text{Eq. 49}$$

Where L_d and L_q are the inductances of d-axis and q-axis respectively. E is called back-EMF, it represents an electromotive force contributed by the flux linkage of permanent magnet with ω_s varying speed. Thus, if the machine is at open circuit, and the rotor with magnet rotates with electrical angular speed ω_s, the induced voltage is equal to back-EMF.

Ignoring the transient state of the current ($\frac{di}{dt}$), the phasor diagram of the voltage can be plotted as Fig. 67, where φ is the angle between voltage u_s and current i_s. cos(φ) is so called power factor. Power factor defines the ratio of real power and apparent power. Real power is absorbed by the load. Apparent power is flowing in the circuit. There are two kinds of power factors - lagging power factor and leading power factor – depending on whether the phase current is leading or lagging the phase voltage. For the lagging power factor, the load is inductive. On contrary, for the leading power factor, the load is capacitive. Electrical machines are typical inductive loads; thus they have lagging power factor.

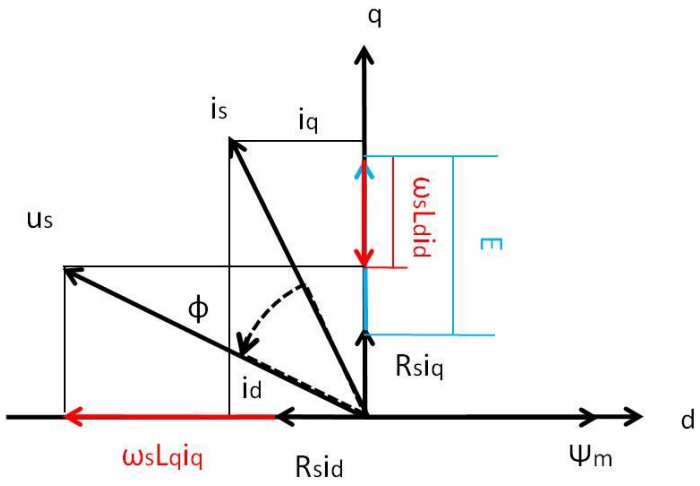

Fig. 67 Voltage and current phasors diagram on *dq* frame

Hence with the voltage and current, power can be derived. The expression for the total power is shown as Eq. 50,

$$
\begin{aligned}
P &= i_{abc}^{T}.u_{abc} \\
&= [\,T_{32}.T_{dq}^{-1}(\theta).i_{dq}]^{T}[\,T_{32}.T_{dq}^{-1}(\theta).u_{dq}] \\
&= i_{dq}^{T}[\,T_{32}.T_{dq}^{-1}(\theta)]^{T}\big[\,T_{32}.T_{dq}^{-1}(\theta)\big].u_{dq} \\
&= \frac{3}{2}\,i_{dq}^{T}.u_{dq} \\
&= \frac{3}{2}(i_d u_d + i_q u_q)
\end{aligned}
\qquad \text{Eq. 50}
$$

As seen from the expression, Clarke Transformation needs to multiple $\frac{3}{2}$ to preserve the power of the machine.

Then substituting Eq. 49 into Eq. 50, there is Eq. 51.

$$P = \frac{3}{2}.[Rs(i_d^2 + i_q^2) + \omega_s(\Psi_d.i_q - \Psi_q.i_d) + \left(\frac{d\Psi_d}{dt}.i_d + \frac{d\Psi_q}{dt}.i_q\right)] \qquad \text{Eq. 51}$$

For the steady state of power, $\frac{d\Psi}{dt} = 0$. Besides, it is well known that in the equation, the part with resistance is a loss term. Thus, the mechnical power Pm can be expressed as Eq. 52.

$$P_m = \frac{3}{2}.\omega_s(\Psi_d.i_q - \Psi_q.i_d) \quad \text{Eq. 52}$$

From the mechanical power, the torque can be derived by Eq. 53.

$$T = \frac{P_m}{\omega_{mech}} = \frac{3}{2}p(\Psi_d.i_q - \Psi_q.i_d) = \frac{3}{2}p[\Psi_m.i_q + (L_d - L_q).i_d.i_q] \quad \text{Eq. 53}$$

In the bracket of Eq. 53, the first part contributed by flux linkage of PM is magnet torque. The second part contributed by the difference of *d* and *q* inductances is reluctance torque. Thus, torque can be also derived from the aspect of current and inductance, which is more control related.

The available voltages and currents depend on the limit of electrical machine drive. Thus the machine drive decides the operation region of the machine. The expression of current operation limit is Eq. 54,

$$i_d^2 + i_q^2 \le I_N^2 \quad \text{Eq. 54}$$

where I_N is the maximum allowed current of a motor drive. The expression of voltage operation limit is Eq. 55,

$$u_d^2 + u_q^2 \le U_N^2 \quad \text{Eq. 55}$$

where U_N is the maximum allowed voltage of a motor drive. Substitute Eq. 49 into Eq. 55 results in Eq. 56.

$$(R_s i_d + L_d\frac{di_d}{dt} - \omega_s L_q i_q)^2 + (R_s i_q + L_q\frac{di_q}{dt} + \omega_s L_d i_d + \omega_s \Psi_m)^2 \le U_N^2 \quad \text{Eq. 56}$$

Assuming for steady state, there is $\frac{di_s}{dt} = 0$. Comparing to the inductive voltage part, normally resistive voltage drop can be ignored as it is very low. Mechanical speed ω_{mech} is used to replace electrical angular speed. Thus, Eq. 56 can be rewritten as Eq. 57.

$$\left(\frac{i_d}{L_q} + \frac{\Psi_m}{L_d L_q}\right)^2 + (\frac{i_q}{L_d})^2 \le (\frac{1}{L_d L_q}.\frac{U_N}{p\omega_{mech}})^2 \quad \text{Eq. 57}$$

If i_d, i_q are seen as two variables on x and y axis respectively, Eq. 57 is a general elliptical equation. Normally there is $L_q \ge L_d$. Thus, the focus is on *x*-axis, and the focal length is expressed as Eq. 58,

$$|F_1F_2| = 2(\frac{1}{L_d L_q}.\frac{U_N}{p.\omega_{mech}}).\sqrt{L_q^2 - L_d^2} = 2m\sqrt{L_q^2 - L_d^2} \quad \text{Eq. 58}$$

where *m* is used to represent $(\frac{1}{L_d L_q}.\frac{U_N}{p.\omega_{mech}})$. Besides, the ellipse is translated $\frac{\Psi_m}{L_d}$ towards the negative direction of d-axis. Thus, the ellipse can be plotted on *dq* plane. For PM electrical machines, $\frac{\Psi_m}{L_d}$ is the three-phase short circuit current I_{cc}, as Eq. 59 denotes.

$$I_{cc} = \frac{\Psi_m}{L_d} \qquad \text{Eq. 59}$$

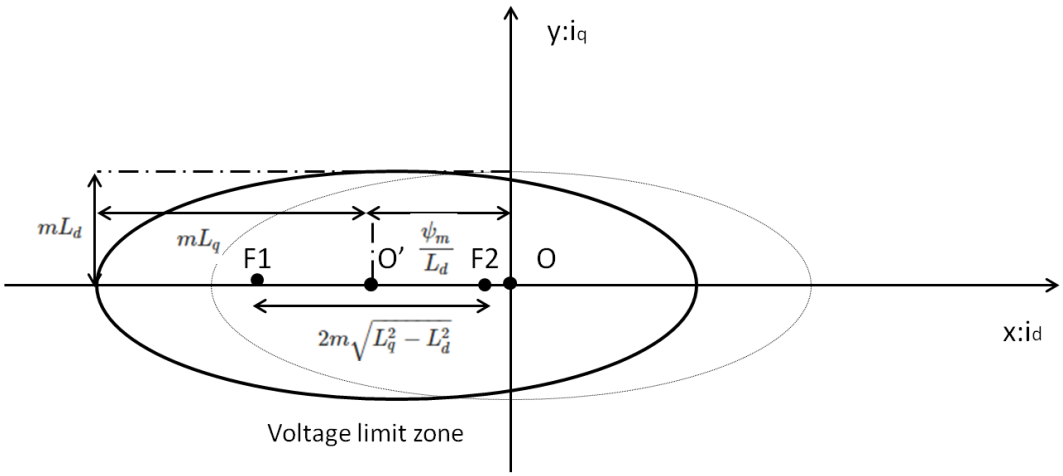

Fig. 68 Schematic diagram of voltage limit zone on id and iq reference frame

The amplitude of m is proportional to the maximum voltage of the drive. It is inverse proportional to the inductances L_d and L_q, pole number and mechanical rotation speed. As the pole number, drive voltage and inductances are pre-defined; only the mechanical rotation speed is a continuous changing variable. Thus, the voltage limit zone is changing with the rotation speed. Combining with the current limit equation Eq. 54, and torque equation Eq. 53, the schematic diagrams for the machine operation zone are shown in Fig. 69.

From Fig. 69 (a) and (b), it can be found that the voltage limit with the speed variation is represented by a group of concentric ellipses (black curve) - the higher the speed, the smaller the ellipse. The current limit is represented by the red circle. When combining the voltage ellipses and current circle, two situations can be categorized – the centre of ellipse lies outside current circle, as (a) shows; and the centre of ellipse lies inside current circle, as (b) shows. It is clear that the operation has to be executed within the common region of current and voltage. Thus, for (a), when the speed reaches ω_{max}, the common area of current and voltage merges to only one point. In this case, it is classified as finite speed type. From Eq. 57, it can be found that when $i_q=0$, $i_d=-I_N$, ω_{max} can be expressed as Eq. 60.

$$\omega_{max} = \frac{U_N}{p.(\Psi_m - I_N L_d)} \qquad \text{Eq. 60}$$

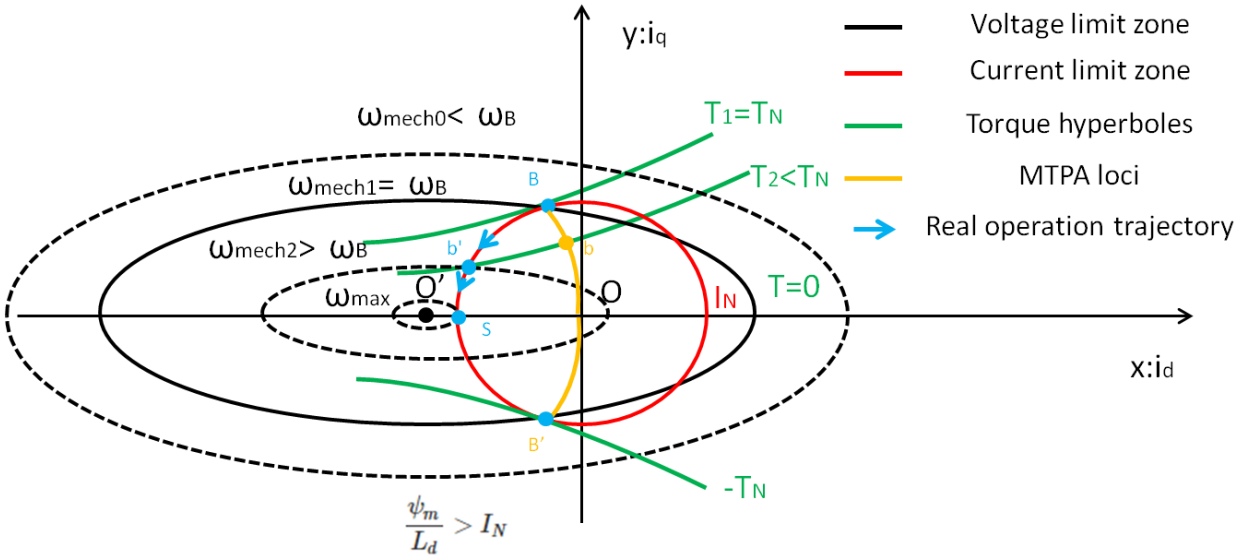

(a)

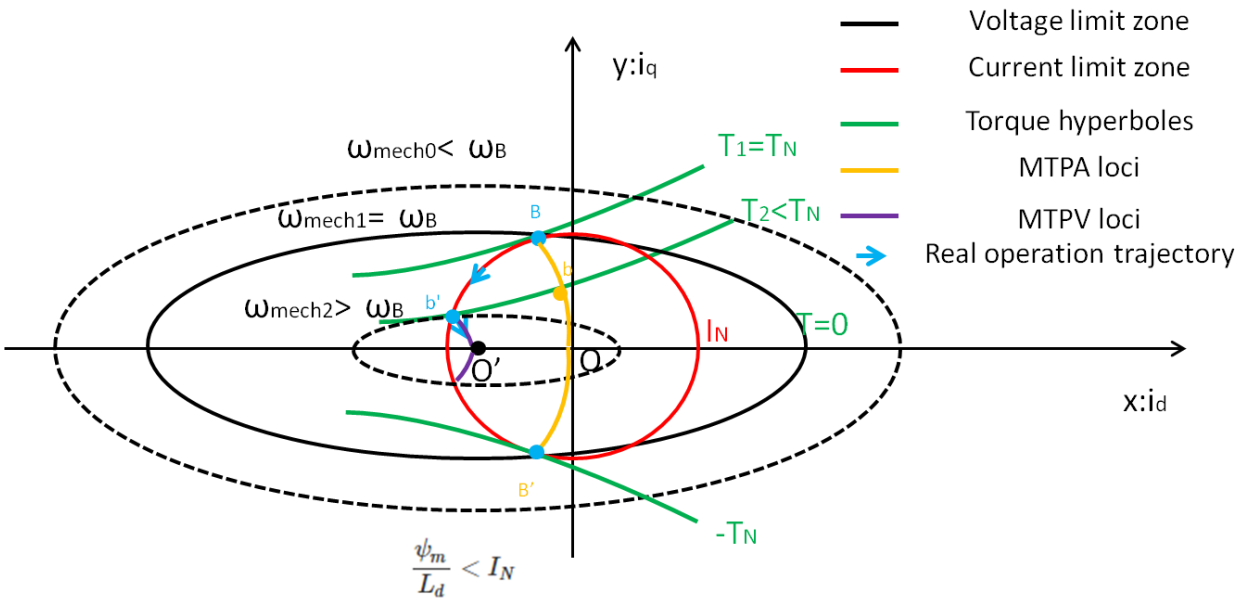

(b)

Fig. 69 (a) Schematic diagram of operation limit of a PM machine with finite speed; (b) schematic diagram of operation limit of a PM machine with infinite speed.

However, as for (b), no matter how high the speed is, there is always a common area between current and voltage zone. Thus, the operation point can infinitely close to the centre point *O'*. In this case, it is classified as infinite speed type.

The torque of Eq. 53 can be expressed by a series of hyperboles shown as green lines. There is an orange locus which represents a series of tangent points between the torque hyperboles and the current circles at different current values. This locus is called Max Torque Per Ampere (MTPA) operation. When the voltage ellipse with ω_{mech0} has no intersection point with the current circle in the second quadrant, the max torque T_N can always be achieved, no matter what the speed is. This operation point falls on the point *B* which is at the end of MTPA locus. Point *B* is also the intersection point between voltage ellipse with base speed ω_B and current circle in the second quadrant.

Once the speed is higher than ω_B, the torque starts to reduce. The operation point that can achieve the highest torque then is always moving along the current limit circle.

For Fig. 69 (a), this operation lasts till point *s* with the max speed and zero torque. To achieve the operation from point *B* to point *s*, i_d needs to keep increasing with negative value. As the flux from PM is weakened by the d-axis armature reaction, the process is so called Flux-Weakening (FW).

For Fig. 69 (b), the flux-weakening process is the same with (a) until point *b'*. Since point *b'* with the speed ω_{mech2}, the torque hyperbole starts to be tangential with the voltage ellipse. There is a purple locus which represents a series of tangent points between the torque hyperboles and the voltage ellipses at different high speeds. This locus is called Max Torque Per Voltage (MTPV) operation. Therefore, after point *b'*, the operation point is moving along MTPV locus until infinitely close to the centre point *O'*.

The operation can also be interpreted to the torque speed plane. As they are shown in Fig. 70 (a) and (b) correspond to the types of finite and infinite speed respectively. Here both motor and generator operations are shown, regardless of resistance influence, the torque speed curves, as well as power speed curves, are symmetrical with x-axis.

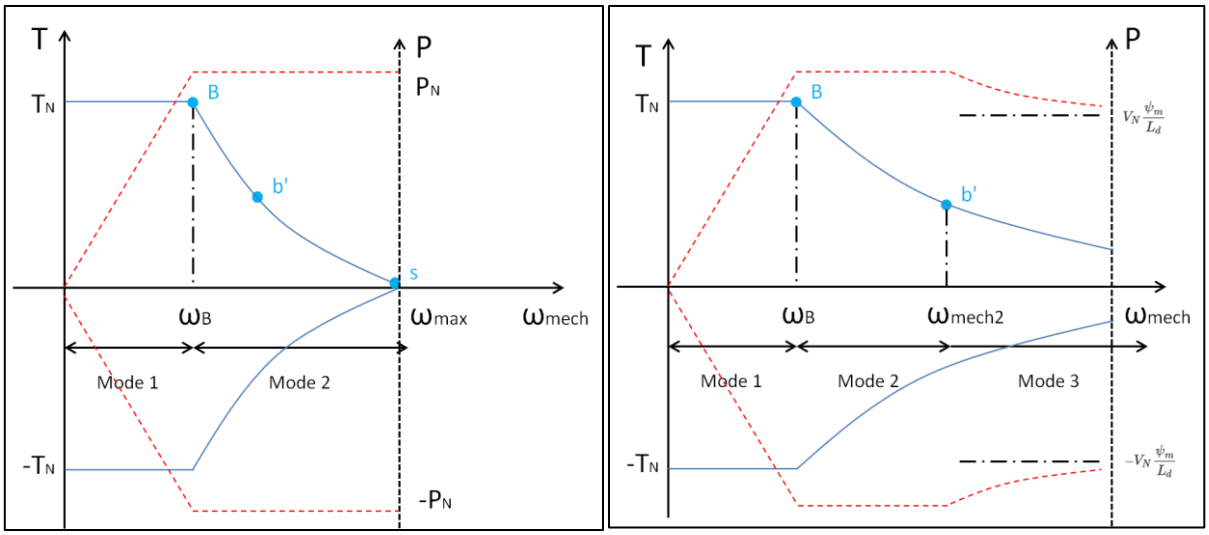

(a) (b)

Fig. 70 (a) Torque speed operation region of a PM machine with finite speed; (b) Torque speed operation region of a PM machine with infinite speed;

Therefore, the entire operation behaviors can be summarized by three operation modes.

Mode 1: namely constant torque mode. As long as the rotation speed is lower than ω_B, max torque T_N is always possible to be achieved. Since the torque is constant, the current is constant as well. While the voltage increases along with the speed. Therefore, the power is also increasing with the speed, as the red dash line indicates.

Mode 2: namely FW constant power mode. Even though the rotation speed increases and larger than ω_B, the voltage can be always kept its limit V_N. Meanwhile the total current is also at its limit I_N. Thus, the power $P = V_N * I_N$ is kept constant, as the red dash line indicates. However, the current vector angle γ_d increases with the increasing of speed. Finite speed type machine only end up with Mode 2, with the condition $\frac{\Psi_m}{L_d} > I_N$.

Mode 3: namely decreasing power region. Only with the condition $\frac{\Psi_m}{L_d} < I_N$. When the operation point comes across the point *b'*, the current starts to decrease with the increase of speed. The total power decrease as well, despite the unchanged maximum voltage. However, no matter how high the speed is, the power will always be higher than $V_N \frac{\Psi_m}{L_d}$. Besides, as i_q is very small compared to i_d at high speed, the voltage and current vector are almost in phase, thus power factor is close to 1.

For the finite speed type machine, there is a common index to measure the capability of FW. The index is called Constant Power Speed Range (CPSR). The expression of CPSR is shown as Eq. 61. Generally, the larger CPSR, the better FW capability.

$$CPSR = \frac{\omega_{max} - \omega_B}{\omega_B} \qquad \text{Eq. 61}$$

2.2.3.2 Dual-three phase windings

For electrical machines used for hybrid electrical vehicle with low voltage, it is common to apply multiplex (larger than three phases) windings. One of the most notable examples is dual-three phases winding. Under the constraints of current loading of each single inverter, applying multiplex winding is an effective way to increase the power density of the electrical machine, through increasing the quantity of the inverters, instead of capability. For industry, considering the production line, research activities and cost, it is much easier to increase the quantity than capability of the inverter unit. Besides, there are many other benefits of multiplex windings, such as fault tolerance increase and torque ripple reduction.

Let's take dual-three phase winding for an example. Here dual phase sets are assumed to be controlled by two individual current controllers with identical configurations. Then the phasors of these two phase sets can be drawn on two independent *dq* reference frames, as Fig. 71 shows.

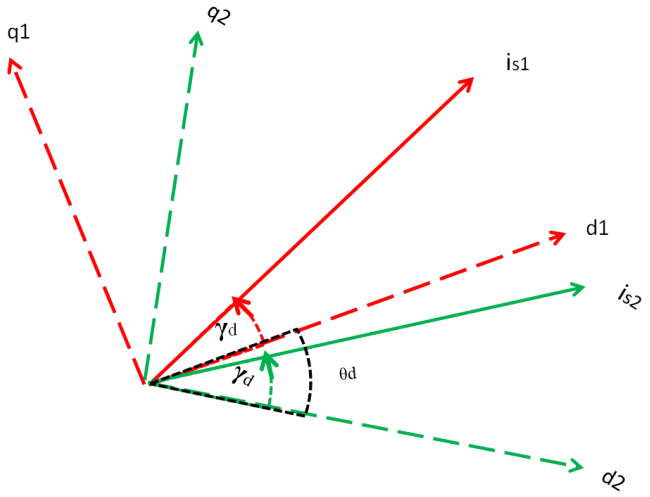

Fig. 71 Current phasor diagram of a dual-three phase configuration

The red and green coordinates represent first and second phase set respectively. The synthetic current of each phase set is also marked out. As the current control of each phase set is identical, the current angle γ_d of both phase

sets are the same. The only variable that can be changed in Fig. 71 is the phase shift angle between the two phase sets, which denotes θ_d. Thus, the Park transformation of

Eq. 40 and Eq. 42 can be rewritten as Eq. 62 and Eq. 63 respectively.

$$\begin{bmatrix} i_{s\alpha1} \\ i_{s\beta1} \\ i_{s\alpha2} \\ i_{s\beta2} \end{bmatrix} = \underbrace{\begin{bmatrix} \frac{2}{3} & -\frac{1}{3} & -\frac{1}{3} & 0 & 0 & 0 \\ 0 & \frac{1}{\sqrt{3}} & -\frac{1}{\sqrt{3}} & 0 & 0 & 0 \\ 0 & 0 & 0 & \frac{2}{3} & -\frac{1}{3} & -\frac{1}{3} \\ 0 & 0 & 0 & 0 & \frac{1}{\sqrt{3}} & -\frac{1}{\sqrt{3}} \end{bmatrix}}_{T_{64}} \cdot \begin{bmatrix} i_{a1} \\ i_{b1} \\ i_{c1} \\ i_{a2} \\ i_{b2} \\ i_{c2} \end{bmatrix} \quad \text{Eq. 62}$$

$$\begin{bmatrix} i_{d1} \\ i_{q1} \\ i_{d2} \\ i_{q2} \end{bmatrix} = \underbrace{\begin{bmatrix} \cos(\theta) & \sin(\theta) & 0 & 0 \\ -\sin(\theta) & \cos(\theta) & 0 & 0 \\ 0 & 0 & \cos(\theta - \theta_d) & \sin(\theta - \theta_d) \\ 0 & 0 & -\sin(\theta - \theta_d) & \cos(\theta - \theta_d) \end{bmatrix}}_{T_{d12q12}(\theta, \theta_d)} \begin{bmatrix} i_{s\alpha1} \\ i_{s\beta1} \\ i_{s\alpha2} \\ i_{s\beta2} \end{bmatrix} \quad \text{Eq. 63}$$

Considering the voltage from Eq. 48, the voltage of dual three phase can be written as Eq. 64.

$$\begin{aligned} u_{d1} &= R_s i_{d1} + \frac{d\Psi_{d1}}{dt} - \omega_s \Psi_{q1} \\ u_{q1} &= R_s i_{q1} + \frac{d\Psi_{q1}}{dt} + \omega_s \Psi_{d1} \\ u_{d2} &= R_s i_{d2} + \frac{d\Psi_{d2}}{dt} - \omega_s \Psi_{q2} \\ u_{q2} &= R_s i_{q2} + \frac{d\Psi_{q2}}{dt} + \omega_s \Psi_{d2} \end{aligned} \quad \text{Eq. 64}$$

Since the flux linkages can be expressed by inductances, *d* and *q* flux linkages can be expressed as Eq. 65,

$$\begin{aligned} \Psi_{d1} &= L_{d1} i_{d1} + M_{d21} i_{d2} + \Psi_m \\ \Psi_{q1} &= L_{q1} i_{q1} + M_{q21} i_{q2} \\ \Psi_{d2} &= L_{d2} i_{d2} + M_{d12} i_{d1} + \Psi_m \\ \Psi_{q2} &= L_{q2} i_{q2} + M_{q12} i_{q1} \end{aligned} \quad \text{Eq. 65}$$

where $M_{d,q}$ are the *d*, *q* mutual inductances between the two phase sets. Besides, there are $M_{d21} = M_{d12}$, $M_{q21} = M_{q12}$. Normally mutal inductance is much smaller than self-inductance. So in order to simplify the problem, these mutual inductances are ignored and set to zero. Therefore, with the currents and flux linkages, torque can be obtained with similar format of Eq. 53, as Eq. 66 shows.

$$T=\frac{3}{2}p\left[\Psi_m.\left(i_{q1}+i_{q2}\right)+\left(L_{d1}-L_{q1}\right).i_{d1}i_{q1}+\left(L_{d2}-L_{q2}\right).i_{d2}i_{q2}\right] \quad \text{Eq. 66}$$

Normally for the balance of the two phase sets, the number of turns for each phase is the same. Thus, the self-inductances of the two phase sets are identical. Also for the healthy state operation, there are conditions as Eq. 67 shown.

$$\begin{aligned} i_{d1} &= i_{d2} = i_d, \\ i_{q1} &= i_{q2} = i_q \end{aligned} \quad \text{Eq. 67}$$

Therefore, Eq. 66 can be rewritten as Eq. 68.

$$T=3p\left[\Psi_m i_q+\left(L_d-L_q\right).i_d i_q\right] \quad \text{Eq. 68}$$

Thus, with the same current limit of the inverter, the torque of dual-three phase motor is double of three phase motor. Moreover, even one phase set stop work, half of the torque still can be provided. Thanks to the system redundant, the fault tolerance is increased.

2.2.4 Efficiency

Efficiency is one of the key parameters of the electrical machine. With higher efficiency of a machine, the CO_2 emission can be less, meanwhile the required battery capacity can be smaller for the same mileage of the vehicle. Thus, it is always necessary to have efficient electrical machine, due to the large energy consumption of user phase.

The efficiency is determined as Eq. 69.

$$E=\frac{P_{Output}}{P_{input}} \quad \text{Eq. 69}$$

For the motor mode, input power is electrical, output power is mechanical, as Eq. 70 expressed.

$$\begin{aligned} P_{input} &= 3u_s.i_s.cos(\varphi), \\ P_{Output} &= \omega_{mech}T \end{aligned} \quad \text{Eq. 70}$$

The power equation aims for three phase winding configuration. u_s and i_s are phase voltage and phase current respectively. $cos(\varphi)$ is the power factor. The output power is the product of mechanical speed and torque.

For the generator mode, the input and output powers are reversed. However, no matter what machine modes are, input power is always larger than output power. The difference between input power and output power are total losses of the machine, as Eq. 71 shows. The losses are mainly transformed into heat.

$$Loss = P_{input} - P_{Output} \quad \text{Eq. 71}$$

2.2.4.1 Loss separations

For an electrical machine, the total losses can be segregated into three main types – copper loss (sometimes it is directly called Joule loss), iron loss (sometimes called core loss) and mechanical loss.

Copper loss is a loss generated from conductors. It is mainly defined by Joule's law. As the most common conductor material is copper, thus this Joule loss is called "copper" loss. The copper loss of a three phase system is expressed by Eq. 72.

$$P_{copper} = 3I^2R \qquad \text{Eq. 72}$$

In the equation, for DC, *I* is just the amplitude of the phase current. While for AC, *I* is the [RMS] value of the phase current. *R* is the resistance of one phase. The calculation of the phase resistance *R* can be defined by Eq. 73,

$$R = \rho \frac{N.(l_{active} + l_{end})}{S_{conductor}} \qquad \text{Eq. 73}$$

where ρ is the resistivity of the conductor; $S_{conductor}$ is the cross section area of a single turn of the conductor. For each conductor, it is possible to have a bunch of copper filaments. l_{active} is the active length of the stator stack. l_{end} is the total length of a single turn of the end windings, as Section 2.1.2 calculated. *N* is the total number of turns per phase. Thus, copper loss can be calculated by substituting Eq. 73 into Eq. 72.

However, this is just an ideal situation of copper loss calculation. Because the premise of applying Eq. 72 is that current is evenly distributed on the conductor cross section. However, this is not the case for the current with high frequency. It is well known that the high frequency current will approach the skin of the conductor. This is so called skin effect. Besides, as a conductor with high frequency current can result in significant change of magnetic field, the current distribution of adjacent conductors will be influenced. This is so called proximity effect. Both effects fundamentally reduce the effective area of the conductor, thus they makes the AC copper losses larger than DC copper losses. As the electrical machines for (H)EVs nowadays tend to run faster and faster, the AC copper losses need to be give special attention.

Iron loss was specifically introduced in Chapter 1.2. In general, the loss is assumed to be proportional with the electrical frequency *f* and magnetic strength density *B*.

Finally, **mechanical loss** is a loss generated by windage or friction. The expression of mechanical loss is commonly written as Eq. 74,

$$P_{mech} = a\omega_{mech} + b\omega_{mech}^2 + c\omega_{mech}^3 \qquad \text{Eq. 74}$$

where *a* and *b* denotes the coefficient of friction loss from bearing, *c* denotes the coefficient of windage loss [108]. It is not such straightforward to derive the coefficients of mechanical loss. Instead, to identify the coefficient of mechanical loss, a rotor decay test can be carried out. First, an initial velocity is given to a rotor. Then without any electrical energy input, let the rotor rotate. Under the mechanical resistance, finally the rotation will stop. A time constant can be derived from the period of the rotation, combining with the rotor inertial. Finally the mechanical loss coefficient can be estimated. For PM electrical machines, it is worth noting that removing magnets is necessary before the rotation. Because magnets can induce iron loss in open circuit condition due to the flux variation seen by the stator.

In summary, the total losses can be expressed as Eq. 75.

$$P_{loss} = P_{copper} + P_{iron} + P_{mech} + P_{stray} \quad \text{Eq. 75}$$

It is found that besides the three types of losses aforementioned, there is one more loss called stray losses. In fact, it represents miscellaneous loss types, which are the losses hard to be defined in the established physical models of electrical machines. For instance, [109] claimed that stray losses in large synchronous machines are caused by leakage and fringing flux. However, the nature of these flux is always complex. Besides, for PM machines, even inside magnets, there might be eddy current loss [110], which can also be taken into account as stray losses. Nevertheless, with more accurate physical model, more types of losses can be identified, and the stray losses part is supposed to be smaller.

2.2.4.2 Maximum efficiency control

With the analysis of each loss type, the relationship of efficiency versus currents, flux and electric frequency are clear. Then it is a matter of how to control the machine to obtain the maximum efficiency at each operation point. For Mode 1 - constant torque mode, it is straightforward to find the operation point with the highest efficiency. The operations are always on MTPA locus. In this case the target torque can always be achieved with the minimum current. For Mode 2 - FW constant power mode and Mode 3 - decreasing power mode, they are more complicated regarding the highest efficiency operations, as there are many possibilities to achieve the same torque with different current strategies. Since the efficiency strategies for Mode 2 and Mode 3 are similar, Mode 2 is discussed in details.

A series of operation points in Mode 2 are selected, as shown in Fig. 72.

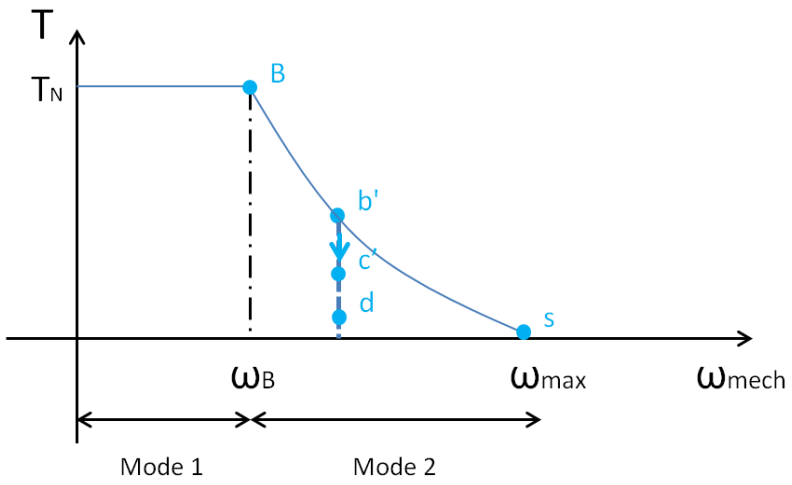

Fig. 72 Selected operation points (b', c', and d) at the same speed for a finite speed type electrical machine.

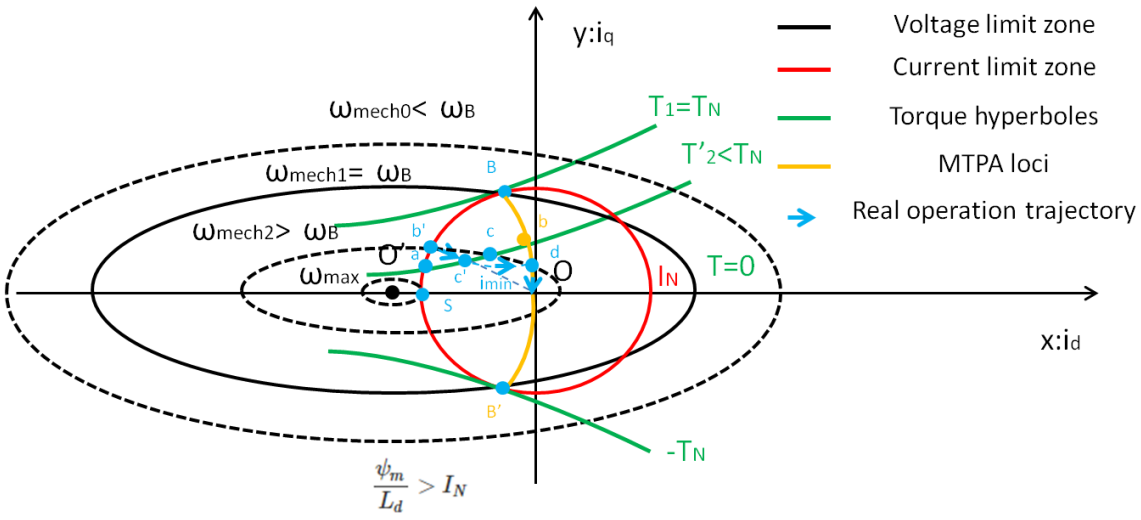

Fig. 73 Schematic diagram of the maximum efficiency operation trajectory of a PM machine with finite speed

The selected points have the same speed. All the points are in Mode 2 region. The start point is *b'*, the max torque can be achieved at this speed. Then operation trajectory is moving along the blue dash line that passes through points *c'* and *d*, and finally reach zero torque point.

As Eq. 74 indicates, at the same speed, mechanical loss is a constant number. Besides, to simplify the problem, first iron loss is not considered in the total loss. Thus, the only loss that changes with the torque is copper loss. The operation trajectory on *dq*-plane can be seen in Fig. 73.

It can be found that at rotation speed ω_{mech2}, with the decrease of torque, the intersection part between torque hyperbole T_2 and the common area of voltage and current limit zones is no longer a single point. The new intersection part is a curve segment from point *a* to point *c*. On this curve segment, point *c'* has the shortest distance to the origin point *O*. This indicates that for point *c'*, the copper loss is the smallest (regardless of skin effect or proximity effect). Thus the maximum efficiency operation trajectory is *b'* to *c'*, which is instructed by the blue arrow in Fig. 73.

It needs to be highlighted that, for PM electrical machines without reluctance torque (SPMSM), point *c'* and point *c* are overlapped, since the torque hyperbole becomes a straight line parallel to d-axis. In this case, voltage limit line from point *b'* to point *c* is the max efficiency operation trajectory. This condition is also true for machines with dominated magnet torque. However, for reluctance electrical machines (SRM, SynRM) or electrical machines with dominated reluctance torque (PMASynRM), point *c'* and point *c* may be not overlapped.

With further decrease of toque, the torque hyperbole may meet the intersection point *d*, which is the voltage limit line and MTPA locus. Since point *d*, the shortest distance between operation point and origin point is always on MTPA locus. Thus, from point d to zero torque, the maximum efficiency operation trajectory switches to MPTA locus. If at high speed there is no intersection between voltage limit line and MPTA locus, the max efficiency trajectory will only contain *b'* to *c* segment. It is worth noting that along *b-c'-d- o* trajectory, the current angle γ_d (between current phasor and d-axis positive direction) decreases with torque; but γ_d will be always larger than 90°. Moreover, the decreasing rate of γ_d is much higher at low rotation speed than the rate at high rotation speed.

Besides, for Mode 1 operation, it is easy to observe that the max efficiency trajectory is overlapped with MPTA locus, which is from point *B* to origin point *O*. For Mode 3 operation, the operation principle has no difference with Mode 2 regarding max efficiency searching.

However, once iron loss is considered, the max efficiency trajectory might be different. If the iron loss does not change significantly with the torque, then the max efficiency trajectory can be maintained. This condition is

normally suited for Mode 1 operation (without FW), or SPMSM. However, in FW regions, especially for IPMSM, at the same speed, iron loss decrease with the torque, due to the decrease of flux density in iron cores. In this case, max efficiency trajectory needs to be re-planned. Usually some algorithms are used to derive the minimum total loss.

2.2.5 Mechanical and thermal studies

Besides electromagnetic analysis above, it is also necessary to take care of other aspects of electrical machines, such as mechanics and thermal.

The main concerns of mechanical problems are the centrifugal force and stress level of a rotor. For electrical machines used in hybrid electrical vehicles, the highest rotation speed may go up to 20000 rpm. On the one hand, the centrifugal force can be very large on the rotor peripheral surface. If the machine is a SPMSM, glue is not enough to attach the magnet on the surface at such a high speed. It is necessary to add a retention sleeve on the surface of the magnet, as Fig. 49 shows. On the other hand, the high speed can induce high stress inside the rotor. For IPMSMs, the rotor is comprised of many iron "islands" connected by iron bridges. The stresses on these bridges need to be given special care at high speed.

For SPMSM machine, the relationship between sleeve stress, speed and machine parameters are shown in Eq. 76,

$$\delta_c = \rho_m \omega_{mech}^2 r_m^2 \text{ [81]} \qquad \text{Eq. 76}$$

where ω_{mech} is the rotor rotation speed [rpm]; r_m is the outer radius of the rotor (includes PM height); ρ_m is the mass density of the PM. Also, the thickness of the sleeve is proportional to the stress tolerance. Thus, the thicker the sleeve, the higher stress it can be tolerated.

The calculation of rotor internal stress is similar to Eq. 76. However, the radius is corresponding to the location of the internal point. Also, the mass density is for the iron steel instead of PM.

For the thermal problem, the main concern is the stator temperature rise. A simple analytical method called thermal circuit is used, as Fig. 75 shows.

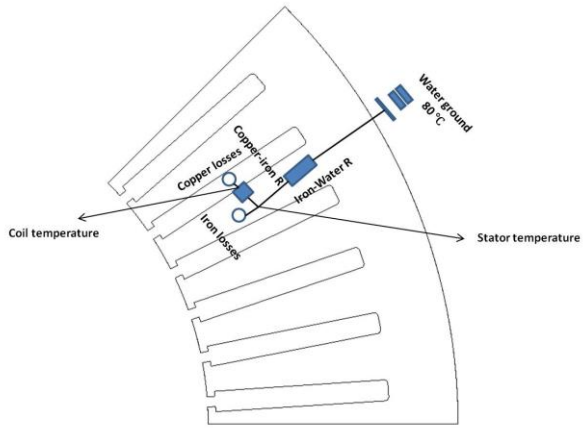

Fig. 74 The thermal circuit of a stator (4 poles, 1/8 portion) based on 2D geometry plot

In the figure, losses source such as copper loss and iron loss are considered. Two thermal resistances - "iron-to-water" and "coil-to-iron" are considered. The temperatures of coil and stator iron core are finally calculated. For

this thermal circuit, it is assumed that there is no heat convection or conduction from stator to rotor or vice versa. The cooling water temperature is assumed constant. The thermal circuit can be further simplified as Fig. 75 shows.

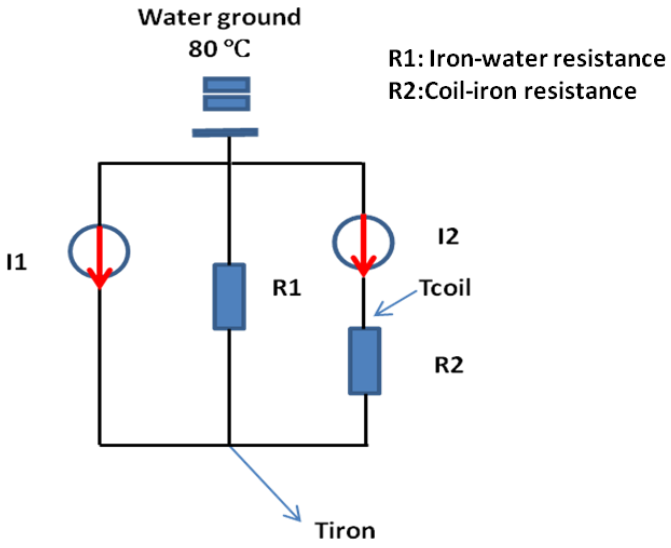

Fig. 75 Simplified stator thermal circuit with water cooling

In the figure, I_1 and I_2 represent copper loss and iron loss respectively. R_1 and R_2 represent "iron-to-water" thermal resistance and "coil-to-iron" resistance respectively. T_{coil} and T_{iron} are the temperatures of coil and stator iron core respectively. Thus, the thermal circuit can be totally equivalent to electric circuit. The losses [W] which are heat sources, are equivalent to current sources; the thermal resistances [°C/W] are equivalent to the electric resistances; the temperatures [°C] at different nodes are equivalent to voltages. thermal capacitors are ignored in the circuit. Thermal resistances can be derived from geometry parameters. For instance, R_1 can be derived by Eq. 77,

$$R_1 = \frac{l1}{A1.k1} \qquad \text{Eq. 77}$$

where l_1 denotes the total thickness of stator yoke and teeth. A_1 denotes the contact surface between stator and cooling water. k_1 denotes the iron core conductivity. Then R_2 can be derived in similar form, as Eq. 78 shown,

$$R_1 = \frac{l2}{A2.k2} \qquad \text{Eq. 78}$$

where l_2 denotes the total thickness of insulation layer. A_2 denotes the total wall surface of the slot. k_2 denotes the conductivity of the insulator.

However, these analytical methods are normally not such accurate, due to the non-linearity and convection influences in practice. Instead, thermal resistances are often estimated by experiment methods. Normally a thermal test is carried on a reference machine. The iron loss and copper loss are known for the reference machine. Then until the thermal state of the machine is stable, the temperature rises of copper coil and iron core are observed. Thus, a macro thermal resistance R_{ths} can be derived. This R_{ths} can be used to derive thermal resistances of new machines by geometry proportions. For instance, the macro thermal resistance is inverse proportional to the volume of the machine. Thus, R_{ths} is inverse proportional to the outer diameter and active length of a stator. The calculation details will be shown in Section 4 and Section 5.

Based on the insulation thermal aging limit, the temperature upper limit for copper coil is normally 200 ℃, and for iron core is 300 ℃. Thus, the machine should be designed to fulfill these thermal constraints.

2.3 Finite element method

2.3.1 Finite element method introduction

Due to the vast nonlinear properties of electrical machines, nowadays analytical methods are not accurate enough to give good predictions of results. Instead, with significant improvements of calculation capability of computers, people are fond of Finite Element Analysis (FEA, or FEM). Fundamentally, it is a type of numerical calculation that switches unique physical problems into general mathematic problems expressed by partial differential equations. Thus, it has been widely used in the areas of electromagnetic, mechanical, heat transferring and CFD.

There are many kinds of FEM software. Depending on the needs of the physical problems, suitable FEM software needs to be selected. For electrical machine designs, there are many classical FEM softwares, such as JMAG, ANSYS, FLUX, FEMM and OPERA, *etc*. JMAG is chosen for the machine designs. The advantages are highlighted in this section based on [128]:

1. JMAG provides FEM models that are dedicated to electrical machine designs. For instance, the set up for winding, iron core and magnets are very easy. The rotor motion and symmetry boundary setups are straightforward without manual mesh adjustment. The FEM models can be simply coupled with electrical circuits that generate arbitrary current or voltage waveforms. Thus, complex machine operation scenarios can be analyzed. Advance physical models are implemented and updated frequently, such as a recent iron loss model that takes DC bias field into account. The post process for machine performances is professional. Electrical information, torque pulsation and losses breakdown can be easily extracted and displayed. Parametric study and embedded optimization methods can be easily implemented.
2. JMAG has embedded a CAD geometry editor that is user friendly. All the geometry items can be empowered with mathematical expressions, which enable easy parametric studies. Mesh generation is always a trouble for many FEM softwares. However, in JMAG, mesh can be generated intelligently, rapidly and with high quality. It is also well coherent with the geometry.
3. JMAG solver can calculate a model with an impressive speed, even if the model is three dimensions with massive elements. Besides, with proper set up, the solver can deal with some unique problems of electrical machines, such as transient states of short circuit conditions, and excessive non-linear situations. If necessary, JMAG can do parallel computation with the help of cluster.
4. JMAG has a complete and precise materials database. For instance, the soft magnetic materials library is very huge. For each soft magnetic material, at least a non-linear *B-H* curve is given. Thus, the phenomenon of flux saturation and flux leakages can be included. Most of iron loss curves up to 1kHz are given; some iron materials even have temperature dependency. For hard magnetic materials like PMs, demagnetization curves with different temperatures are clearly depicted. All PMs can be simulated with reversible properties. Some PMs can be even simulated with irreversible properties, which indicates the recoil curves after demagnetization are given. Thus, demagnetization analysis can be easily carried out. Finally, customized materials library can be created easily. This will be very useful for some recycled magnets properties setting.
5. JMAG has multi-physics study features, such as electro-mechanical coupling and electro-thermal coupling. Besides, JMAG can be easily coupled with third party scripts, such as Matlab or Python, which can be used for efficiency map plotting. Thus, there are many possibilities to extent the research based on existed models.

Nevertheless, the FEM model was validated with the analytical methods. This work can be found in Appendix part 2 FEM model validation.

2.3.2 SPMSM studies based on FEM

2.3.2.1 MHEV specification and basic machine types selection

The main requirements and specifications for a SPMSM are shown in **Table VII**. Some points need to be highlighted:

- The DC side voltage limitation is around 48V.
- A switch frequency of the machine drive constraints the pole number.
- No base speed is specified. Instead, additional requirements such as different powers at different speeds are specified.
- Under the given thermal cycle, a constant power operation needs to be achieved. The stator temperature becomes a range instead of a single value.
- Limits such as max torque ripple, total length including end winding is constrained, which means end-winding height should not exceed 50 mm.

Table VII REQUIREMENTS AND SPECIFICATIONS OF A SPMSM FOR MHEV APPLICATION

Requirements	**Abbreviation**	**Unit**	**Value**
Outer diameter	D_o	mm	150
Axial length	L	mm	60
Total length	L_{total}	mm	110
Airgap height (Sleeve excluded)	δ	mm	0.5
DC supply voltage	V_{DC}	V	48~52
Maximum inverter current	I_N	Arms	<300
Max switch frequency of drive unit	f_m	kHz	10
Max operation speed	Ω_{max}	rpm	18000
Max electrical power @ max operation speed	P_{me}	kW	14
Full load max torque	T_m	N.m	55
Max mechanical power(motor) @10000 rpm	P_m	kW	14
Nominal water temperature (S1 thermal cycle)		℃	75
Constant electrical power @ 6000 rpm with S1 thermal cycle	P_c	kW	7
Torque ripple ratio	$\frac{T_{ripple}}{T_1}$	%	5
Stator temperature		℃	80~200

Thus with all these specifications, it is necessary to select the types of SPMSM step by step - distributed windings or concentrated windings, three-phase windings or dual-three-phase windings, as well as conductor types. Then what is the suitable pole number? Finally, details of optimization need to be carried.

Concentrated windings are investigated first. Based on the criteria of winding factor, harmonics and pole number limit, suitable slot pole combinations can be screened out.

According to the analysis in Fig. 59, the winding factor that larger than 0.9 has the following pole slot combinations:

- 4p9s, 5p12s, 7p15s, 8p15s for both double layers (DL) and single layers (SL).

Within the combinations above, according to Fig. 60, the combinations with low sub-harmonic component have:

- 4p9s, 7p15s only for DL.

As for the pole number, it is constrained by two conditions - inverter switch frequency and end winding height. As the concentrated winding has very low end-winding height. Only switch frequency constraints the upper limit of pole number. The maximum switch frequency of machine drive is denoted as f_0. Due to the minimum sampling frequency of the machine drive, the electrical frequency f_e of the electrical machine is limited by Eq. 79. Besides, the relation between f_e and p is shown by Eq. 80.

$$12 * f_e < f_0 \qquad \text{Eq. 79}$$

$$f_e = \omega_{mech}\, p/120 \qquad \text{Eq. 80}$$

Thus, with the given ω_{mech} and f_0 which are 18000 rpm and 10 kHz respectively, the upper limit of p is obtained and approximated to 5.

Therefore, the only slot pole combination that can fulfill all the conditions is 4p9s DL.

However, the possibility of applying three phase winding is small, as the simulation results of Section 3.2-Chapter 2 reflected. Thus multi-phase has to be implemented. Dual-three-phase windings are better than four phases or five phases regarding modular application concept. Because the drive of three-phase windings can be directly used on dual-three phase winding, while four or five phases need to be customized.

In this case, the same screening criteria with three-phase concentrated winding are used. The analysis for dual-three -phase concentrated windings can be found in [130].

For the winding factor larger than 0.9, the slot pole combinations have:

- 5p12s, 7p12s, 10p24s, 11p24s, for DL only.

Within the combinations above, the two combinations that result in low rotor losses, which equivalent to low harmonics content are：

- 10p24s, 11p24s, for DL only.

Finally, with the known pole number constraint, it was found that none of the pole slot combinations can fulfill the condition. Therefore, normal concentrated windings are not suitable for this MHEV application. Although some special design strategies for concentrated windings may overcome the problems, such as using different turns per coil [115], or applying conducting sleeve [131], this is out of the scope of the thesis.

2.3.2.2 SPMSM designs for MHEV application

Only distributed windings are possible to be applied for MHEVs. Again, the pole slot combinations of machines with distributed windings need to be checked by the aforementioned criteria. This time only dual-three-phase windings are discussed. First, the winding factor is not a problem for distributed winding. It is always equal or close to one. Second, no sub-harmonic is produced by distributed winding. The total harmonic distortions (THD) are much lower than concentrated windings, which result in small rotor losses. Thus, the only constraint is the pole number.

2.3.2.2.1 Poles and turn number selection

The upper limit of pole number is also constrained by the switch frequency of the drive. Thus, the max pole pairs number is still $p=5$. The lower limit of pole number is constrained by end-winding height. Table VII indicates that the total heights of end winding should be less than 50 mm.

Based on the end-winding length calculation, as Eq. 23 shows, and still assuming end winding height $h_d = 0.5\ L_{Aa}$, it is found that h_d is correlated to the coil pitch in slot y_{sp}, slot number Q_s and an approximate sum of stator inner radius (inner rotor) and stator teeth height r. Assuming that no matter what Q_s is, r is constantly equal to 64 mm. Then the total end winding heights $2* h_d$ of different pole slot combination are shown in Table VIII. In the table, SPP stands for Slot per Pole per Phase. The table only lists the max pole pair number p which is 5. Also considering the manufacture difficulties, teeth mechanical strength and flux saturation, the highest slot number Q_s is limited to 72.

Table VIII TOTAL END WINDING HEIGHTS OF DIFFERENT POLE SLOTS COMBINATIONS

Machine number	***p***	***SPP***	***Q_s***	***y_{sp}***	***$2*h_d$***
1	1	1	12	6	201
2	2	1	24	6	101
3	3	1	36	6	67
4	3	1	36	5	56
5	3	1.5	54	9	67
6	3	2	72	12	67
7	3	2	72	11	61
8	4	1	48	6	50
9	4	1	48	5	42
10	4	1.5	72	9	50
11	5	1	60	6	40
12	5	1	60	5	34

It can be found that the total end winding heights go below 50 mm when pole pairs number is larger than 3. It is also worth to highlight that when coil slot pitch y_{sp} equals to 5 or 11, they are short pitch windings. The SPP value does not influence the end winding height. When SPP=1.5, it is impossible to have short pitch mechanically. Nevertheless, Table VIII is just a brief calculation. Certainly, for different pole numbers, radius r is different. Normally with lower pole number, a larger stator yoke width is needed for saturation reduction, which results in smaller r. Thus, there is a chance for machine number 4 to have an acceptable end winding height.

Therefore, the following analysis will only focus on machine number 4, 8, 9, 10, 11 and 12.

For the conductor type, rectangular conductor with formed winding can be chosen, since it always has high filling factor. The exposed surface of rectangular coils is also larger than random wound round coils, thus the cooling factor is better for rectangular coils than round coils. These advantages are important for the scenarios with large currents and compact space, such as MHEV applications. However, using the form winding in turn brings to extra constraints, as it can no longer "randomly" wound the coils. Conductor size needs to be carefully selected. The number of turns per slot, as well as the stator slot shape, has much less freedom than round coils to modify.

The turn number per phase N is decided by the maximum output power P_m and full load max torque T_m. The upper limit is constrained by P_m, where $P_m \propto 1/N$, the lower limit is constrained by T_m, where $T_m \propto N$.

Sometimes it is not straightforward to observe the output power directly. Instead, for an infinite speed type machine, short circuit current can be used as the observing target. As the machine needs to serve at very high speed, most probably it needs mode 3 of FW. With the increase of speed, the operation point is approaching to the short circuit point O', as Fig. 69 shows. Eventually, the amplitude of the phase current at high speed is close to the short circuit current I_{cc}; the current angle γ_d is close to 180°. It indicates that the current is mainly comprised of i_d, and $i_q << i_d$.

The voltage formulas were shown in Eq. 49. Transient states and resistance voltage drops can be ignored. As the machine is a SPMSM, d and q inductances are almost identical. Thus, it is assumed $L_d = L_q = L$. Then the terminal voltage at max angular operation speed $\omega_{\max}$ can be written as Eq. 81,

$$\overrightarrow{u_s} = \overrightarrow{u_d} + \overrightarrow{u_q} = p\omega_{mech\_max} L\overrightarrow{i_q} + p\omega_{mech\_max} L\overrightarrow{i_d} + \vec{E} = \overrightarrow{V_L} + \vec{E} \qquad \text{Eq. 81}$$

where V_L denotes the voltage induced by inductance L at max speed. E is the back-EMF at max speed. The direction of E is towards q-axis positive. The amplitude of E can be derived from Eq. 59, which can be rewritten as Eq. 82.

$$\left|\vec{E}\right| = p\omega_{max} L i_{cc} \qquad \text{Eq. 82}$$

Moreover, based on the condition $i_q << i_d$ at max speed, the amplitude of V_L is almost identical to E.

The limit of the terminal phase voltage u_s is equivalent to the back-EMF at base speed, as Eq. 83 shows.

$$\overrightarrow{|u_s|} \leq p\omega_B L i_{cc} \qquad \text{Eq. 83}$$

For the relationship between ω_{max} and ω_B , Eq. 61 already specified. It can be rewritten as Eq. 84.

$$\omega_{max} = (CPSR + 1)\omega_B \qquad \text{Eq. 84}$$

Thus if the terminal voltage limit is seen as the base value, the per unit value of E and V_L are both CPSR+1. The voltage phasor diagram at ω_{max} can be drawn as Fig. 76.

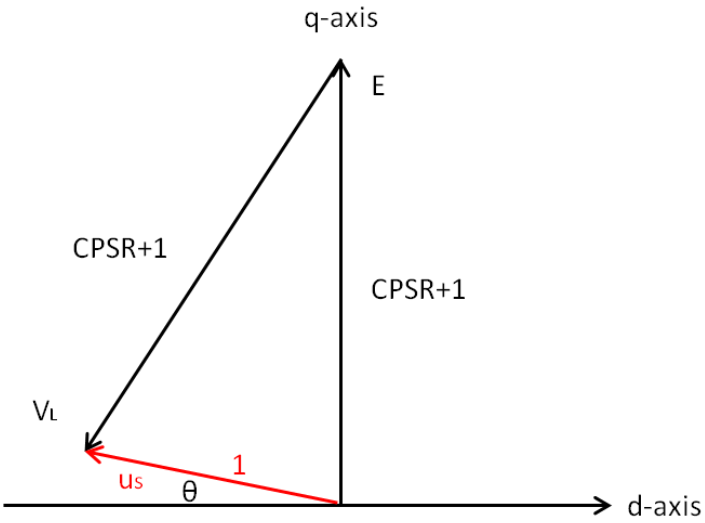

Fig. 76 Voltage phasor diagram at top speed ω_{max}

As the phase current phasor is assumed equivalent to i_d, the angle between voltage and current can be seen as θ. For the dual-three-phase SPMSM, the max electrical power at top speed P_{me} can be expressed as Eq. 85.

$$P_{me} = 3\hat{u}_s\hat{\imath}_d cos(\theta) \quad \text{Eq. 85}$$

It is found that since CPSR ≥ 4, θ ≤ 7°. As cos7°≈0.993, the power factor $cos(\theta)$ can be approximated as 1. In addition, $\hat{u}_s$ and $\hat{\imath}_d$ can be expressed as Eq. 86,

$$\hat{u}_s = k_m \frac{V_{DC}}{\sqrt{3}}, \quad \hat{\imath}_d = \sqrt{2}\bar{\imath}_{cc} \quad \text{Eq. 86}$$

where k_m is the modulation factor of the drive; $\bar{\imath}_{cc}$ is the *rms* value of short circuit current. Substituting Eq. 86 into Eq. 85, the electrical power can be rewritten as Eq. 87.

$$P_{me} = 3 * k_m * \frac{\sqrt{2}}{\sqrt{3}} * V_{DC}\bar{\imath}_{cc} \approx 2V_{DC}\bar{\imath}_{cc} \quad \text{Eq. 87}$$

As the DC voltage is a fixed value in this application, electrical power is directly linked with the short circuit current. Thus, eventually the number of turns is constrained by the short circuit current. For the machine with $P_{me} = 14\ kW, V_{DC} = 48\ V$, the target short circuit current is $\bar{\imath}_{cc} \approx 146\ A_{rms}$.

It needs to be highlighted that Eq. 87 is not suitable for all types of machine. For the finite speed type machines, as i_{cc} is larger than i_N, V_L will be smaller than E, which results in large θ. However, for an IPMSM of infinite speed type, Eq. 87 can be applied as well.

Then some trial-and-error calculations based on the FEM model are carried. Regardless of conductors arrangement in one slot, The max torque T_m and $\bar{\imath}_{cc}$ at Ω_{max} of each N is shown in Table IX, It needs to be highlighted that N cannot be a prime number, thus N = 13 or 17 is excluded.

Table IX TORQUE AND SHORT CIRCUIT CURRENT OF THE SPMSM MODEL(FOUND IN APPENDIX 2.3) WITH DIFFERENT TURN NUMBER PER PHASE

N	T_m [N.m]	$\bar{I}_{cc}$ [Arms]
14	54	168
15	57	157
16	60	147
18	65	131

It is found that a reasonable range for N is between 14 and 16 turns. For $N > 16$, i_{cc} is too small, T_m higher than 65 N.m is unnecessary. For $N<14$, torque is too small, i_{cc} larger than 170 A_{rms} is unnecessary. Besides, bear in mind that these are the results of 2D modeling. For the real condition, the leakage flux from end region of the machine should not be ignored. These leakage flux lead to lower T_m and i_{cc} than the results of 2D models. Thus, it is necessary to leave some margins for both T_m and i_{cc} from 2D simulation.

Then different poles and slots combinations can be investigated. Assuming for the short pitch winding, the number of turns per slot has to be even number. Besides, due to the constraints of rectangular conductor, as well as filling factor, the number of turns per slot has to be smaller than 5. Thus, with the assumptions above, and combining with the candidate machines from Table IX, all possible machine designs are shown in Table X (machine number is rearranged).

Table X SPMSM POLE/SLOT COMBINATIONS WITH DUAL-THREE-PHASE DISTRIBUTED WINDING AND REC-CONDUCTOR

Machine Number	p	SPP	Q_s	y_{sp}	Turns/slot	Turns/phase
1	3	1	36	5	4	12
2	4	1	48	6	3	12
3	4	1	48	6	4	16
4	4	1	48	5	4	16
5	4	1.5	72	9	2	12
6	5	1	60	6	3	15
7	5	1	60	5	4	20

Therefore, with these condition filters, only machine numbers 3, 4 and 6 are able to fulfill all constraints. The following optimizations and comparisons will be carried out only among these three machines.

Before the start of optimization, some parameters need to be predefined. It is assumed that the values of tooth wedge height h_{wed} and slot opening width w_{open} are always kept constant, h_{wed} = 1 mm and w_{open} = 1.3 mm. Their impacts to the performance are not discussed in this thesis. Then the dimension of the stator slot, as well as conductor size for each machine is set in advance. In order to have the same slot current density, all three machines use the same conductor. The conductor height (coating included) h_{con} =5.3 mm. The conductor width (coating included) w_{con} =2 mm. Then the slot dimension is varied with the number of turns per slot. For machine numbers 3 and 4, the slot width w_{sl} =2.6 mm ; the slot depth h_{slot} =22 mm. For the machine number 6, the slot width w_{sl} =2.6 mm ; the slot depth h_{slot} =16.5 mm. Details of the machine geometry can be found in Fig. 77. Thus the maximum slot current densities of all these three machines are around 16 [Arms/mm^2]. Therefore, based on Table VI, it is compulsory to use water or oil cooling method.

For the rotor, the shaft diameter is fixed. Considering the shaping of the magnet later on, only the thickness part of the magnet is set as 3 mm.

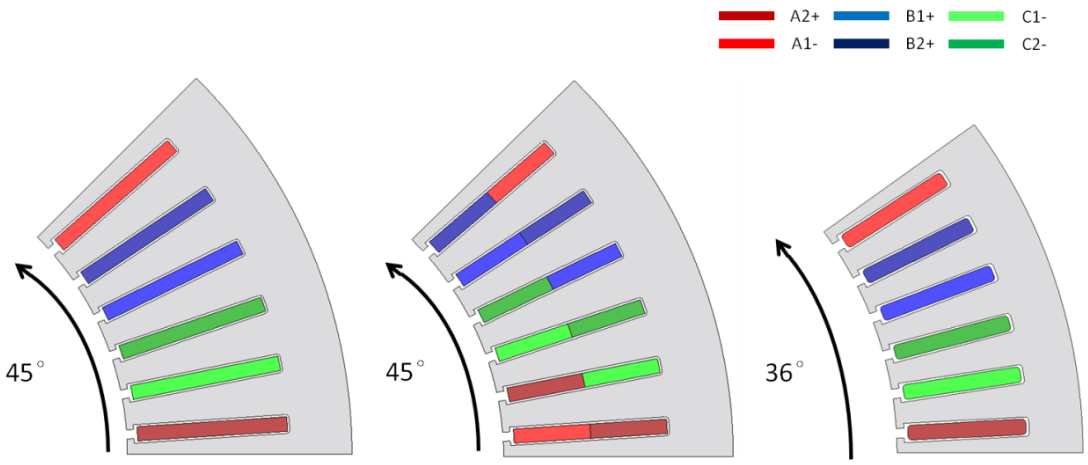

(a) (b) (c)

Fig. 77 Cross sections of a stator for one pole span (a) machine number 3, (b) machine number 4(short pitch), (c) machine number 6. The color blocks in the slot represent all windings area.

2.3.2.2.2 Split ratio optimization

Therefore, the parameters which can be changed are rotor outer diameter D_r, inner stator diameter D_{in} and stator yoke height h_{yoke}. However, as magnet, sleeve and airgap thicknesses are fixed, D_r must change with D_{in}. The tooth width is an indirect parameter to be controlled, thus the tooth width can be slightly varied with D_{in}. From the studies of [132] and [133], a design factor called split ratio was involved, and it can be expressed as D_{in} / D_o. For each machine type, such as 4p or 5p, an optimal split ratio can be found in order to obtain the max torque with the same input current. If the split ratio is too small, the magnet surface will be small, so does the flux linkage. If the split ratio is too large, the stator yoke will in turns become too thin to be saturated. In this case, parametric studies for optimal split ratio searching has been done and the results are shown in Fig. 78.

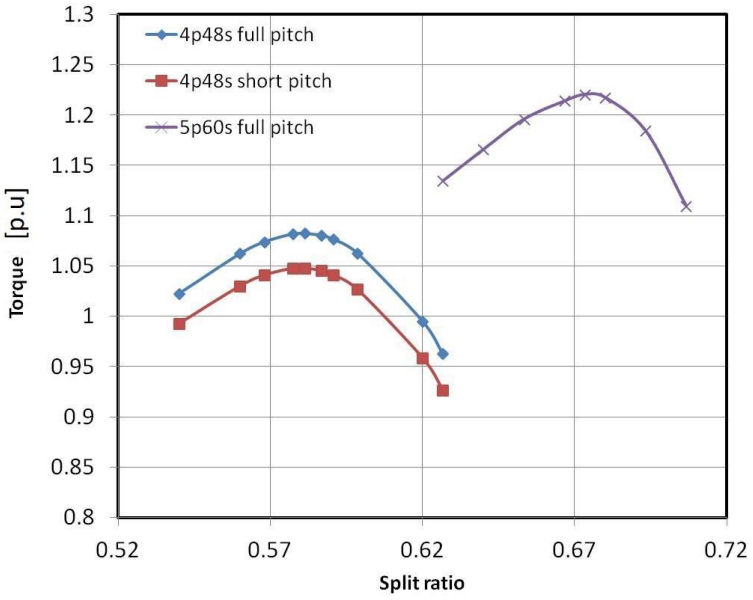

Fig. 78 Split ratio curves for the machine numbers 3, 4 and 6.

The max torques (expressed in Per Unit) of each SPM machines are derived by FEM 2D models. There are some assumptions for the parametric studies - for each machine type, the shape of the slot and conductor is kept the same. So, the copper loss does not change during the optimization. The magnet coverage is always kept as 99%, which can be seen as a magnet ring outside the rotor core. Finally, as the iron losses have small influence to the torque, their impacts were ignored in this split ratio study. From Fig. 78, it is found that the pole number has a great impact on the optimal split ratio, this impact is also found in [132]. With the increase of pole number, the optimal split ratio is also increased.

This can be explained that with higher pole number, less flux travel between each pole pair. Thus, compared to low pole number, the demanded stator yoke thickness can be smaller for higher pole number. Flux distributions of two machines with different poles and optimal split ratios are demonstrated in Fig. 78. Although the split ratio of 5p60s machine is higher than 4p48s machine, the saturation levels of the two stator yokes are almost the same. Therefore, smaller stator yoke thickness implies higher split ratio.

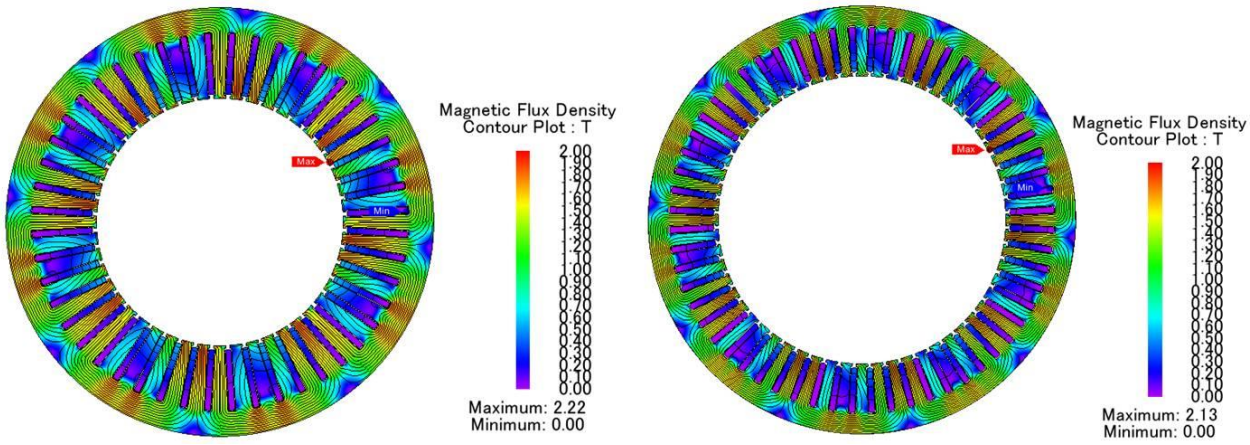

Fig. 79 Full load flux distributions of electrical machines with optimal split ratios (a) 4p48s full pitch with 0.58 split ratio (b) 5p60s full pitch with 0.67 split ratio.

2.3.2.2.3 Torque ripple reduction by changing magnets shape

The next step is torque ripple control. Only the torque ripple during constant torque range was studied. There are several common ways to reduce torque ripple from machine design point of view, such as magnet skewing, magnet shaping and control of magnetization direction.

Here magnet skewing is not considered in the design. Because skewing may lead to unbalanced axial electromagnetic forces, this may reduce the life time of shaft and bearing. Besides, from some studies, skewing cannot contribute the torque ripple rate reduction when the machine run at rated current. Finally, skewing increases the cost of manufacturing, as the skew steps need to be accurately controlled.

Hence for this design, the main idea is to shape the magnets. One usual way is to control the span of the magnet. As Fig. 80 shows, magnet coverage per pole can be expressed in percentage. For 99% magnet coverage, the magnet on each pole occupies 178^{o} electrical degree. For 56% magnet coverage, the magnet on each pole occupies 101^{o} electrical degree. No matter the percentage of the coverage, the magnet thickness is always 3 mm.

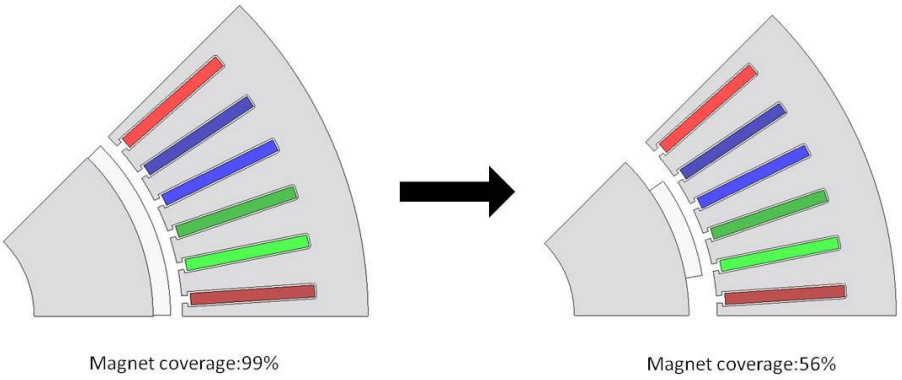

Fig. 80 Schematic of the magnet coverage percentage per pole, e.g. a 4p48s full pitch electrical machine

Another way is to use breadloaf shape magnets that the magnet sharpness can be controlled. [136] investigated that torque ripple can be reduced with the increasing of magnet sharpness. In addition, the harmonics of Back-EMF waveform can be reduced, which can lead to less iron losses. An example is shown in Fig. 81.

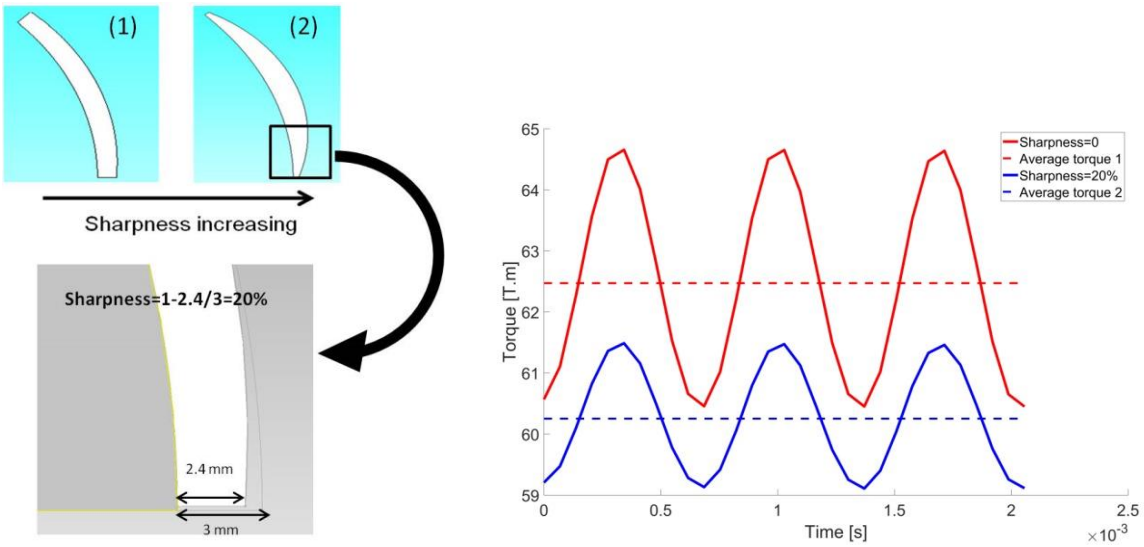

(a) (b)

Fig. 81 Torque ripple control by magnet shaping (a) sharpness definition; (b) Torque ripple of machine 4p48s full pitch with different magnet sharpness

The sharpness of the magnet is controlled by changing the eccentricity of the outer arc. The sharpness rate was calculated by the magnet reduced fringe length over maximum magnet thickness, as Fig. 81 (a) shown. In this case the max magnet thickness is 3 mm.

No matter to decrease the coverage of a magnet or to increases the sharpness of a magnet, the average torque reduces as well. Thus, it was necessary to make a compromise between torque amplitude and torque ripples. Parametric studies about magnet coverage and sharpness are shown in Fig. 82. Two machines - 4p48s full pitch and 5p60s full pitch are studied and compared. Here the magnetization direction of every PM is kept parallel. The ambience temperature for operation is 80 ^{o}C.

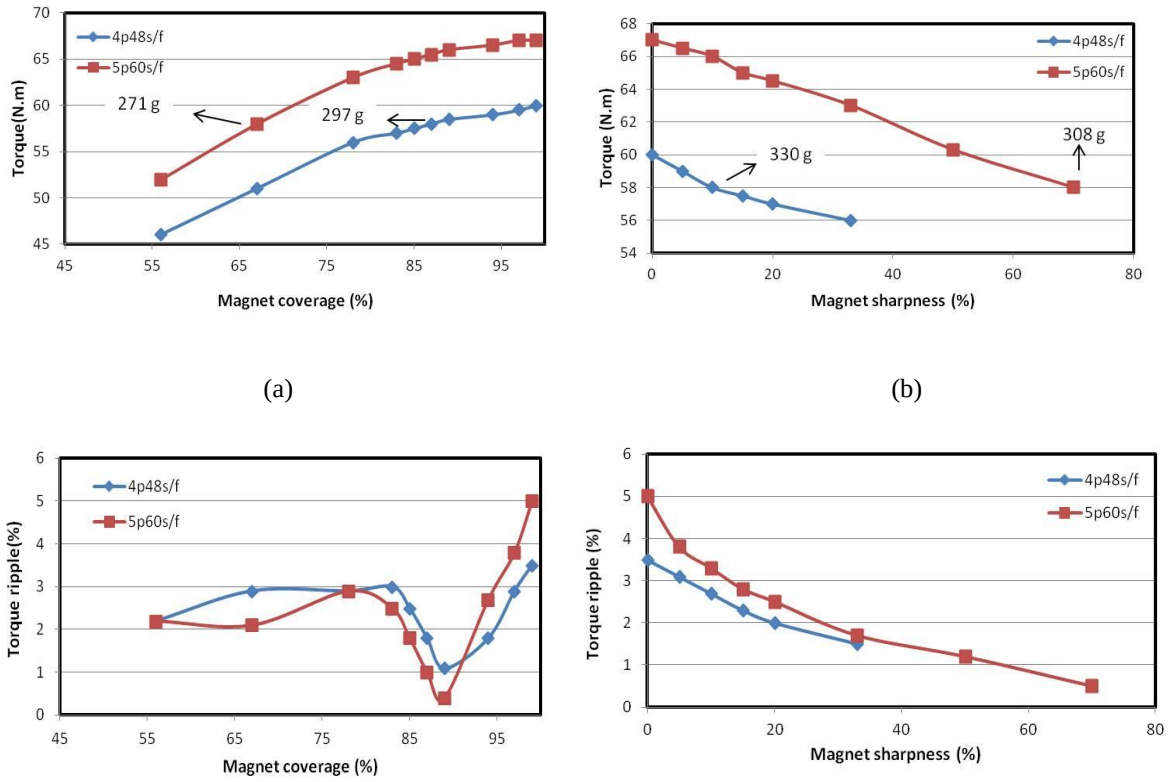

Fig. 82 Curves of 4p48s/f and 5p60s/f : (a) Torque vs Magnet coverage percentage; (b) Torque vs Magnet sharpness; (c) Torque ripple rate vs Magnet coverage percentage; (d) Torque ripple rate vs Magnet sharpness.

Parametric studies can also can done on Back-EMF analysis. SPMSMs with 4p48s full pitch were taken as examples. The variation of Back-EMF with different magnet span or sharpness is shown Fig. 83.

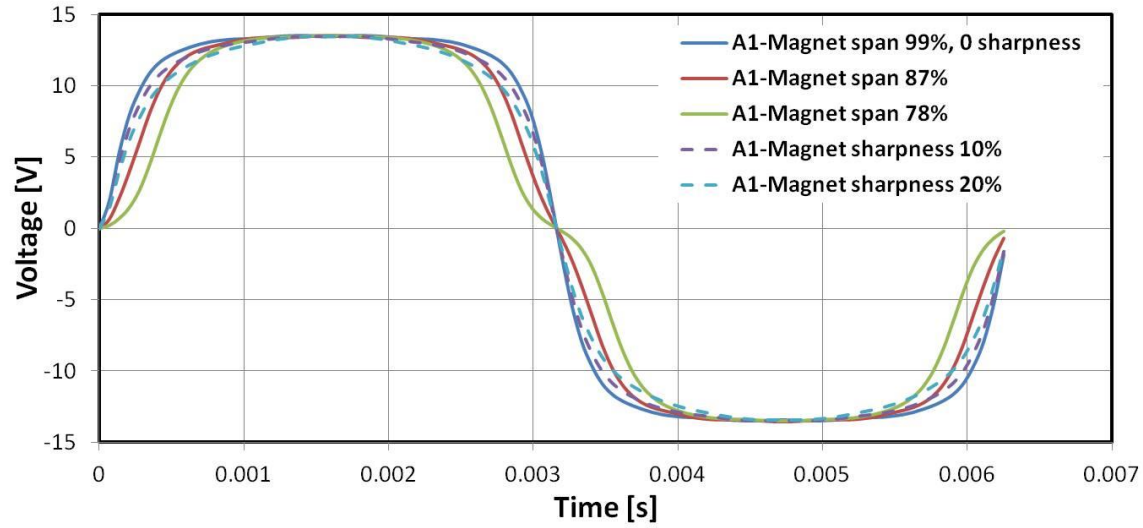

(a)

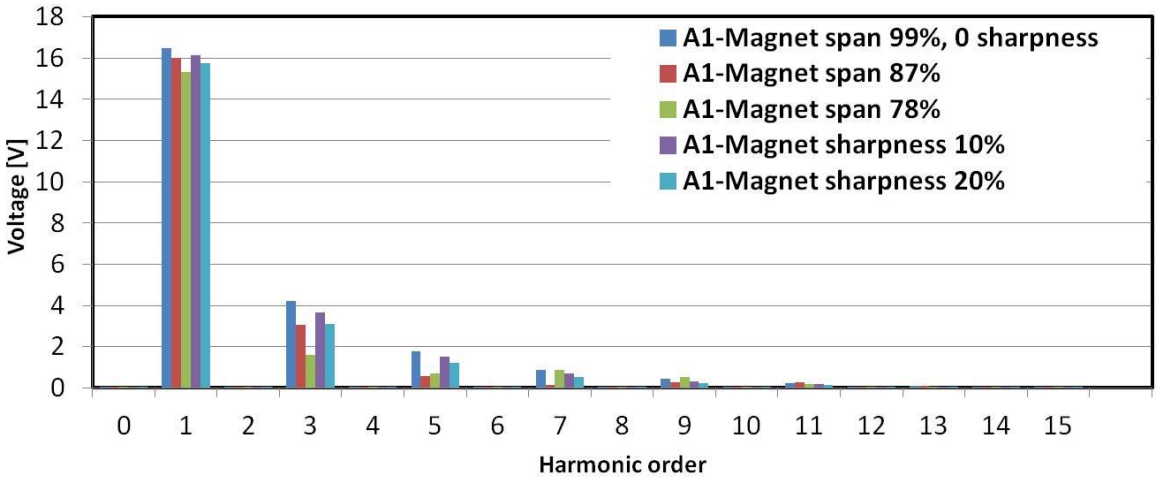

(b)

Fig. 83 Single phase A1 Back-EMF and FFT at 2400 rpm (base speed) of four selected SPMSMs with 4p48s/f and different magnet shapes.

Several connections can be found from the parametric studies above:

- Torque is reduced with magnet coverage decreasing, as the fundamental component in FFT is reducing.
- Torque ripple rate is not simply reduced with magnet coverage decrease. Instead there is an optimal coverage percentage for minimum torque ripple rate. From Fig. 83 (b) it can be observed that although 3rd harmonic is decreasing with the magnet coverage, the high order harmonics, such as 5th or 7th, start to increase when magnet coverage is larger than 87%. Thus, there is an optimal magnet coverage for torque ripple. For *4p* and *5p* machines, the optimal coverage ranges are very close, which are around 87%.
- Before 85% magnet coverage, the torque reduction rate is slow. After 85% coverage, the torque reduction rate becomes fast and linear. This is because when the magnet coverage is large, two adjacent magnets on one pole pair produce large amount of leakage flux near the edge regions. Thus, when the magnet coverage is changing from 100% to 85%, most of reduced flux is leakage flux, which does not contribute to torque. However, after 85%, the flux linkages start to drop linearly.
- Torque reduces linearly with magnet sharpness, as the fundamental component in FFT is reducing linearly.
- Torque ripple is reduced with the magnet sharpness increase. From Fig. 83 (b) it can be observed every order of harmonic reduce with the magnet sharpness increase.
- Comparing two cases – (1) magnet coverage 87% and (2) magnet sharpness 10%, although they have the same fundamental component, the total harmonic distortion (THD) of case (2) is higher than the THD of case (1). Thus case (2) has higher torque ripple than case (1).

Considering these 2D simulations, some leakage flux from the axial end of the machine are not considered. Thus, the target torque of 2D simulation is 58 N.m. The results are collected in Table XI, where machines are re-numbered. For the same torque requirement, changing magnet coverage gains better effect than magnet shaping. Because machine number 1 needs only 271 g PM with magnet coverage 67%, while machine No. 2 needs 297 g PM with magnet coverage 87%. Both torque ripple rates are within 5% limit. However, by changing magnet sharpness, machine No. 3 needs 308 g PM to achieve 58 N.m, and machine No. 4 even needs 330 g PM to achieve 58 N.m.

Table XI CHARACTERISTICS OF EACH MACHINE WITH THE SAME MAX TORQUE, 2D SIMULATION

Machine number	**1**	**2**	**3**	**4**
Machine characteristics	5p60s/f, magnet coverage 67%	4p48s/f, magnet coverage 87%	5p60s/f, magnet sharpness 70%	4p48s/f, magnet sharpness 10%
Max torque [N.m]	58	58	58	58
Torque ripple rate (%)	2.1	1.8	0.5	2.7
Magnet weight [g]	271	297	308	330
Magnet weight (P.U.)	1.00	1.10	1.14	1.22

In additional, there are two shortcomings for magnet shaping:

- For sintered NdFeB magnets, the cost and manufacture difficulties of magnet span modification is less than the magnet sharpness modification. As arc shape is a common shape for a magnet. While for the magnet with accurate sharpness needs a lot of effort on the magnet mold development.
- For the magnet with large sharpness, the reduced magnet thickness on both ends of a magnet may result in partial demagnetization at certain operation conditions, such as deep FW.
- When a retention sleeve covers the magnet surface, the contact area between sleeve and breadloaf shape magnet is less than what with arc shape magnet. Small contact area results in serious uneven centrifugal force distribution on the sleeve. Local stress becomes very high on the vertex of breadloaf shape magnet for the high rotation speed. The overload stress may destruct both magnets and sleeve.

Actually, by using a new magnet shaping method which is so called axial shaping [137], the torque ripple rate as well as cogging torque can be further reduced. As Fig. 84 shows, the outline of the magnet with axial shaping is depicted by the dash line. Briefly speaking, two triangle parts are added to both sides of the arc shape magnet. In this case, the Back-EMF of axial shaping magnet has even less THD than the back-EMF of only short pole pitch magnet. Meanwhile, to enhance the torque, a small notch is made on the top to produce third harmonic.

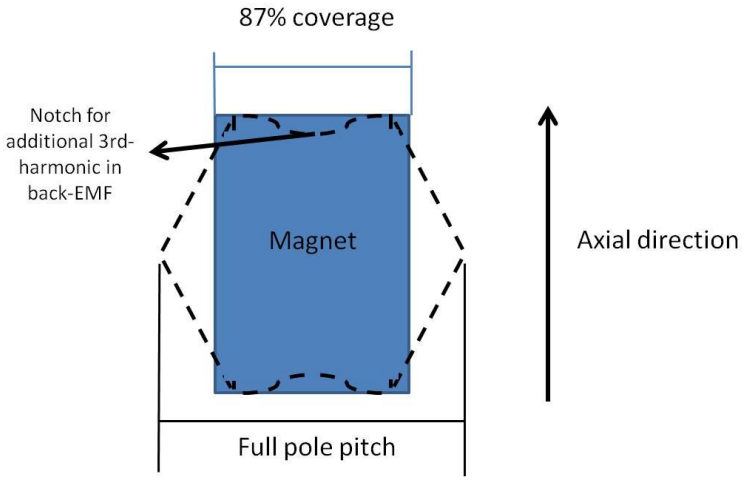

Fig. 84 A pole side view for the axial magnet shaping (represented by black dash line) comparing to the arc shape magnet with 87% circumferential pole coverage (represented by blue block)

However, it is also studied in [137] that these two shaping strategies have very close permanent magnet utilization factor [N.m/g]. Thus, the average torque will not gain much improvement by doing axial shaping. Besides, as the

torque ripple is low enough by controlling the magnet span, it is not necessary to increase the manufacture difficulty by changing the axial shape of the magnet.

Finally, the influence of magnetization direction is studied. Except parallel magnetization, another common way is radial magnetization, as Fig. 85 shows.

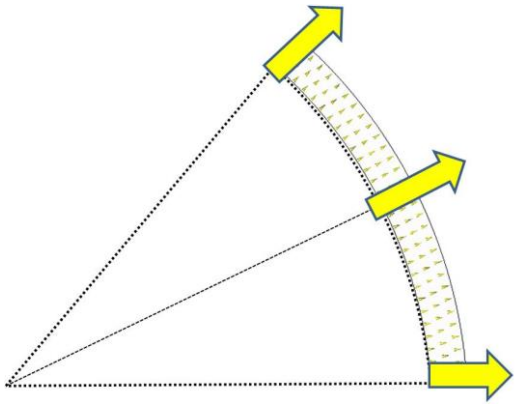

Fig. 85 Schematic of radial magnetization of a PM

For a comparative study, a SPMSM with 4p48s/f and 87% magnet coverage is chosen, every parameter is the same except the magnetization direction, which is radial here. Then the torque comparison results are shown in Fig. 85. It is found that the average torque of the machine with radial magnetization is slightly smaller than the machine with parallel magnetization. The torque ripple rate of the machine with radial magnetization is 1.1%, while the torque ripple rate of the machine with parallel magnetization is 1.8%. Therefore, the radial magnetization can reduce the torque ripple rate, meanwhile the torque is reduced. After all, both changes are negligible. Thus, in the next section, the magnetization direction is still kept parallel.

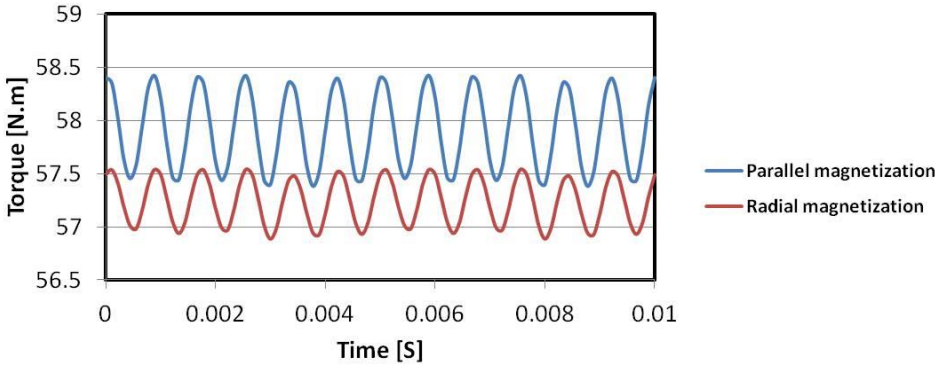

Fig. 86 Torque ripples of 4p48s/f SPMSMs with parallel magnetization and radial magnetization respectively.

2.3.2.2.4 Torque –speed and power-speed characteristics

Therefore, the optimization strategy for magnets is to simply change the magnet coverage. In the following study, the sharpness of the magnet is kept as zero, and only magnet span varies. The selected three SPMSMs are shown in Table XII. The split ratio of each machine is set as the optimized one, just as studied in Fig. 78. The performances obtained in Table XII are all with 80 ºC operation temperature.

Table XII SELECTED SPMSMS FOR TORQUE AND SPEED CURVES COMPARISON WITH THE SAME MAX TORQUE, 2D FEM SIMULATION

Machine name	Unit	4p48s/f	4p48s/s	5p60s/f
Split ratio	%	58	58	67
magnet coverage	%	87	99	67
Magnet weight	g	297	341	271
Magnet weight	P.U.	1.10	1.26	1.00
Turns/phase		16	16	15
Max torque	N.m	58	58	58
Torque ripple rate	%	1.8	3.4	2.1
Short circuit current	Arms	142	150	177

Finally, with the current and voltage limitations of the inverter system, the torque-speed curves, as well as power-speed curves of these three machines are obtained, as Fig. 87 shown. Also based on specification, a reference torque-speed curve and a power-speed curve were plotted. Ignoring the iron loss and resistance voltage drops, as their influences to the torque-speed curves and power-speed curves are very small.

It can be observed that the torque-speed characteristics of machines with 4p48s full pitch and short pitch are very similar. Ignoring the max torque margin (58 [N.m] vs 55 [N.m]), both of the curves are also very close to the reference curve. The power-speed characteristic of 4p48s/f is very close to the reference curve. However, the max power of 4p48s/s exceeds the reference power for about 8%. The machine with 5p60s full pitch has the highest margin for the torque-speed characteristic. However, it also indicates the power of 5p60s/f machine is too large, which exceeds the reference power about 26%. This is due to the lower turns/phase of 5p60s/f compared to the other two machines with 4 pole pairs.

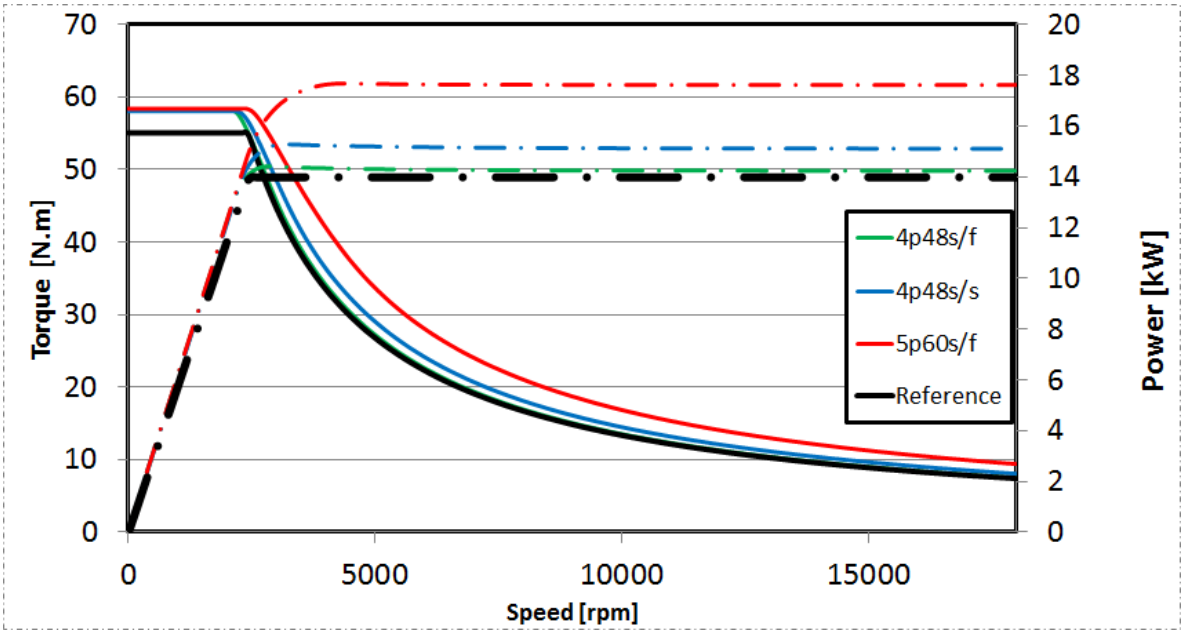

Fig. 87 Torque-speed and power-speed curves of three SPMSMs and the reference machine, with 2D simulation results

It is also necessary to validate Eq. 87, in which the power is derived by short circuit current $\bar{\imath}_{cc}$.

$$P_{me} = 2V_{DC}\bar{\imath}_{cc} \qquad \text{Eq. 87}$$

The comparison between the real power from Fig. 87. and the calculated power from Eq. 87 is shown in Table XIII. The difference means the percentage difference of calculated power over real power. Negative sign means compared to real power, the calculated power is reduced. Therefore, it is found that by using Eq. 87, the power tends to be slightly smaller than the real power. However, the differences are very small, within 5%. Thus, Eq. 87 is proved to be valid. To tune the target of short circuit current, which was 146 Arms, all the machines should rather have I_{cc} which is around 150 Arms.

Table XIII COMPARISON BETWEEEN REAL POWER AND CALCULATED POWER BY Eq. 87

Machine name	**Unit**	**4p48s/f**	**4p48s/s**	**5p60s/f**
Real power	kW	14.2	15.1	17.6
Calculated power by eq.85	kW	13.6	14.4	17.0
Difference	%	-4.2	-4.6	-3.3

Next, in order to gain further accuracy, 3D FEM models are built based on 2D models. Because for a 3D FEM model, some leakage flux which does not exist in 2D model, can be taken into account. For instance, the leakage flux from the end region of the machine can be simulated in 3D model, as Fig. 88 shows. Then, two machines 4p48s/f and 5p60s/f were validated with 3D models, as shown in Fig. 88. Since the structure of 4p48s/s is very similar to 4p48s/f, it is not necessary to repeat building the 3D model for 4p48s/s.

Details of the3D model settings, such as mesh or symmetry can be found in Appendix 2.4.

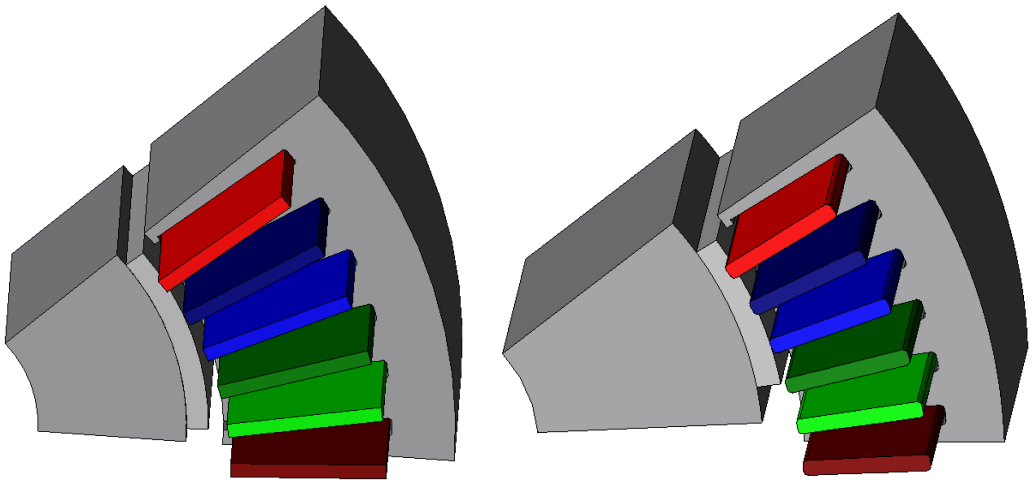

Fig. 88 3D FEM model: 4p48s/f (left), 5p60s/f (right)

The operation conditions are full load at base speed (2400 rpm) and dual three phase short circuit at top speed. The full load operation condition is shown in Fig. 89. It can be observed that in the end region, there are leakage flux from the magnet and armature field, which are supposed to reduce the load.

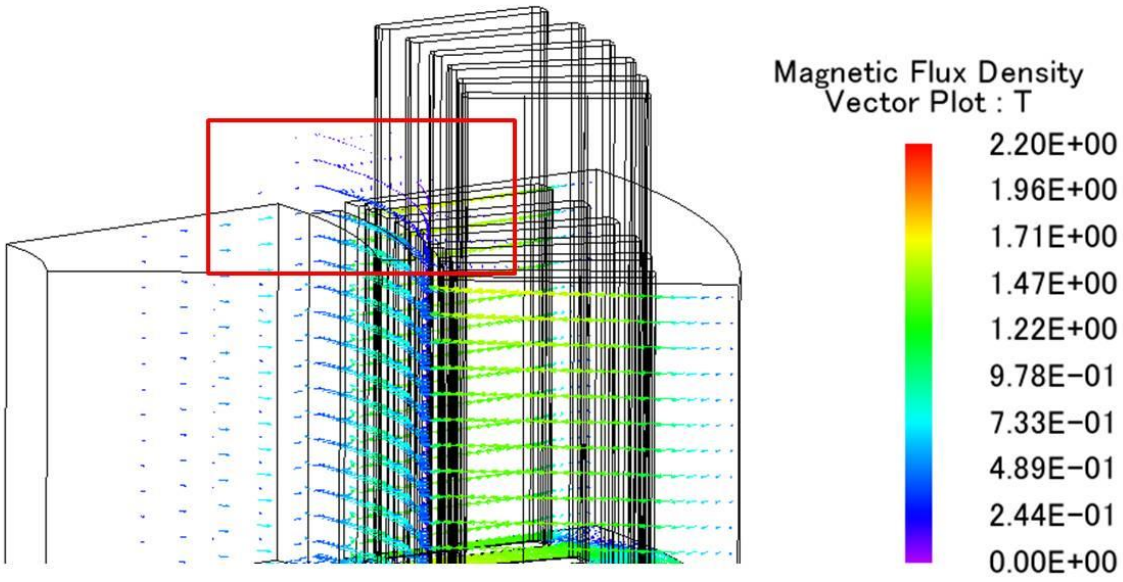

Fig. 89 Leakage flux of a 3D model (5p60s/f) during the full load, base speed operation, from the view of the machine end region.

After calculations, the comparison of results between 2D and 3D models are shown in Table XIV. The difference means the percentage difference of 3D model results over 2D model results. Negative means the reduction of the value of 3D model, vice versa for the positive sign.

Table XIV TORQUE AND SHORT CIRCUIT COMPARISONS BETWEEN 2D AND 3D RESULTS @ 80 °C

E-machine type	Torque [N.m]			Torque ripple rate (%)			Icc [Arms]		
	2D	3D	Difference	2D	3D	Difference	2D	3D	Difference
4p48s/f	58	55.8	-4%	1.8	1.9	+5%	142	124	-13%
5p60s/f	58	56.8	-2%	2.1	2.4	+14%	177	156	-12%

It is found that for all 3D models, torque and short circuit current are reduced. Particularly for short circuit currents, the reductions are more than 10%, which is significant. The reduction of short circuit current also results in the reduction of the power. Thus, compared to the I_{cc} target which is 150 Arms, it is found that for machine 4p48/f, I_{cc} becomes too small. For machine 5p60s/f, I_{cc} is still a bit large. For machine 4p48s/s, the short circuit current will be 130 Arms which is still smaller than the target, if the I_{cc} reduction is kept 13%. For torque ripple rate, 3D models tend to gain larger results than 2D model, but the changes are not considerable. Therefore, machine 5p60s/f is the most ideal design in terms of the torque and power performances.

2.3.2.2.5 Demagnetization study

With the fixed design of the last section, it is necessary to make sure that the PMs are not demagnetized. There are many operation scenarios that may cause the demagnetization, such as deep FW operation, transient states with high demagnetized currents, as well as serious high temperature ambience. In order to examine machines under extreme situation, the PMs of the machines have to overcome the demagnetized field with double times dual three phase short circuit currents at high temperature 150℃. The reason of using 2 I_{cc} is that during short circuit transient state, the amplitude of the instant current may jump to 2 times. High temperature can lead to the decrease of magnet

coercivity. Besides, when the machine is continuously running for a long time, the rotor temperature can be quite high as well. 150℃ is the maximum allowed rotor temperature. Thus, with the scenarios set up, demagnetization studies can be carried out.

Fig. 90 shows the demagnetization curves of the NdFeB magnet used in the FEM model. The magnet is still parallel magnetized. Both BH curves with 80 ℃ and 150 ℃ are plotted. The knee point of each curve is pointed out. If the loading line of the machine exceeds the knee point, irreversible demagnetization will happen.

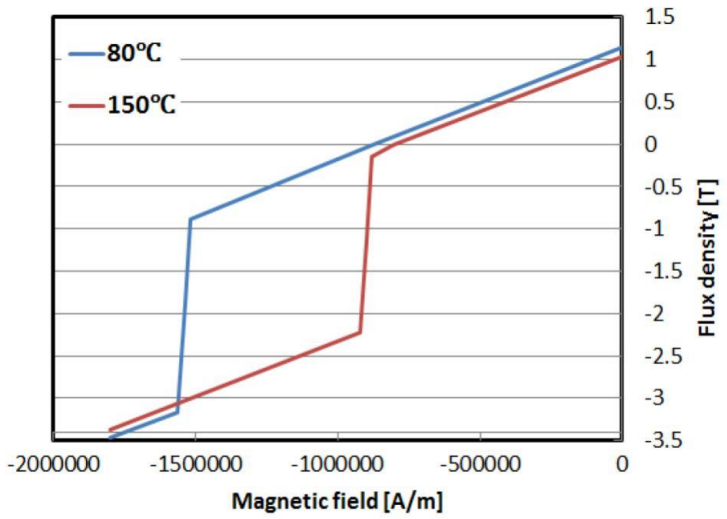

Fig. 90 Demagnetization curves of magnet N41TS at 80 °C and 150°C respectively

The short circuit currents under both 80°C and 150°C were obtained from FEM simulations. Then sinusoidal currents with double times short circuit current amplitude and current angle $\gamma_d = 180^o$ were applied to each model. The amplitude of these currents are shown in Table XV. After each current value, there is an alphabet that denotes the corresponding case. These alphabets will be used in Fig. 91 to represent each case.

Table XV DEMAGNETIZATION CURRENTS ($2*I_{CC}$) OF EACH E-MACHINE AT 80 °C AND 150°C RESPECTIVELY

E-machine type	Demagnetization currents [A_{peak}]	
	80°C	150°C
4p48s/f	402 (a)	366 (b)
4p48s/s	426 (c)	386 (d)
5p60s/f	500 (e)	456 (f)

Finally, the demagnetization state of each case can be observed and measured by the magnetic field strength *H* [A/m] on each magnet. These are shown in Fig. 91. The absolute values as well as the vector plots of *H* are illustrated. From the vector plot it is found that for all cases, most of demagnetization field are exactly anti-parallel to the magnet (except the small part of the field around the edge of the magnet). This means if the magnet is parallel magnetized, the demagnetization field is aligned with the easy axis of the magnet. In this case, the absolute value of *H* represents the easy axis value. If the absolute value of *H* is larger than the absolute value of the knee point of each *BH* curve, the magnet will be irreversibly demagnetized. Irreversible magnetization should always be avoided for the sake of safety.

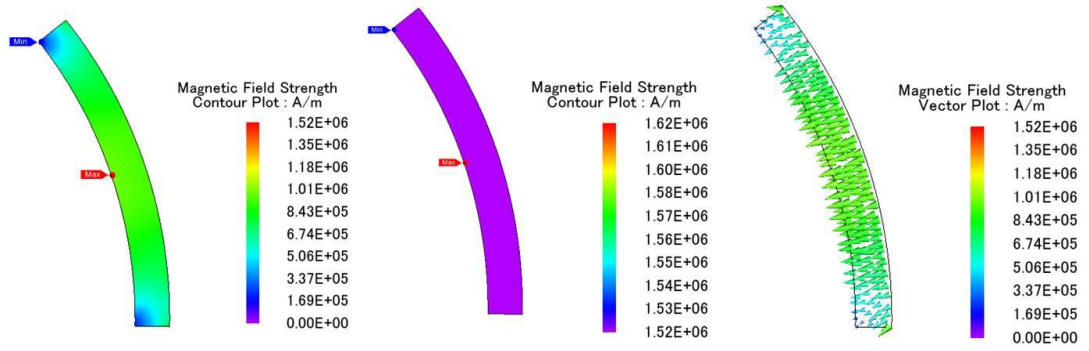
Min
Max
Magnetic Field Strength
Contour Plot : A/m
1.52E+06
1.35E+06
1.18E+06
1.01E+06
8.43E+05
6.74E+05
5.06E+05
3.37E+05
1.69E+05
0.00E+00
Min
Max
Magnetic Field Strength
Contour Plot : A/m
1.62E+06
1.61E+06
1.60E+06
1.58E+06
1.57E+06
1.56E+06
1.55E+06
1.54E+06
1.53E+06
1.52E+06
Magnetic Field Strength
Vector Plot : A/m
1.52E+06
1.35E+06
1.18E+06
1.01E+06
8.43E+05
6.74E+05
5.06E+05
3.37E+05
1.69E+05
0.00E+00

(a)

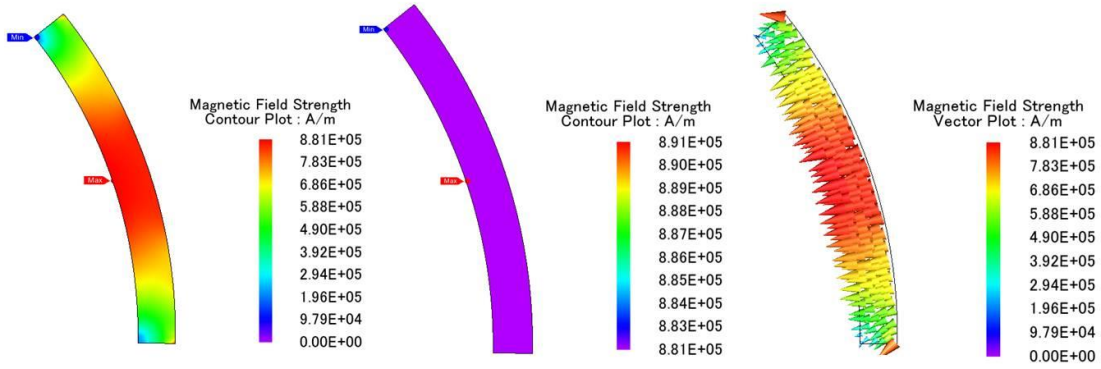
Min
Max
Magnetic Field Strength
Contour Plot : A/m
8.81E+05
7.83E+05
6.86E+05
5.88E+05
4.90E+05
3.92E+05
2.94E+05
1.96E+05
9.79E+04
0.00E+00
Min
Max
Magnetic Field Strength
Contour Plot : A/m
8.91E+05
8.90E+05
8.89E+05
8.88E+05
8.87E+05
8.86E+05
8.85E+05
8.84E+05
8.83E+05
8.81E+05
Magnetic Field Strength
Vector Plot : A/m
8.81E+05
7.83E+05
6.86E+05
5.88E+05
4.90E+05
3.92E+05
2.94E+05
1.96E+05
9.79E+04
0.00E+00

(b)

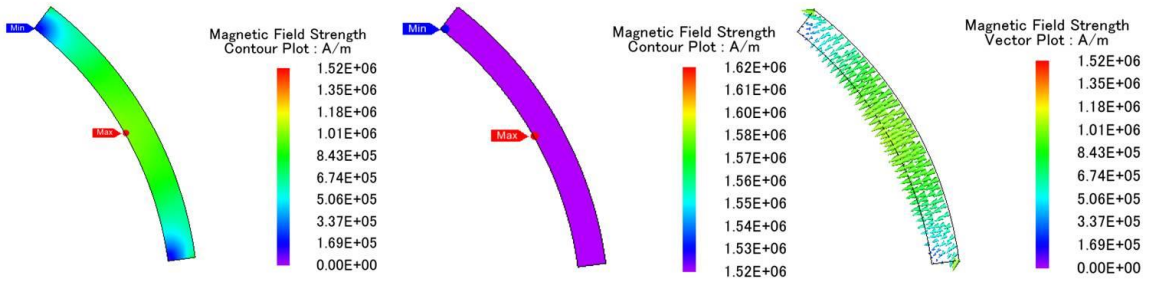
Min
Max
Magnetic Field Strength
Contour Plot : A/m
1.52E+06
1.35E+06
1.18E+06
1.01E+06
8.43E+05
6.74E+05
5.06E+05
3.37E+05
1.69E+05
0.00E+00
Min
Max
Magnetic Field Strength
Contour Plot : A/m
1.62E+06
1.61E+06
1.60E+06
1.58E+06
1.57E+06
1.56E+06
1.55E+06
1.54E+06
1.53E+06
1.52E+06
Magnetic Field Strength
Vector Plot : A/m
1.52E+06
1.35E+06
1.18E+06
1.01E+06
8.43E+05
6.74E+05
5.06E+05
3.37E+05
1.69E+05
0.00E+00

(c)

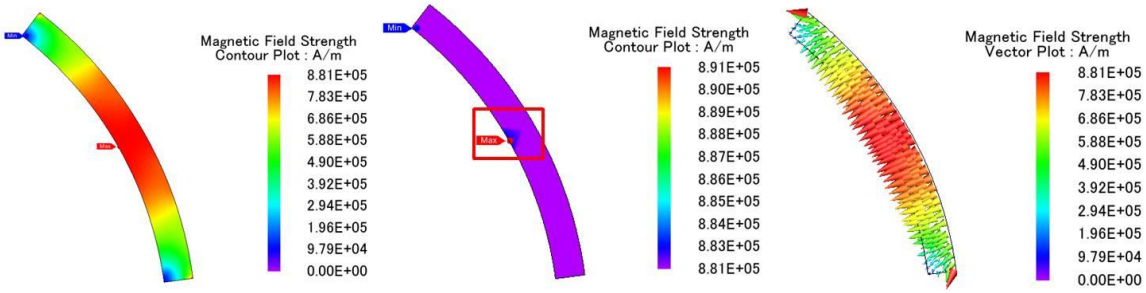
Min
Max
Magnetic Field Strength
Contour Plot : A/m
8.81E+05
7.83E+05
6.86E+05
5.88E+05
4.90E+05
3.92E+05
2.94E+05
1.96E+05
9.79E+04
0.00E+00
Min
Max
Magnetic Field Strength
Contour Plot : A/m
8.91E+05
8.90E+05
8.89E+05
8.88E+05
8.87E+05
8.86E+05
8.85E+05
8.84E+05
8.83E+05
8.81E+05
Magnetic Field Strength
Vector Plot : A/m
8.81E+05
7.83E+05
6.86E+05
5.88E+05
4.90E+05
3.92E+05
2.94E+05
1.96E+05
9.79E+04
0.00E+00

(d)

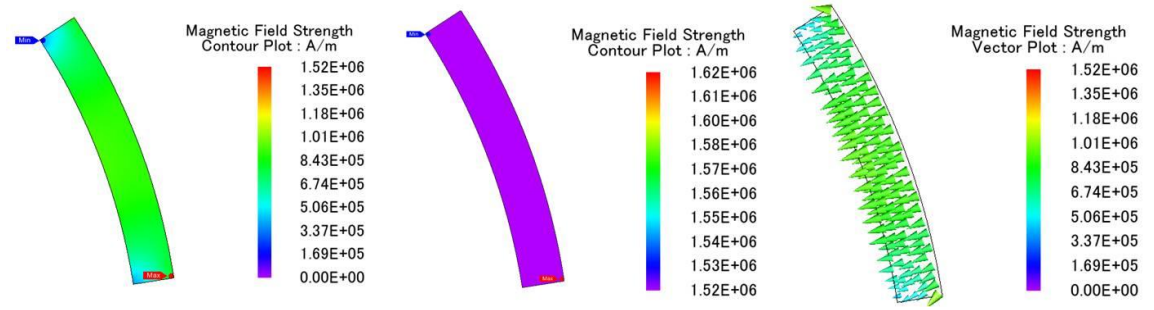

(e)

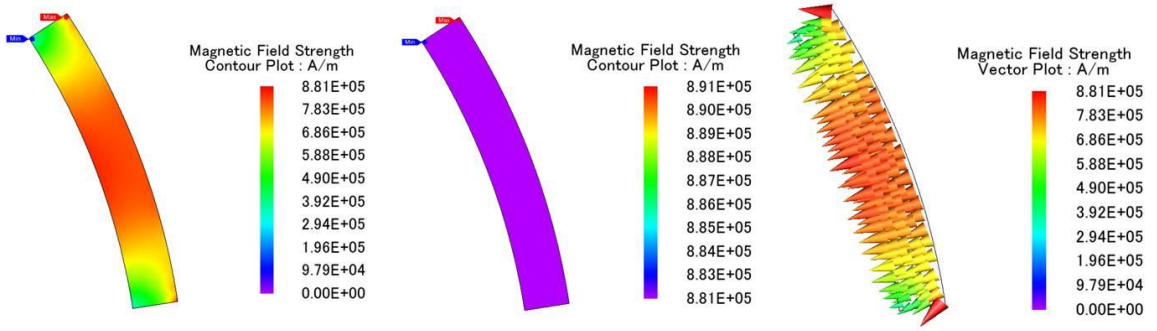

(f)

Fig. 91 The magnetic field strengths H [A/m] of six cases from **Table XV** with different scales and plot methods. Every figure illustrates H with the scale from 0 to the corresponding knee point H (left); H with scale larger than the corresponding knee point H (middle); and H of vector plot with the scale from 0 to the corresponding knee point H (right).

From Fig. 91 (d), it is found that machine 4p48s/s at 150 °C has a small part of irreversible demagnetization in the middle of the magnet, which is highlighted by a red box. The area of the demagnetization occupied around 2% of the whole magnet. Nevertheless, for other cases, no irreversible demagnetization is found. However, it can be observed that for cases with 150 °C, the magnetic field strength is really approaching the limit of irreversible demagnetization.

It is also interesting to take a look of the magnet with radial magnetization. Machine 4p48s/f at 150°C is taken as an example. The short circuit current obtained from a 2D simulation is I_{cc}=182 A_{peak}, and the implemented current amplitude is 2* I_{cc} =364 A_{peak}. Then the demagnetization results are shown in Fig. 92.

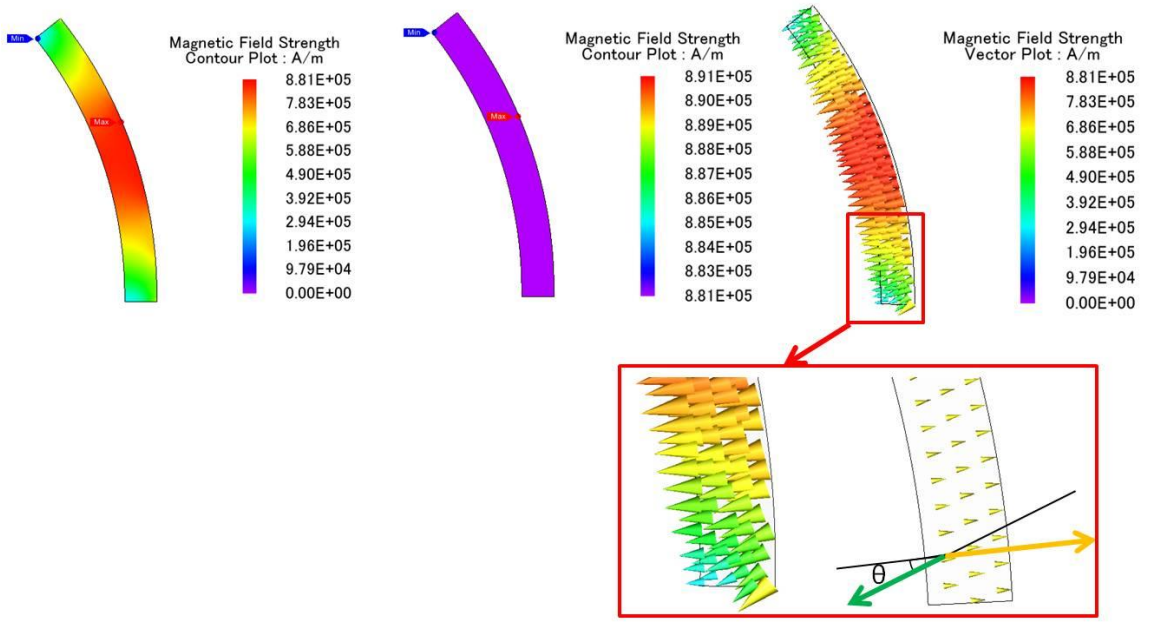

Fig. 92 Absolute demagnetization strength H(A/m) of radial magnetization 4p48s/f, and demag field direction analysis

From the vector plot it can be observed that the demagnetization field is similar to the former cases, which is anti-parallel. Then a problem is appeared – since the magnet is magnetized in radial, there must be some incline angle between demagnetization field and magnetization direction. The incline angle is also illustrated in Fig. 92 as θ, where the green arrow indicates demagnetization field direction; the yellow arrow indicates magnetization direction. For parallel magnetization, $\theta=0$ for most of the magnet area. However, for radial magnetization, $\theta \neq 0$, although at most of the areas, θ are small. Moreover, generally the closer to the magnet edges, the larger θ. While near the middle of the magnet, θ is almost zero.

From [140], the authors had studied the similar problem of inclined demagnetization through experiment. They conclude that under the same demagnetizing field strength, the magnet became harder to demagnetize when incline angle θ increases. Physical explanations about this phenomenon can be found in [139]. Therefore, radial magnetization becomes an advantage against demagnetization, as θ increases, while the demagnetization field strength is kept the same with parallel magnetization.

Therefore, through the study of demagnetization, it is found that all the three machines have good anti-demagnetization capability. Even for machine 4p48s/s, this irreversible demagnetization might be still acceptable, depending on the industry standard. However, the margins of the demagnetization may not sufficient, once the current or temperature further increases. Also if a magnet with weak coercivity is used, such as a recycled magnet, the demagnetization may not be acceptable.

2.3.2.2.6 Efficiency map

As introduced in Chapter 1, regarding the CO_2 emission, fuel saving and recharge mileage of (H)EVs, the efficiency of the e-machine is very important. Moreover, the operation points for an e-machine in (H)EV are widely distributed in a quite random way. Thus, it is not sufficient to inspect only few operation points, such as the common nominal speed, no speed and top speed. The entire efficiency map of the e-machine is necessary to be depicted. Thus, this section focuses on efficiency map.

In order to plot the efficiency map, the losses of every operation points need to be derived. These losses include copper loss, iron losses and mechanical losses. Copper loss simply applies Joule's Law, regardless of the skin

effect and proximity effect of the coil due to AC. In addition, temperature influence to the copper resistivity needs to be taken into account. The mechanical losses only take into account friction loss of bearing. Windage loss is neglected in this study, as there is no fan attached to the rotor. In addition, the windage loss in between the airgap is very small, due to the small size of the rotor, as well as the smooth surface of the rotor. An example of the mechanical loss is shown in Fig. 93. It is found that the mechanical loss does not change with the torque.

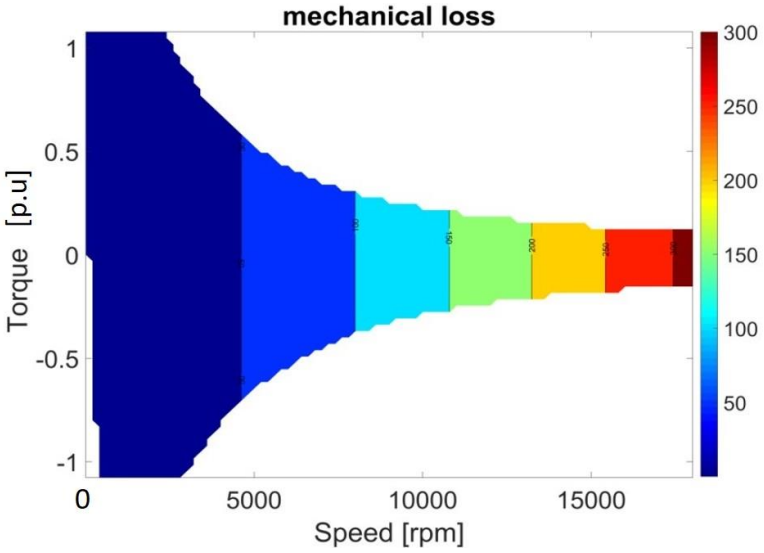

Fig. 93 Mechanical losses with the variations of speed and torque.

For the efficiency map, iron losses were calculated by modified Steinmetz Equation, as Eq. 11 shown. The reason of choosing modified SE is that the flux density variation in the stator core of e-machine is not perfectly sinusoidal. An example is shown in Fig. 94. The absolute value, radial value and tangential value of a flux density waveform at the corner of the stator slot are presented. Obviously the flux waveform is far from sinusoidal.

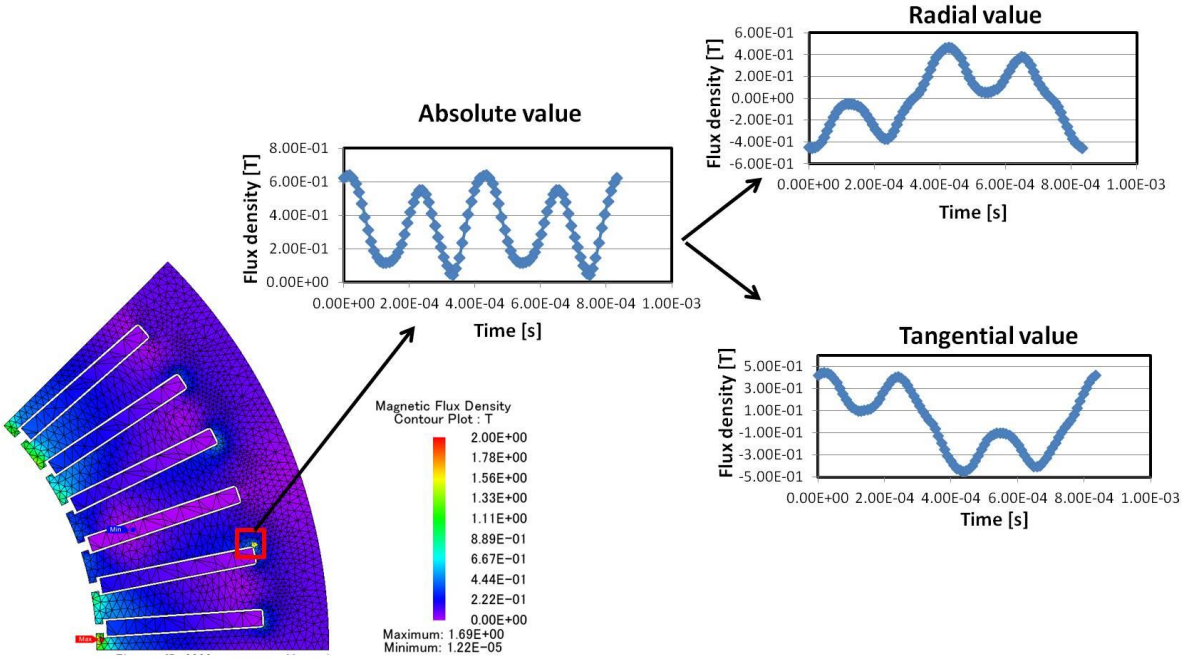

Fig. 94 A local flux density variation of the machine 4p48s/f with top speed operation (deep FW), 2D simulation by JMAG

Thus by applying Eq. 11, the iron losses are separated into hysteresis loss and eddy current loss. One more request to apply Eq. 11 is that the flux waveform has to be symmetric. Therefore, the flux density has to decompose to radial and tangential components, as can be observed from Fig. 94. As for the axial component, it is assumed as zero as this is radial flux machine (2D).

Then for Eq. 11, there are three coefficients that need to be searched by curve fit-in method. The reference for the iron losses validation is the simulation result from JMAG. JMAG uses Eq. 5 with FFT of flux waveform for each element [141]. Although it has the ability to apply more advanced iron loss model, the details of the hysteresis curves of the material were missing. Thus, implementing advance iron loss model in JMAG temporary is not feasible. Besides, 2D results of flux waveforms were used for Eq. 11, as well as Eq. 5. Because the element number for 2D simulation is around 3000, while for 3D simulation the number is about 40000. Thus, 3D results are much more time and space consuming than 2D results. Besides, iron losses comparisons between 2D and 3D simulations were made. Both models are shown in Fig. 95. The settings of studies for iron losses calculation are complete the same. Then the iron losses results are shown in Table XVI.

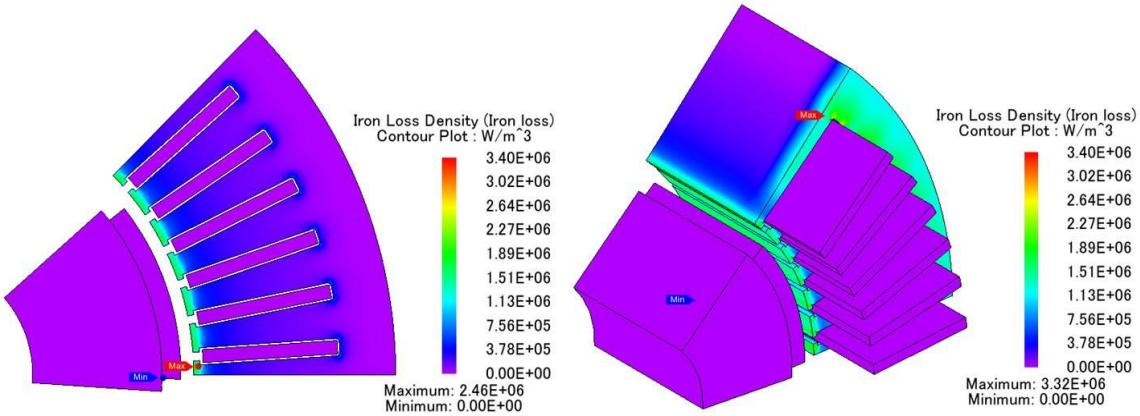

Fig. 95 Iron loss density distributions of a 2D model (left) and a 3D model (right) for the machine 4p48s/f with the operation point - top speed and i_d current only.

Table XVI. 2D AND 3D IRON LOSSES RESULTS OF THE MACHINE 4p48s/f WITH TWO OPERATION POINTS

Operation points	2D [W]			3D [W]		
	P_{hys}	P_{eddy}	P_{total}	P_{hys}	P_{eddy}	P_{total}
Base speed (2400 rpm) with max torque	33	28	61	35	32	67
Top speed with i_d (i_{cc}) current only	21	80	101	32	124	156

It is found that for the first operation point – nominal speed with max torque, the results of 3D are slightly higher than the results of 2D (+10%). However, for the second operation point – top speed operation, the results of 3D are quite larger than the results of 2D (+54%). The difference can be explained by Fig. 95. For the 3D model, there are additional iron losses in the stator end region (Green part). This is caused by the leakage flux of the machine end region, while 2D simulation ignored this part. However, compared to the active power of the operation points (14kW), iron loss is really a small part. The additional iron losses in 3D model will not cause much difference on the final efficiency. Thus, for the tradeoff between calculation effort and efficiency result accuracy, 2D models were selected.

Three operation points were selected for coefficients curve fit-in. Besides the two points in TABLE XVII, one more point – "no load base speed" was selected. The reason to choose these three points is that they represent three considerably different load conditions of an e-machine. The hysteresis losses and eddy current losses of all these

three points are derived by JMAG. The results are shown in TABLE XVII. Meanwhile the flux waveform of each mesh element (stator) was extracted for each case.

TABLE XVII HYSTERESIS LOSSES AND EDDY CURRENT LOSSES OF THREE OPERATION POINTS OF THREE E-MACHINES

Operation points	58 [N.m] with 2300 rpm			0 [N.m] with 2300 rpm			18000 rpm with i_{cc}		
	P_{hys1}	P_{eddy1}	P_{total1}	P_{hys2}	P_{eddy2}	P_{total2}	P_{hys3}	P_{eddy3}	P_{total3}
4p48s/f	33	28	61	11	8	19	21	80	101
4p48s/s	33	28	61	12	10	22	31	150	181
5p60s/f	28	26	54	12	9	21	16	88	104

From TABLE XVII it can be found that for the first two low speed operation points, all the iron loss results are pretty close. However, for high speed operation, 4p48s/s has much larger eddy current loss than the other two machines. This is due to the high back-EMF harmonics of 4p48s/s, especially 3rd and 5th components due to large magnet span.

Then, with the recorded flux waveforms, the per volume iron losses of these three operation points can be calculated by the analytical method, which is Eq. 11.

$$P_{iron\_c} = P_{hys\_c} + P_{eddy\_c} = k_H f (\frac{B_{max} - B_{min}}{2})^{\zeta} + k_E \frac{1}{T} \int_0^T (\frac{dB}{dt})^2 dt \quad \text{Eq.11}$$

For the total iron losses, the volumes of elements need to be taken into account. There is Eq. 88 to express the total iron losses,

$$P_{IRON\_c} = \int (P_{hys\_c} + P_{eddy\_c}).V_n \quad \text{Eq. 88}$$

where n is the total number of the element. As the simulation is 2D, the volume of an element is the surface of the element times the total length of the machine.

Then a curve fit-in algorithm was applied for searching the best coefficients for iron losses. An objective function was established for the algorithm, as shown in Eq. 89. The target of the curve fit-in algorithm is to minimize the objective function.

$$\text{Obj} = \sqrt{(P_{hys1\_c} - P_{hys1})^2 + (P_{Peddy1\_c} - P_{eddy1})^2 + (P_{hys2\_c} - P_{hys2})^2 + (P_{Peddy2\_c} - P_{eddy2})^2 + (P_{hys3\_c} - P_{hys3})^2 + (P_{Peddy3\_c} - P_{eddy3})^2} \quad \text{Eq. 89}$$

In the objective function, the hysteresis loss and eddy current loss are considered separately in order to gain better accuracy for the coefficients. Thus, the progress of minimize '*Obj*' by searching the best coefficients is shown in Fig. 96.

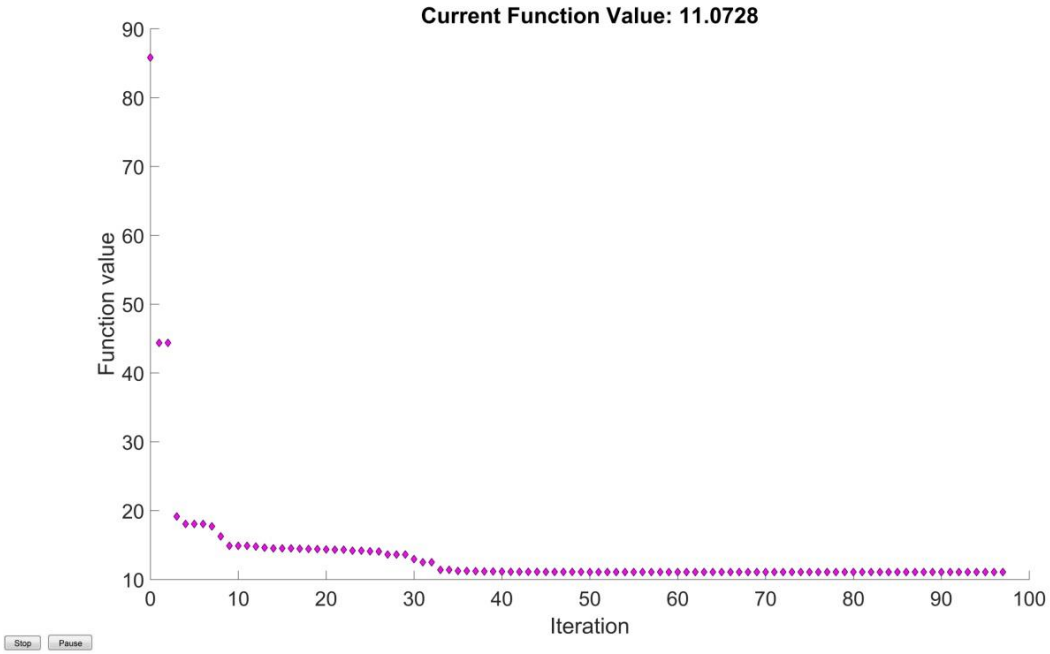

Fig. 96 The progress of minimizing the objective function by using an optimization algorithm

Afterwards, the three coefficients of iron losses were obtained. The results of the three e-machines are shown in TABLE XVIII.

TABLE XVIII IRON LOSSES COEFFICIENTS BY CURVE FIT-IN ALGORITHM

Operation points	Coefficient		
	k_H	ς	k_E
4p48s/f	161.66	1.53	0.01
4p48s/s	153.16	1.46	0.01
5p60s/f	159.49	1.62	0.01
Average value	158.10	1.54	0.01

As the iron material is the same for these three machines, the average value of each coefficient was used for the final calculation of total iron losses. The coefficients were also validated by losses curves of the material given by the supplier. In this case, pure sine waves were implemented. Different flux density amplitudes and frequencies were involved for iron losses derivation. The results are shown in Fig. 97.

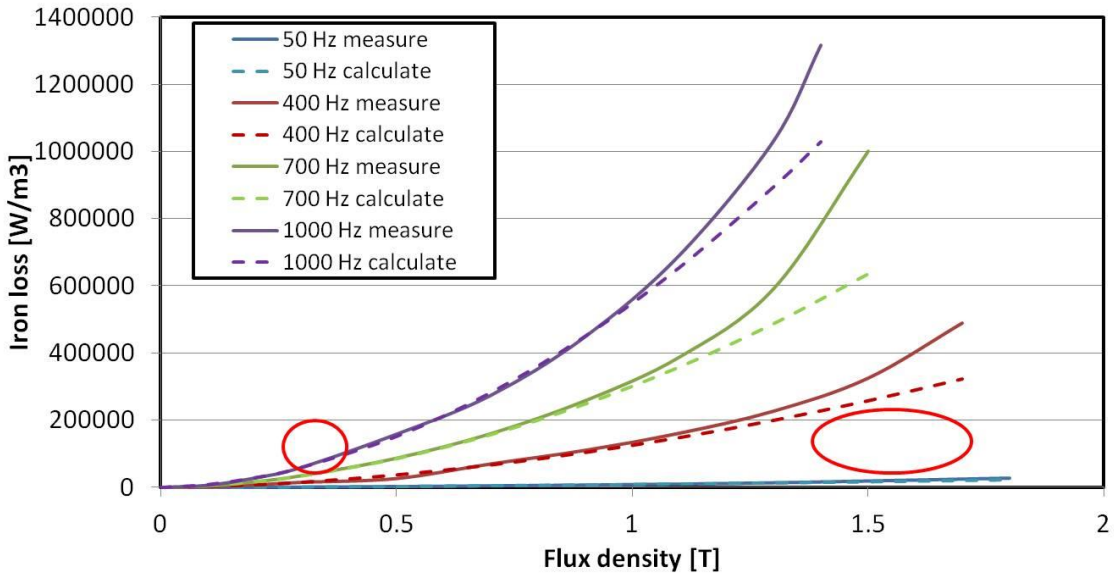

Fig. 97 Iron loss coefficients validation with the given iron loss curves of the iron lamination, red circles are the highlighted operation areas for the curves fit-in method

It is found for the regions with relatively low frequency (around 200Hz) and high frequency (around 1500 Hz) but low flux density strength, the difference between calculation and measured results is small. This is suitable for the three selected operation points. However, for high frequency and high flux density regions, the deviations are obvious. Fortunately for PM e-machines, there are very few operation points that fall in these regions.

Therefore, for an operation point, with the validated iron losses, copper loss and mechanical loss, the total loss can be derived, and then by applying Eq. 69 the efficiency can be derived. For the motor mode, the output power is the mechanical power; the input power is the sum of the mechanical power plus the total loss. For the generator mode, the input power is the mechanical power; while the output power is the difference between the mechanical power and the total loss.

The mechanical power is the multiple of torque and speed. The torque is linked with flux linkages by Eq. 48. Thus, a look up table of I_d, I_q vs dq flux linkages are established. The results were derived by FEM calculations. They can be also expressed as flux linkages maps. An example is shown in Fig. 98. Only one set of three phase system is shown. It is complete the same for the other set. Besides, every flux linkage value between two calculated flux linkages is derived by interpolation method.

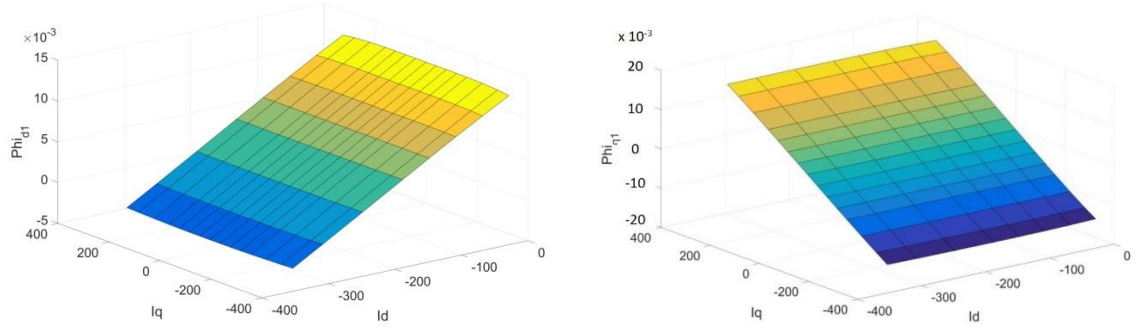

Fig. 98 d and q axis flux linkages maps with corresponding id and iq currents (only one set three phase, 4p48s/f, 80°C)

With the reference torque of an operation point, possible i_d and i_q combinations can be derived. Meanwhile d and q voltages are also linked to flux linkages by Eq. 44. The total voltage amplitude cannot exceed the voltage limit of the inverter. Thus, the possible combinations of i_d and i_q are narrowed down. Finally, the work needs to be done is to find the highest efficiency among the rest of i_d and i_q possibilities. This max efficiency searching can be done by an embedded algorithm in Matlab. An efficiency map of 4p48s/f machine is shown in Fig. 99.

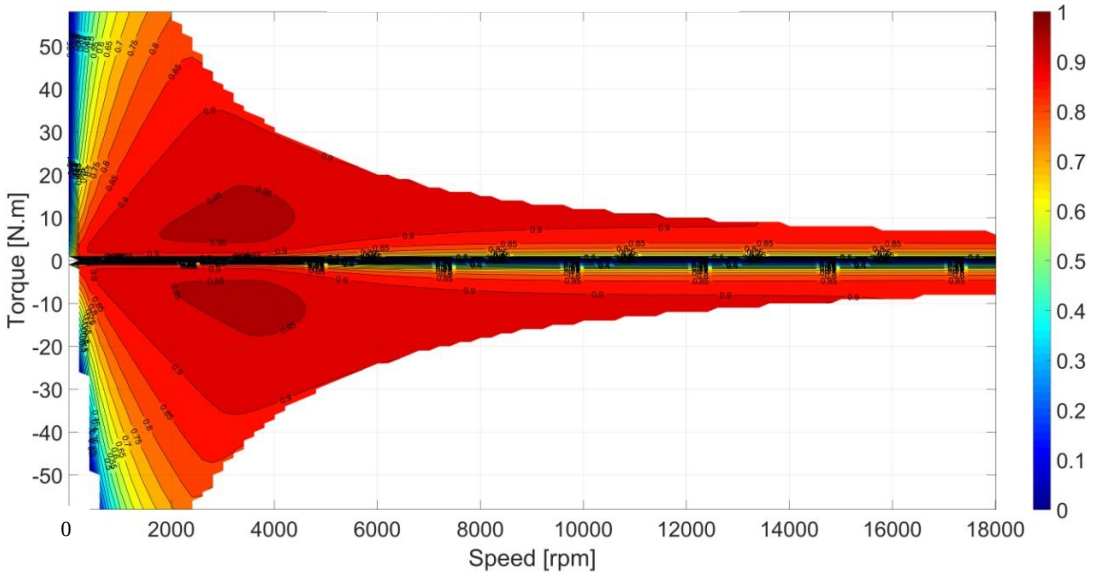

Fig. 99 Optimal efficiency map of 4p48s/f machine at 80°C

It needs to be highlighted that at very low speed, the generator mode does not work. This is due to the fact that input mechanical power is smaller than the output power at low speed. For instance, when the speed is zero and the torque is negative, the mechanical input power is zero, while the copper loss is larger than zero. Therefore, generator mode is impossible.

All the other information for achieving this efficiency map, such as currents, voltage and losses segregation is shown from Fig. 100 to Fig. 105. The mechanical loss is still the same with Fig. 93.

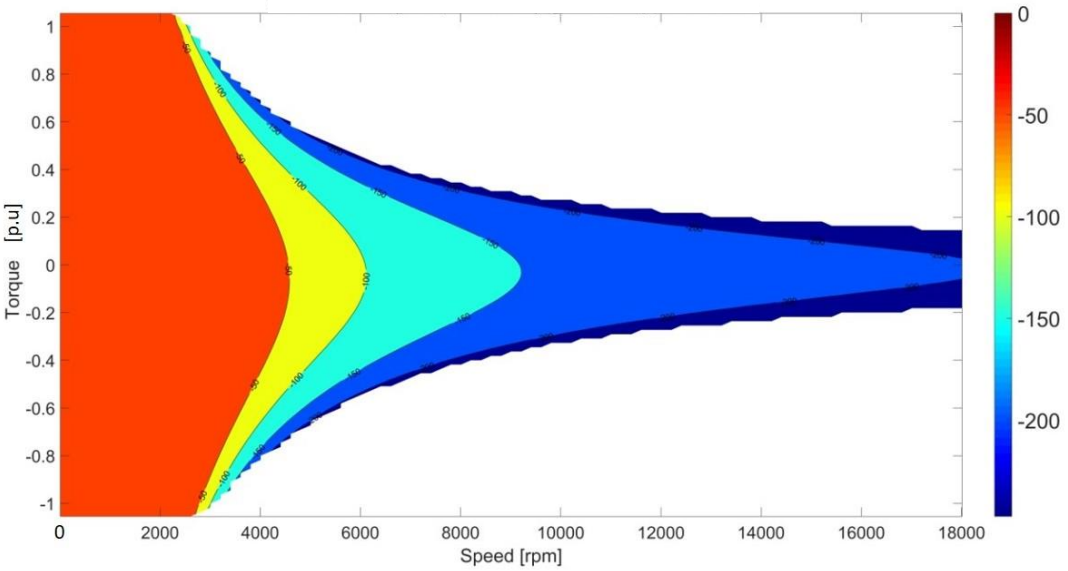

Fig. 100 Id [Apk] of 4p48s/f machine at 80°C

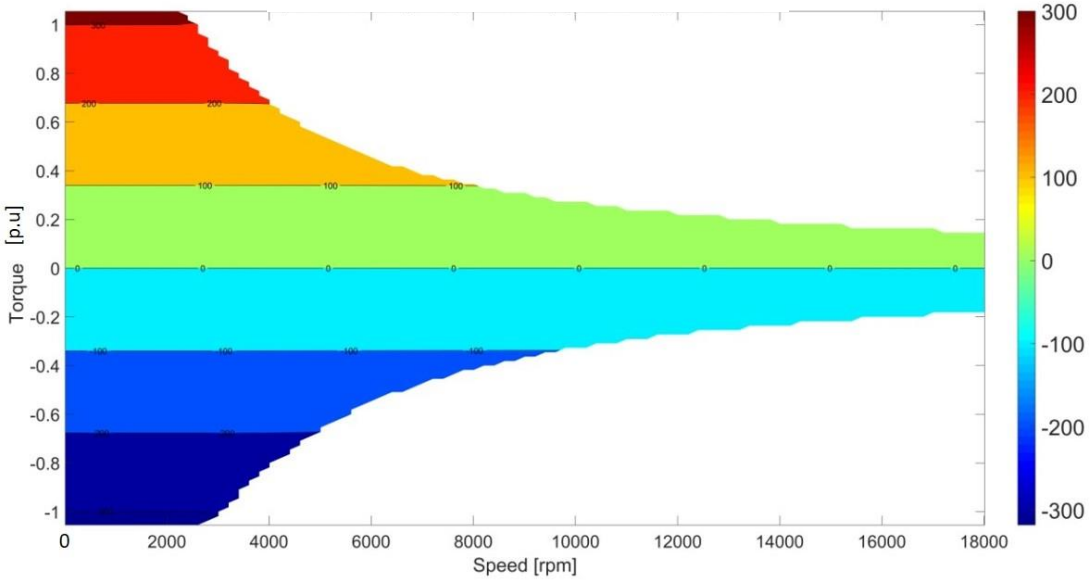

Fig. 101 Iq [Apk] of 4p48s/f machine at 80°C

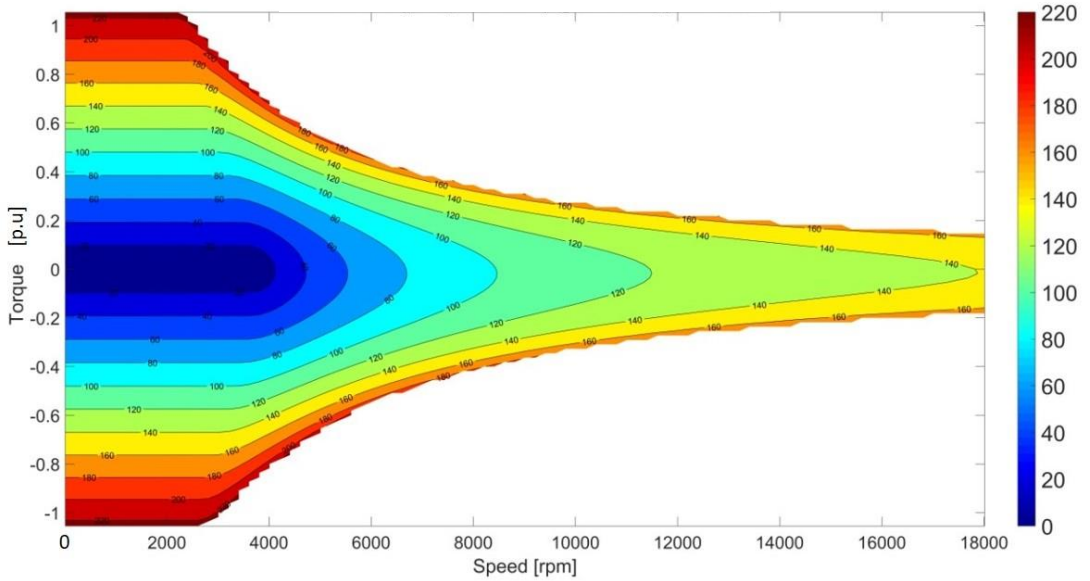

Fig. 102 Total current [Arms] of 4p48s/f machine at 80°C

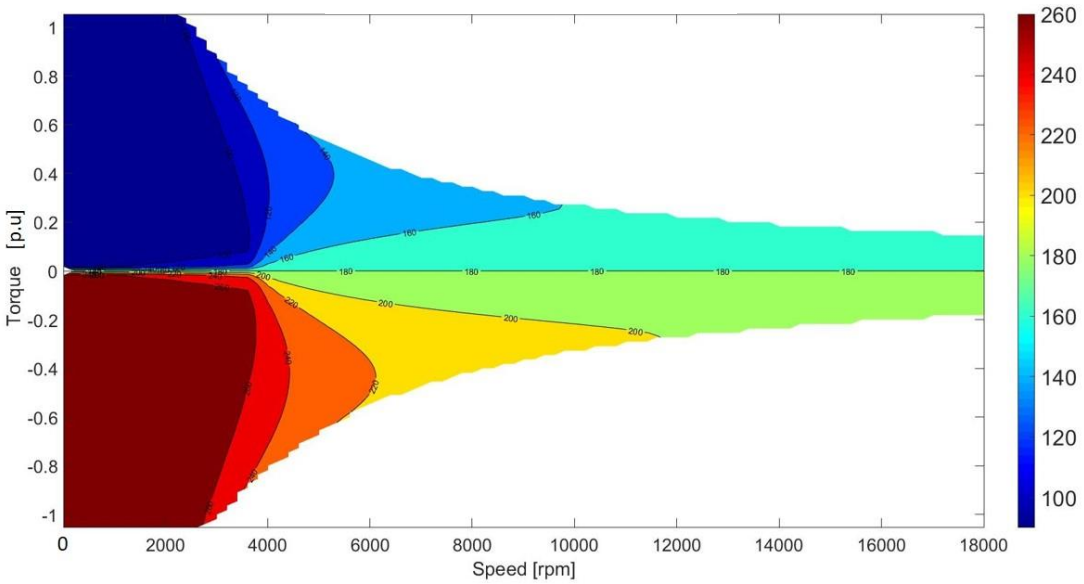

Fig. 103 Current angle [deg] of 4p48s/f machine at 80°C

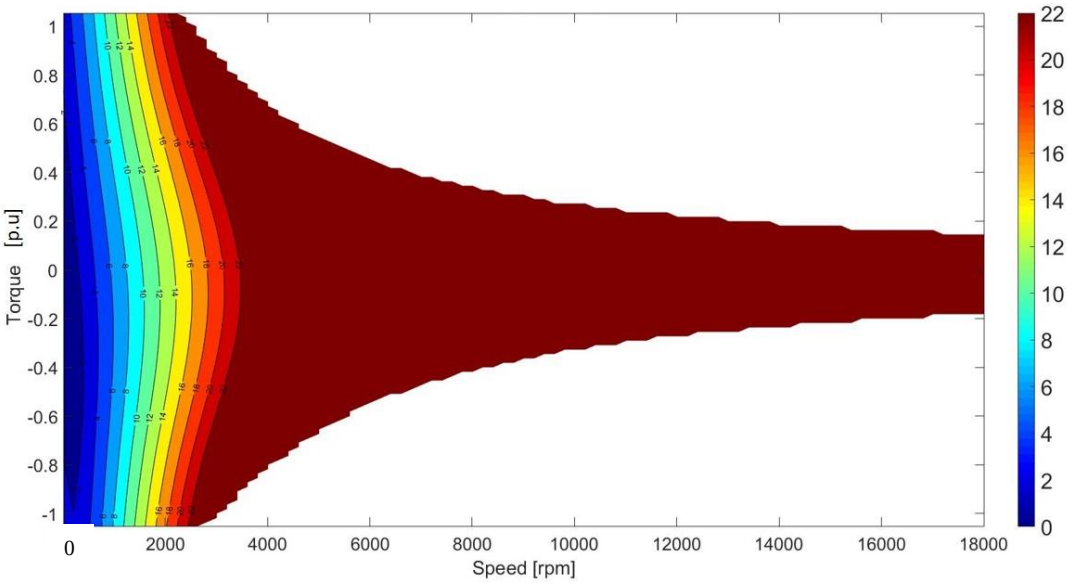

Fig. 104 Total voltage (Vac) of 4p48s/f machine at 80°C

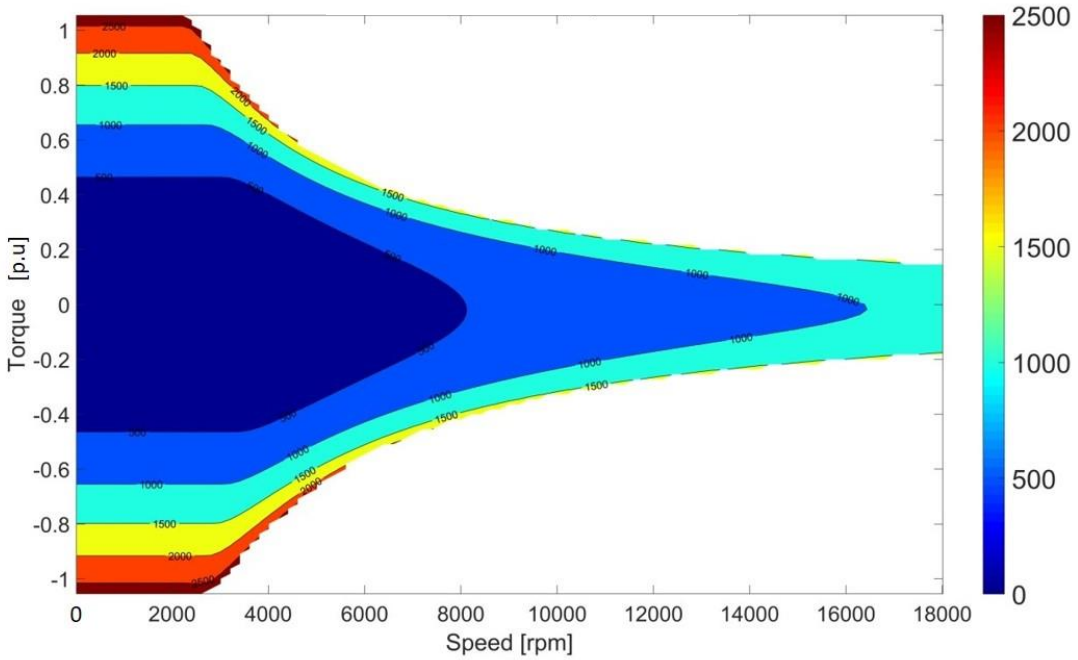

Fig. 105 Copper loss [W] of 4p48s/f machine at 80°C

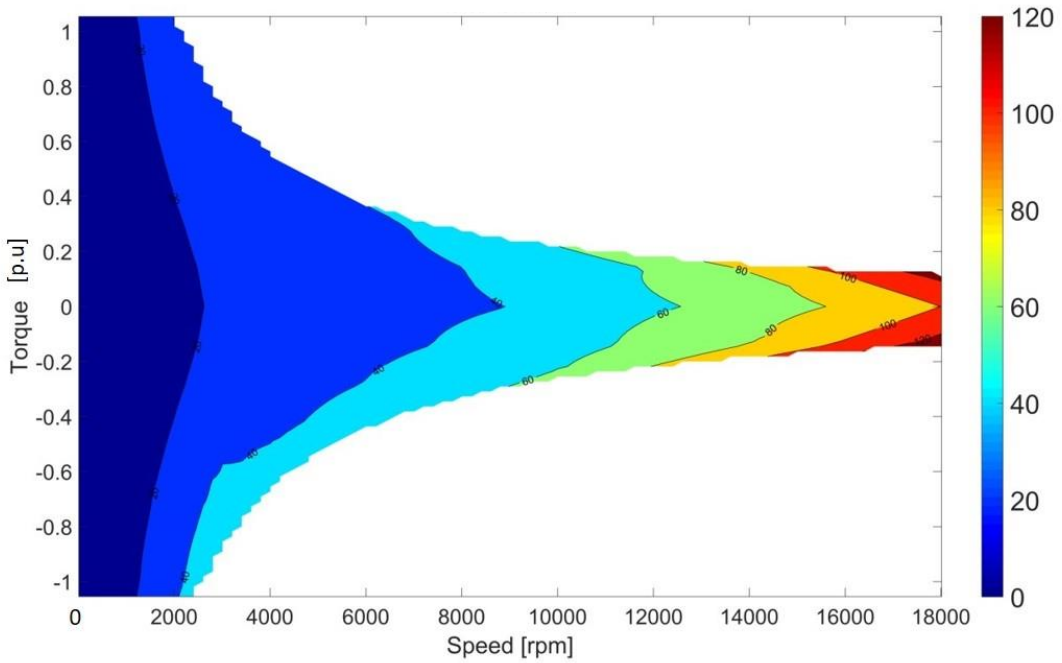

Fig. 106 Iron losses [W] of 4p48s/f machine

It is found that for a SPMSM, before the speed reaching the base speed, i_d is almost zero, as Fig. 100 shown. Thus the torque is only proportional to i_q, as Fig. 101 shown. When the speed is higher than base speed, i_d starts to increase in negative direction, due to FW operation. The FW operation can also be observed from current angle in Fig. 103 and total current amplitude in Fig. 102. The constraint of the voltage can be well observed in Fig. 104. As Fig. 105 shown, the copper loss is proportional to the total current. The copper loss reaches the maximum at the max torque. Moreover, copper losses of majority operation areas are larger than iron losses. Thus, the total loss

is dominated by copper loss. This indicates that there is a benefit to increase the pole number in order to gain the same torque with less current, hence less copper losses, once the limitation on the switch frequency of the machine drive is improved.

Following the same steps, the efficiency maps of 4p48s/s machine and 5p60s/f machine can be derived respectively. The results are shown in Fig. 107 and Fig. 108.

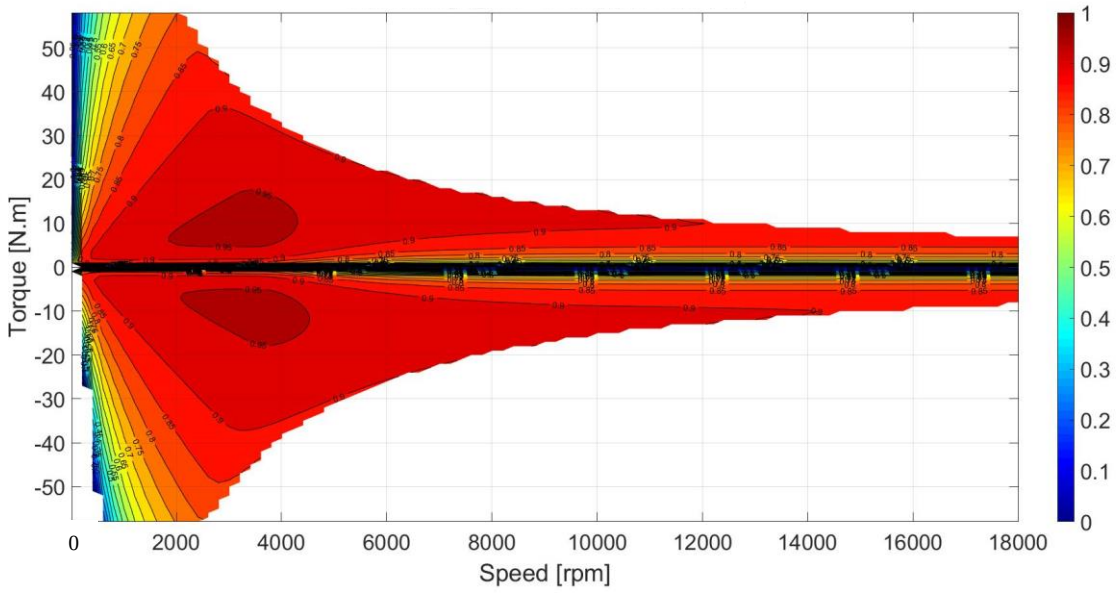

Fig. 107 Optimal efficiency map of 4p48s/s machine at 80°C

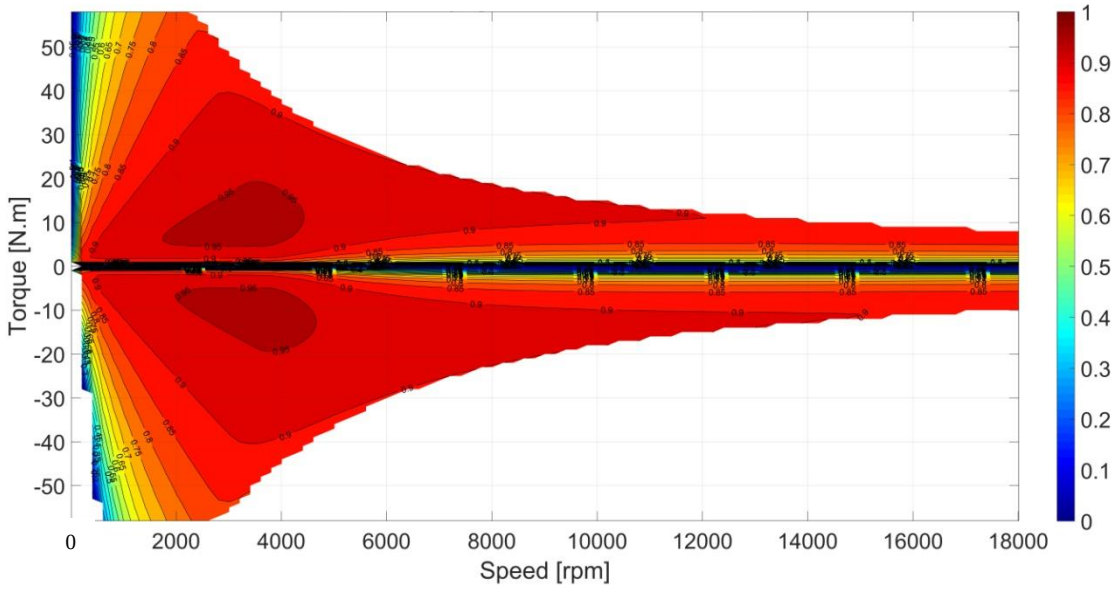

Fig. 108 Optimal efficiency map of 5p60s/f machine at 80°C

At first glance, these three e-machines have similar efficiency maps. However, subtle differences still exist. Efficiency differences maps between each two machines are made. They are shown in Fig. 109 and Fig. 110.

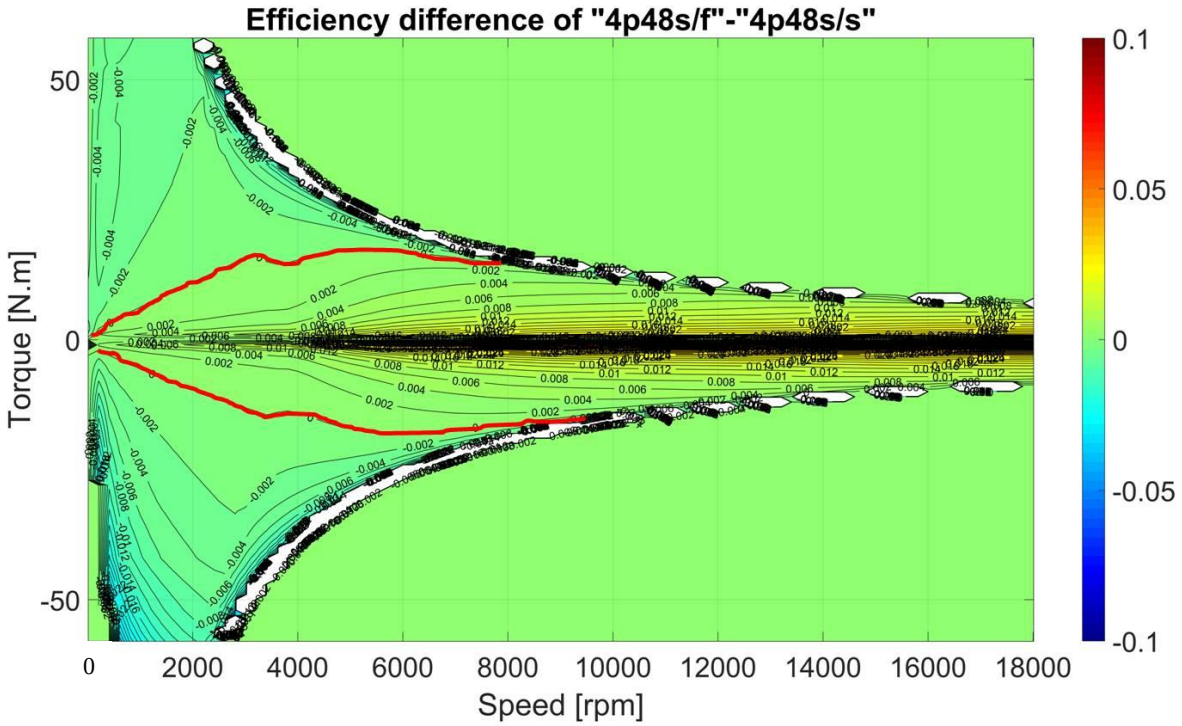

Fig. 109 Efficiency difference between 4p48s/f and 4p48s/s ('4p-4ps'); white areas are the region that 4p48s/f machine cannot achieve; the red highlight curve is the equal efficiency boundaries of these two machines.

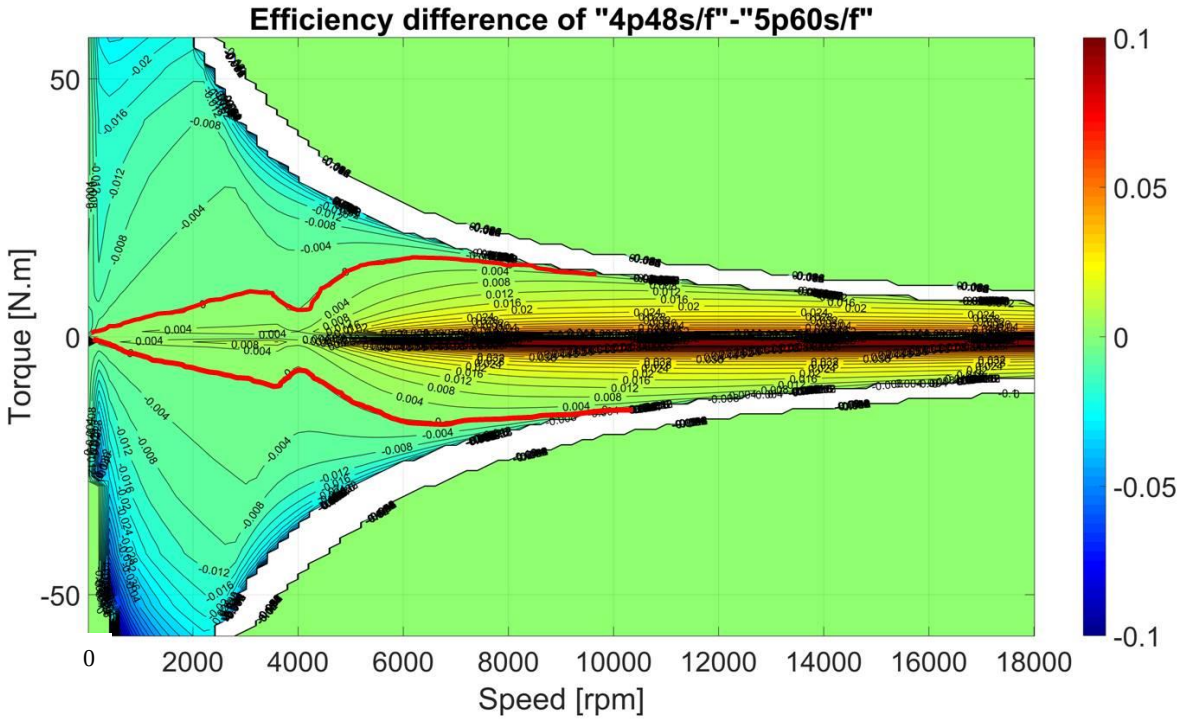

Fig. 110 Efficiency difference between 4p48s/f and 5p60s/f ('4p-5p'); white areas are the region that 4p48s/f machine cannot achieve; the red highlight curve is the equal efficiency boundaries of these two machines.

These figures show that there is no machine with superior efficiency over the whole operation area. Compared to 4p48s/f machine, both 4p58s/s and 5p60s/f machines illustrate higher efficiency for low speed high torque

operation area, but lower efficiency for high speed low torque operation area. The boundaries are highlighted in the figures. For Fig. 109, the differences are mainly in the range of -0.4% to +1.2%. However, for Fig. 110, the differences are mainly in the range of -2% to 2.4%, which is much larger than 4p48s/s. Moreover, for the area with positive differences (means the efficiency of 4p48s/f is higher than others), Fig. 109 is larger than Fig. 110, based on the areas depict by the red lines. Thus, from efficiency point of view, 5p60s is the best candidate for the application.

2.3.3.2.7 Thermal study

The last criterion for SPMSM is the thermal condition. Based on the requirements of the insulation, the coil temperature should not exceed 200 °C. For both the stator core and rotor core, the temperature should not exceed 300 °C. The highest temperature for the NdFeB magnet is suggested to be 150°C.

In this study, only stator thermal condition is analyzed. Because in SPMSM, the rotor has very little heat generated. For the stator thermal state calculation, as discussed in Section 2.2.5, a simple thermal circuit based on 2D model was implemented, as Fig. 75 shown. The thermal circuit is only based on conduction phenomenon. It is assumed that the rotor and the stator are completely thermal insulated. Finally, only steady thermal state was analyzed. Thus, no thermal capacitor is considered.

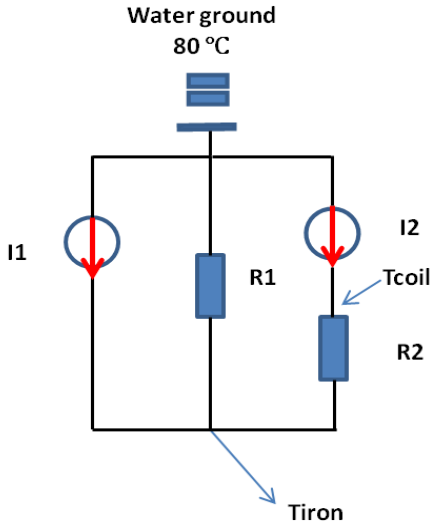

Fig. 111 Simplified stator thermal circuit

As a reminder of Section 2.2.5, In Fig. 111, I1 represents iron losses, I2 represents copper losses, R1 denotes iron-water thermal resistance, R2 denotes the copper-iron thermal resistance. Finally, there is a water jacket as the temperature ground which is constantly 80 °C. The derivation of the thermal circuit follows the principle of electric circuit. Hence, the following work is to derive these parameters.

The thermal resistances were derived by a macro thermal resistance, which was obtained from experiments. A standard machine with 166 mm stator outer diameter and 129 mm length were measured. The macro thermal resistance is 0.045 °C/W.

Then with our own machine dimensions which are 150 mm outer diameter, and 60 mm length, the macro-thermal equivalent resistance R0 can be derived. R0 was calculated by Eq. 90.

$$R0 = 0.045\ [°C/W] * (166/150)\ [mm] * (129/60)\ [mm] = 0.107[°C/W] \quad \text{Eq. 90}$$

Then the two local thermal resistances R1 and R2 were derived from equivalent resistance respectively, which is shown as Eq. 91. Eq. 91 is correlated to experimental data.

$$R1 = (1/3)\ R0 = 0.036\ [℃/W] \quad \text{Eq. 91}$$
$$R2 = (2/3)\ R0 = 0.072\ [℃/W]$$

For the stators of 4 pole pairs and 5 pole pairs, no difference the thermal resistances is assumed. Then two scenarios were analyzed for thermal conditions – the scenario of constant load operation S1, which is half of the torque (28 N.m) at base speed (2300 rpm) and the scenario of dual three phase short circuit at top speed S2. The losses of both scenarios are shown in TABLE XIX and TABLE XX respectively.

TABLE XIX LOSSES OF THREE E-MACHINES UNDER THE CONSTANT LOAD OPERATION SCENARIO

Machine type	I1 [W]	I2 (80°C) [W]	I2 (200°C) [W]
4p48s/f	61	637	942
4p48s/s	61	617	914
5p60s/f	54	600	888

TABLE XX LOSSES OF THREE E-MACHINES UNDER THE TOP SPEED SHORT CIRCUIT SCENARIO (STEADY STATE)

Machine type	I1 [W]	I2 (80°C) [W]	I2 (200°C) [W]
4p48s/f	101	923	1365
4p48s/s	181	984	1456
5p60s/f	104	1300	1923

It is noticed that the copper loss (I2) change vastly with the coil temperature. Thus, when calculating the coil temperature, it should be interlocked with the copper resistance, which is increased with the temperature. How to interlock copper loss and coil temperature can be found in Appendix part 3. As for iron losses, it is assumed they are independent to temperature changes. The calculated temperatures are shown in TABLE XXI.

TABLE XXI COIL AND IRON CORE TEMPERATURES UNDER TWO SCENARIOS

Machine Type	S1(°C)		S2(°C)	
	T_{iron}	T_{coil}	T_{iron}	T_{coil}
4p48s/f	114	178	140	252
4p48s/s	113	174	150	276
5p60s/f	112	170	192	409

In TABLE XXI, if the coil temperature limit is set as 200 °C, then in Scenario 1 all machines are within the limitation with some margins. The thermal performance from good to bad is 4p48s/f > 4p48s/s > 5p60s/f. However, all machines under Scenario 2 are in catastrophe situations, and the thermal performance from good to bad is just the opposite with Scenario 1. Especially for 5p60s/f machine, the coil temperature attains 409 °C for steady state. This thermal condition is not even acceptable for the transient state. Therefore, with a rough analysis of thermal conditions, all SPMSMs are not acceptable for SC condition.

2.3.3.2.8 Summary

From the aforementioned analyses for SPMSM designs, the advantages and disadvantages of three SPMSM candidates are shown in TABLE XXII.

TABLE XXII SUMMARY OF THE PROS AND CONS OF THREE CANDIDATES SPMSMS

Machine type	Torque	Power	Demagnetization	Efficiency	Thermal state	Magnet usage
4p48s/f	√	√	√	x	x	-
4p48s/s	√	-	-	-	x	x
5p60s/f	√	x	√	√	x	√

* √ Satisfactory; *X* Not-satisfactory; - Barely satisfactory

Some key points are highlighted:

- The efficiency of 4p48s/f machine is worse than the efficiencies of the other two machines, regarding the normal operation regions.
- The power of 4p48s/s machine is slightly higher than the requirement. Demagnetization appears at high temperature (150°C). The machine uses the most PM among all three machines.
- The power of 5p60s/f machine exceeds the requirement quite a lot, while regarding the performances of torque, efficiency and magnet usage, the machine present the best results.
- The thermal conditions of all machines are not acceptable, especially for the top speed short circuit condition.

Therefore, currently the e-machine that mostly approaching the requirements is 4p48s/f machine. However, if 5p60s/f machine can solve the fatal power and thermal problem, it will be the best candidate.

2.3.3 IPMSM comparative studies based on FEM

In order to tackle the thermal problem, meanwhile maintain the performances of the SPMSMs, it is necessary to investigate IPMSMs. As the torque generated by an IPMSM is the combination between magnet torque and reluctance torque, the needed MMF of an IPMSM can be less than the MMF of a SPMSM, with the same amount of magnets and the same torque generated. Hence, the turn number per phase of the IPMSM can be low which result in less copper loss than the SPMSM. Finally, the coil temperature rise of the IPMSM can be smaller than the SPMSM.

In this case, a new IPMSM is designed based on the 5p60s/f SPMSM. The dimension of the conductor, as well as the filling ratio is kept the same. For the IPMSM, the rotor is changed with magnets inside the rotor. There are many types of magnets arrangement for the rotor. A very popular magnets arrangement is V-shape, which is introduced in [144] and used on TOYOTA Camry HEV series. In [144], there is one layer of magnet in the rotor. For each pole, two iron bridges are remained on the rotor circumference; one iron bridge is in between the two magnets. These three iron bridges can retain the rotor unbreakable during the high speed operation (In [144], the top speed of the IPMSM is 17000 rpm). On both sides of each magnet, there are air pockets for the reduction of leakage flux. Thus, the structure of the rotor of the IPMSM is applied in this newly designed model. A cross section of one pole of this IPMSM is shown in Fig. 112.

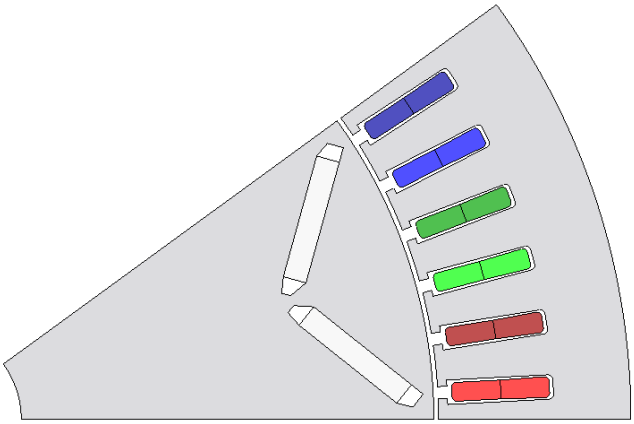

Fig. 112 The cross section of 5p60s/f IPMSM (remove winding)

The plot shown in Fig. 112 is the IPMSM after optimization. The machine is still designed for achieving the max torque of 58 N.m (2D). The power of the machine needs to be maintained the same, which can be observed by the short circuit current I_{cc}. On the premise of completing the last two goals, the torque ripple and magnet weight are supposed to be as small as possible. During the optimization, there are some constraints regarding the mechanical strength at high speed. For instance, the minimum thickness is 1mm for all three iron bridges. The aforementioned performances of the optimized IPMSM are shown in Table XXIII.

Table XXIII 3 SPMSMS AND THE IPMSM FOR TORQUE AND SPEED CURVES COMPARISON WITH THE SAME MAX TORQUE, 2D SIMULATION

Machine name	Unit	4p48s/f	4p48s/s	5p60s/f	5p60s IPM
Split ratio	%	58	58	67	73
Magnet weight	g	297	341	271	305
Turns/phase		16	16	15	10
Max torque	N.m	58	58	58	58
Torque ripple rate	%	1.8	3.4	2.1	19
Short circuit current	Arms	142	150	177	165

Table XXIII shows that the turn number per phase of the IPMSM is much smaller than SPMSMs. This was already explained by the reluctance torque theory. Thus, the turn number per slot for the IPMSM becomes two rather than three. Lower turn number per slot leads to higher optimal split ratio, results in further torque increasing. However, with larger rotor size, the demanded magnet amount is also higher. Thus, the magnet weight of the IPMSM is higher than the 5p60s/f SPMSM, while it is close to the magnet weight of the 4p48s/f SPMSM. I_{cc} of the IPMSM indicates a reasonable power level. Moreover, the I_{cc} of IPMSM is lower than the 5p60s/f SPMSM, with even lower copper resistance, the thermal state of the IPMSM can be significantly improved.

With the identical voltage and current limits, the torque speed and power speed curves of these four machines are compared in Fig. 113.

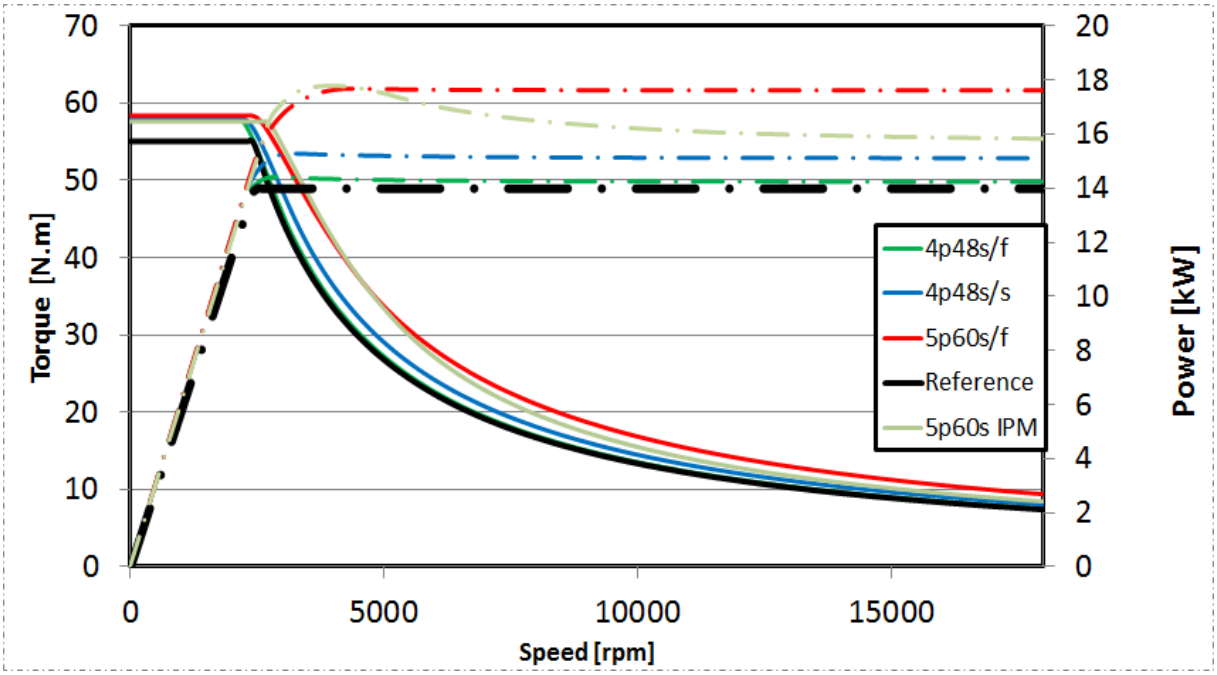

Fig. 113 Power speed and torque speed curves comparisons

It can be observed that the performances of the IPMSM are between the SPMSMs of 5p60s/f and 4p48s/s. The comparison of 2D and 3D models is made for the IPMSM. With the same 3D model setting, the results are shown in Table XXIV. It is found that the torque and short circuit current are reduced as well for the 3D model. However, this time, the I_{cc} reduction becomes mild and is only 7%. Nevertheless, the value obtained is very close to the target I_{cc} = 150 Arms. Therefore, it can be concluded that the power and torque of the 5p60s IPMSM are ideal.

Table XXIV TORQUE AND SHORT CIRCUIT COMPARISONS BETWEEN 2D AND 3D RESULTS @ 80 °C

E-machine type	Torque [N.m]			Torque ripple rate (%)			Icc [Arms]		
	2D	3D	Difference	2D	3D	Difference	2D	3D	Difference
4p48s/f	58	55.8	-4%	1.8	1.9	+5%	142	124	-13%
5p60s/f	58	56.8	-2%	2.1	2.4	+14%	177	156	-12%
5p60s IPM	58	56.1	-3%	19	21	+11%	165	153	-7%

Next step is the demagnetization study. The same two scenarios are still analyzed – 2 I_{cc} at 80°C and 150°C respectively. The magnet material and the BH curves are the same with the SPMSM. Besides, the magnet is still parallel magnetized. I_{cc} under both 80°C and 150°C were obtained from simulations. Thus, the demagnetization currents are shown in Table XXV.

Table XXV DEMAGNETIZATION CURRENTS (2*I_{CC}) OF EACH E-MACHINE AT 80 °C AND 150°C RESPECTIVELY

E-machine type	Demagnetization currents [A_{peak}]	
	80°C	150°C
5p60s IPM	467	406

The demagnetization currents were implemented in each model. The demagnetization state of the magnets still uses the magnetic field strength H [A/m] to present. The results are shown in Fig. 114. It is observed that the demagnetization state of both 80 °C and 150 °C are well beneath the safe limits. Besides, it can be told from the color of the magnets that there are much more margin than the magnets of SPMSMs. Thus, IPMSM rotor can well protect the magnets.

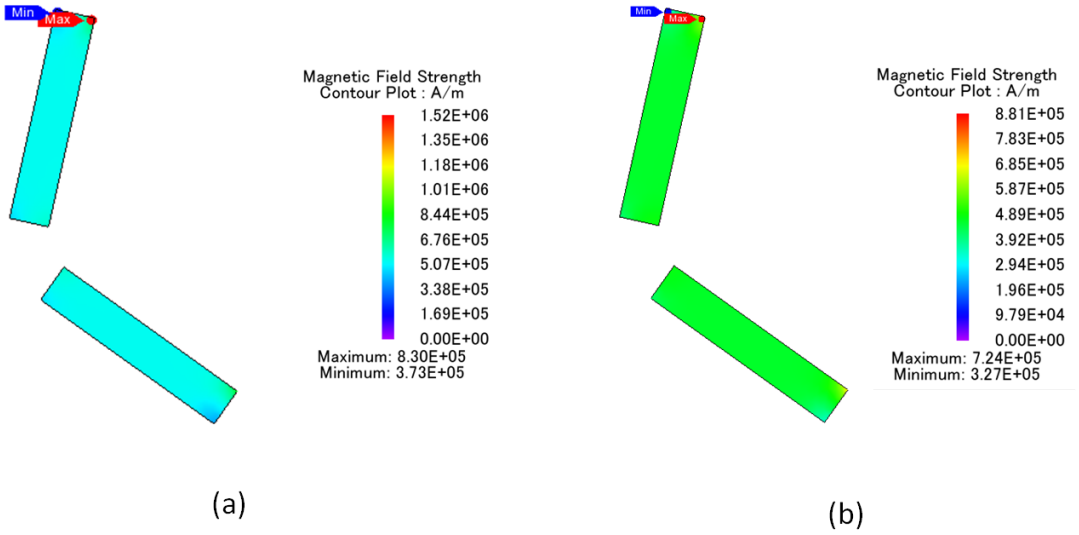

Fig. 114 The magnetic field strengths H [A/m] with the scenarios of Table. (a) 80℃, (b) 150℃. Every figure illustrates H with the scale from 0 to the corresponding knee point H.

A look up table of I_d, I_q vs one phase set of dq flux linkages is established. The results are derived by using the same FEM simulation method and interpolation method. The flux linkages maps of d,q axes are shown in Fig. 115. It can be observed that compared to the SPMSM, the flux linkages of the IPMSM are more non-linear.

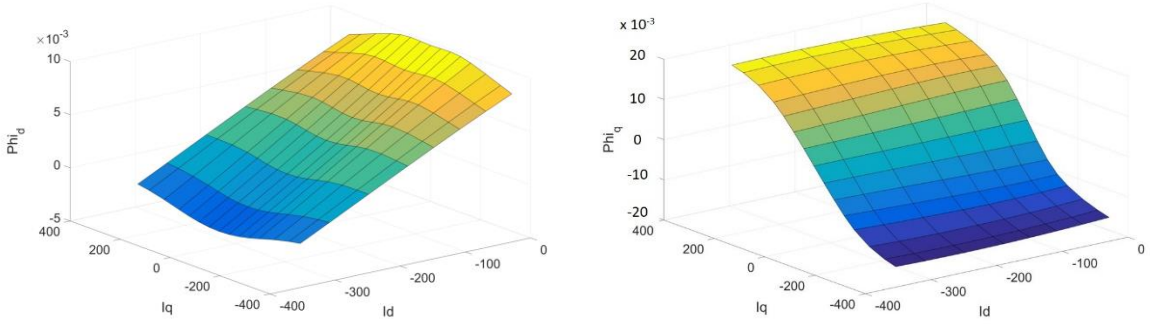

Fig. 115 Flux linkage of d-axis (left) and q-axis (right) of the 5p60s/f IPMSM

Then, with the same torque-speed envelope as shown in Fig. 113, the efficiency map of the 5p60s/f IPMSM is derived, and is shown in Fig. 116. The max efficiency searching algorithm is the same as the one used in SPMSMs. An efficiency comparison between 5p60s/f IPMSM and 4p48s/f SPMSM is shown in Fig. 117.

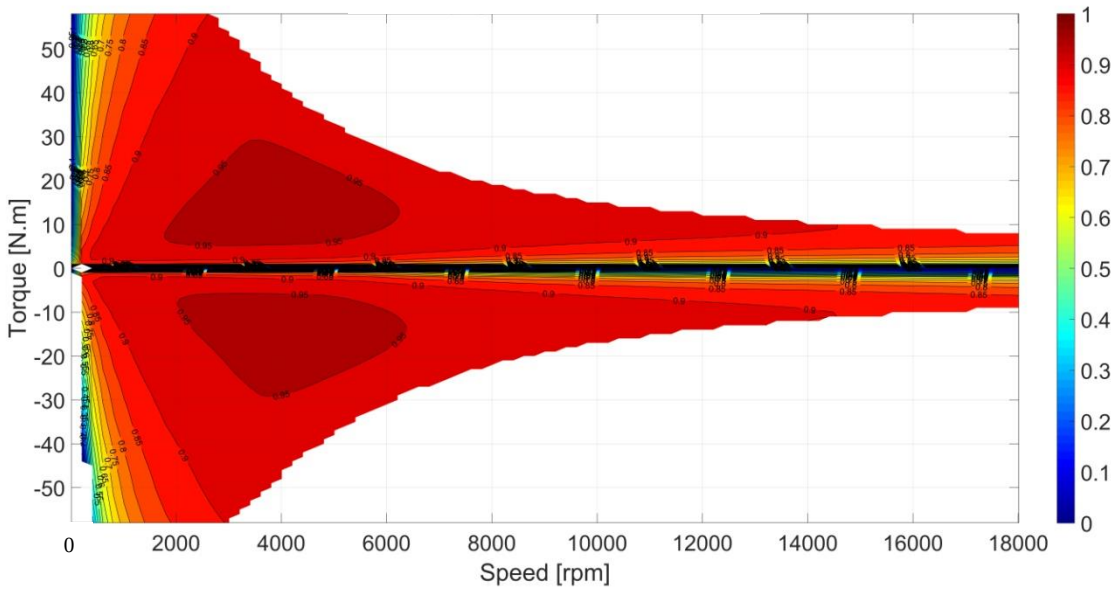

Fig. 116 Optimal efficiency map of 5p60s/f IPM at 80°C

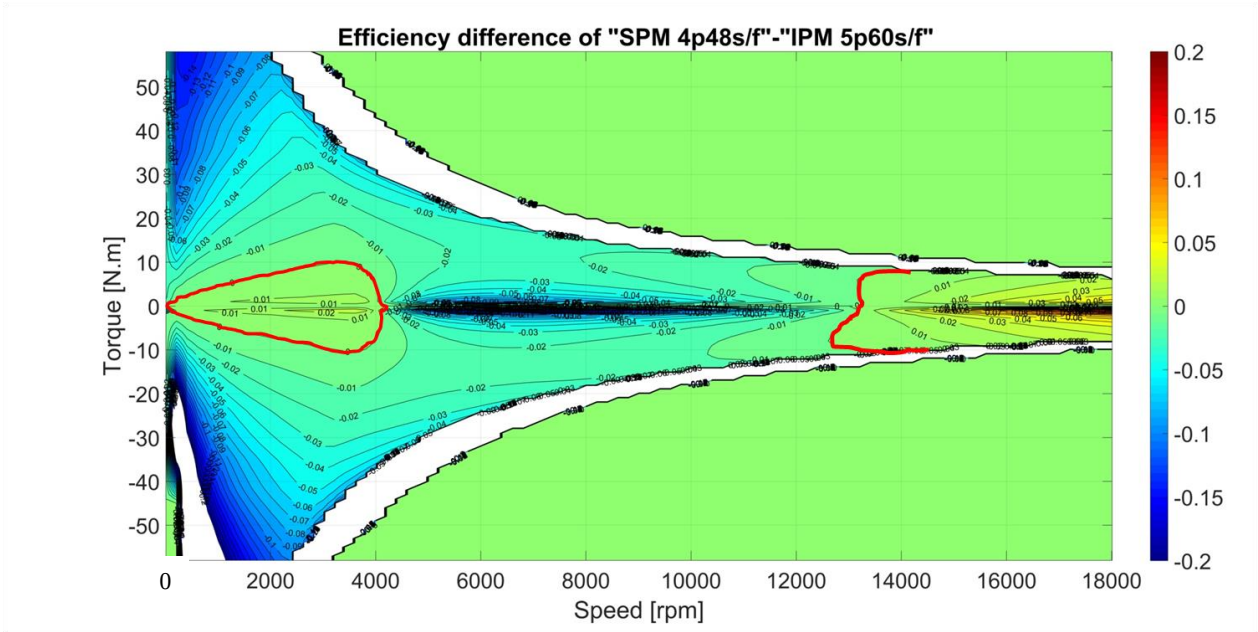

Fig. 117 Efficiency difference between 4p48s/f SPM and 5p60s/f IPM ('4p-5p'); white areas are the region that 4p48s/f SPM cannot achieve; the red highlight curve is the equal efficiency boundaries of these two machines.

From Fig. 116, it can be observed that the highest efficiency is larger than 95%. The area with 90% efficiency occupies the most operation region. Then Fig. 117 also illustrates the comparisons between the efficiency maps of IPMSM and SPMSM (4p48s/f). It can be easily observed that most of the operation area of IPMSM has higher efficiency than 4p48s/f SPMSM. Even comparing with the other 2 SPMSMs by Fig. 109 and Fig. 110, IPMSM still has huge superiority. Therefore, fuel consumption can be obviously reduced by using the IPMSM rather than SPMSMs.

Same details for the operation of the highest efficiency are shown from Fig. 118 to Fig. 124. There are several obvious operation differences between the IPMSM and SPMSMs. First, the current controls are quite different. For IPMSM, during the low speed and high torque operation, the current angle is much larger than 90°, as shown in Fig. 121. Thus, there are large amount of i_d, even when the speed is smaller than the base speed, as shown in Fig. 118. Meanwhile, i_q is not simply increased with the torque. It is also changed with the speed, particularly when the speed is getting high. Second, the change of the current operation leads to the change of the copper loss. It becomes more speed related. Nevertheless, the texture of the iron losses map is quite similar with what of SPMSMs. However, at top speed, compared to Fig. 124 and Fig. 106, the iron losses of the IPMSM go up to 800 W, against 100 W of 4p48s/f SPMSM. This is due to the higher pole number, as well as higher flux harmonics of the IPM rotor than SPM rotor. Thus, iron losses of the IPMSM cannot be ignored.

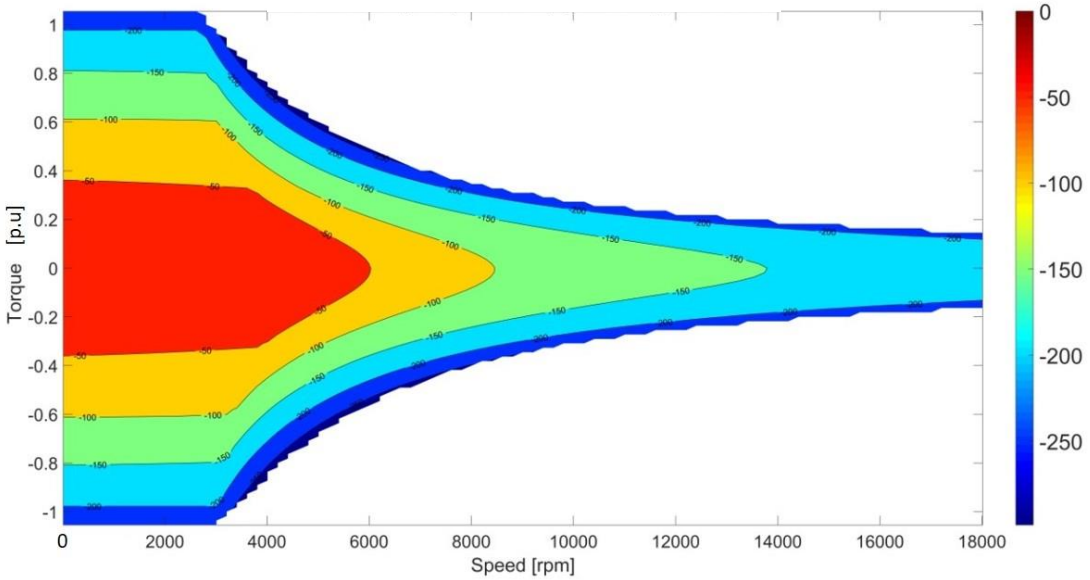

Fig. 118 Id map [Apk] of 5p60s/f IPM at 80°C

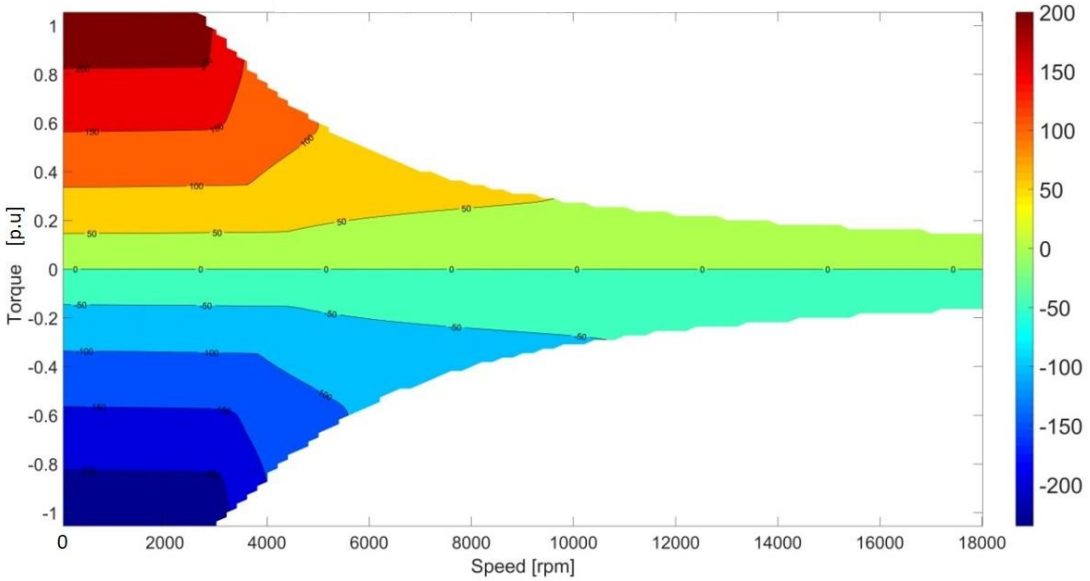

Fig. 119 Iq map [Apk] of 5p60s/f IPM at 80°C

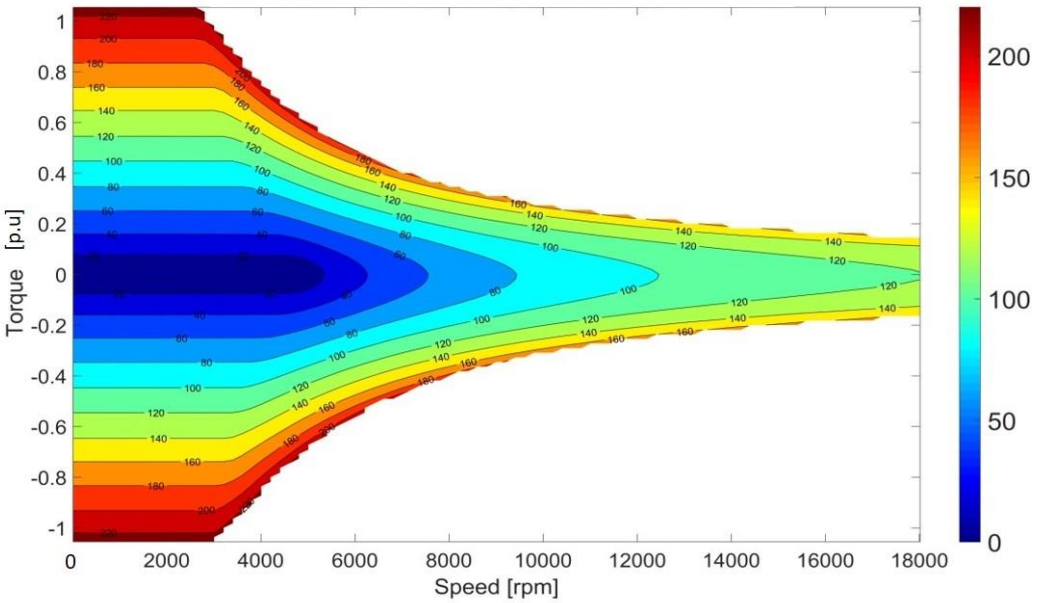

Fig. 120 Total current map [Arms] of 5p60s/f IPM at 80°C

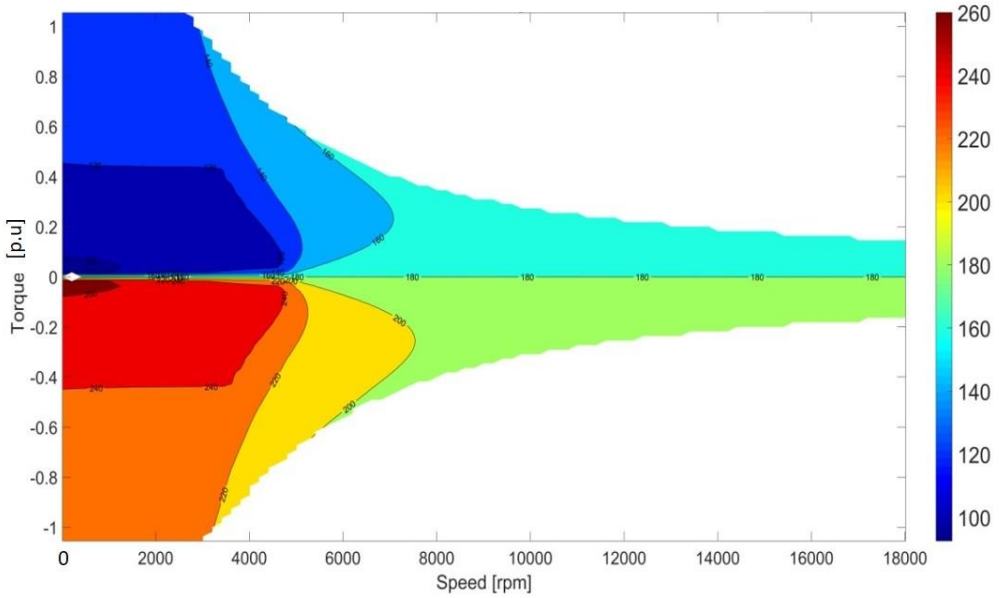

Fig. 121 Current angle [deg] map of 5p60s/f IPM at 80°C

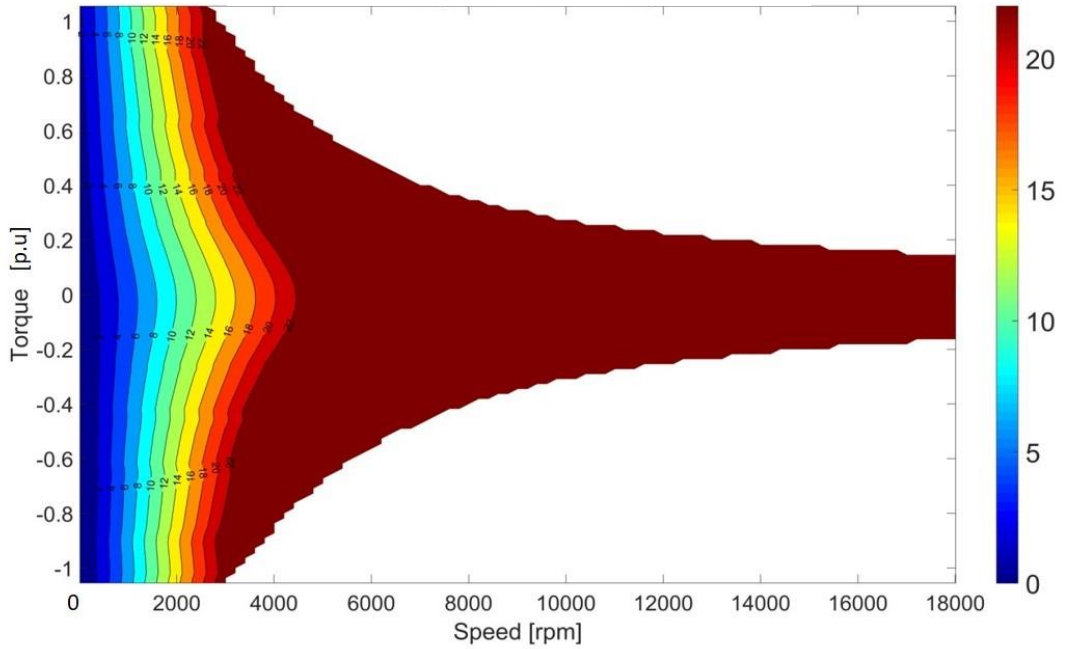

Fig. 122 Total voltage map (Vac) of 5p60s/f IPM at 80°C

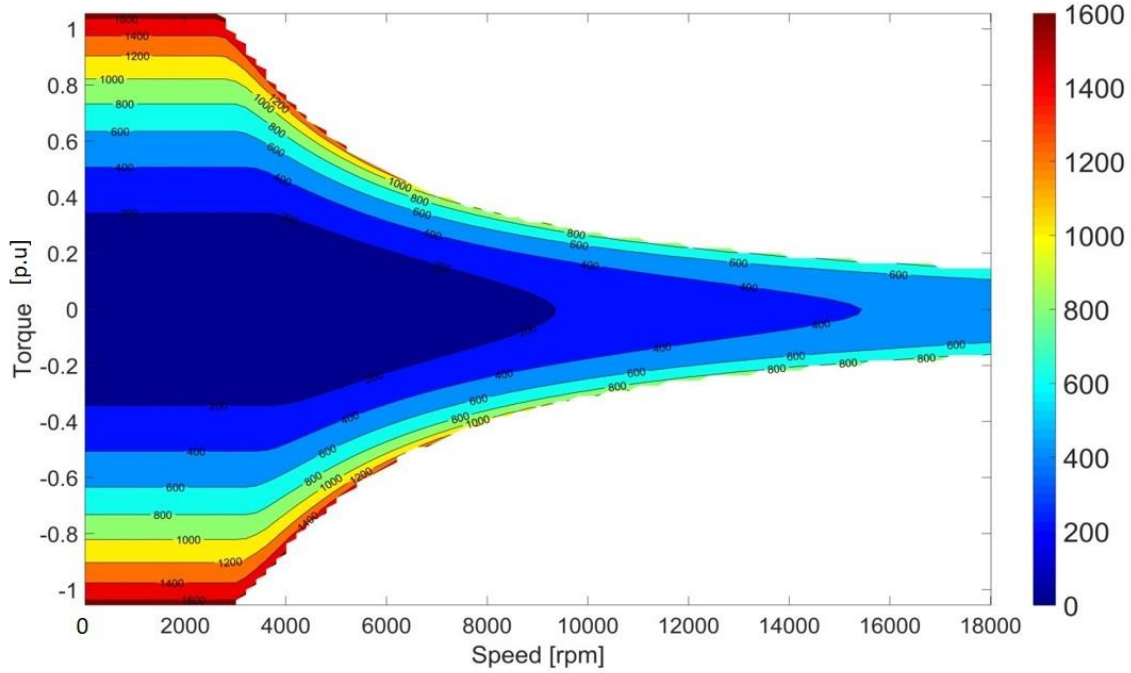

Fig. 123 Copper loss [W] of 5p60s/f IPM at 80°C

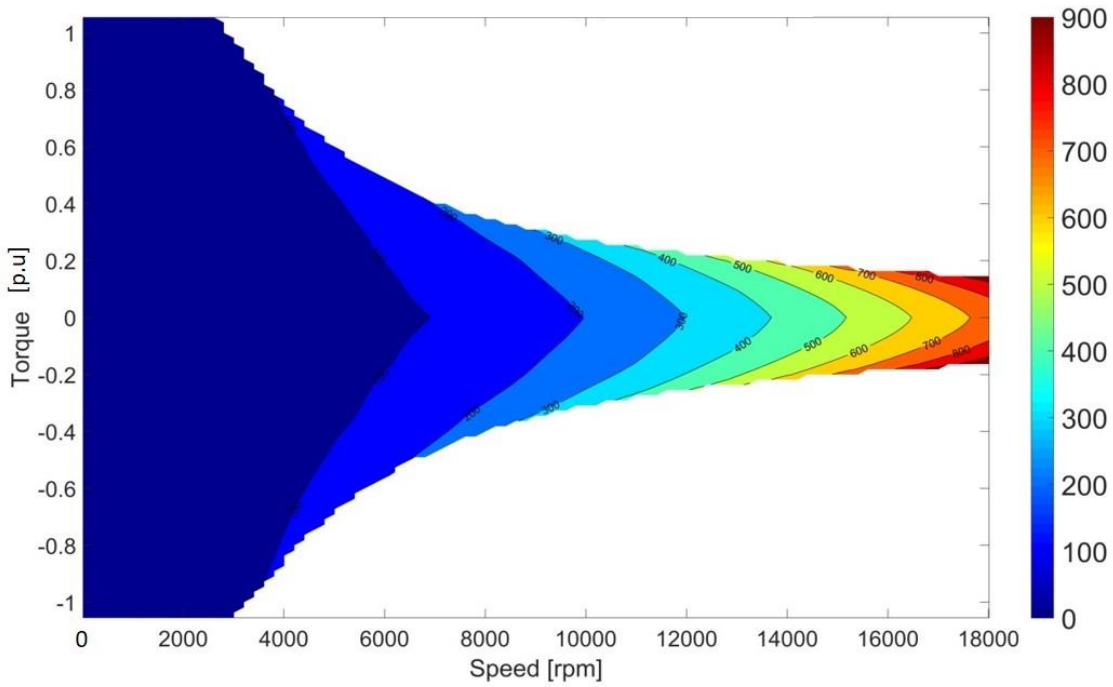

Fig. 124 Iron losses [W] of 5p60s/f IPM

With the losses, thermal states of the IPMSM can be derived, which is also the main concern of the SPMSMs. The identical thermal circuit (Fig. 111) of SPMSMs is used for the IPMSM, due to the same size of the machine. Then the inputs of losses for the constant operation scenario (S1) and the short circuit scenario (S2) are shown in TABLE XXVI and TABLE XXVII respectively.

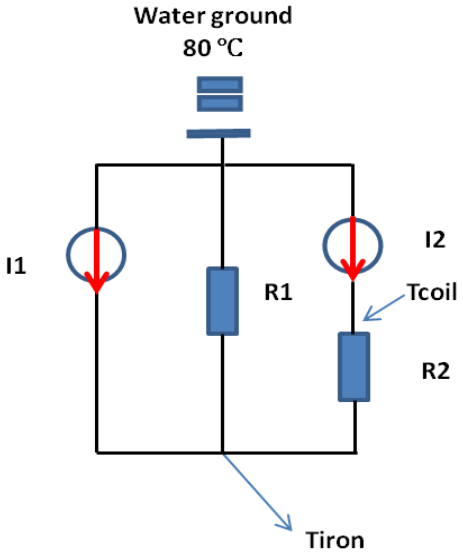

Fig.112 Simplified stator thermal circuit

TABLE XXVI LOSSES OF THREE SPMSMs AND IPMSM UNDER THE CONSTANT LOAD OPERATION SCENARIO (S1)

Machine type	I1 [W]	I2 (80°C) [W]	I2 (200°C) [W]
4p48s/f	61	637	942
4p48s/s	61	617	914
5p60s/f	54	600	888
5p60s IPM	42	406	610

TABLE XXVII LOSSES OF THREE SPMSMs AND IPMSM UNDER THE TOP SPEED SHORT CIRCUIT SCENARIO, STEADY STATE (S2)

Machine type	I1 [W]	I2 (80°C) [W]	I2 (200°C) [W]
4p48s/f	101	923	1365
4p48s/s	181	984	1456
5p60s/f	104	1300	1923
5p60s IPM	800	744	1102

Then with the losses input and the same thermal resistances, the temperatures of the iron core and the copper coil can be derived. The results of the two scenarios are shown in TABLE XXVIII. It can be found that compared to all SPMSMs, the IPMSM gains the lowest temperatures for both core and coil under every scenario. For the constant load condition, there is a large margin for the coil temperature (135 °C vs 200 °C). For the short circuit condition, the coil temperature becomes very close 200 °C. Comparing to its counterpart 5p60s/f SPMSM, there is a huge improvement for the thermal condition. However, it has to be acknowledged that the thermal state of short circuit for the IPMSM is still not completely ideal. New materials may be used for loss reduction. More accurate thermal calculation needs to be carried out in the future. For instance, convection in the airgap is better to be taken into account. Moreover, cooling method also needs to be improved to be more efficient.

TABLE XXVIII COIL AND IRON CORE TEMPERATURES UNDER TWO SCENARIOS

Machine Type	S1(°C)		S2(°C)	
	T_{iron}	T_{coil}	T_{iron}	T_{coil}
4p48s/f	114	178	140	252
4p48s/s	113	174	150	276
5p60s/f	112	170	192	409
5p60s IPM	99	135	153	241

In general, using IPMSM can greatly improve the performances. The summary of the IPMSM performances is shown in TABLE XXIX. The margins of the demagnetization and thermal conditions of the IPMSM are extended. High efficiency areas are largely increased. However, the magnet usage is not likely to be reduced, due to the compensation of the reduced MMF. More problems arise, such as increased torque ripple, high iron losses and high magnet usage. These problems might be solved by increasing the number of magnet layers, or optimizing the shape of the air pockets (currently the air pocket shape is kept the same all the time). Nevertheless, the IPMSM design still has potential to be improved. The point to have this section is to prove that the IPMSM has more superiorities than SPMSMs regarding the major performances.

Then comes back to the main topic, the problem of reusing the magnets from the IPMSM with sintered NdFeB still remain to be solved. Thus, by referring the recycling tactics in Section 2.1, a new type of NdFeB magnet material – bonded NdFeB has been used for a new IPMSM design. Moreover, a mock-up has been made for validating the calculation results.

TABLE XXIX SUMMARY OF THE PROS AND CONS OF THREE CANDIDATES SPMSMS AND THE IPMSM

Machine type	Torque	Power	Demagnetization	Efficiency	Thermal state	Magnet usage
4p48s/f	√	√	√	x	x	-
4p48s/s	√	-	-	-	x	x
5p60s/f	√	x	√	√	x	√
5p60s IPM	√	-	√	√	-	-

2.4 Conclusion

In this chapter, finite element method was introduced. Key concepts for electrical machine designs were studied, such as winding, torque, Park transformation, etc. Then the procedures to design a PMSM (mainly SPMSM) were illustrated. Several key parameters were optimized to obtain the best performances. The thermal states of the machines were simply verified. It was found that all the SPMSM designs cannot perfectly fulfill the requirements. An optimized IPMSM with 5 pole pairs 60 slots can achieve the performances without demagnetization or overheating. Thus, it can be the suitable candidate for the applications.

Chapter 3- Design of IPMSM mock-up and experiment validations

3. 1 Design of IPMSM mock-up

A new IPMSM is designed with the magnet reuse ability. The design philosophy follows the method in Section 2.1. Thus, magnets can be reused from the IPMSM. This IPMSM is aimed to manufacture a mock-up. Thus corresponding experiments can be done to validate key simulation results.

3.1.1 Structure of the IPMSM with bonded NdFeB magnets

3.1.1.1 Stator

Due to the time and resource constraints, an off-the-shelf stator was used for the mock-up production. Thus, for the design of the machine, the stator configuration is also fixed. Nevertheless, the stator design is still reasonable regarding the requirements. The specification is slightly different with the previous one of SPMSM. Key parameters are shown in Table XXX.

Table XXX REQUIREMENTS AND SPECIFICATIONS FOR A THREE-PHASE SPMSM

Requirements	Abbreviation	Unit	Value
Outer diameter	D_o	mm	161
Axial length	L	mm	66
Max average torque	T_m	N.m	65
Constant operation torque	T_c	N.m	33
Mechanical speed tolerance	Ω_m	rpm	18000
Slot current density limit (for water cooling)	J_{slot}	Arms/mm^2	15
Max mechanical power(motor) @10000 rpm	P_m	kW	14
Torque ripple ratio	T_{ripple}	%	5

Compared to the former specification, the outer diameter and active length of this IPMSM are slightly over-dimensioned. Thus, these changes result in higher torque. The power is trying to be kept the same. As for the drive system, such as input voltage and current, it is completely identical.

As discussed in the last chapter Section 2.3.3, the stator with 5p60s full pitch is ideal for the IPMSM. Thus, the off- the-shaft stator is chosen as the 5p60s/f configuration. Also as analyzed in Section 2.3.4, 10 turns per phase still leads to high short circuit current, not to mention the current large stator size. Thus, it is better to increase the turn number per phase to reduce the short circuit current. As the interval of the turn number per phase jumps too much for Star connection (10 turns or 15 turns, as shown in **Table X**), Delta connection is used, as mentioned in Section 2.2.1, with Eq. 29, the turn number per phase of Delta connection can be well tuned to 11.5 turns in Star

connection(N_Y can be fractional). Thus, the turn number is slightly increased to suppress the short circuit current. The cross section of the stator iron core is shown in Fig. 125.

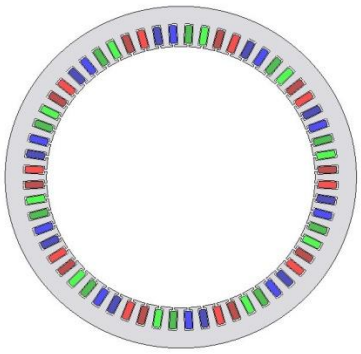

Fig. 125 Stator structure of 5p60s/f IPMSM with Delta connection

Besides, due to the change of the conductor size, the slot current density is increased to 15 [A_{rms}/mm^2], compared to the previous current density of SPMSMs or V-shape IPMSM, which is 12 [A_{rms}/mm^2]. Nevertheless, this current density is still suitable for water cooling.

Finally, for the iron core, a new iron material NO30-16 was selected. It was illustrated by Fig. 17 in Chapter 1 that NO30-16 has less iron losses than M270-35A at high frequency, such as 1 kHz. The BH curve of the material is shown in Fig. 126.

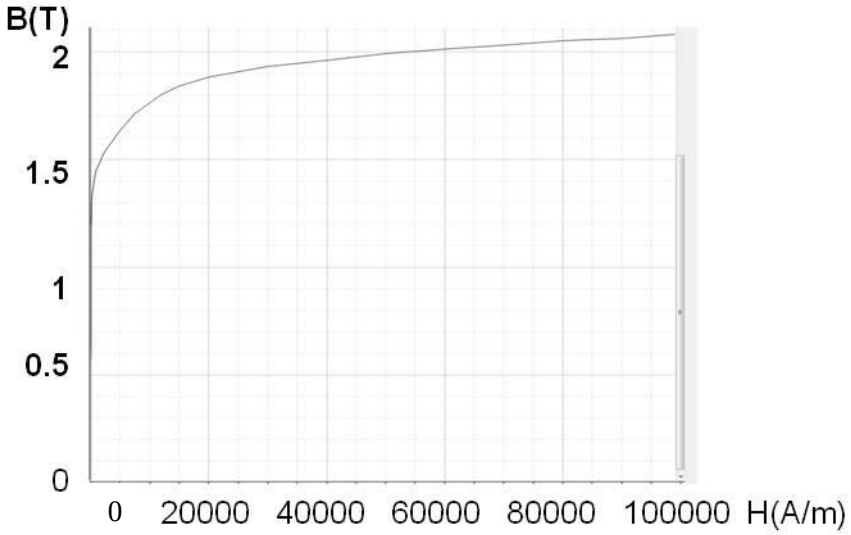

Fig. 126 BH curve of the stator iron sheet NO30-16

3.1.1.2 Rotor

As the stator dimension is kept the same, the rotor radius is also fixed. The airgap is kept as 0.5 mm (if no rotor shaping considered).

The rotor is still comprised of magnets and iron core. The material of the rotor iron core is the same with the stator – NO30-16. The magnet material was mentioned in Section 2.1. The magnet type is a bonded anisotropic HDDR NdFeB. The BH curves of the magnet under different temperatures are shown in Fig. 127.

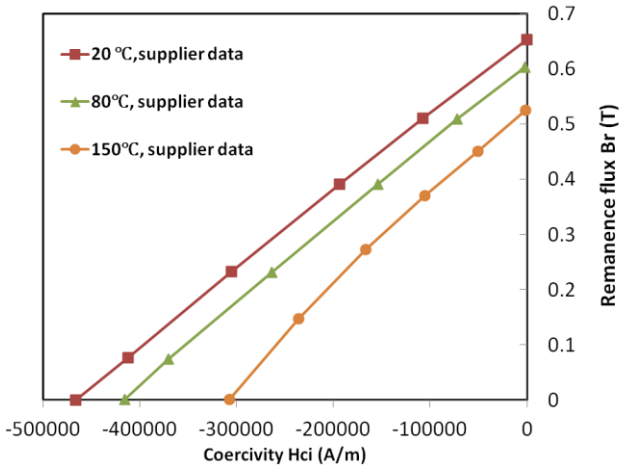

Fig. 127 B-H curves of implemented bonded - type NdFeB magnet with different temperatures

It can be observed that this type of magnet has both lower *Br* and *iHc* than traditional sintered NdFeB magnets. Yet the *Br* and *iHc* are higher than that of ferrite magnets. Thus, with the compensation of reluctance torque, it may still achieve the performance targets.

For the new design, the shape of the magnet is no longer the simple rectangular shape. Instead, in order to fully take advantage of the plasticity feature of the bonded magnet, the magnet is a kind of crescent shape. An example of the rotor with two layers of magnet is shown in Fig. 128. The details of the structure are highlighted.

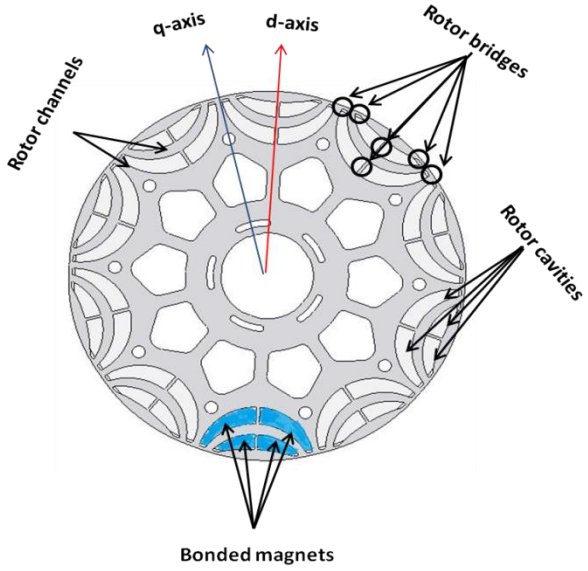

Fig. 128 Optimized rotor structure with Dy-free NdFeB bonded magnet

For each magnet layer, or so called cavity, there are three rotor bridges. This is similar to the V-shape IPMSM - two side bridges are located on the rotor circumference, and one bridge in the middle of the layer to separate the two magnets. The thickness of these iron bridges are also fixed in order to overcome the centrifugal force. The thickness of the side bridges is always 0.8 mm, while the thickness of the middle bridge is always 1 mm. From the mechanical study later on, the rotor can sustain the maximum stress during the top speed operation.

The shapes of the bonded magnets are identical with the cavities. Thus, magnets can be well fitted in the cavities. However, there is still a small empty space on the top of each magnet, which is so called air pocket. It is set that the width of the air pocket between the magnet and the rotor bridge is always 1 mm.

Between each layer, the iron region is called rotor channel. The channel cannot be too thin regarding the manufacture feasibility. The minimum thickness of the channel width is 1 mm.

Besides the parameters above, the rotor circumference can also be shaped, as presented in Fig. 129. The rotor circumference can be shaped to become more sinusoidal. With more eccentricity, the shaping becomes stronger. The highlighted area by green dash line displays the final shape of 1/10 of the rotor.

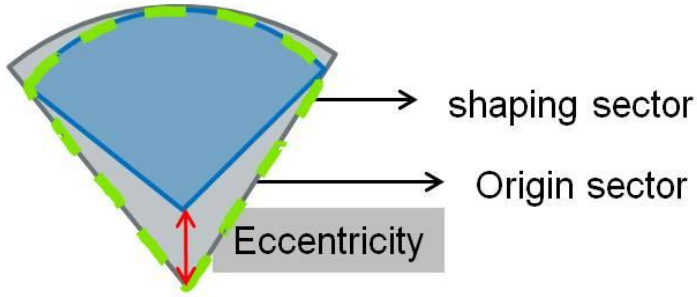

Fig. 129 Shaping of the rotor circumference by using eccentric circle

Finally, the layer of the magnets can be single or multiple. Here only rotors with 1, 2 and 3 layers are studied, as the manufacture cost and difficulty will be too high to produce layers more than 3. An example of these layers are shown in Fig. 130.

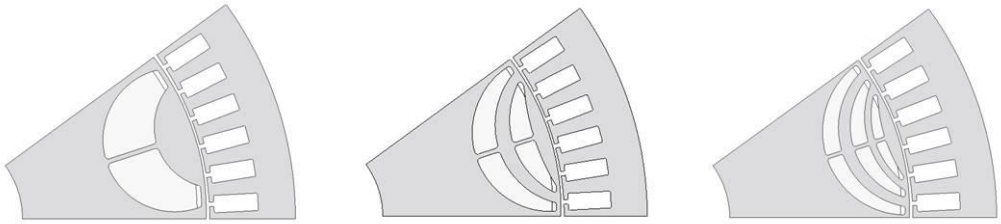

Fig. 130 IPMSM with the same stator and different rotor with 1, 2 and 3 layers of magnet respectively

In the next section, each layer of the rotor is optimized by FEM in order to achieve their best performances. Then the results of three optimized rotors can be compared. Not only the performances, but also the magnet usage and manufacture feasibility need to be taken into account.

3.1.2 Optimization of the rotors of IPMSMs with 1, 2 and 3 layers of magnets

3.1.2.1 Performances

As studied in the last section, there are many parameters, as well as constraints for these IPMSM rotors. Thus, the rotor optimization can be complicated. In general, the optimization steps can be summarized in Fig. 131.

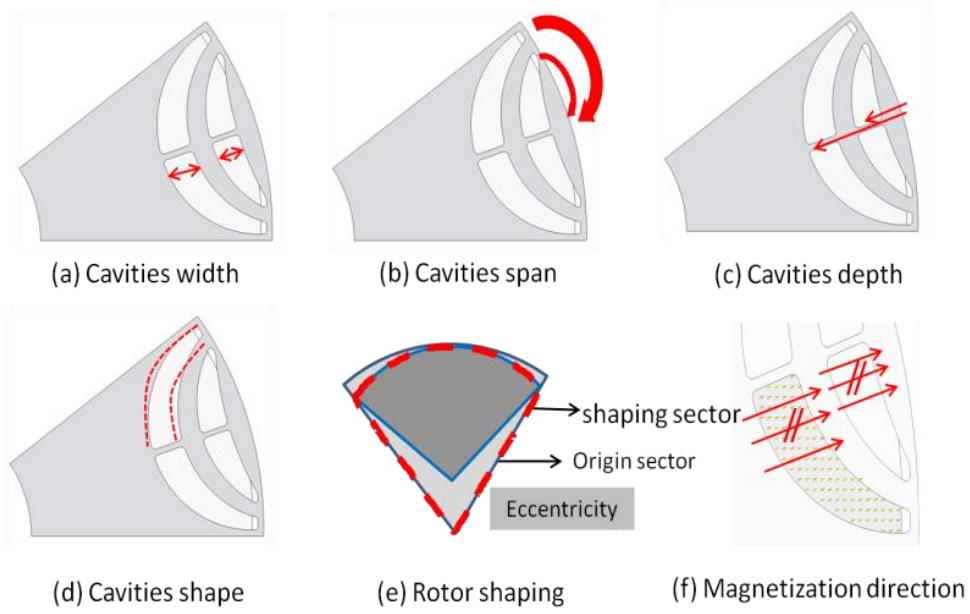

Fig. 131 Parametric study for IPM rotor e.g. 2-layer rotor

It is intuitive to find their meanings from (a) to (c). (d) denotes the shape changes of the cavities without the change of the surface. The shape can be paralleled for both edges, or it can be narrow at the head and wide at the end. (e) was discussed in Fig. 129. (f) is a pre-defined magnetization direction of magnets. It has to be magnetized in parallel direction rather than radial or centralized magnetization, due to the pattern of Post - Assembly Magnetization (PAM).

The optimizations are conducted on IPM rotor with 1, 2 and 3 layer(s) respectively. The sensitivity of optimal performances to the variation of geometry parameters is studied, as Table XXXI shows. In the table, the geometry parameters from (a) to (e) are identical with the parameters in Fig. 131. Some definitions are also shown in the bottom of the table. The focused performances still include torque, power (i_{cc}), torque ripple and losses (mainly iron loss). It needs to be highlighted that due to the high resistivity of bonded magnets, as well as applied distributed windings which induce low harmonics, the eddy current losses in magnets can be ignored.

TABLE XXXI SENSITIVITY STUDY FOR ROTOR OPTIMIZATION

		Geometry Parameters				
		(a)	(b)	(c)	(d)**	(e)
Performance	*Torque*	↑*	↑	-	-	↓
	Icc	↑↑	↑	-	-	↑
	Torque ripple	-	↕↕	↑	↓	↕
	*Iron loss****	-	↕	↑	↕	↓↓

* ↑ denotes positive correlation, ↓ denotes negative correlation, ↕ denotes bidirectional correlation, – denotes no correlation, single symbol denotes weak correlation, double symbols denote strong correlation.

** Increasing cavities shaping means to increase the sharpness of the cavities, while the cavities area are kept the same.

*** In fact, iron loss is more related to iron channels width. However, the width of iron channel is an indirect variable to be controlled in simulations.

Therefore, the sensitivity of each performance can be found. For instance, both torque and torque ripple are sensitive to the cavities span. Normally the larger the cavities span, the higher the torque. Meanwhile there are optimal positions for torque ripple, and small change of cavities span can lead to large difference on torque ripple. An example of this sensitivity is shown in Fig. 132. Motor A and Motor B are both 2-layer rotor IPMSMs. Every geometry parameter is identical except the second cavity span, where A is 8.2° and B is 7.9° - around 4% difference. Then with the same full load current and the same current phase angle 135°, stable torque curves are obtained. The average torques of Motor A and B are 1.06 and 1.05 respectively. Thus it is 1% torque reduction from Motor A to B. However, for the torque ripple, Motor A has around 3%, while Motor B has around 8%, which is 5% torque ripple increase This kind of sensitivity can also be found on the correlations between cavities width and I_{cc} (due to the reduction of L_d), rotor shaping and iron loss (reduced harmonics), as Table XXXI shows.

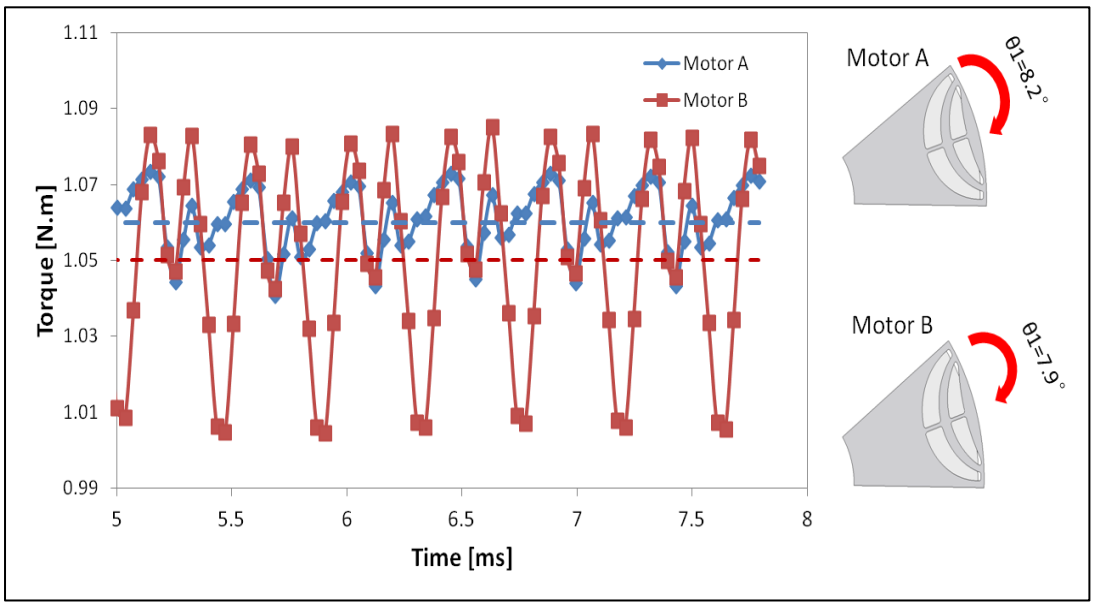

Fig. 132 Torque curves comparison between two IPM motor with different cavity spans.

Thus, as the correlations between different performances and parameters were figured out, a quadratic response surface method [145] has been used for optimization. Max torque, min torque ripple and suitable I_{cc} are treated as responses. For each supplied current, different current angles were searched to obtain the max torque and minimum torque ripple. Eventually, the optimal IPMs with 1, 2 and 3 layers rotor respectively can be compared.

Fig. 133 shows the induction maps of optimized 1, 2 and 3 layers rotor respectively. It can be observed that with the same load input, the flux densities of three stators are almost identical. The main differences are on rotors. Ideally, with more layers on rotor, more reluctance is obtained, due to the reduction of Ld and increase of Lq. However, regarding mechanical constraints in practice, with more layers, number of iron bridges also increases, which leads to large flux leakages. In addition, if the iron channel becomes too thin, the saturation will be severe. Therefore, all these effects lead to reluctance torque reduction. Thus, Fig. 133 shows that 2-layer has a good balance between leakage flux and saturation. While 1 and 3-layer(s) have either too large leakage flux or severe iron channels saturation. Thus, 3-layer may have no benefit on reluctance torque compared to 2-layer. This can be further proved in Fig. 134.

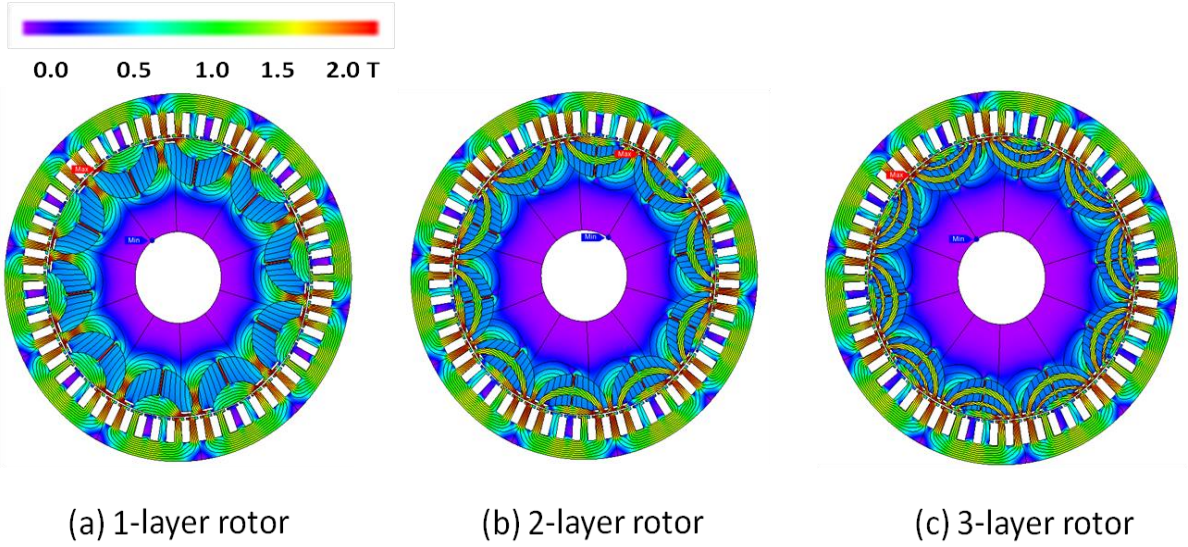

Fig. 133 Three machines induction mapping at full load of three optimized IPM machines

Fig. 134 shows the torques variation with current angle θ of the three IPMSMs. Obviously, 1-layer IPM has lower torque than the other two IPMs. While the torque curves of 2 and 3 layers almost overlap to each other, which indicates 3-layer has no superiority than 2-layer.

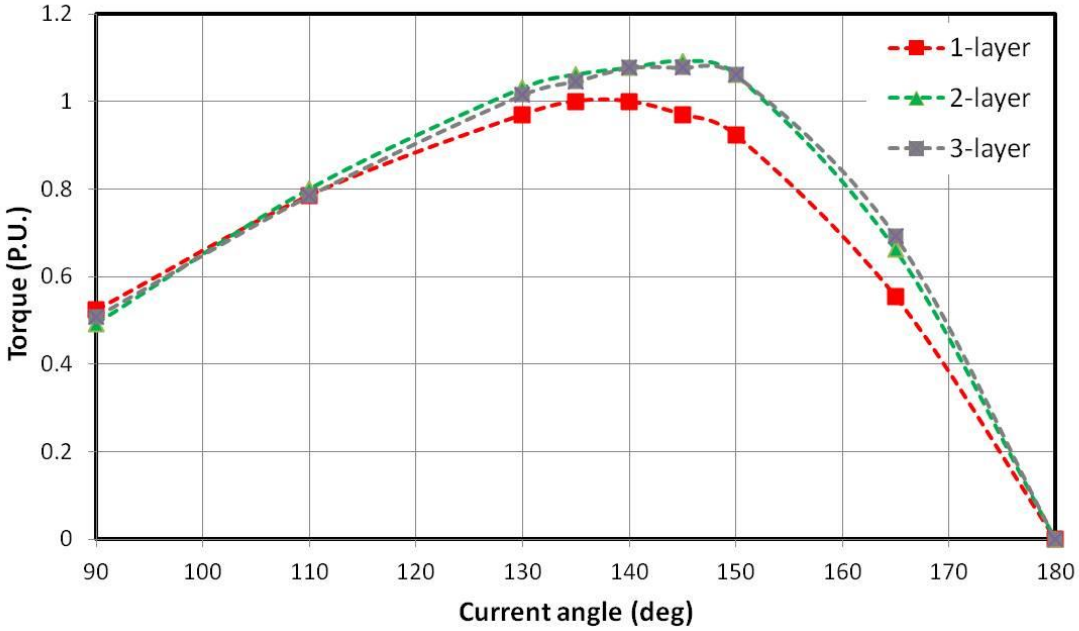

Fig. 134 Torque- current angle curves with per-unit torque value and maximum current supply of the three optimized IPM machines @ 80 °C.

Then from 3D simulations, other key performances and final magnets usage are obtained which are shown from Fig. 135 to Fig. 137.

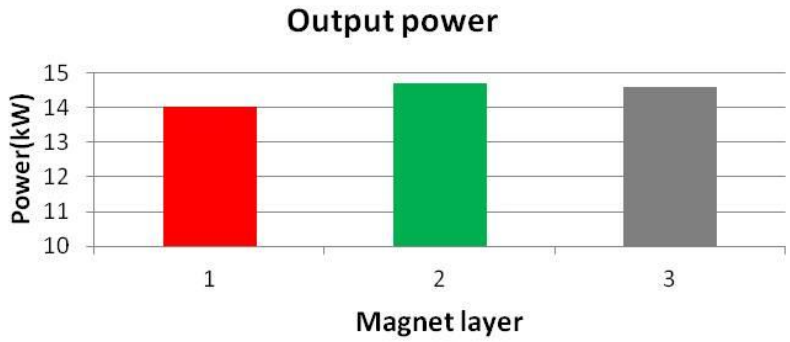

Fig. 135 Output power of 1, 2 and 3 layers rotor respectively

Fig. 135 shows the max electric power of each IPM. The max power was still derived by I_{cc} and DC voltage. It is found that due to the smaller I_{cc} of 1-layer compared to 2 and 3 layer IPMs, the electric power of 1-layer is correspondingly lower.

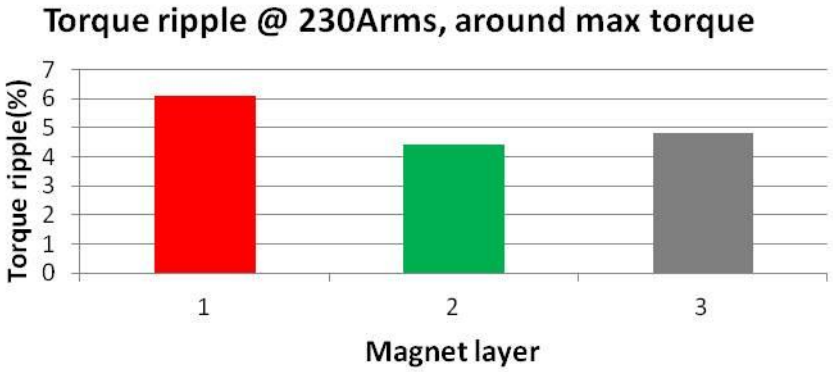

Fig. 136 Torque ripple of 1, 2 and 3 layers rotor respectively

Fig. 136 shows the smallest torque ripple of each IPM with full load current operation. Apparently, the torque ripple of 1-layer is higher than both 2 and 3 layer IPMs. For 1-layer, the smallest torque ripple is around θ =135°. While for both 2 and 3 layer, the current angles are θ =140°. All these current angles are not far from the angles with max torques.

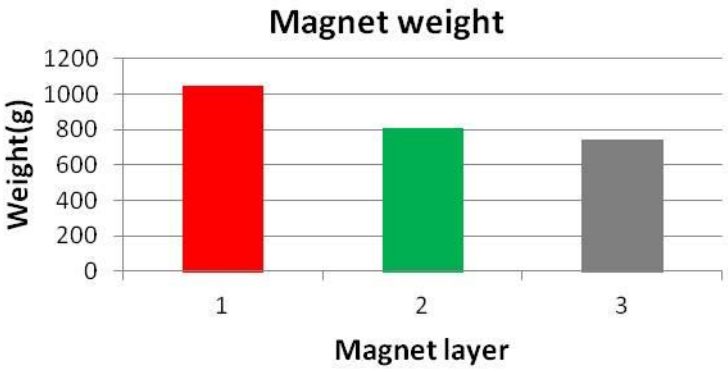

Fig. 137 Magnet usage of 1, 2 and 3 layers rotor respectively

Fig. 137 shows the magnets usage regarding total weight. Apparently 1-layer cost much more magnets than 2 and 3 layer IPMs. 2-layer also costs more magnets than 3-layer IPM, but not illustrious.

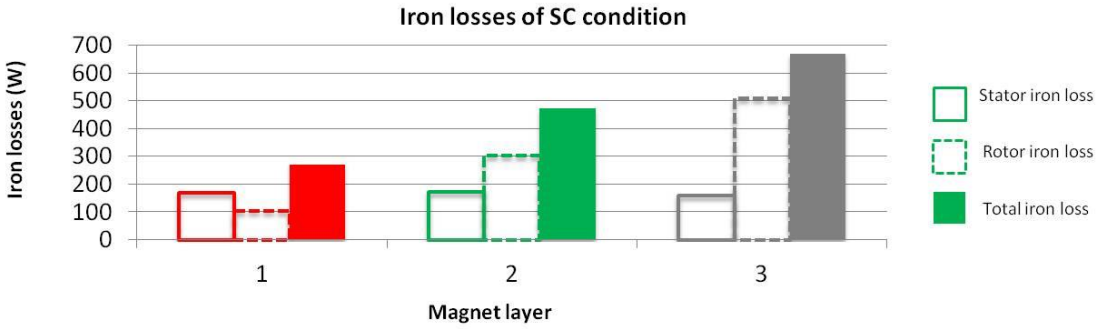

Fig. 138 Iron losses of 1, 2 and 3 layers rotor respectively

Finally Fig. 138 shows the iron losses of stator, rotor and sum. All the iron losses were calculated by the embedded Bertotti model in JMAG, as expressed by Eq. 15. However, k_{exc} is set as 0 in JMAG which shows the limits of the decomposition model. It is found that with the increase of rotor layers, the iron losses increased as well. This is particularly remarkable for the rotor iron loss. The phenomenon was explained in [146]. The reasons are likely that the airgap permeance variation due to the stator slot results in high rotor surface iron losses. Also, high number of layers enhances the stator slot harmonics, which act on the rotor to produce high iron losses. Finally, with thinner rotor cavities, there is more flux crossing them, which results in more iron losses on channels. But it to be highlighted that the hysteresis loss of the iron losses in the rotor might be overestimated by using Bertotti model in JMAG, due to the influence of DC bias field.

Finally, the moment of inertias of each rotor can be obtained. From the results of the software, their value of the moment of inertias of 1, 2 and 3 layers rotors are 0.0090, 0.0092 and 0.0093 kg.m^2 respectively. Thus, not much difference is found on the moment of inertia. The control of each rotor speed regarding the inertia should have no difference.

In summary, Fig. 134 to Fig. 137 indicated that, from 1-layer to 2-layer designs, the performance improvement as well as magnets reduction is significant. However, from 2-layer to 3-layer designs, there are not too much benefit except magnet usage, and not to mention the increased iron loss and higher manufacture difficulties for 3-layer. Therefore, eventually 2-layer rotor wins out. The following analysis will only focus on the 2-layer IPMSM.

3.1.3 Finalized IPMSMs design and its performances

The 2-layer IPMSM is selected for further analysis. The torque *vs* current angle is shown in Fig. 139.

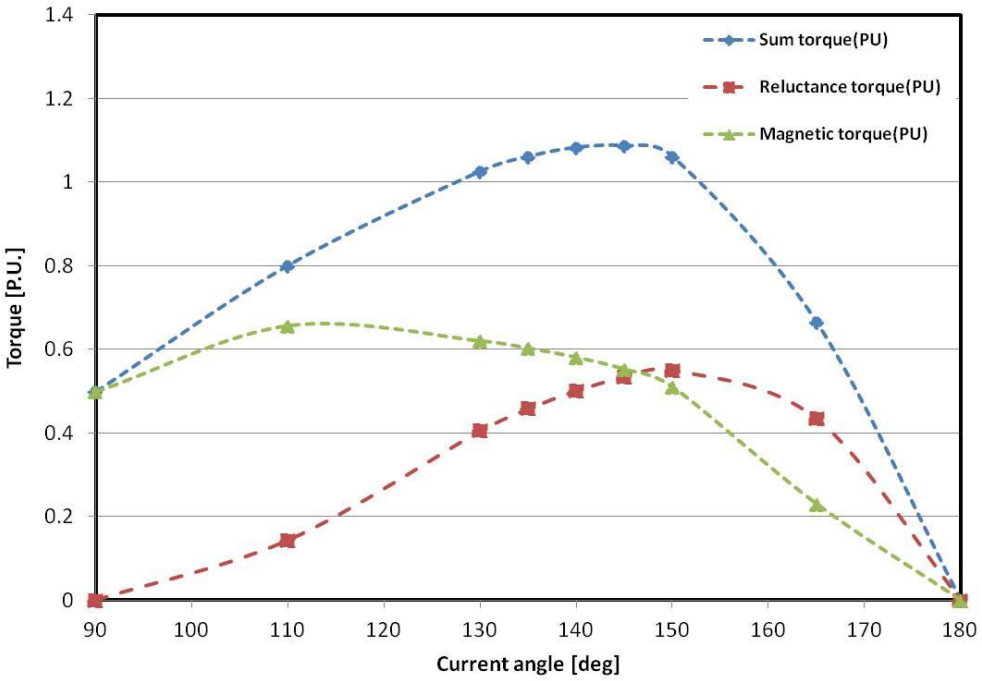

Fig. 139 Total torque and its separation of magnetic and reluctance torques of the 2-layer IPMSM by removing the magnets

In Fig. 139, the total torque was split into reluctance torque and magnet torque. The reluctance torque was also derived from FEM simulation. By removing the magnets from the rotor and using frozen permeability method, the torque was only produced by the reluctance of the rotor (including saturation). It can be found that the maximum reluctance torque did not appear at 135°. The reason is that the saturation of the rotor highly influences the inductances. The max difference of L_d and L_q is dragged behind 135° due to this saturation. Then the magnet torque can be derived by doing the difference between total torque and reluctance torque. It can be found that the magnet torque is not the highest when the current angle equals to 90°. This can also be explained by the saturation.

When the total torque reaches the maximum, the reluctance torque and magnet torque are almost identical. Thus, the magnets provide the same effort of torque with the reluctance, even though it has relatively low B_r.

3.1.3.1 Demagnetization

It is notorious for the demagnetization problem of using Dy-free PMs. Therefore, comprehensive demagnetization studies were carried out for the optimized 2-layer IPM. Fig. 140 and Fig. 141 show two extreme situations for demagnetization - magnets with 80 ℃ and 150 ℃ respectively that were exposed to demagnetized fields generated by $2*I_{cc}$ of the corresponding temperatures. In Fig. 140 the demagnetization area is 2.6%, which is within the safe limit. In Fig. 141 the demagnetization area is 4%, which is on the edge of the safe limit. Thus, the case of 150 ℃ needs to be further investigated.

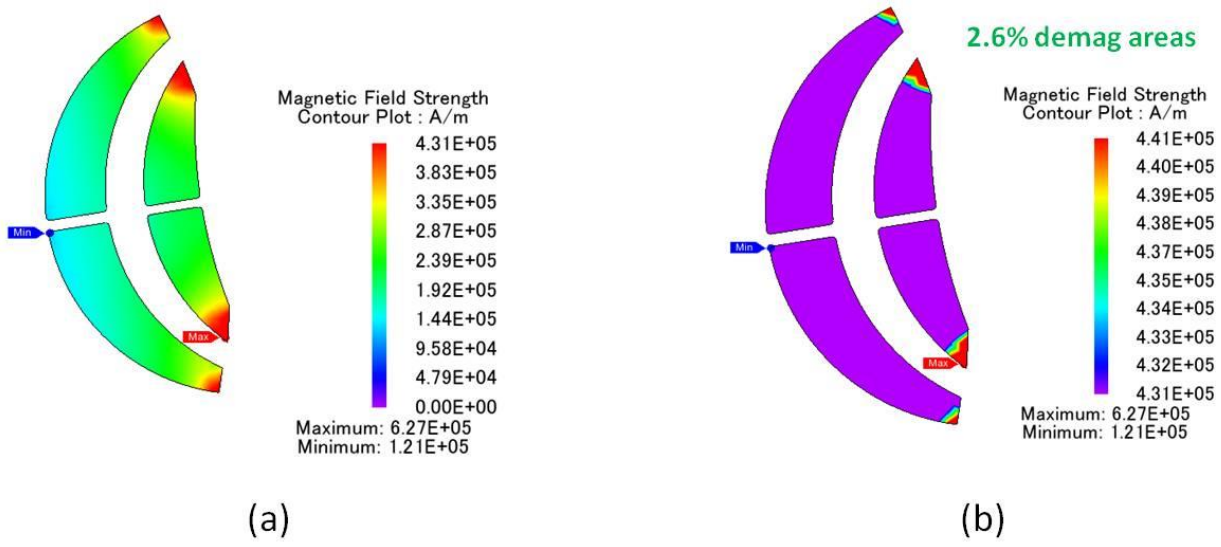

Fig. 140 The magnetic field strengths H [A/m] of magnets of 2-layer rotor at 80 ℃: (a) scale of H is from 0 to the corresponding knee point H; (b) scale of H is larger than the corresponding knee point H

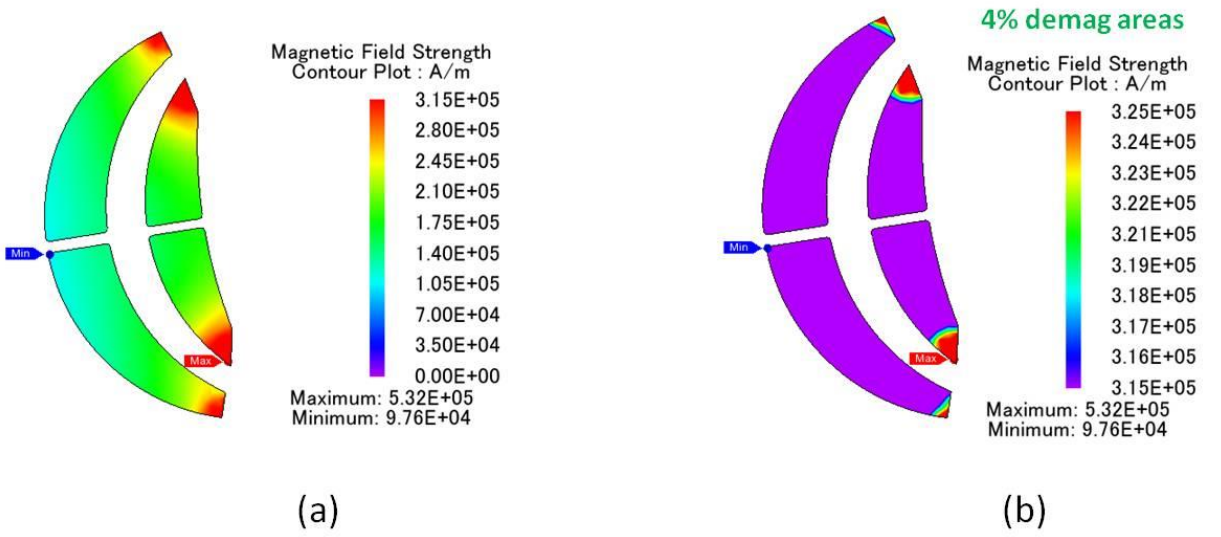

Fig. 141 The magnetic field strengths H [A/m] of magnets of 2-layer rotor at 150 ℃: (a) scale of H is from 0 to the corresponding knee point H; (b) scale of H is larger than the corresponding knee point H

Fig. 142 shows a methodology of estimating the torque reduction due to the effects of irreversible PM demagnetization. This function can be enabled in the FEM software which so called “reuse demagnetization” function [128]. In Fig. 142, the torque reduction of 150 ℃ after reuse demagnetization is 1.1%. Moreover, it can be observed that from *torque 3*, there is no further torque degradation with the reuse magnet properties. Thus, the demagnetization level of 150 ℃ is still acceptable.

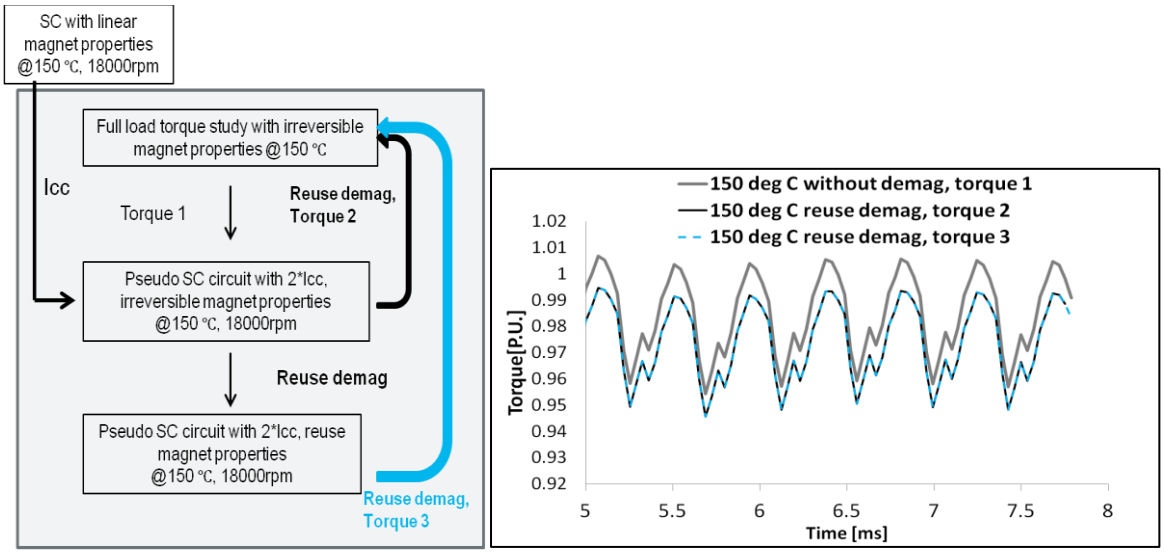

Fig. 142 Reuse demagnetization function (left) simulation flow, (right) Torque comparison between orginal torque and torque after reuse demagnetization for the optimized 2-layer IPMSM at 150 °C.

In conclusion, due to the fact that the mild hybrid application does not demand high power, the MMF is not strong enough to cause severe demagnetization. Thus, it is fairly acceptable to use Dy-free PMs for MHEV applications without demagnetization concerns.

3.1.3.2 Efficiency

A look up table of I_d, I_q vs one phase set of *dq* flux linkages is established and the flux linkages maps of d,q axes are shown in Fig. 143. The results are derived by using the same FEM simulation method and interpolation method. It can be observed that despite the amplitude, Fig. 143 and Fig. 115 are quite similar, as both of the machines are IPMSMs.

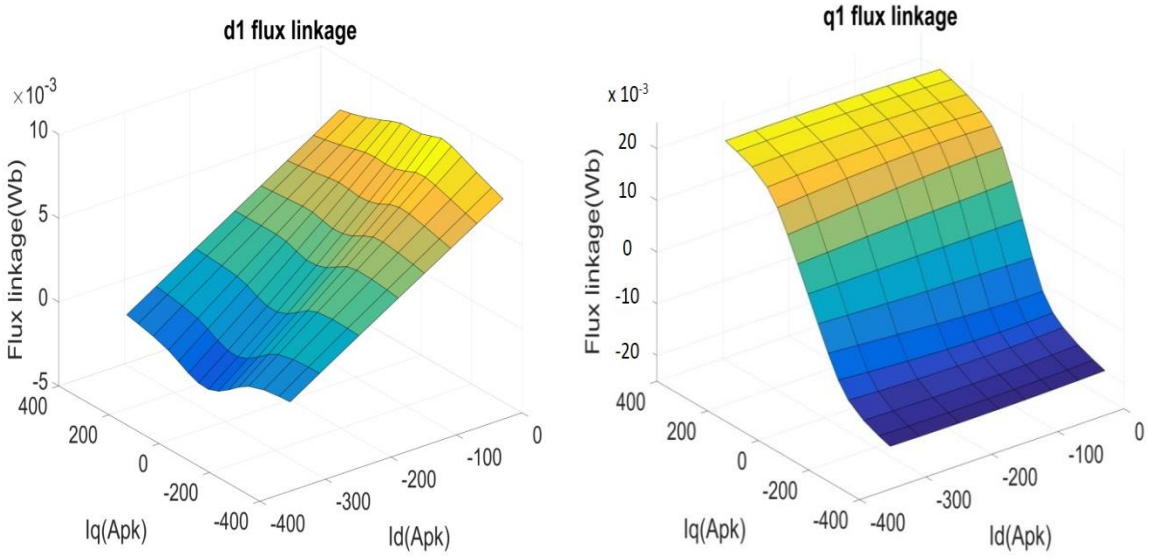

Fig. 143 *d* (left) and *q* (right) axis flux linkages maps with corresponding i_d and i_q currents of the IPMSM

Then the efficiency map of the 2-layer IPMSM is derived, which is shown in Fig. 144. Since the simulation results need to be compared with experiment results. Thus, many miscellaneous losses need to be taken into account in the efficiency map to gain high accuracy. This time, the efficiency map has considered two additional losses – AC copper loss and iron losses with manufacturing impact.

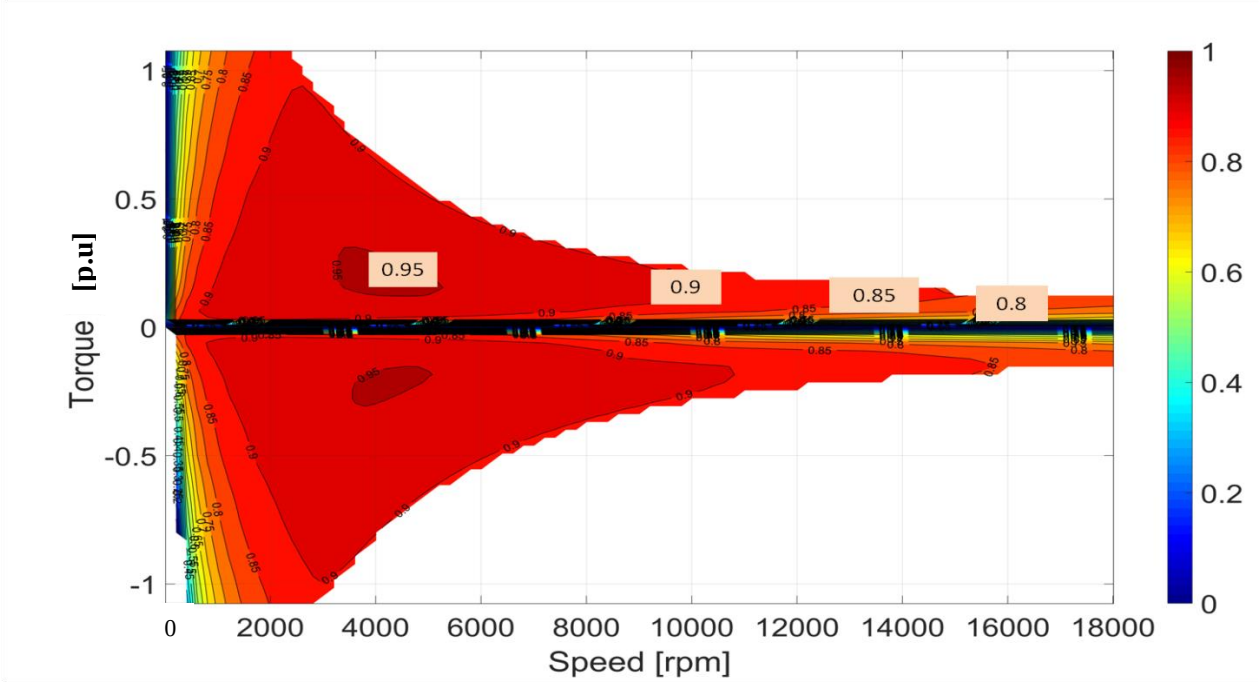

Fig. 144 Efficiency of the 2-layer IPMSM @ 80 °C with AC copper loss and iron losses considering manufacturing impact

AC effects on copper loss need to be explained first. When the carried currents on conductors have very high frequency, their distribution in the wires may be changed and become uneven. There are two renowned AC effects – skin effect and proximity effect. The schematic diagram of these two effects is shown in Fig. 145. The red color regions indicate high current density areas. Naturally, the white regions indicate low current density areas. The deeper the color, the higher the current density.

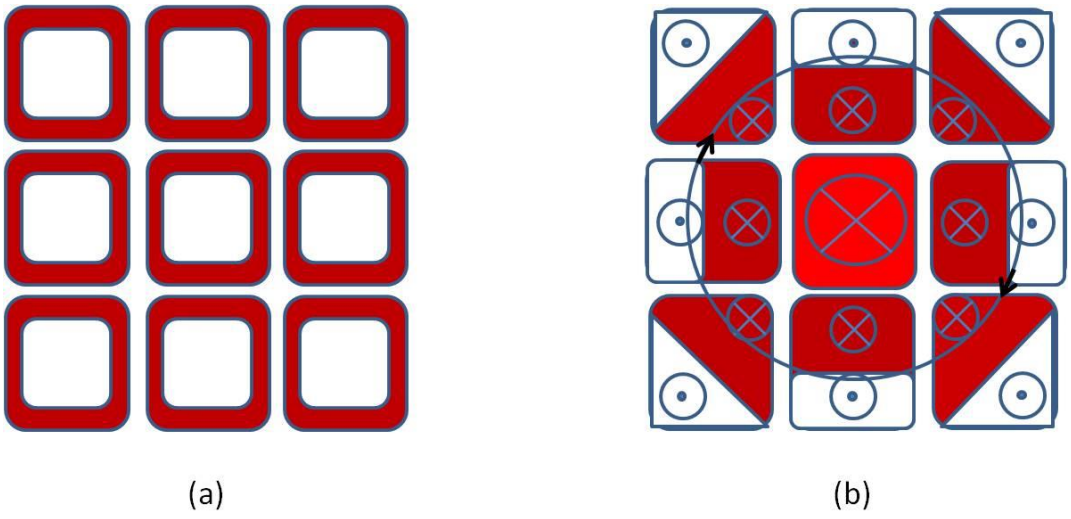

Fig. 145 AC loss effects on rectangular conductors (a) skin effect, (b) proximity effect. Red represent current concentrated areas; white areas are vice versa.

Fig. 145 (a) shows the skin effect on rectangular conductors. When a conductor is carrying an AC current, opposing eddy currents to the carrying current direction can be induced by the changing magnetic field resulting from the AC current. In this case, the current in the central of the conductor is canceled by the oppose eddy current. While the current near the conductor skin is enhanced. This phenomenon is called skin effect.

Fig. 145 (b) shows the proximity effect on rectangular conductors. Assumes that the center conductor carries an evenly distributed current. Then the current distribution of the conductors around it is influenced. eddy currents induced in these surrounding conductors. Thus, normally the area of each conductor next to the center conductor has higher current density than the area far from it. This phenomenon is called proximity effect. It needs to be highlighted that the proximity effect depends on the arrangement of the conductors. Sometimes, there are leakage flux with straight direction instead of round loop. They can also cause proximity effect, but the current distribution is presented in a different way.

In reality, it is impossible to separate these two effects clearly. Thus in this thesis, only FEM method is been used to analyze the entire AC effects.

For this analyze, it is critical to set up the conductor mesh size. As it is well known that there is a skin depth for the skin effect. Eq. 92 shows the skin depth expression.

$$\delta = \sqrt{\frac{2\rho}{\omega\mu}} \qquad \text{Eq. 92}$$

Where δ is the skin depth; ρ is the resistivity of the conductor; ω is the electrical frequency; μ is the permeability of the conductor. Smaller δ indicates stronger skin effect. From Eq. 92 it can be concluded that with higher AC frequency, the skin effect is stronger. With lower resistivity of the conductor, the skin effect is stronger. Thus, Copper wires tend to have stronger skin effect than Aluminum wires. As for the proximity effect, since it depends on the windings arrangement, there is no uniform analytical expression.

With the known copper resistivity, as well as max electrical frequency derived from the top speed, the skin depth of the copper conductor can be calculated. In order to acquire the skin effect in FEM simulation accurately, the mesh size of the conductor surface has to be smaller than the skin depth. Thus, by default the mesh size in the 2D simulation is 3 times smaller than the calculated skin depth. For the 3D simulation, the mesh size of the radial cross section is also 3 times smaller than the skin depth, while the axial size is set as 2 mm. Thus the copper loss of the active length part can be derived by taking into account both AC effects. The 3D and 2D simulation results are shown in Fig. 146. A parametric study about the AC copper loss *vs* rotation speed was carried.

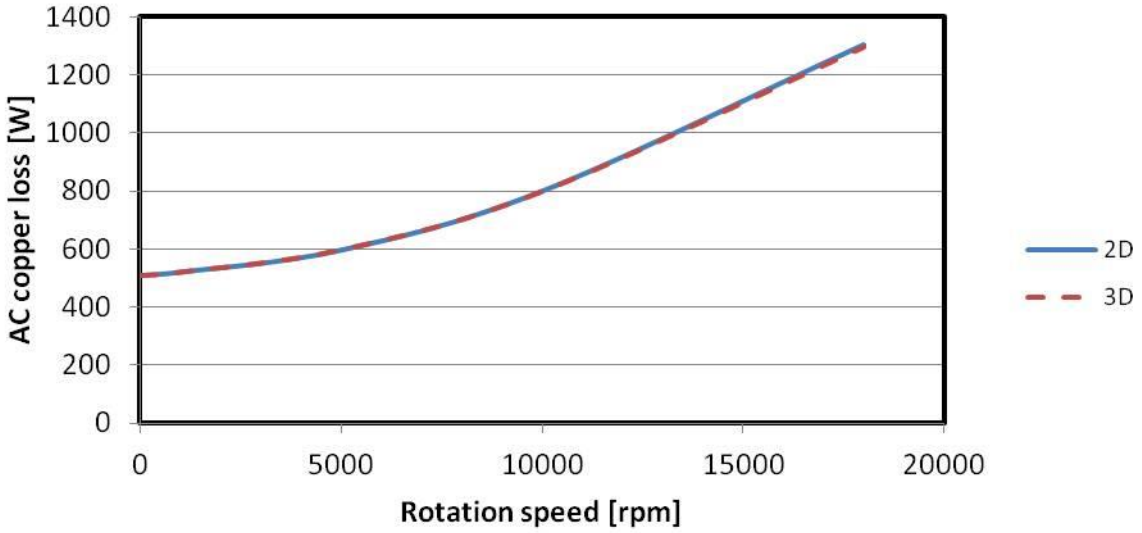

Fig. 146 AC copper loss 2D&3D results comparisons at 80 °C for both magnet and copper coil

It can be found that 2D and 3D results are totally identical. Considering much smaller time and resource consumptions of 2D simulation than 3D, the rest of analyses were done by 2D simulations.

In Fig. 147, a parametric study about the ratio of AC copper loss over DC copper loss, vs rotation speed was carried out. When the rotation speed increases, the AC/DC ratio also increases. Besides, the increasing rate of the winding with low temperature is higher than with high temperature. In fact, for the copper winding, the resistivity is increasing with the temperature. Thus high temperature can suppress the AC loss effects. It needs to be highlighted that Fig. 147 did not take into account the AC loss effect on end winding parts. Because in order to obtain the correct AC behavior of the end windings, a complete 3D end-winding (including both end sides) model need to be established. However, the calculation load for this model is out of the current computing capability. Thus, only DC copper losses of end windings were included.

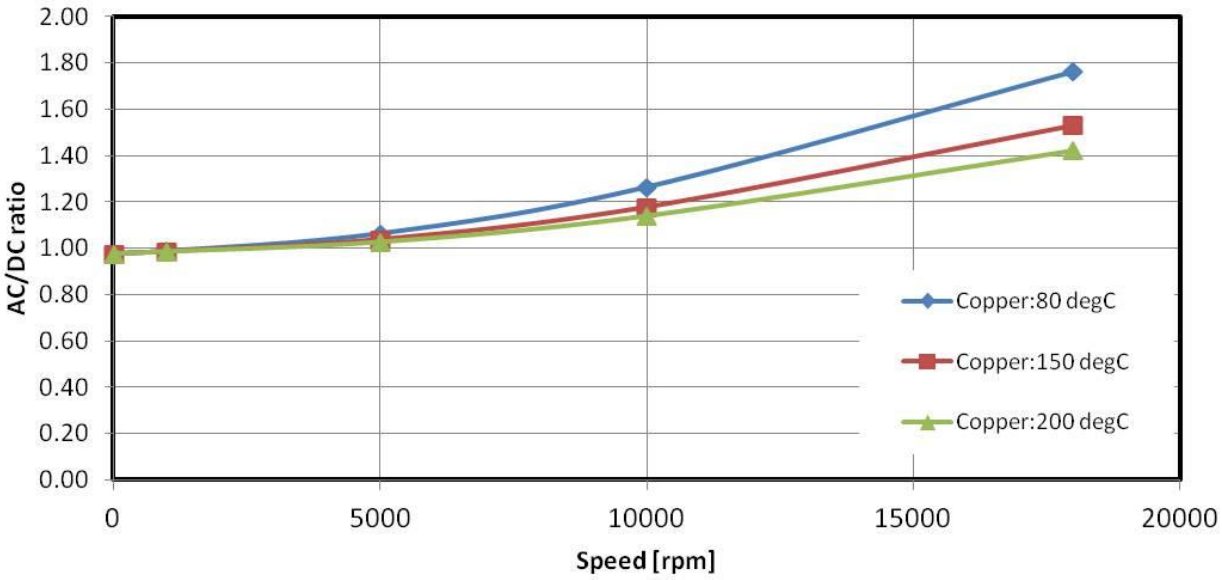

Fig. 147 AC/DC copper loss ratio under dual-three phases short circuit condition, with 80°C constant magnet temperature. Calculated by 2D FEM, the short circuit currents depended on each copper temperature, the AC effects of end winding were not considered.

Therefore, with the aforementioned method, the final copper loss map is shown in Fig. 148 It can be noted that with the consideration of AC effect, high copper losses can also occur at high speed region (as red circle highlighted), rather than copper loss decreasing with the speed, such as Fig. 123 for the comparison.

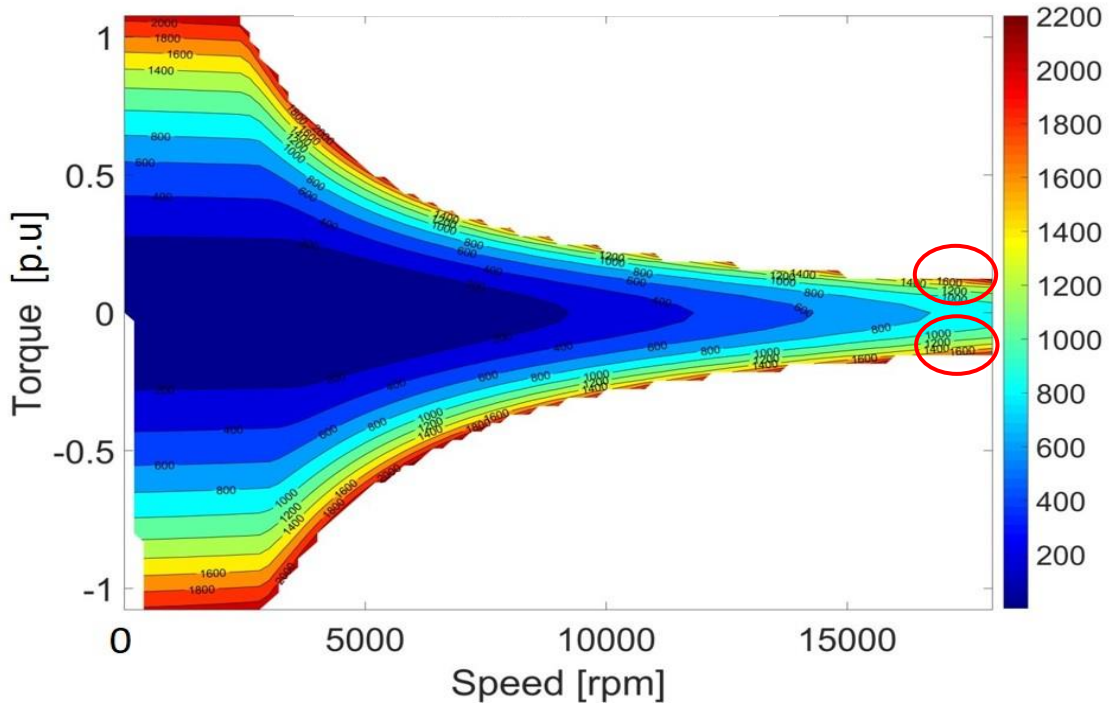

Fig. 148 AC copper loss map [W] at 80 °C magnet and copper coil

The iron losses include both stator and rotor iron losses. Besides, an experience coefficient equals to 2 was taken into account in the calculation. This coefficient represents the manufacturing impacts to the iron losses. Such as cutting, punching and annealing, etc. processes.

From Fig. 149 it can be found that the relationship between loss, speed and load does not look as linear as the iron losses maps of the previous SPMSMs. This can be explained by the complex saturation behavior on the IPMSM rotor, which results in irregular rotor iron loss distribution.

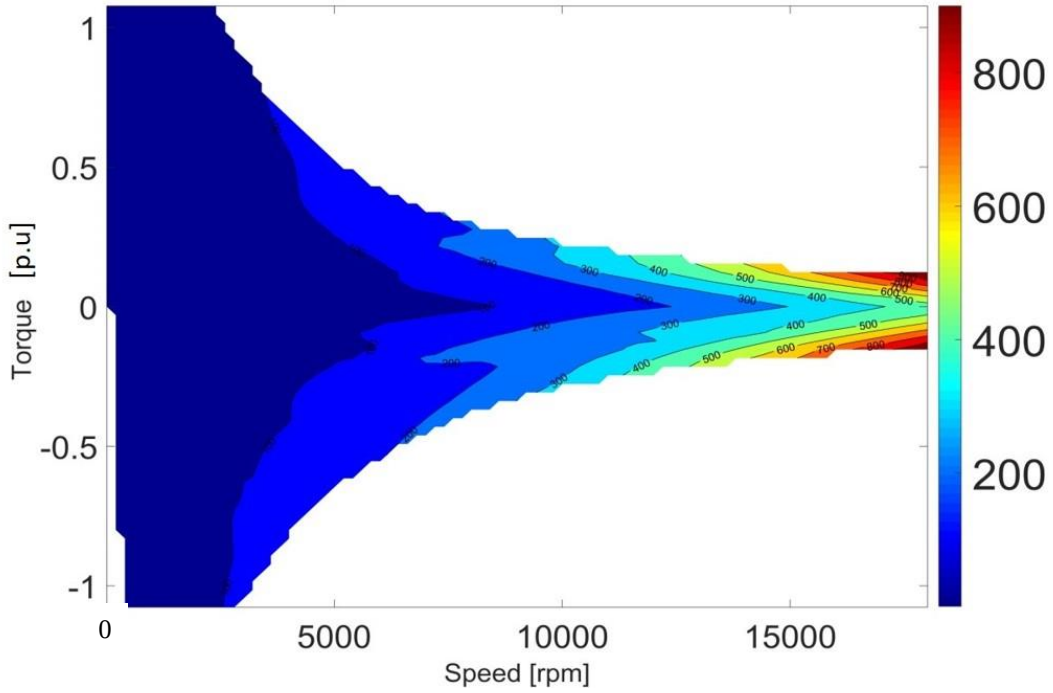

Fig. 149 Iron losses [W] including both stator and rotor losses and considering the manufacturing impacts (2 times)

The mechanical loss was kept the same with SPMSMs, as the same bearing was used. Also, the small change of the rotor dimension would not result in large difference on mechanical loss.

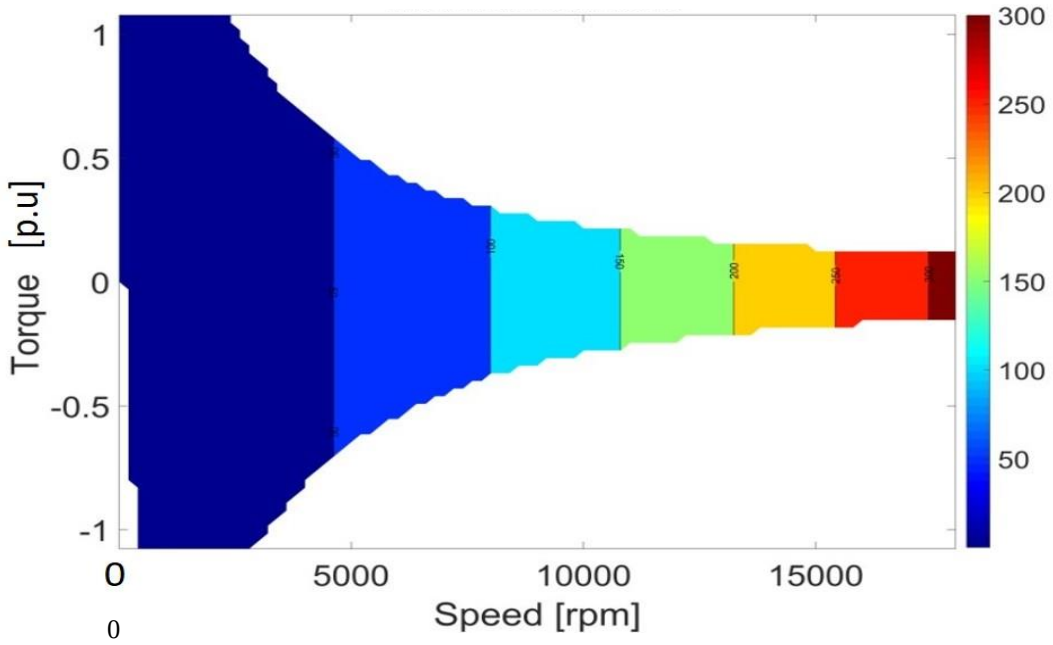

Fig. 150 Mechanical loss of the 2-layer IPMSM

All the other information related to this efficiency map, such as currents, voltage maps are shown from Fig. 151 to Fig. 155. Generally, the controls of this 2-layer IPMSM are similar to the V-shape IPMSM with sintered NdFeB magnets.

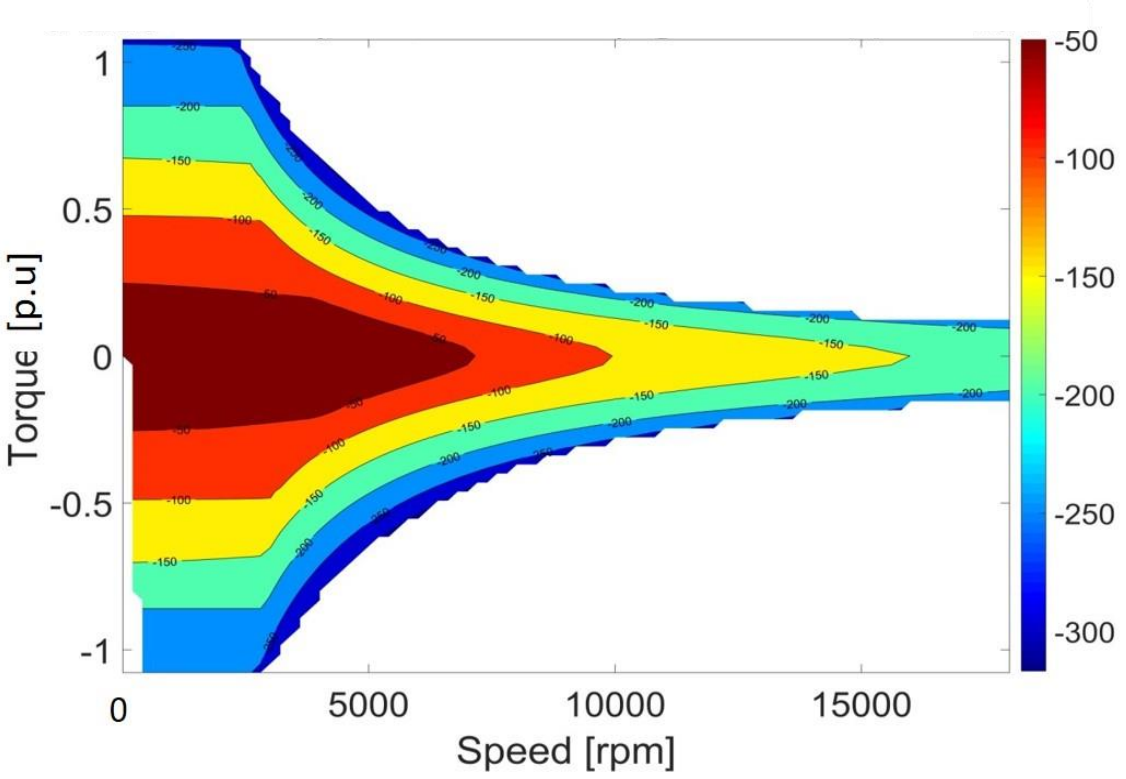

Fig. 151 I_d [Apk] map of the 2-layer IPMSM at 80°C

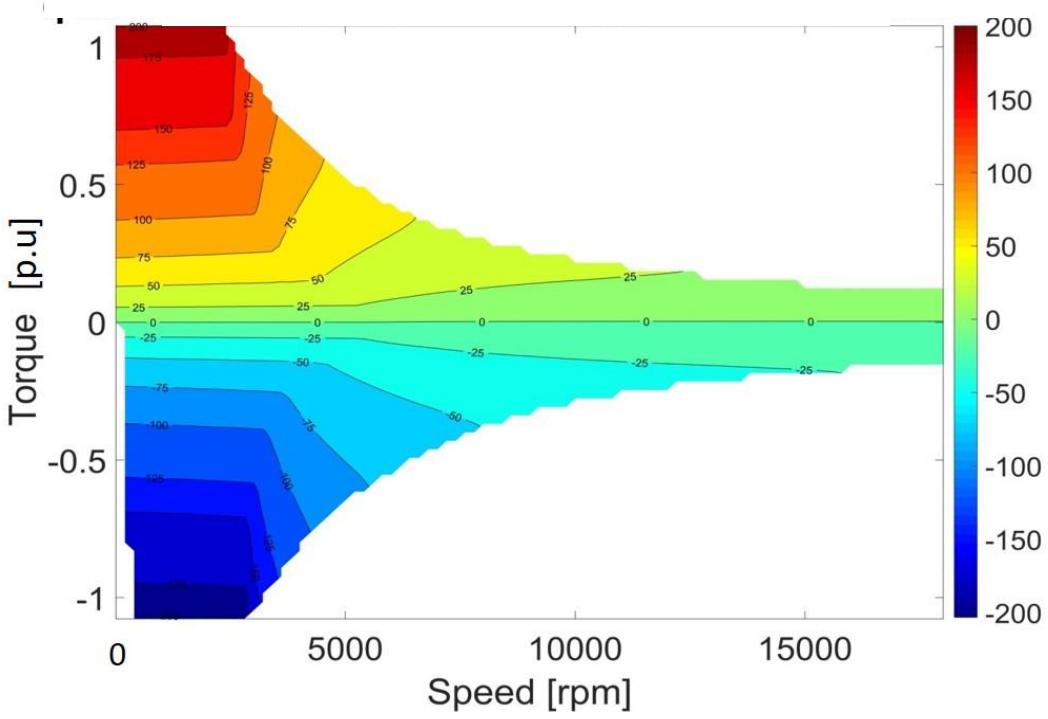

Fig. 152 I_q [Apk] map of the 2-layer IPMSM at 80°C

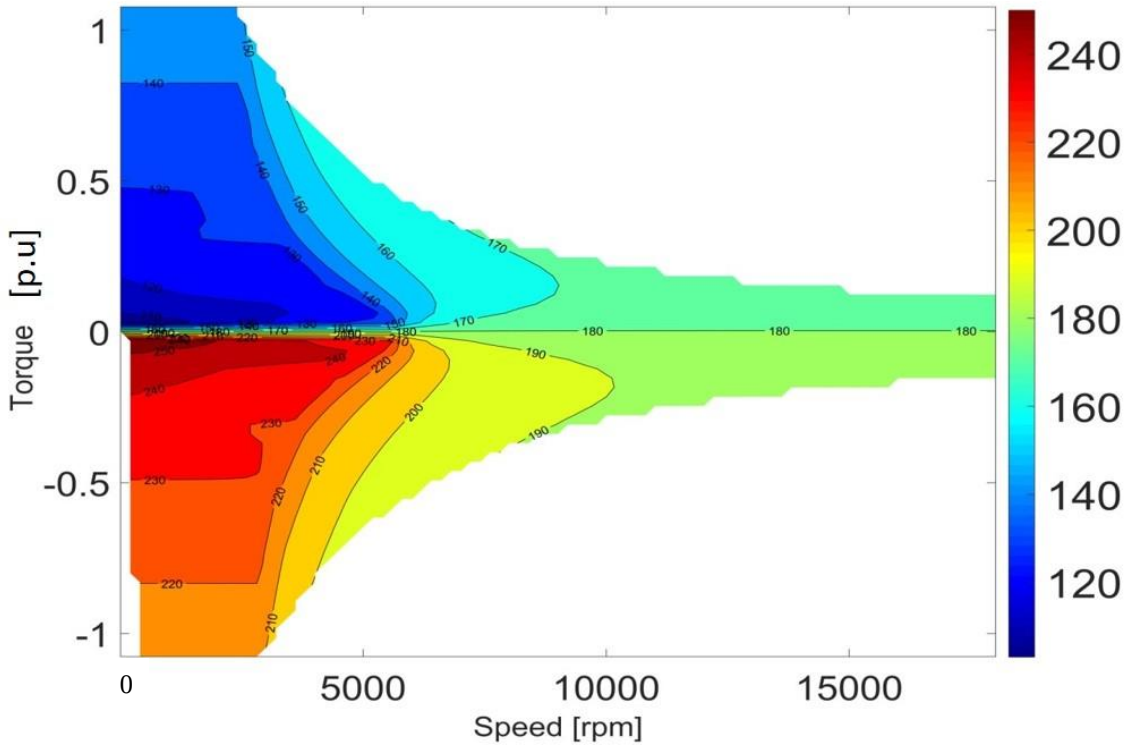

Fig. 153 Current angle map [deg] of the 2-layer IPMSM at 80°C

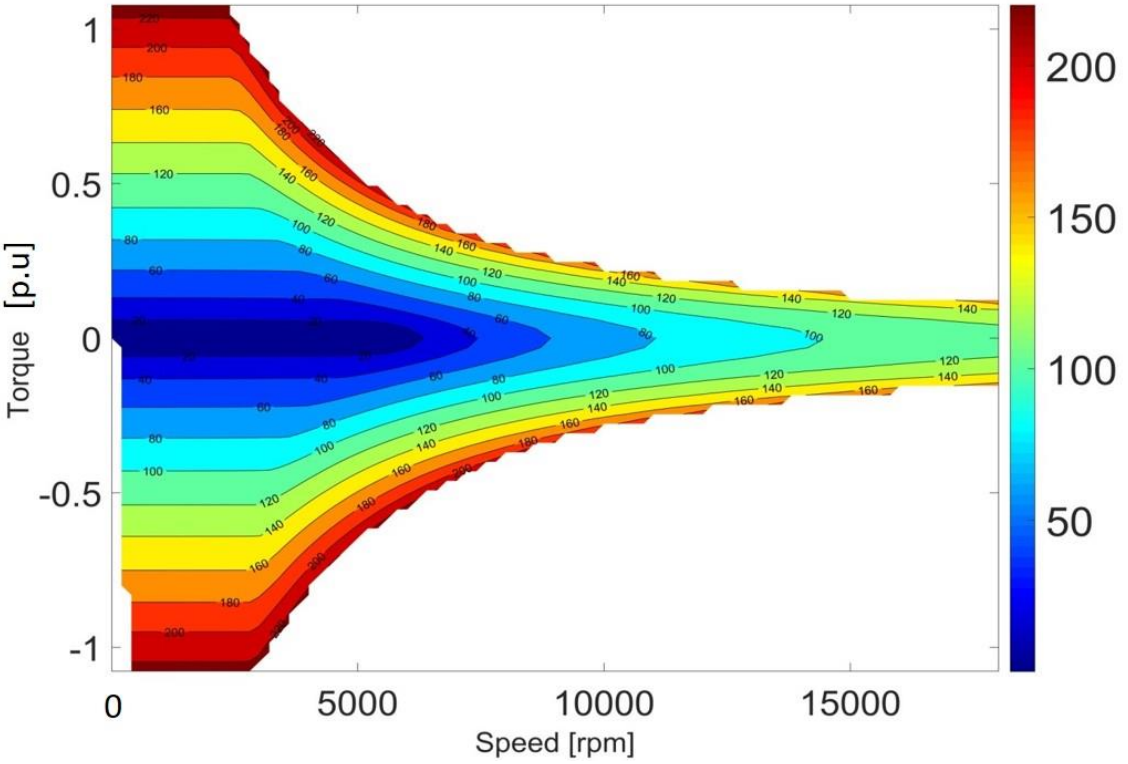

Fig. 154 Total current map [Arms] of the 2-layer IPMSM at 80°C

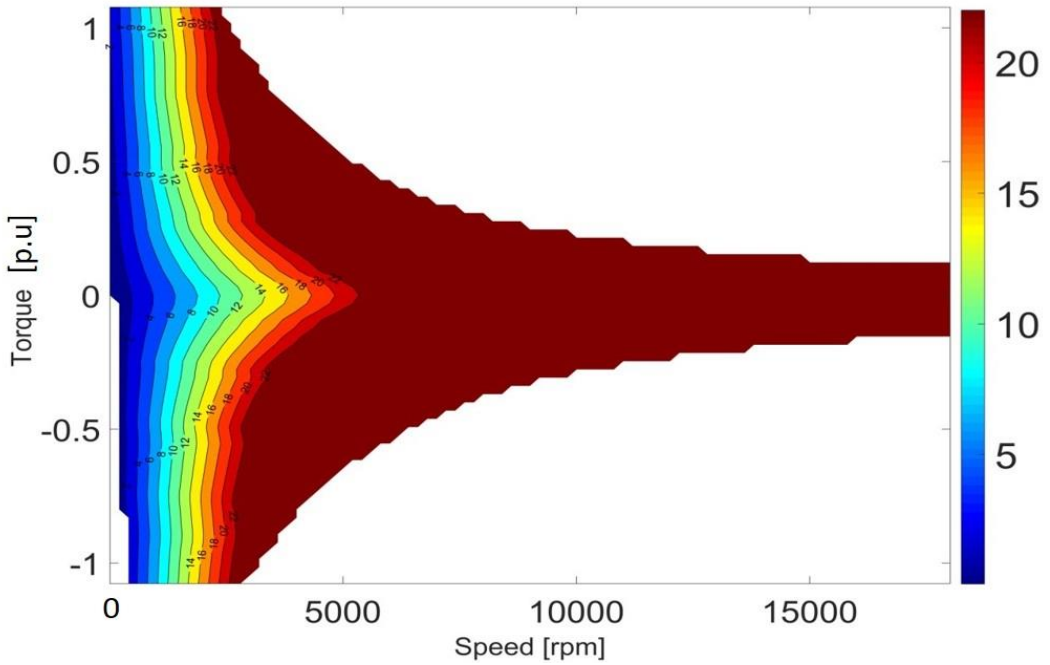

Fig. 155 Voltage map (Vac) of the 2-layer IPMSM at 80°C

In general, even considering all the miscellaneous effects on different losses, the highest efficiency can still be larger than 95%. Therefore, the efficiency of the 2-layer IPMSM can fulfill the requirement.

3.1.3.3 Mechanical and thermal studies

The mechanical stresses of the 2-layer rotor were analyzed in another professional FEM software (ANSYS). The topology parameters were kept the same. In order to make sure that the rotor does not break even under the worst situations, several assumptions were made:

1. No adhesive force between magnets and iron core was considered in simulation.
2. The air pockets had no filler in the simulation.
3. The Young's module of magnet was seen as normal bonded magnet value, which is 24.8GPa.

Then the maximum stresses at different rotor position were analyzed in the simulation. Two results are shown in Fig. 156 and Fig. 157. The safe stress limits are also specified.

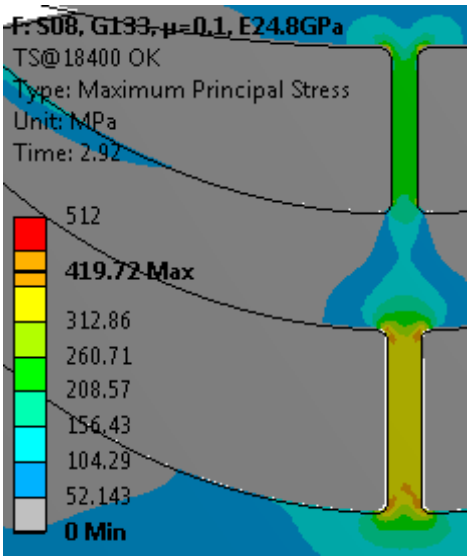

Fig. 156 2-layer rotor von mises stress around the top speed. Safe von mises stress limit was set as 420 Mpa

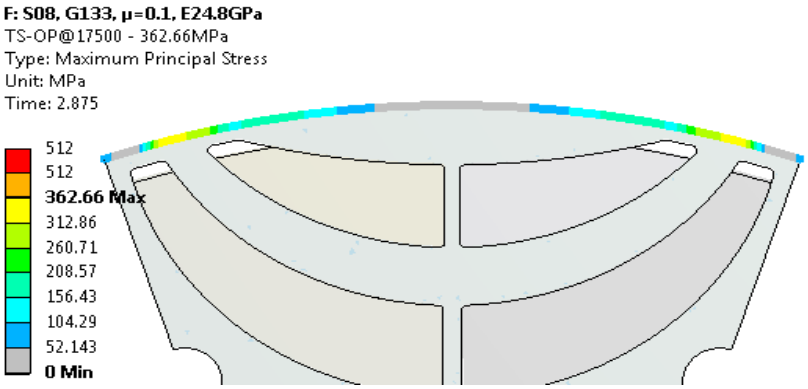

Fig. 157 2-layer rotor circumference principal stress around the top speed. Safe circumference stress limit was set as 360 Mpa

From the results it can be concluded that the max stresses were within the safe limits. 2-layer rotor can safely run up to the top speed, even with some harsh assumptions.

The last criterion for the 2-layer IPMSM is the thermal condition. The safe limits of coil and iron core temperature are still identical, which are 200 °C and 300 °C respectively. The highest temperature for the NdFeB magnet is 150°C. In this study, only stator thermal condition is analyzed. As discussed in Section 2.2.5, the same thermal circuit based on 2D model was implemented, as Fig. 75 or Fig. 158 shows.

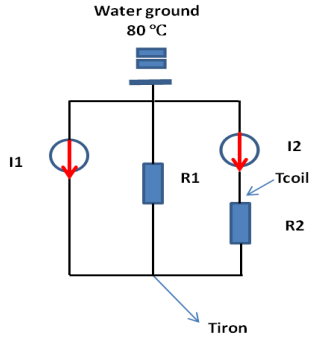

Fig. 158 Simplified stator thermal circuit

The thermal resistances were derived by a macro thermal resistance. The macro resistance was obtained from experiments, which was 0.06 °C/W for this IPMSM.

Then the two local thermal resistances R1 and R2 were derived from the equivalent resistance respectively, which is shown as Eq. 93.

$$R1 = (1/3)\ R0 = 0.02\ [℃/W] \qquad \text{Eq. 93}$$
$$R2 = (2/3)\ R0 = 0.04\ [℃/W]$$

Then two scenarios were analyzed for thermal conditions – the scenario of constant load operation S1, which is constant torque (33 N.m) at base speed (2300 rpm); the scenario of dual three phase short circuit at top speed S2. The magnet temperature of both scenarios is 80 °C.

Besides, the impacts of AC effects of copper losses to the thermal conditions were studied. The AC/DC ratios were still taken from Fig. 147. However, it should be noted that these ratios are changing with the temperature. An interesting effect is that with the increasing of the coil temperature, the ratio is decreasing. Thus, somehow the copper loss is a negative feedback to the AC/DC ratio.

Finally, for the iron losses, only stator part was considered. This time the manufacturing coefficient was taken into account. The losses results of both scenarios are shown in TABLE XXXII and TABLE XXXIII respectively.

TABLE XXXII LOSSES OF THE 2-LAYER IPMSM UNDER THE CONSTANT LOAD OPERATION SCENARIO

Machine Type and assumption	I1 [W]	I2 (80°C) [W]	I2 (200°C) [W]
2-layer IPMSM without AC effects	80	480	660
2-layer IPMSM with AC effects	80	500	700

TABLE XXXIII LOSSES OF THE 2-LAYER IPMSM UNDER THE TOP SPEED SHORT CIRCUIT SCENARIO (STEADY STATE)

Machine Type and assumption	I1 [W]	I2 (80°C) [W]	I2 (200°C) [W]
2-layer IPMSM without AC effects	200	920	1280
2-layer IPMSM with AC effects	200	1620	1920

As the copper loss (I2) changes vastly with the coil temperature, the coil temperature was still interlocked with the copper resistance. As for iron losses, it is still assumed that they are independent of temperature changes. The calculated temperatures are shown in TABLE XXXIV.

TABLE XXXIV COIL AND IRON CORE TEMPERATURES UNDER TWO SCENARIOS

Machine Type and assumption	S1(°C)		S2(°C)	
	T_{iron}	T_{coil}	T_{iron}	T_{coil}
2-layer IPMSM without AC effects	104	115	134	157
2-layer IPMSM with AC effects	106	117	166	200

From TABLE XXXIV it can be summarized that AC effects have nearly no influence to the constant load scenario, while they can greatly deteriorate the thermal condition of the SC top speed scenario. It is also interesting to mention that in S2, the increased T_{coil} on contrary suppressed the AC effects, so that in the end T_{coil} did not break the safe limit. Nevertheless, for all high speed operations, it is necessary to consider the AC loss effects for the thermal calculation.

In summary, from torque speed performance, efficiency, demagnetization, to mechanical and thermal conditions, all indexes of this 2-layer IPMSM are in line with the requirements. Therefore, it was decided to use this design for mock-up manufacturing, in order to validate these simulation results.

3. 2 IPMSM experiment validations

A rotor mock-up was built based on the design, which is shown in Fig. 159. Due to the lack of the envisaged injection molding instruments, the bonded magnets were still fabricated in a conventional way before the inserting process. Another difference needs to be highlighted is that there is a small groove on each pole. These grooves were caused by welding. Thus new simulations need to be carried out by taking into account these welding grooves. However, the additional rotor iron losses caused by the welding groove could not be considered due to the limitation of the iron loss model used. Apart from the rotor, an off-the-shaft stator with the same dimensions of the design, and with the same winding configuration, was being used.

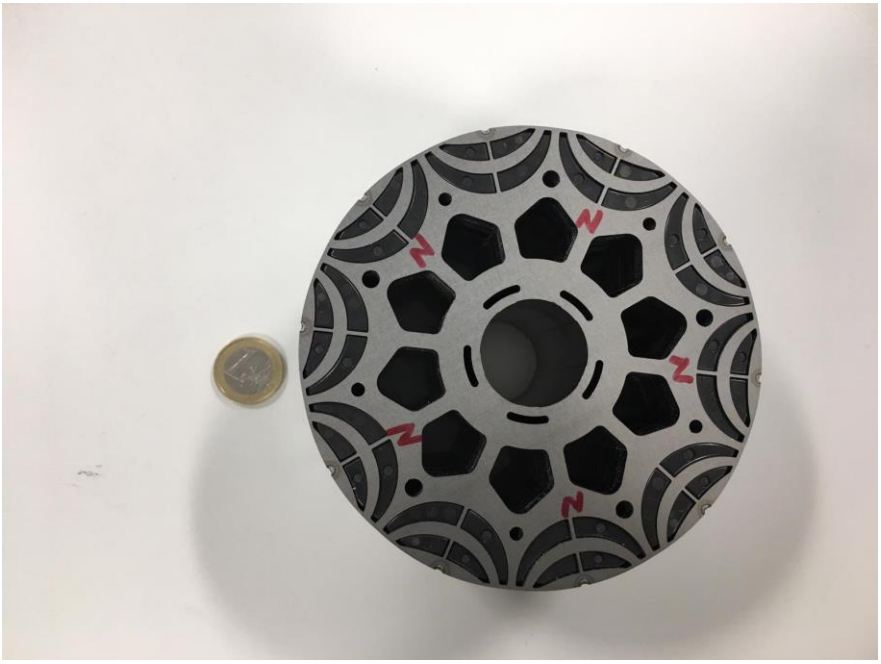

Fig. 159 Rotor mock-up of the IPMSM with bonded NdFeB magnets

Unfortunately, after receiving magnets from a supplier, it was figured out that the magnets cannot achieve the ideal performances. It was found that Br was around 35% less than the ideal Br property at 20 °C. Thus, based on the new BH curves, new simulations were carried out. The dimension of the machine was kept the same, only the magnet properties changed.

Then no load tests, short circuit tests and load tests were carried on a test bench respectively. The test bench configuration is shown on Fig. 160. This is a belt driven system with pulley. The pulley ratio is 3.36. The highest torque the belt system can tolerate is 55 N.m. Water cooling system is integrated in the bench as well. In addition, due to a special balancing ring used on the rotor mock-up with weak mechanical tolerance, the highest speed the rotor can run was 10000 rpm. The current sensor is used to obtain the DC side current, thus with the constant DC voltage, the input power of the motor mode (or the output power of the generator mode) can be obtained. The torque sensor can be used to measure the torque, with the rotation speed, the output power of the motor mode (or the input power of the generator mode) can be obtained. Finally, the test results were compared with 3D FEM simulation results.

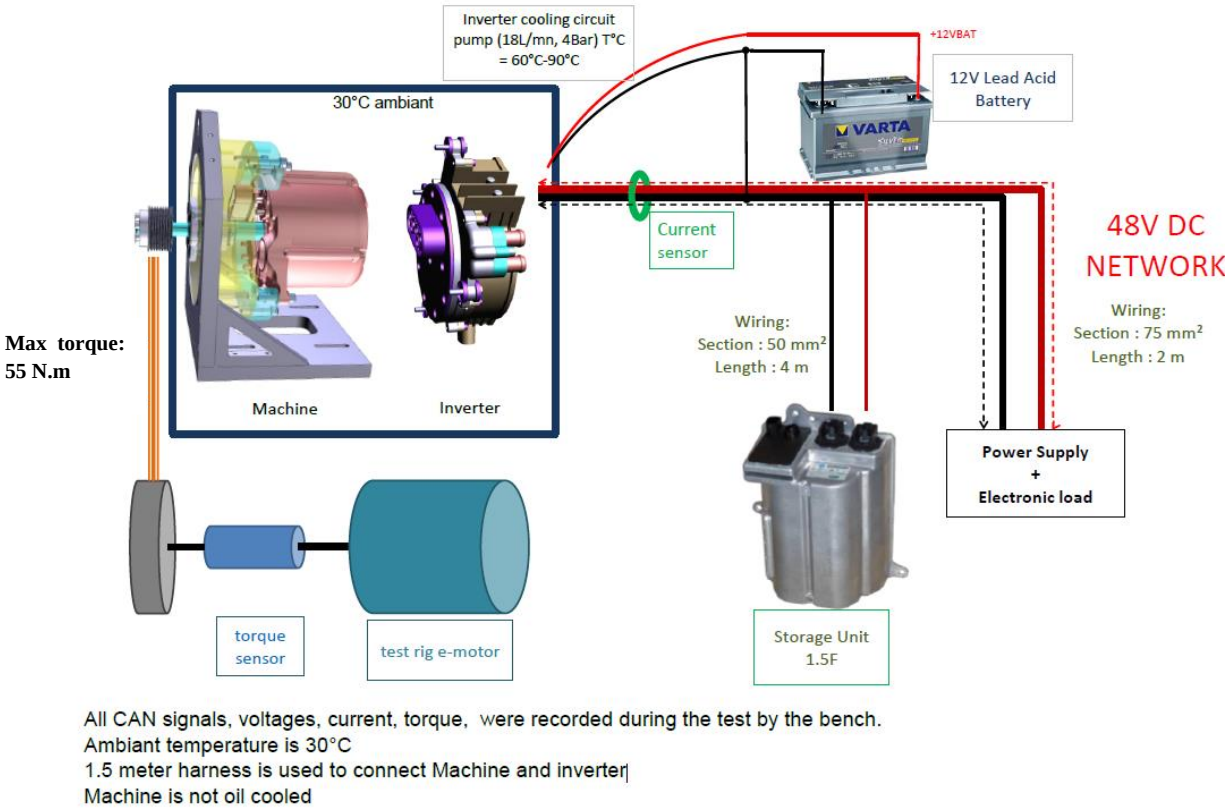

Fig. 160 Test bench configuration for the IPMSM mock-up tests

When the motor assembly was received, each phase was separated. The resistance of each phase was measured by a AOIP microhmmeter. Every phase showed the same resistance measurement results, which is 17 mΩ at 20 °C, which is only 7% larger than our theoretical estimation. Then as the delta connection should be used, the entry of one phase should be connected with the exit of the other phase. Afterwards, there were 6 terminals. 3 terminals represented one phase set. The terminals were named A1, B1, C1 and A2, B2, C2 respectively. Then all the phase to phase (e.g. A1-B1) resistance was measured. The results showed every phase to phase resistance show the same resistance, which is 11.5 mΩ at 20 °C. The result is in accordance with the delta connection law.

3.2.1 No load test

No load test, or so called open circuit test, is to run up the motor without electric connection. As the machine has permanent magnets, the back-EMF is induced as long as the rotor rotates. The back-EMF can be measured from the phase terminal voltages. Oscilloscope can be used to record the voltage waveforms. For this test, the phase-phase voltage was measured.

The type of oscilloscope used was YOKOGAWA DL850EV, which has 12 channels. Thus it is enough to measure six phases signals synchronously. The probe used was with 10:1 gain.

2.3.2.1 Back-EMF

The simulated induction mapping of the no load conditions with two temperatures are shown in Fig. 161.

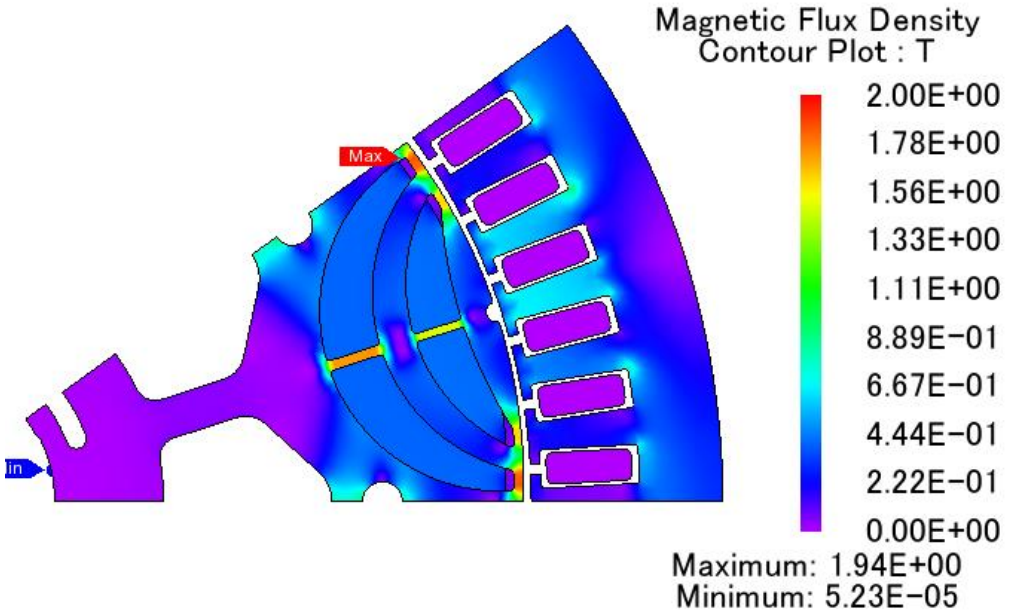

(a)

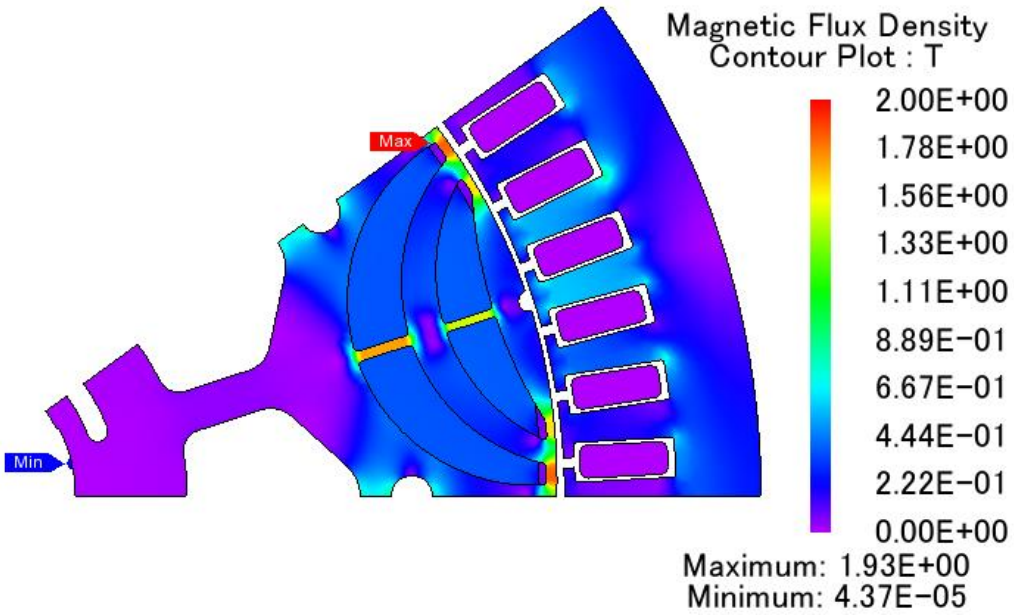

(b)

Fig. 161 Induction mapping of no load simulation at 500 rpm (a) @ 20 °C (b) @ 80 °C

Here it can be noted that on the rotor pole a groove was created, and the radius was 1 mm. It can be found the flux density at 80 °C is generally lower than the flux density at 20 °C. Thus, the induced back-EMF at 80 °C should be

lower than at 20°C. The measured back-EMF at these two temperatures are shown in Fig. 162 (a). Also the comparisons between measured results and simulated results can be found in Fig. 162 (b) and (c).

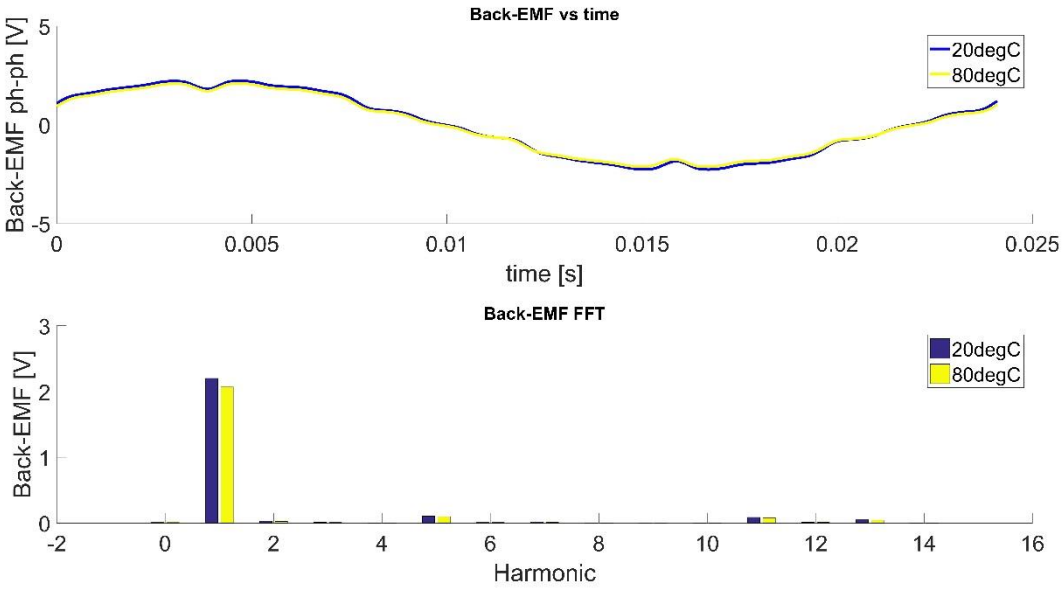

(a)

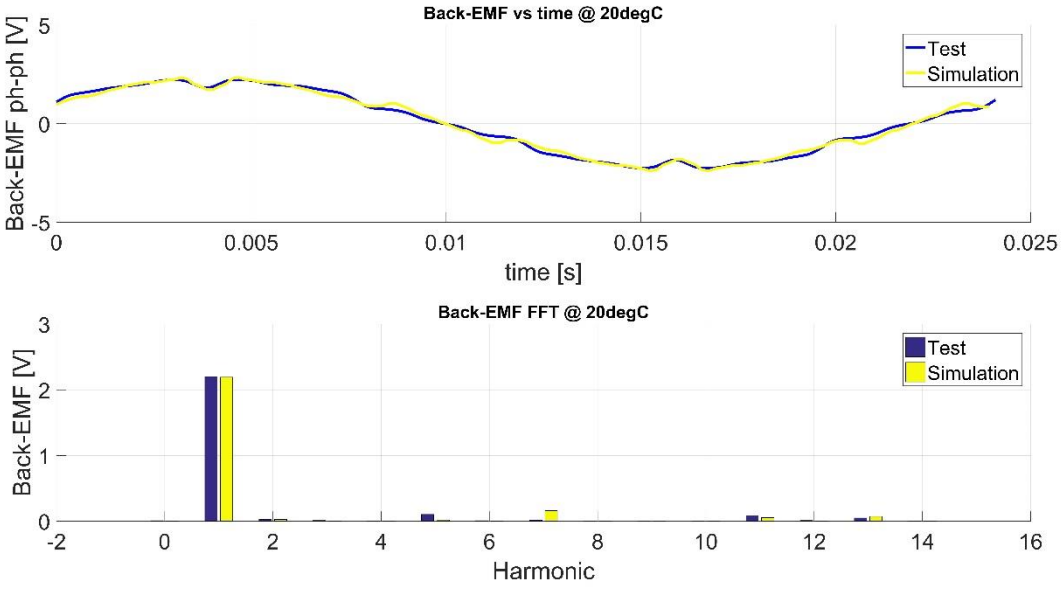

(b)

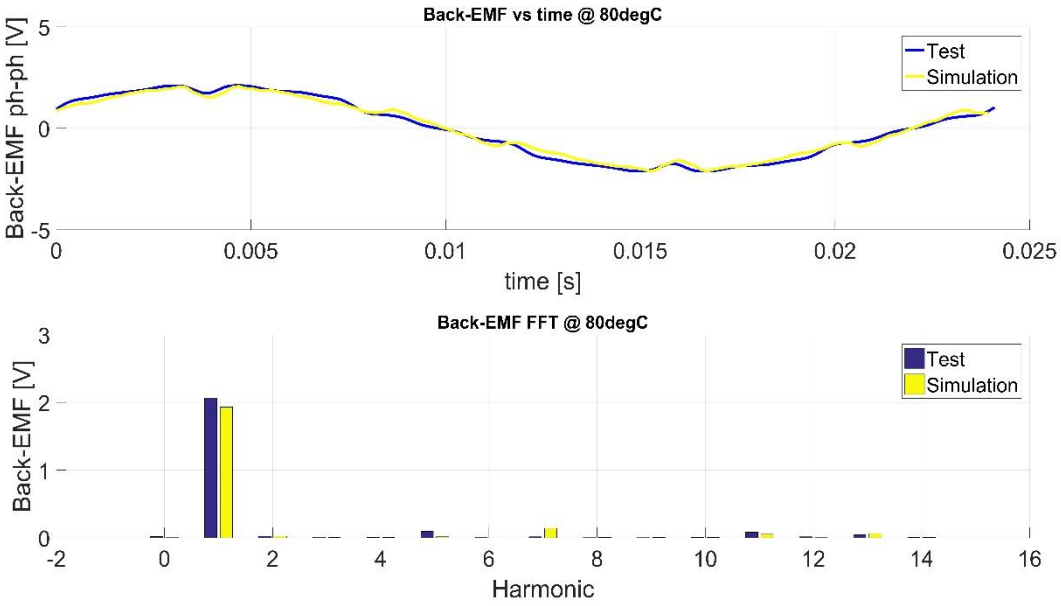

(c)

Fig. 162 Comparisons of back-EMF (phase-to-phase voltage) at 500 rpm (a) between measured Back-EMF at 20 °C and 80 °C respectively; (b) between measured and simulated Back-EMF at 20 °C; (c) between measured and simulated Back-EMF at 80 °C.

Fig. 162 (a) shows that, with the same speed, the fundamental value of the back-EMF at 80 °C is 6% lower than the back-EMF at 20 °C. In the FEM model setting, the Br of the magnet at 80 °C is 7% lower than the Br at 20 °C. Thus, the results are reasonable. Moreover, at 20 °C, the fundamental values of the back-EMF for both simulation and measurement are the same. The only difference is on the high order harmonics – there is a high 5th harmonic component in the test result, while instead there is a high 7^{th} harmonic component in the simulation result. This difference might be caused by the manufacturing tolerance of the rotor, such as the shaping of the rotor surface, or the position of magnet cavities. However, the most important part is that no 6^{th} harmonic component appeared, due to the implement of dual three-phases windings with 30^{o} phase shift. Similar results can be found in the case of 80 °C. However, this time the fundamental value of the simulated result is 5.7% lower than the measured result. There are mainly two reasons to explain the error. First one, in the simulation, we also assumed that Br of the magnet at 80 °C is 35% lower than the ideal situation. However, this degradation might not be such serious in reality. Unfortunately, there was no way to measure the real BH curves of the magnet at 80°C. Second one, when heating the motor from 20 °C to 80 °C, it took around 40 mins. Although the temperature of the coil showed around 80°C, the rotor temperature might not reach 80°C. Thus the back-EMF was supposed to be higher. Nevertheless, the error showed in Fig. 162 (c) is still acceptable.

3.2.2 Short-circuit test

The short circuit test is to make three phases short circuit for both 2 phase sets. The short circuit can be done by one of the operation mode from the power module. It should be highlighted that the short circuit current should by pass the MOSFET component once using the operation mode, and there is an internal resistance in the MOSFET component, which is 0.64 mΩ. During the short circuit, the RMS value of the current was measured by a clamp meter with AC current mode (Fluke 325).

The waveform of the short circuit current was detected by a current transducer (LEM LF 1005). The current signals then were converted to voltage signal and was recorded by the same oscilloscope YOKOGAWA. The converting ratio is 10:1. Thus the comparisons between the measurement and simulation can be made.

2.3.2.1 Short-circuit current

Firstly, the short circuit ramping up test was done. The results of I_{cc} (Arms) are shown in Fig. 163. As the temperature of the coil rapidly increased during the short circuit test, even with 20 °C water cooling, the coil temperature soon reached 30 °C. Thus, the resistance setting in the simulation should be at 30 °C. During the low speed, as the short circuit current is mainly constrained by the resistance (constant), the current increases with the speed. Then starting from 500 rpm around, the short circuit current turns to be constrained by the inductive reactance. As the reactance also increase with the speed, I_{cc} became stable, even with the increasing of the speed. It can be observed that the simulated I_{cc} at low speed (blue curve) is higher than measured I_{cc}. To further reduce the error, it is necessary to take into account the internal resistance of MOSFET in the simulation. Then in Fig. 163, the green curve is obtained. The errors are narrowed down, but not significant. Other reason that may contributed to the error could be the additional joint resistances during the soldering.

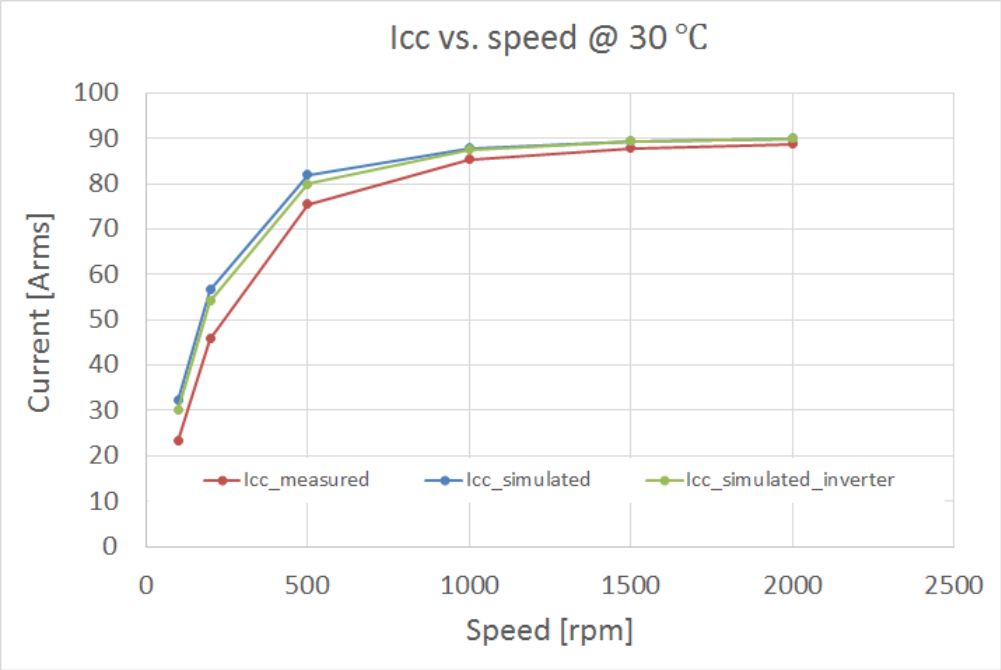

Fig. 163 Short circuit current vs. speed @30 °C

Nevertheless, when the machine is running at 1500 rpm, the short circuit current is stable. Thus its waveform was recorded and was compared with the simulation result, which is shown in Fig. 164. It can be observed that the two waveforms match fairly well. From the FFT analysis, the fundamental value of the simulation result is slightly higher than the measured result. This might be caused by the larger inductive reactance in the mock-up compared to the simulation. Moreover, the high harmonic components are also found in the test results. This also can be explained by the manufacturing tolerances. Nevertheless, the errors are acceptable.

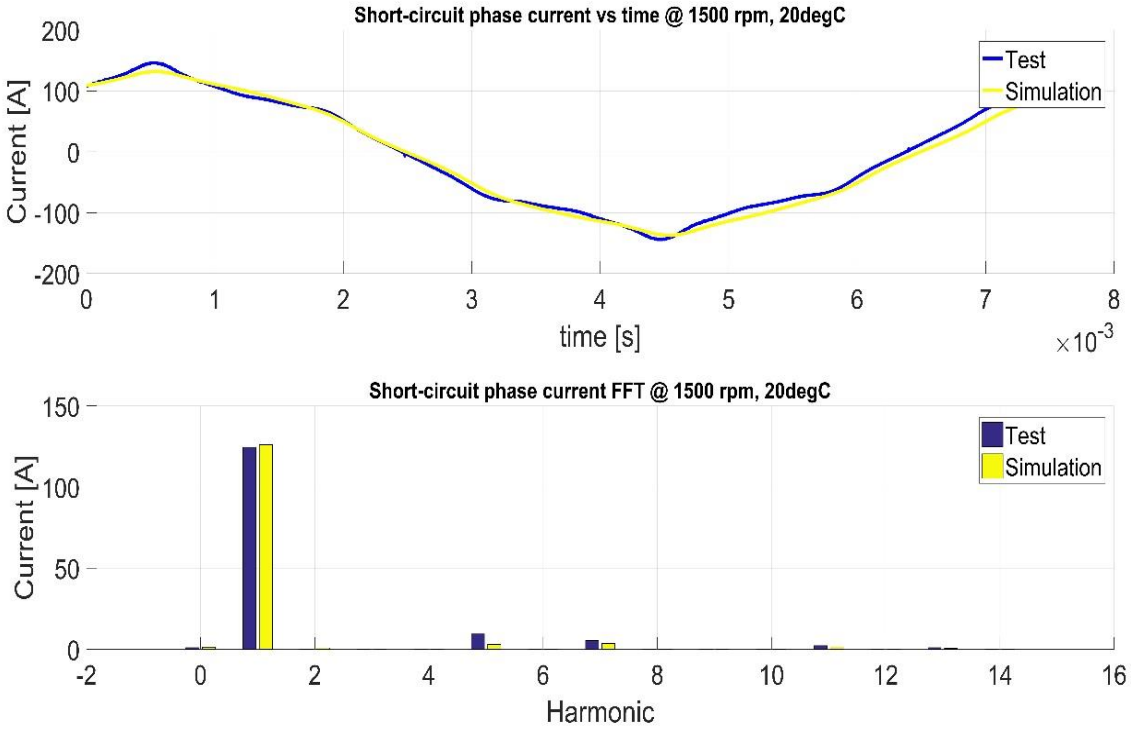

Fig. 164 Comparison of short circuit current at 1500 rpm, 20 °C between measurement and simulation.

2.3.2.2 Short-circuit braking torque

During the ramping up test, the braking torques were also recorded. The braking torque is caused by the losses which are comprised of copper loss and iron loss during the short circuit running. The braking torque can be derived by Eq. 94

$$T_{braking} = \frac{P_{loss}}{\omega_{mech}}$$

Eq. 94

Thus, this is a good way to validate the losses and calibrate the torque transducer. The measured result and calculated result are shown in Fig. 165, with dash lines.

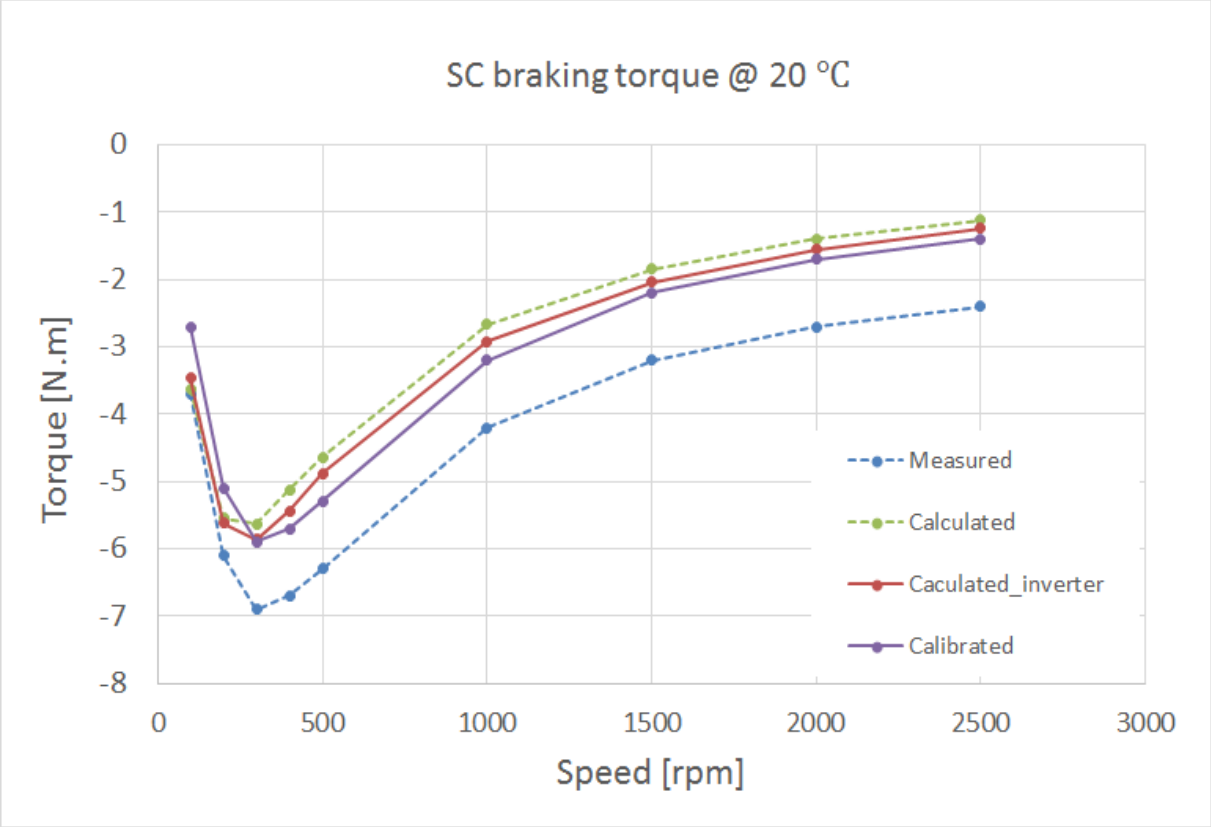

Fig. 165 Comparisons of braking torques during short circuit @ 30 °C between measured, simulated and calculated results.

It can be observed that the original measured torque and calculated torque have very large differences. This might be caused by two reasons – first one, the torque transducer was not well calibrated before the test. It was found during the no load test, there was around -1 [N.m] shown by the transducer. Thus, for a simple calibration, the measured results can be added 1 [N.m]. Second one, still the inverter internal resistance influenced the copper loss, thus with more loss, the braking torque can be larger. After taking into account these two factors, the new curves are shown with solid line. This time the errors becomes very small. Thus, the envisages are reasonable.

2.3.2.3 Thermal states

A short circuit test at 2000 rpm with 80 °C water cooling was done for the thermal measurement. 5 Thermal couplings were placed around the end winding to monitor the temperature of the coils. The results are shown in Fig. 166. It can be observed that for the first 5 minutes, the coil temperature was ramping up quite fast. Afterwards, the coil temperature stayed at a stable level, around 97 °C. Actually even at the top speed, the short circuit current will be basically the same. Only the iron loss and mechanical loss will increase. However, compared to the copper loss, the iron loss is still very small. Thus, for the mock-up, the thermal state is totally acceptable.

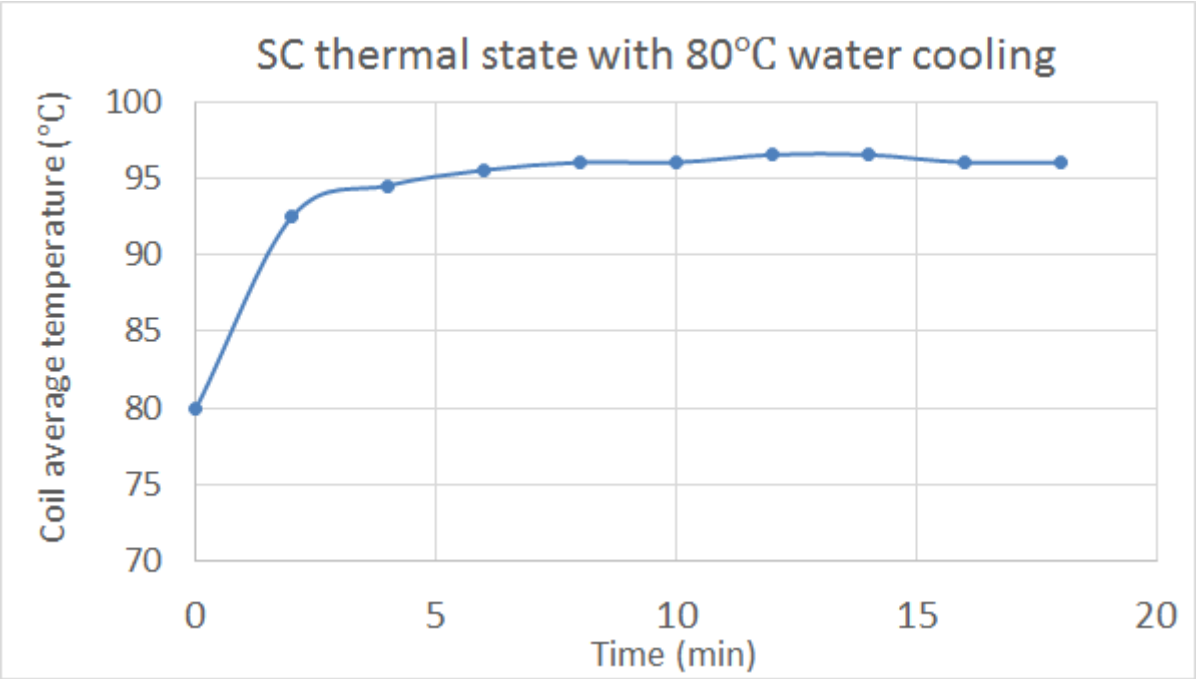

Fig. 166. Thermal states of the coil during short circuit test with 80 °C water cooling at 2000 rpm

3.2.3 Load tests

Finally, with the validated data and calibrations, load tests could be carried out. First, at a certain speed, say 500 rpm, the torques could be measured with the ramping up of the current amplitude and the sweeping of the current angle. Then the load tests with optimal efficiency control could be carried to validate the proposed efficiency maps.

2.3.2.1 Torque angle curves

The machine was set running at 500 rpm. Then different current amplitudes were given with current angle changing from 90° to 270°. The torque results are shown in Fig. 167 (a) and Fig. 167 (b) respectively for 20 and 80 °C. Due to the controller problem, the points (150 Arms, 270°) and (200 Arms, 250, 270°) were not able to be tested. Besides, due to the risk of over torque, tests with 200 Arms at 20 °C were abandoned.

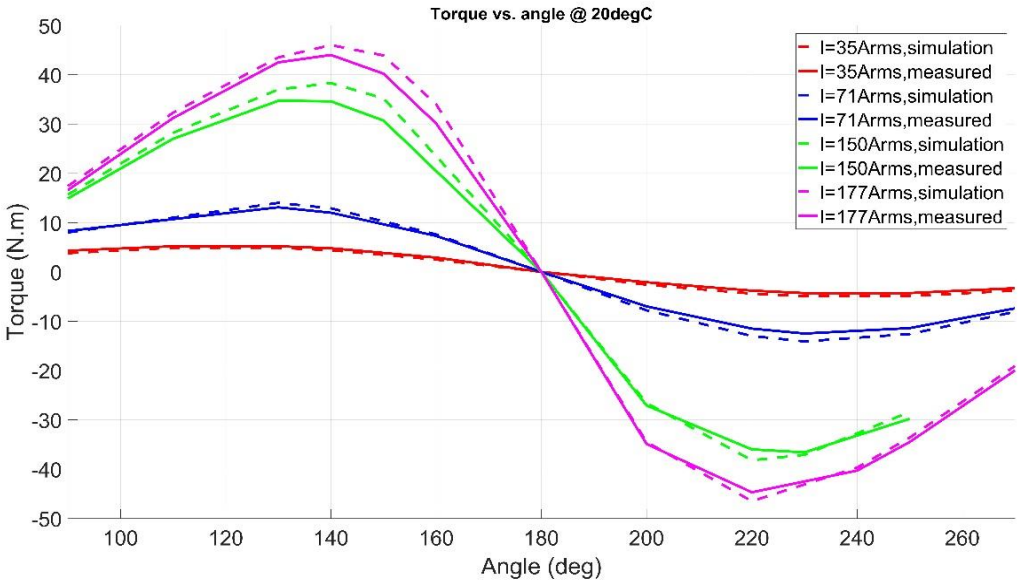

(a)

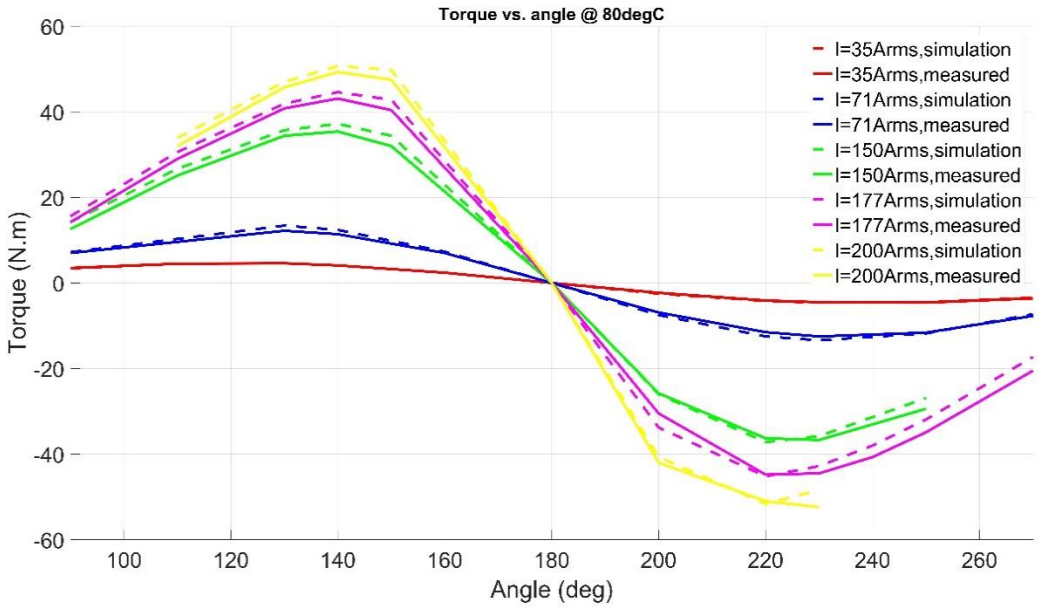

(b)

Fig. 167 Comparisons of measured and simulated results of torque vs. angle curves with different current levels at 500 rpm after calibration (a) @ 20 °C, (b) @ 80 °C

It can be found the trend of change of the torque with current amplitude and angle was aligned with the simulation results. Small errors can also be found between measurement and simulation results. To better observe the errors, Eq. 95 can be made to show the error. The results are shown in Fig. 168.

$$\mathrm{T}_{error}(\%) = \left(\frac{\mathrm{T}_{\mathrm{measured}}}{\mathrm{T}_{simulated}} - 1\right) * 100 \qquad \text{Eq. 95}$$

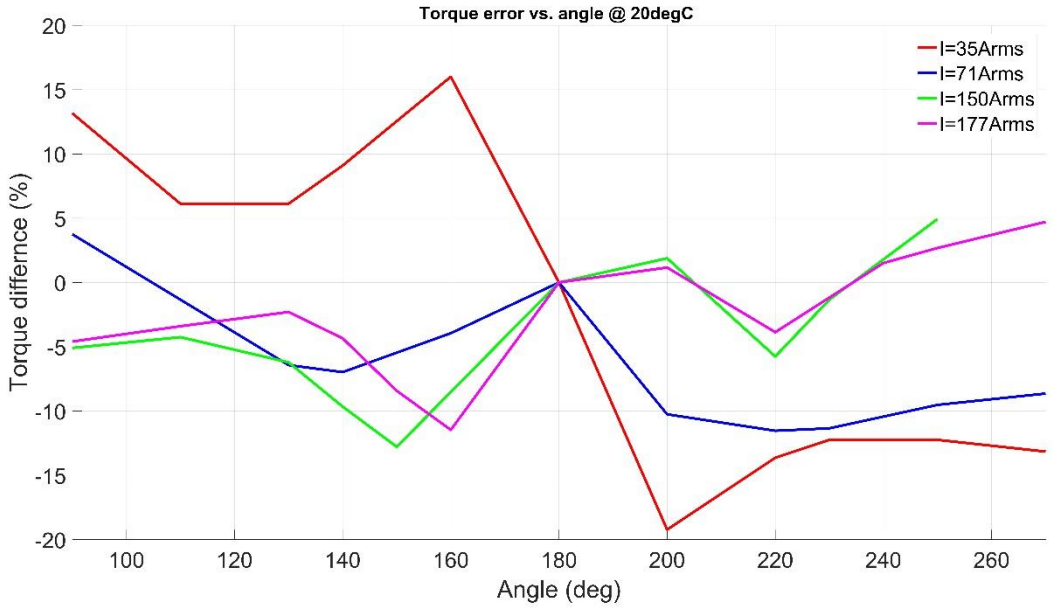

(a)

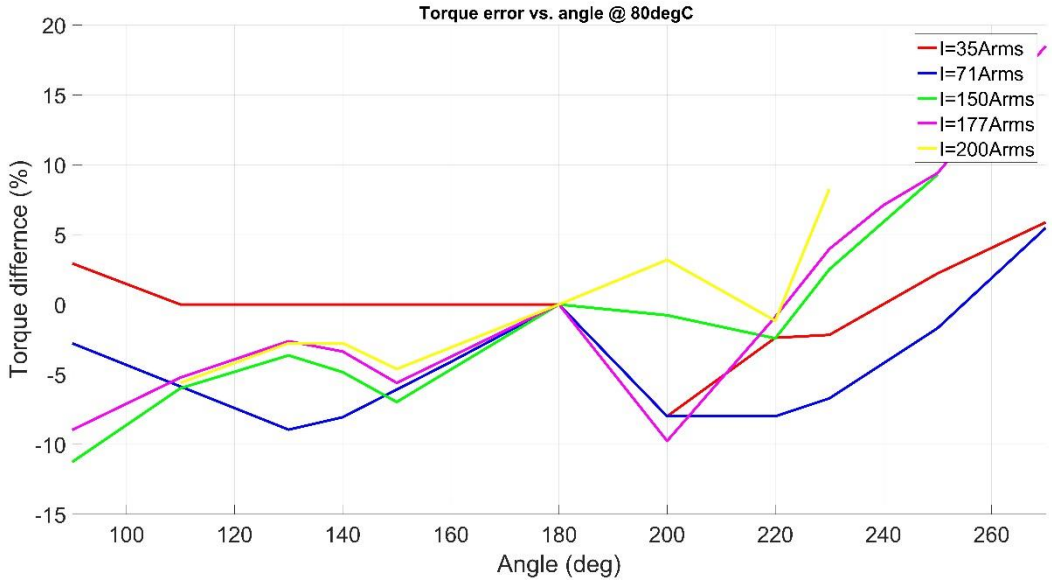

(b)

Fig. 168 Torque error between measurement and simulation vs. angle with different current levels at 500 rpm after calibration (a) @ 20 °C, (b) @ 80 °C

It can be observed that, no matter what current or what temperature was, the patterns of the error that changing with the current angle were quite similar. The error is a kind of symmetry distribution with 0 [N.m] axis. Most of the differences in percentage are within ±15%. It needs to be highlighted that although the error percentage looks quite significant for cases I=35 [Arms], the errors in fact were very small once they were switched to absolute value, as Fig. 169 shows. It is only because the lower torque regions are very sensitive to the errors.

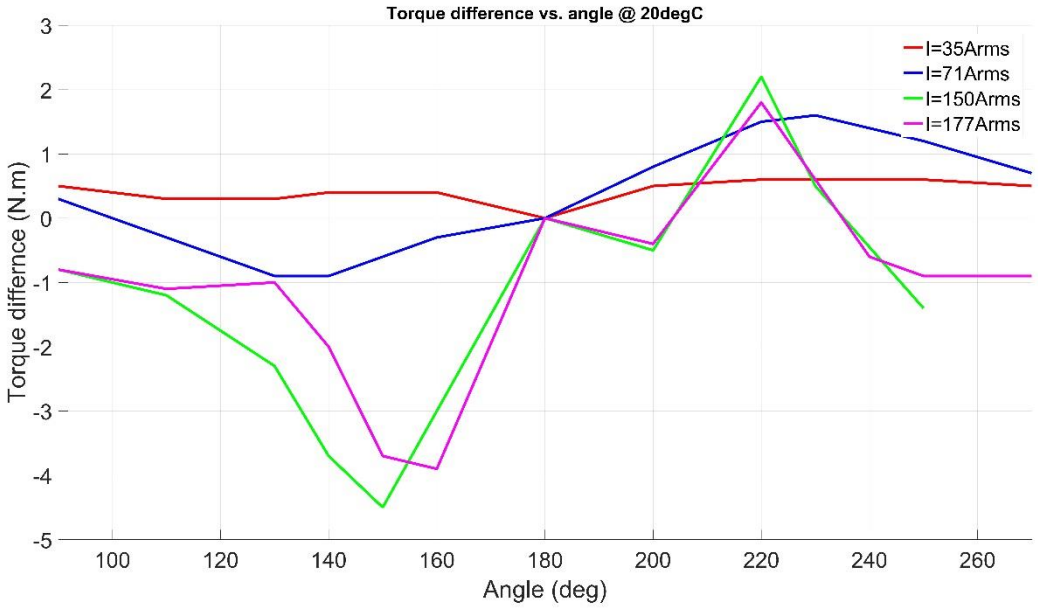

(a)

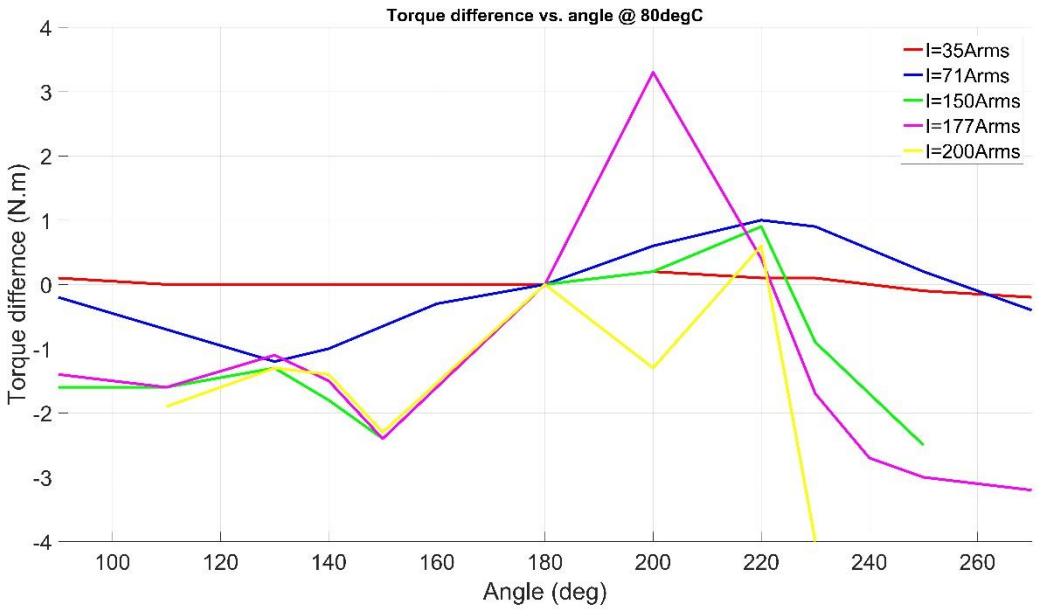

(b)

Fig. 169 Torque difference between measurement and simulation vs. angle with different current levels at 500 rpm after calibration (a) @ 20 °C, (b) @ 80 °C

It can be observed that normally with higher torque, the error was larger as well. Thus, it can be deducted that the torque transducer with the belt system might enlarge the torque error with the increase of the torque. It was not enough by simply adding 1 [N.m]. Unfortunately, it was not able to calibrate the torque with load condition. Nevertheless, the errors shown in Fig. 168 and Fig. 169 are in acceptable level.

2.3.2.2 Efficiency

Finally, the efficiency tests were done. The efficiency could be measured by the test bench. As discussed in the beginning of section 3.2, the input and output power could be obtained. However, by measuring the DC side current and voltage, the losses in the inverter cannot be separated from the total losses. Besides, the mechanical loss model used in the previous efficiency map calculation was mainly for a gear system. However, the mechanical loss model of the belt system is very different with the gear system. Normally the belt driven mechanical loss is larger than gear system. Moreover, the loss not only changes with the speed, but also with the torque, due to the tension changed in the belt. Unfortunately, it is not available to obtain the belt system mechanical loss model. Besides, the PWM control can generate high order harmonics, which is also ignored in the iron loss simulation. Thus, efficiency errors are supposed to be large. Unfortunately, due to some control problem at high speed, the machine tests could only run up to 4000 rpm with the right torque. Nevertheless, for the no load test, the machine had successfully run up to 9000 rpm. Thus, the rotor mechanical strength was proved to be acceptable at least at 9000 rpm.

Totally 37 operation points were tested at 20 °C; 39 operation points at 80 °C. For these operation points, the efficiency, as well as the I_d and I_q input currents were first being estimated by using the same methodology in Chapter 2 efficiency map plot. Then the measurements were done based on the extracted I_d and I_q currents. Finally, the measured results of torque and efficiency were compared with the estimated results. It needs to be noted that these measured results were also calibrated with the same way shown in the last sections.

First, the torque errors were shown in Fig. 170. The torque error was expressed by Eq. 96,

$$T_{error} = \frac{T_{measured}}{T_{estimated}} - 1 \qquad \text{Eq. 96}$$

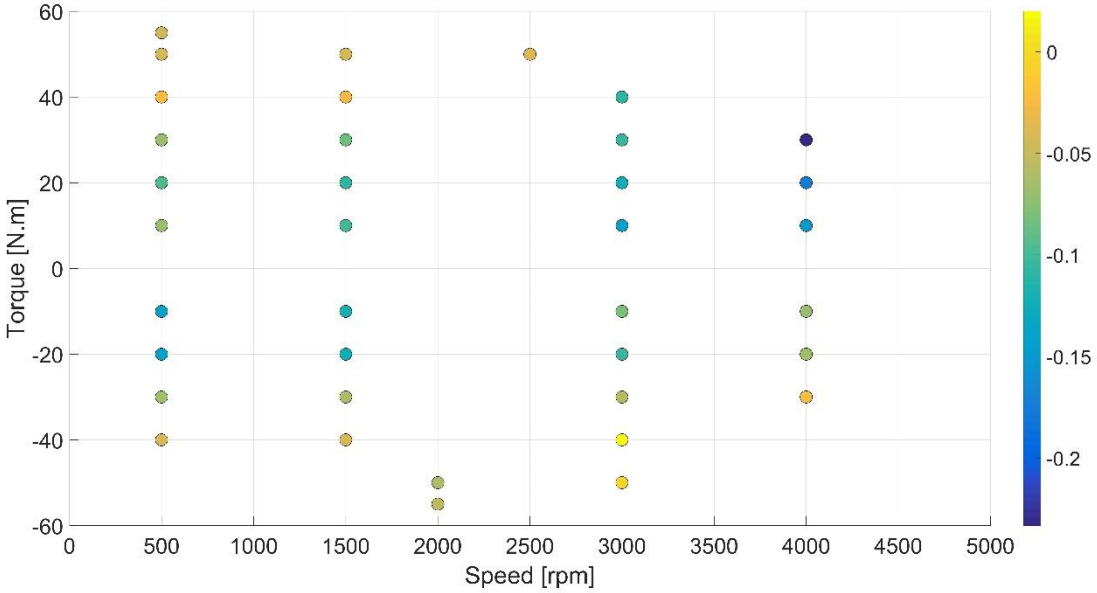

(a)

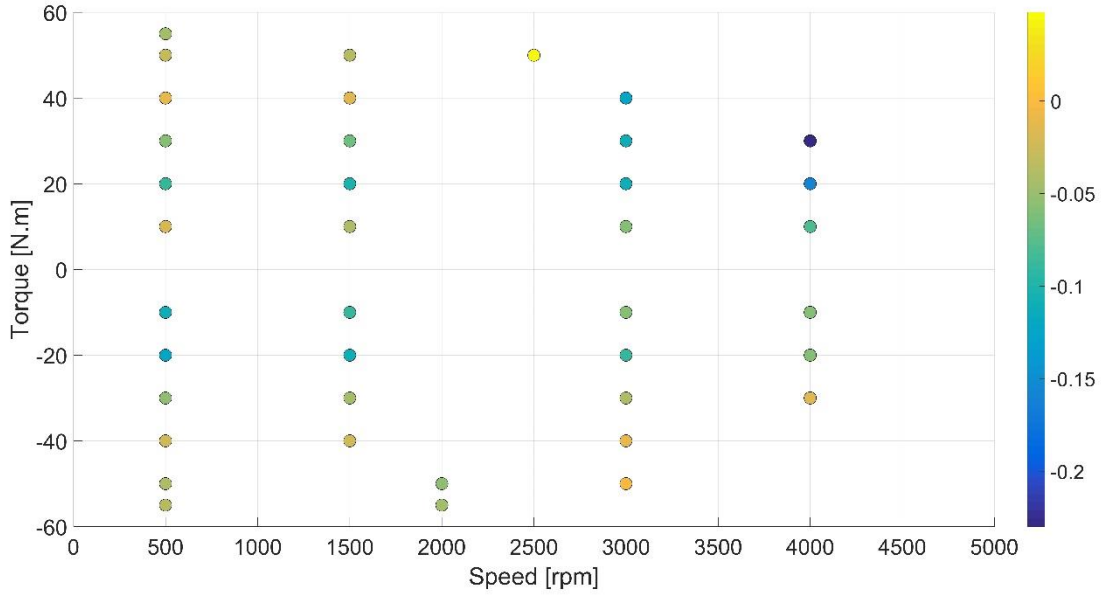

(b)

Fig. 170 Torque error between measurement and simulation with optimal efficiency control after calibration (a) @ 20 °C, (b) @ 80 °C

It can be observed that the measured torque was commonly lower than estimated torque. These errors were quite large in the high speed with high torque and low torque regions. The errors in the high speed and high torque region further indicate the calibration problem of the belt system with load. The high errors in the low torque region are still due to the high sensitivity in this region.

Then the loss errors are shown in Fig. 171. The expression for the loss error is Eq. 97,

$$L_{error} = \frac{L_{measured}}{L_{estimated}} - 1 \qquad \text{Eq. 97}$$

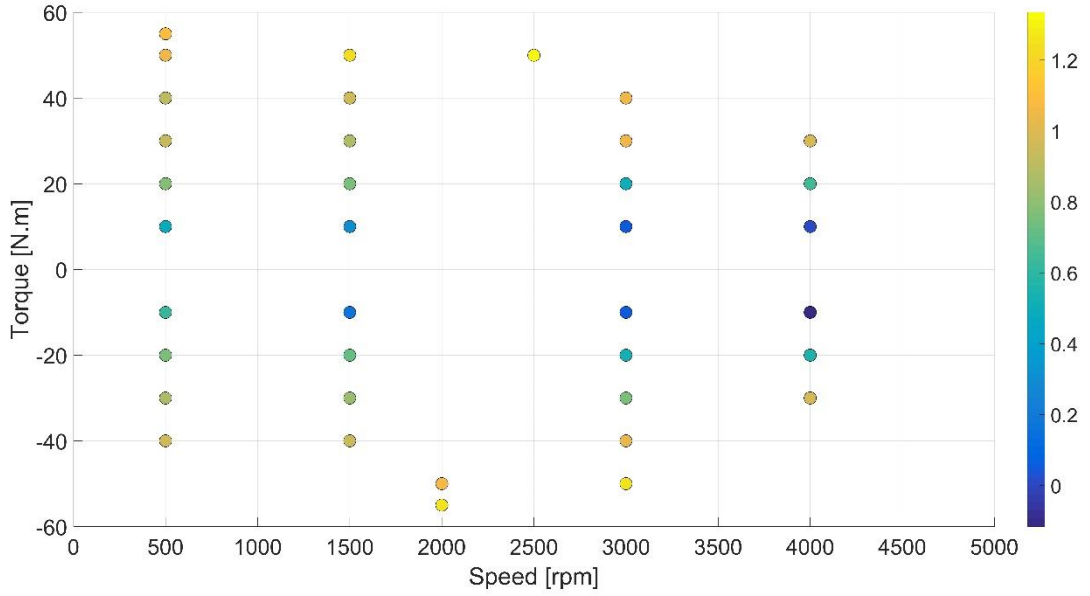

(a)

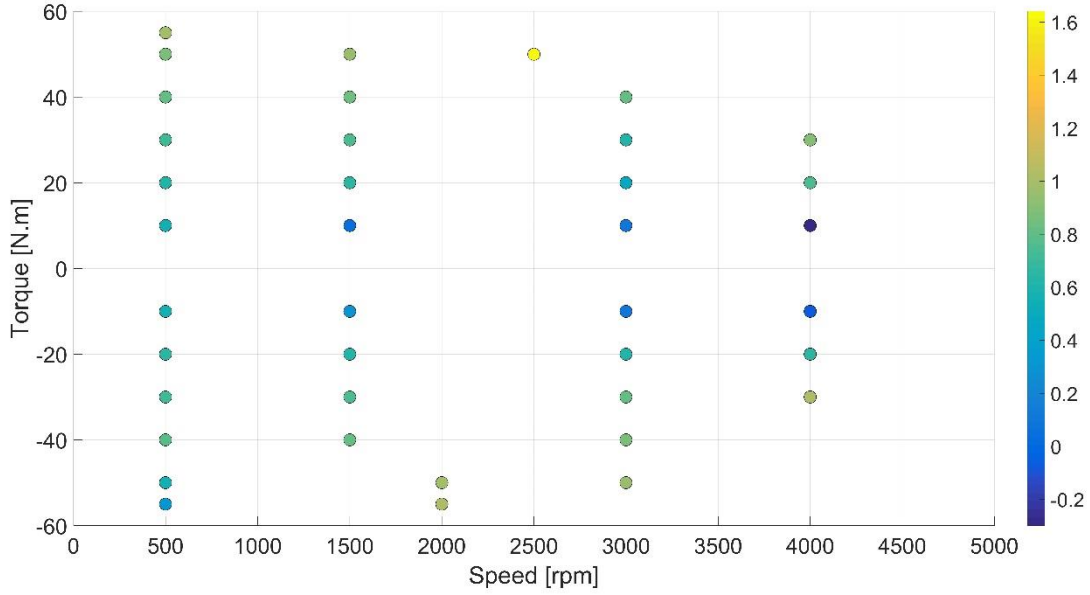

(b)

Fig. 171 Loss error between measurement and simulation with optimal efficiency control after calibration (a) @ 20 °C, (b) @ 80 °C

It can be observed that most of the measured losses are higher than the estimated losses. This is expected as the measured losses had taken into account inverter losses and additional belt mechanical losses. The loss error increased with the torque, which indicates the inverter losses and mechanical losses also increased with the current and the torque. Moreover, it is possible that the iron losses were under estimated at high speed.

Finally, the efficiency could be obtained, which is shown in Fig. 172.

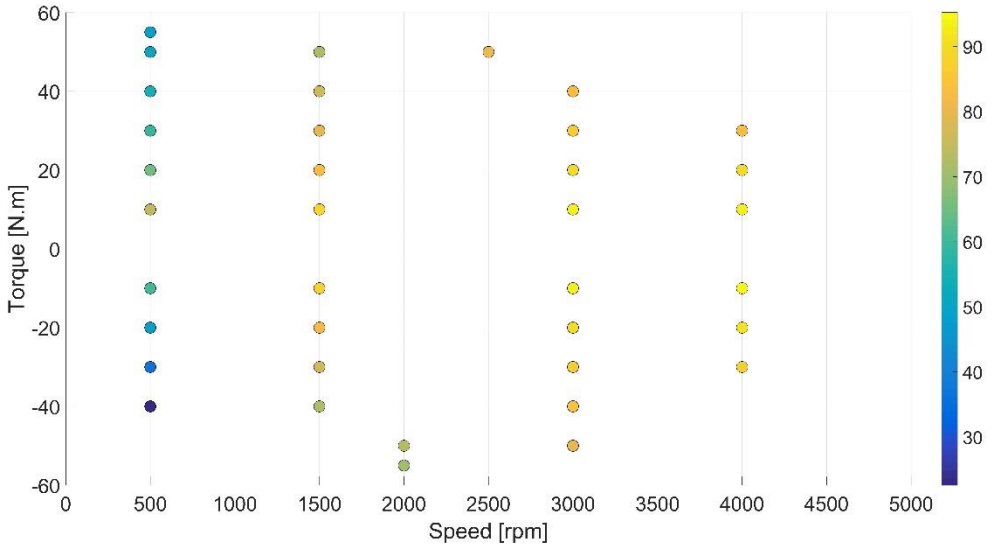

(a)

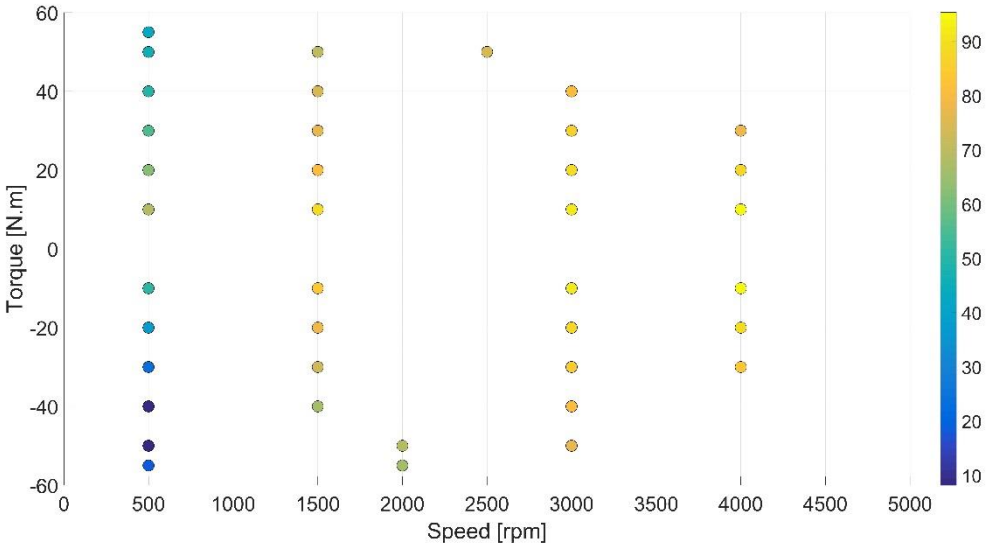

(b)

Fig. 172 Measured efficiency after calibration with optimal control (a) @ 20 °C, (b) @ 80 °C.

From Fig. 172 (a) and (b), it can be observed that the high efficiency areas are in high speed and low torque regions for both thermal conditions. This is due to the facts that in these regions, the e-machine, the inverter and the belt system all running in their most efficient area. On the other hands, the efficiency was very low in low speed high torque regions. Again, these regions were coincided with the least efficient region of the e-machine, the inverter, as well as large the belt system. Nevertheless, the distribution of the efficiency is in our expectation.

3. 3 Conclusion

An IPMSM with a special bonded NdFeB magnet that can be easily reused was studied. The rotor of the IPMSM was optimized by trying different numbers of layers. It was found the rotor with two-layer magnets could make a good compromise between performances and manufacture difficulty.

Then based on the 2-layer rotor design, an IPMSM mock-up was fabricated and tested. It was found that the magnet cannot meet the requirements, remanence flux density was 35% lower than the ideal case. Thus, new simulations were then performed on the basis of these new measured magnetic characteristics of the magnets. Numerous reference tests have been carried out at different temperatures to evaluate the performance of this machine, such as no-load, short-circuited or load tests for both generator or motor mode. The results showed that the differences between measurements and simulations are in reasonable levels that allowing simulation results to be validated.

Chapter 4 –Recyclability indexes

4.1 Introduction of WIRE methodology

In this project, apart from new design ideas of electrical machines, another goal is to evaluate e-machines with respect to the recyclability. Here the definition of the recyclability has two aspects :

- If the e-machine can be easily disassembled, and if the material can be easily recycled?
- If the e-machine can utilize the recycled materials without or with acceptable performance degradation?

At present no tool is found to evaluate this recyclability for e-machine designs. No experiment had been conducted for benchmark. Based on the two aspects of the recyclability, in this thesis two methods are presented to analyze and evaluate the recycling of PM e-machines for EVs:

- The first method evaluates recyclability of the production and recycling phases of a PM e-machine, regarding its assembly, disassembly and standardization.
- The second method evaluates the recyclability at the user phase. Mainly the impacts of utilizing recycled materials (in this case is recycled PM only) on the energy consumption of an e-machine over the complete user phase is analyzed.

The results of both methods are presented by two indexes. These indexes together can be named Weighted Index of Recycling and Energy (WIRE). By using WIRE, the recyclability between different machines can be compared, even with different dimension or power.

In this chapter, WIRE was first established and validated on a commercial PM HUB motor used for a small golf car. The HUB motor was disassembled for evaluating the WIRE index of production and recycle phases. Then an identical HUB motor was used for efficiency benchmark. Finite Element Method (FEM) results were validated with experiment results. Afterwards the energy consumptions of the machines with virgin magnets and recycled magnets respectively were calculated, thus the second WIRE index of user phase could be evaluated.

Finally, the validated WIRE methods were used to evaluate the 2-layer IPMSM. The scores of indexes are presented and discussed.

4.2 Methodology of weighted recycling index

The first part of the WIRE methodology is to evaluate the ease of assembly/disassembly of PM e-machines. The evaluation process is divided in two parts - **Standard** and **Cost**. Each part has three categories - **Material**, **Assembly** and **Disassembly**. Moreover, the evaluation of each material or process in each category is done by two parts. The first one is **Score (S)** which depends on its relative scale of the respective section. The second one is **Importance (I)** which can be understood as weight, depends on material/process relative criticality in terms of the recyclability of materials. The final score is the product of both i.e. (**S x I**).

The Score for each activity is in the range of 1-5. For evaluation of WIRE it is recommended to have a group of 5-6 people from different fields, involved in design and manufacturing process of the PM e-machines. Fig. 173 shows part of the evaluation sheet for the different materials of a motor for both standard and cost. Although, the evaluation largely depends on the mutual agreement of the group formed for evaluation i.e. standard and cost, certain guidelines are formed to evaluate different sections. Furthermore, the process/materials in different sections are different depending on the criticality of the material/process. For example, the wires of sensor are important while assembling however, their importance is negligible while disassembly.

Scoring pattern	0-5	1 - Lowest score		5 - Highest score				
		1 - Lowest score		5 - Highest score		3 = neutral score		
Assumption	The motor developed is new and for the first time and manual disassembly with high volumes i.e. 50,00(							
MOTOR ID	**Hub motor for in-wheel application**							
Component/ Parts		**Standard**			**Cost**			**Recyclability SCORE**
		S	**I**	**SxI**	**S**	**I**	**SxI**	
Materials								
- Stator								
	Lamination S	5	5	25	1	5	5	30
	Copper	5	5	25	2	1	2	27
- Rotor								0
	Steel R	5	5	25	1	4	4	29
	Magnets	5	4	20	5	1	5	25
-Shaft								0
	Shaft	4	5	20	1	2	2	22
-Endshileds								0
	Drive Side	2	5	10	1	2	2	12
	Non-Drive side	2	5	10	1	2	2	12
			34	135		17	22	157
	section score			79.41 %			25.88 %	

Fig. 173 A glimpse of WIRE evaluation sheet of material for standardization and cost

4.2.1 Definitions of WIRE sheet

Since the WIRE evaluation is relative, the accuracy of the method largely depends on the definitions of different sections. Different processes/materials have different significance in the final recycling phase of the machine. It is important to note that the tool is reasonable for comparing e-machines only if the same scaling is kept. For instance, if two e-machines use the same magnets with the same quantity, the cost of their magnets should be the same.

In the following section definitions of different terms used for the evaluation are given.

- **Standard**: The category focuses on the use of standard material/processes. The evaluation for Standard category is done with the view that use of standard parts/process will simplify and encourage the recycling. Furthermore, higher the number of standard component in the motor, easier it will be for recycling and quality improvement of the recycled output.

1) Material

– 'S' depends on the standardization of a material. The score is high for the material, which are easily available (off the shelf) and widely used. For example, random wound copper winding are more used and widely available than rectangular strand cable of certain dimension.

– 'I' depends on materials recyclability. For example, NdFeB magnet with and without coating is easily available however, in terms of recyclability the magnet without coating will be easier for recycling and hence its index shall be higher.

2) Assembly

– 'S' depends on the process/activity standardization. While scoring it is also important to consider the tools used. More non-standard tools or process used in assembly shall lower the score. For example, if special heat treatment/ or other special environment (such as oxygen free environment) is needed for assembly, process will be non-standard and thus the index shall be lower.

– 'I' depends on the criticality of the step/process for recycling of the part. For example, if the assembly of the copper facilitates the recycling of the copper. Therefore, the index shall be high.

3) Disassembly

– 'S' depends on the process/activity standardization. While scoring it is also important to consider the tools used. More non-standard tools or process used in disassembly shall lower the index. For example, if some chemical is needed for extraction of certain component, the score shall be lower for the process.

– 'I' depends on the criticality of the step/process for recycling of the part. Same as assembly, if disassembly process of copper makes recycling easier, the index shall be higher.

- **Cost**: The category focuses on the cost of material/processes and its impact on recycling. The evaluation for Cost category is done with the view that higher cost of any process will increase the overall recycling cost and hence, has negative impact on the recycling. On the other hand, higher material cost incentives the recycling of that particular material like magnets and encourages recycling.

1) Material

– 'S' depends on the cost of the material. Higher the material cost higher the score. The processing cost of the component varies over a wide range. Therefore, to keep the tool simple and to avoid processing cost variation of the component only material cost is considered. Moreover, the non-standard design or the impact of processing will be taken care while scoring standard category. For example, NdFeB magnet is roughly 10 times costlier than normal laminations in the motor. Therefore, score of magnet will be higher than the laminations. The impact of different shapes of magnet should be considered while scoring standard material category.

– 'I' depends on the impact of the material on recycling of the whole motor. For example, if the weight of the material is very low comparing to other materials, the material recovered will be very small. Therefore, the recovery in terms of economic value will be small, even with high price of the material.

2) Assembly

– 'S' depends on cost required to execute the assembly process/activity. Higher the assembly cost lower the score shall be as it impacts the recycling process negatively. For example, if there is a need of special environment for assembly, it increases the complexity and hence cost.

– 'I' depends on the impact of cost on the process of recycling. For example, if a motor uses powder NdFeB magnet technology. The assembly cost is higher but this cost does not impact the recycling of the magnet at the end of life (EOL) of the motor. Therefore, the index shall be neutral.

3) Disassembly

– 'S' depends on cost required to execute the disassembly process/activity. Higher the disassembly cost lower the score shall be as it impacts the recycling process negatively. For example, if there is a need of special environment for disassembly, it increases the complexity and hence, cost which in turn discourages recyclability economically.

– 'I' depends on the impact of cost of the process in recycling. For example, the cost of disassembly of the magnet is very critical for the recycling of the magnet. Therefore, the index shall be high for that process.

It needs to be noted that to simplify the scoring system, the scales of both **S** and **I** are in the range of 1-5. No matter how expensive the magnets can be, the highest score is 5. No matter how cheap a normal iron lamination can be, the lowest score is 1.

The final weighted recyclability index (R) is calculated by using Eq. 98 and Eq. 99. The R_w is in the scale of 1-5, and Eq. 99 is expressed in percent, R.

$$R_w = \frac{S_1 I_1 + S_2 I_2 + \cdots + S_n I_n}{\sum I} \quad \text{Eq. 98}$$

$$R = \frac{R_w * 100}{5} \quad \text{Eq. 99}$$

4.2.2 General guidelines for scoring

This section provides some general guidelines, which can be used to score different parts of WIRE sheet. It is important to note here that the scores are relative and can be varied on general consensus or when scenario changes. The authors decided the scores after discussing different scenarios.

1) Scoring of materials for Standard category: TABLE XXXV shows the scoring of material and its importance for recyclability with respect to their standardization. The table shows the scores for main components of the motor like lamination, magnet and copper. The materials are scored based on the definition given in Section 4.2.1.

TABLE XXXV
SCORING OF MATERIAL FOR STANDARD
CATEGORY (A) SCORE; (B) IMPORTANT

(A)

Magnet Type	**S**
Rectangular small pieces with/ without coating sintered, Bonded Magnet	5
Sintered/bonded shape parallel/radially magnetized	4
Halbach bonded	3
Sintered or Bonded powder but magnetized in rotor	2
Sintered Halbach multi-pole	1
Lamination Type	**S**
Silicone iron 0.35-0.6mm, Single solid rotor	5
Silicone steel modular type	4
Cobalt Steel	3
Amorphous, different shapes	2
SMC	1
Winding Type	**S**
Copper / aluminum strand circular	5
Copper rectangular standard, aluminum cast rotor	4
Copper rectangular/circular non standard	3
Hollow circular copper wire	2
Any thing special	1

(B)

Magnet Type	**I**
Rectangular small pieces or powder without coating or binder	5
Sintered with coating	4
Sintered any shape with coating/glue	3
Bonded magnets	2
Bonded magnets with glue	1
Lamination Type	**I**
Any silicone iron lamination or solid rotor or Aluminum	5
Cobalt steel	4
Amorphous Steel	3
Soft Magnet Composites (SMC)	2
Any new special handling material	1
Winding Type	**I**
Copper any type	5
Aluminum wire/Cast aluminum /Copper rotor	4

2) Assembly/Disassembly score for Cost: TABLE XXXVI gives the scoring guideline for assembly/disassembly in terms of cost. Simpler the process higher the score shall be.

TABLE XXXVI S OF ASSEMBLY/DISASSEMBLY FOR COST CATEGORY

Assembly/Disassembly Cost	**S**
Easy assembly/disassembly without any tool	5
Easy assembly/disassembly with standard tools /process	4
Complex / Hard process with standard tools	3
or more than one person required	2
Special pre/post treatment with special tools	1

3) Assembly/Disassembly of stator and rotor: The scoring guideline for individual components (stator, rotor, bearing etc) was shown in TABLE XXXVI. However, there is one more critical step in assembly/disassembly, which is separation of a rotor from a stator. The complexity of the process is even higher in PM motors. The ease of assembly / disassembly mainly depends on the force of extraction and the size of the machine (mainly rotor size). Therefore, to scale the process following method is used. Larger the volume and airgap flux density i.e. power of the e-machine, separation of rotor and stator will be difficult and hence, the score shall be lower. Mathematically it can be presented by Eq. 100.

$$S \propto \frac{1}{V * B_{\delta}^{2}} \qquad \text{Eq. 100}$$

Where V is the volume and B_{δ} is the average airgap flux density of the motor.

4) Scoring of material for Cost category: The scoring of *'I'* depends on the weight of the material in the motor. Higher the weight of the material higher will be the recovery of material from recycling. The proposed method to estimate that is as follows. Let's assume, the motor has *Wc* kg of Copper, *Ws* kg of Stator steel, *Wr* kg of rotor steel and *Wm* weight of Magnet, and the weight *Ws* of stator steel is the higest. The 'I' score for stator steel *Ws* is 5 and the rest is scaled in proportion to the *Ws*. The fraction numbers are rounded to nearest integer.

$$\text{I for magnet is } \frac{W_m * 5}{W_s}$$

$$\text{I for copper is } \frac{W_c * 5}{W_s}$$

TABLE XXXVII shows the relative score of material used in the motors. It needs to be highlighted the proportion of the cost scores between different materials is not the same with the proportion of the real prices between different materials. There are mainly two reasons for that:

- The price of each material is changing all the time, different material suppliers also provide different prices.
- Some proportion of the real prices is way out of 5, which is incompatible with the method. For instance, the proportion of the real prices of NdFeB magnet vs steel is always above 10. If the price of NdFeB magnet at year 2011 is taken into account, the proportion is around 100.

Therefore, it is only possible to give a general idea of the material cost.

TABLE XXXVII SCORE OF MATERIAL COST IN AN E-MACHINE

Material cost	S
Sintered Magnet	5
Bonded Magnet	4
SMC, Amorphous steel	3
Copper	2
Silicone Steel lamination	1

5) *'I'* of assembly/disassembly for Standard & Cost category: The criticality of each step during assembly and disassembly is shown in TABLE XXXVIII. While indexing, the recycling of steel, copper and magnet was considered important and hence, the process that affecting their recycling was indexed accordingly. If some steps of assembly are very important for the recycling of that material, they shall have high importance. For example, assembly standard of magnet and rotor is essential for the extraction of magnets. Thus, it gains high importance. Otherwise, if the criticality is neutral to recycling, thus 'I' should be given by 3.

TABLE XXXVIII IMPORTANCE OF ASSEMBLY/DISASSEMBLY PROCESS

Process	Standard Importance	Cost Importance
Assembly of stator lamination	3	3
Assembly of copper winding	3	3
Assembly of rotor lamination	3	3
Assembly of magnet and rotor	5	3
Assembly of sensor wires	1	3
Assembly of rotor and stator	3	3
Assembly of end shields	3	3
Assembly of shaft	3	3
Disassembly of end shields	3	3
Separation of rotor and stator	4	4
Disassembly of copper	3	4
Disassembly of stator	3	3
Disassembly of magnets from rotor	5	5
Disassembly of rotor	3	3

4.2.3 Demonstration of the recycling index calculation of HUB motor

The developed methodology was used for evaluating a commercial PM based HUB motor. The motor was disassembled manually with standard tools, and the process was observed and recorded regarding the recycling of the parts. Fig. 174 shows the different stages while disassembly of the motor. This is an outer rotor surface mounted PM motor. It has random wound windings (concentrated winding), and segmented lamination.

After completing the disassembly, the WIRE sheet was filled. For simplicity many assembly/disassembly steps were clubbed together and S and I were given. The details of the WIRE scoring table are shown in Appendix part 4.

A statistic plot of the standard and cost of the HUB WIRE evaluation is shown in Fig. 175. It is found that the final cost index is lower than the final standard index. The motor is a commercial motor and has used more standard parts and processes. The index for cost of the material is lower compared to assembly and disassembly. It is important to note here that the index is relative and in absolute terms cost of material can be higher than the assembly and disassembly of the motor. As mentioned earlier the method is developed to compare different motors recyclability. The final recycling index (R) of the motor is 68.5%. This can be a baseline for scorings of other machines.

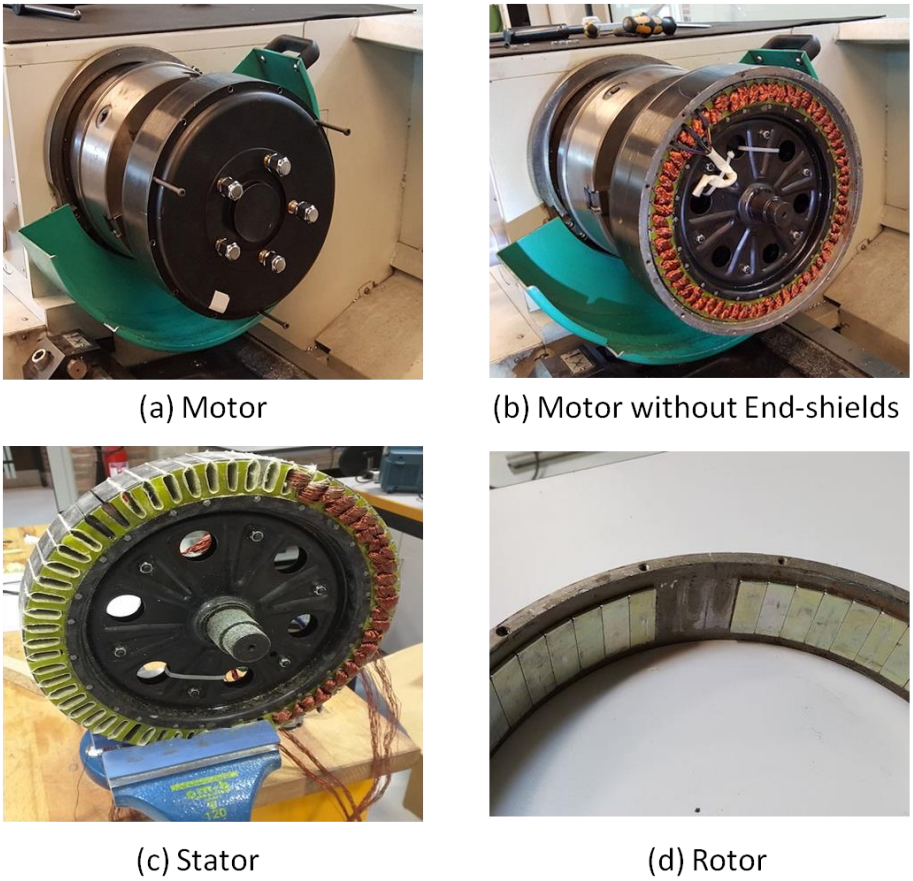

Fig. 174 HUB motor disassembly step by step

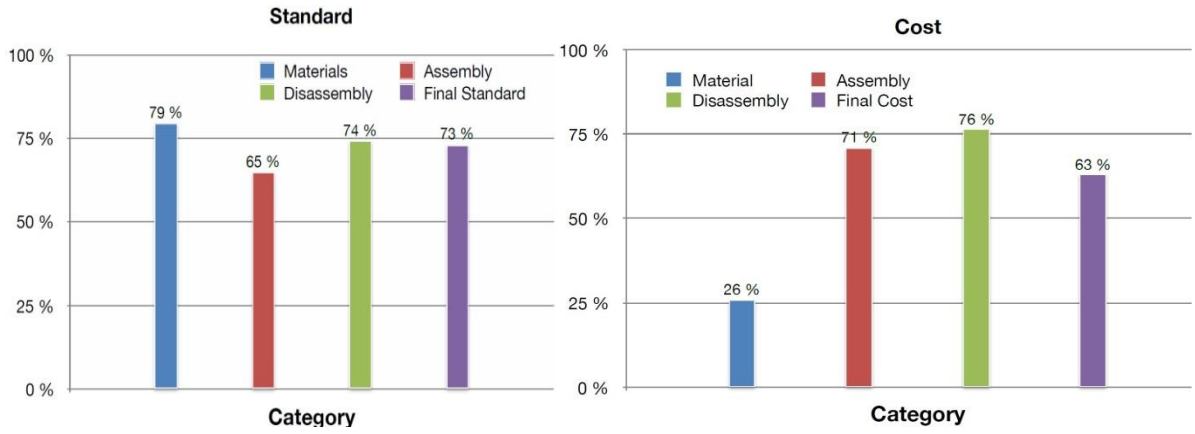

(a) (b)

Fig. 175 Index distribution of the recycling index of the sample HUB motor

4.3 Energy index

4.3.1 Methodology of energy index for pure EV

The second part of the WIRE methodology is to evaluate the impact of utilizing recycled magnets to the energy consumption of an e-machine. An evaluation flow diagram is proposed in Fig. 176.

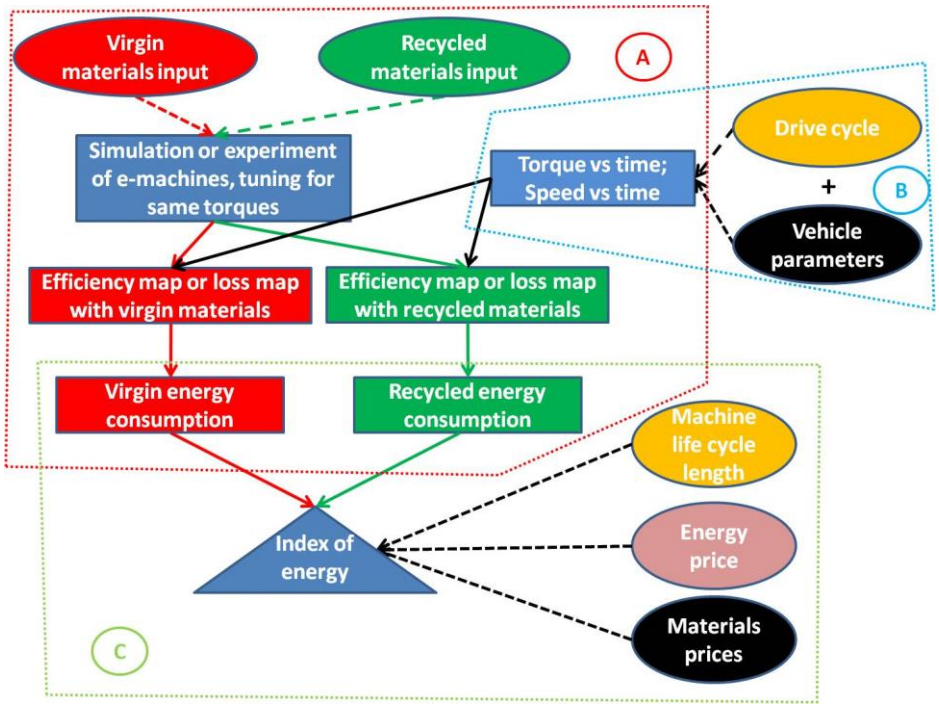

Fig. 176 Index of energy calculation flow diagram for EV (A) Machine performances (B) Torque and speed requirements (C) Index of energy calculation

The evaluation flow is mainly divided into three parts – (A) Machine performances calculation; (B) Torque and speed requirements; and finally (C) Index of energy calculation. These three parts are circled out in Fig. 176.

This evaluation flow can be seen as an open loop response system, which means there are inputs, system ontology and response results. In Fig. 176, oval boxes represent the inputs; square boxes represent the system ontology; Triangle box is the response of the input. Each part of the methodology will be introduced successively.

(A) Machine performances calculation - Here it is assumed that the machine design is frozen, or that the machine product existed already. Once the machine is defined, the basic topology of the e-machine cannot be changed. Other factors such as the operation temperature of E-machines or number of E-machine on one car also cannot be changed. Then two sets of simulation or experiment need to be done. Here the simulation method is taken as an example, and the simulation mainly indicates FEM method.

The first set of simulation is the machine with virgin materials. Here the focused virgin material is the virgin PM. In the simulation, the main performances of a PM are remanence flux density *Br* and coercivity *Hc*. Hence, these two parameters represent the inputs of a virgin PM.

Then in Fig. 176, red boxes and arrows represent the calculation path of the machine with virgin magnets. With the predefined FEM model, an efficiency map or a loss map can be obtained. Combined with the given operation request based on torque-time and speed-time of the e-machine, the final electricity energy consumption of the e-machine with virgin PMs in one drive can be obtained. This is the end of the virgin path.

The second set of the simulation is the machine with recycled PMs. First, *Br* and *Hc* of recycled magnets are inputted to the model. Then the calculation flow is identical to the virgin path. In Fig. 176, green boxes and arrows represent the calculation path of the machine with recycled magnets. Hence following this path, the electricity energy consumption within one drive cycle by the machine with recycled PMs can be obtained.

It needs to be noted that when using recycled PMs, the performances of the e-machine may be degraded. For instance, if the used recycled PM has less Br than the virgin PM, the torque certainly cannot be fulfilled the requirement with the same currents input or the same machine dimension. In this case, the torque of the E-machine with recycled PM must to be tuned to be the same with the virgin one. Here the way of tuning is to change the currents or to change the active length for the E-machine with recycled PM. The torque of the E-machine is basically proportional to the current, regardless of the non-linear effect. Thus, if the torque is proportionally reduced with the *Br* of the recycled PM, the input currents can be proportionally increased. This is the same for the active length, which is also proportional to the torque. However, changing active length has dependent on machine topologies. If the E-machine is radial flux, then the length changing can be applied. Moreover, from the production point of view, the length of the radial flux machines can be easily extruded, due to the same lamination that is used. However, for axial flux machines or complex 3D flux machines, such as transverse flux or claw pole machines, the torque is not proportional to the length. Thus, changing length is not applicable for them. Only current tuning can be used for these types of machine. Nevertheless, these are the two ways to tune the torque of the recycled E-machine for fair comparisons.

Hence, in order to calculate the energy consumption, it is necessary to know the torque and speed conditions of the e-machine, which are the introduction of part (B).

(B) Torque and speed requirements - The machine torque and speed conditions need to be derived by the inputs of drive cycle and vehicle parameters.

Drive cycle is a series of points that represent the speed vs time of a vehicle. In Europe, the standard drive cycle was New European Driving Cycle (NEDC). However, with the strengthen of the emission regulation after Paris Agreement, NEDC was not suitable for automotive industry anymore. From September 2018, all European automakers need to apply a new standard drive cycle called World Harmonized Light Vehicles Test Procedure (WLTP), which is shown in Fig. 177. The comparison between NEDC and WLTP is shown in Fig. 178. It can be found WLTP has more time duration than NEDC. The operations of WLTP are more irregular than NEDC.

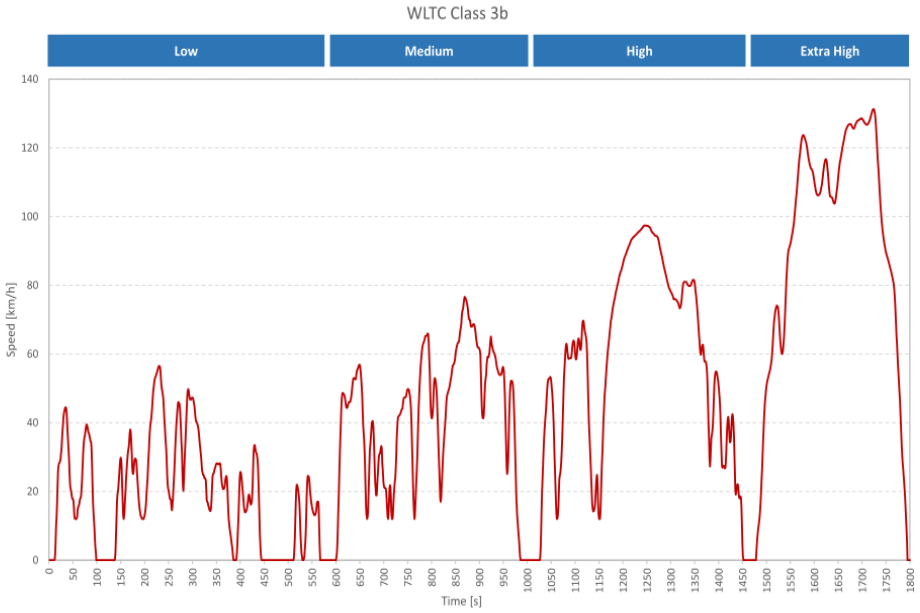

Fig. 177 WLTP drive cycle

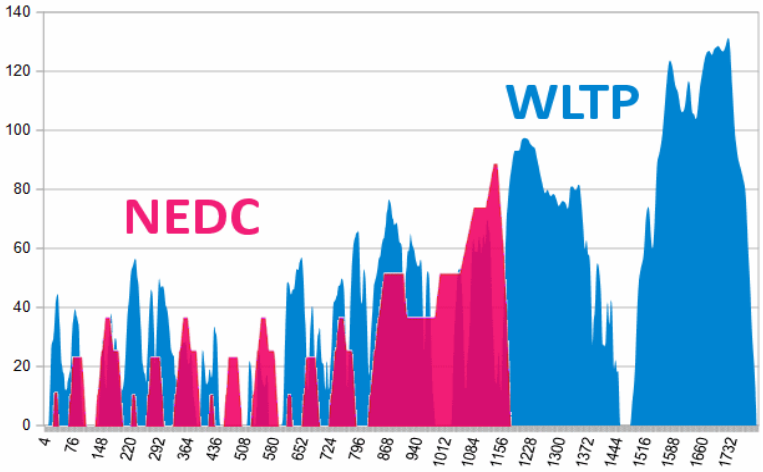

Fig. 178 Drive cycles comparison between NEDC and WLTP [147]

The following work is to change the velocity of the car to the velocity of the E-machine, as well as the torque. In this section, as the aim is only for EV, the wheel is driven by the e-machine directly with a speed reducer. Thus, the speed of the E-machine is multiple of the speed of the car. The diameter of the wheel as well as the reducer ratio needs to be involved for e-machine rotation speed calculation.

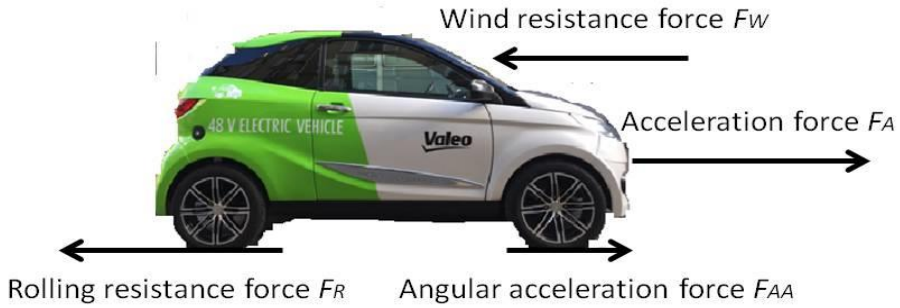

$$F_A = m*a$$
$$F_W = 0.5*rho*A*Cd*v$$
$$F_R = murr*m*g$$
$$F_{AA} = I*a/(r^2)$$

Total force needed: $F_{te} = F_A + F_{AA} + F_R + F_W$

Total torque of E-machine(s): $T_{te} = F_{te}*r/R_{Gear}$

Abbreviation	Meaning	Abbreviation	Meaning
m	Mass of vehicle	**Cd**	Drag coefficient
g	Gravity acceleration	**V**	Vehicle speed
a	Vehicle acceleration	**murr**	Rolling resistance coefficient
r	Tire radius	**T**	Torque of powertrain
rho	Air density	**I**	Inertia of the rotor
A	Frontal area	**RGear**	Gear ratio

Fig. 179 EV driving model for E-machine(s) torque derivation

Then the acceleration and deceleration of the vehicle along the time can be derived based on the drive cycle. Considering the vehicle parameters, such as weight, wind resistance and rolling resistance, the traction torque needed for the e-machine can be calculated. A general model for a driving model is shown in Fig. 179.

Therefore, with the given parameters of a driving model, the torque and speed requirements of the E-machine can be obtained as inputs. Finally the index output (C) can be introduced.

(C) Index of energy calculation – First, the total energy consumption of the E-machine(s) in their entire lifetime need to be estimated. Assuming the total operation hours are T, E(t) is the average energy consumption in a time duration *dt* which is imposed by the drive cycle analysis. Then the total energy consumption is *Ec*. The equation is shown in Eq. 101.

$$E_C = \int_0^T E(t)dt \text{ [kWh]} \qquad \text{Eq. 101}$$

Energy consumptions of both E-machines with virgin and recycled PM respectively can be derived by looking up their efficiency maps. Then the total cost of the energy consumption can be obtained by taking into account the energy price, which is the electricity price from the power grid.

Hence the cost of the energy can be compared with the cost of a magnet. In this case, the price of the magnet with the unit [€/kg] needs to be known. The total magnet cost is the product of total magnet weight in an E-machine and the magnet price. Finally, the Energy Index *EI* can be calculated by Eq. 102,

$$EI = \left(\frac{E_C(r).x}{E_C(v).x}\right).\left(\frac{Mag_C(r)}{Mag_C(v)}\right) \quad \text{Eq. 102}$$

where $E_C(r)$ is the energy consumption of the E-machine with recycled magnets, $Ec(v)$ is energy cost for the energy consumption of the E-machine with virgin magnets; x is the energy price. In Eq. 102, x is cancelled finally. Then $Mag_C(r)$ is the recycled magnets total cost scenario; $Mag_C(v)$ is the virgin magnets total cost.

When *EI* equals 1, it indicates that recycled magnet E-machine is equivalent to virgin magnet one. If *EI* is smaller (respectively larger) than 1, the using recycled E-machine has better (worse) impact on energy consumption than the virgin E-machine.

This is the point of using the index, as it does not give people an absolute conclusion about using recycling strategy. Instead, people can obtain their own index value by combining with their local scenarios, such as magnets prices or energy prices.

4.3.2 Demonstrations of energy index for pure EV

4.3.2.1 Validation of efficiency map

Apparently the key of the energy calculation is the E-machine efficiency map. Thus, it is considerably important to make sure that the efficiency map of an E-machine is accurate and reliable. In this case, the same HUB motor as shown in Section 4.2.3 was taken again as an example. An efficiency map of the motor was obtained first by FEM simulation. Then experimental measurements were done on the motor, including measurements of torque, speed, and most importantly efficiency. Comparisons were then made between the results of simulation and measurements.

Thanks to the disassembly task from Section 4.3.1, the main dimensions of the machine were obtained, and the results are shown in TABLE XXXIX. Then a 2D FEM model was built based on this information.

As for the materials data, the sample of the magnet were taken and analyzed with Physical Property Measurement System (PPMS) from Quantum Design [R]. The test performed to the magnet with PPMS yielded a value of remanence of approximately B_r = 1.2 T at room temperature. The iron sheet thickness was measured as 5mm, thus a standard 5mm gauge SiFe lamination was applied in the simulation, with 5W/kg at 1.5 T and 50 Hz.

TABLE XXXIX MAIN DIMENSIONS OF THE HUB MOTOR

Parameters	Value
Stack length L_{stack} [mm]	40
Maximum speed [rpm]	700
Air-gap length [mm]	0.6
Magnet axial length [mm]	40
Magnet thickness [mm]	3
Magnet width [mm]	14
Stator radius [mm]	126.5
Number of poles	56
Number of slots	63
Winding type	concentrated

Then simulations were run by applying the currents which would also be used for measurements. Fig. 180 illustrates the flux density of one load condition in 2D FEM.

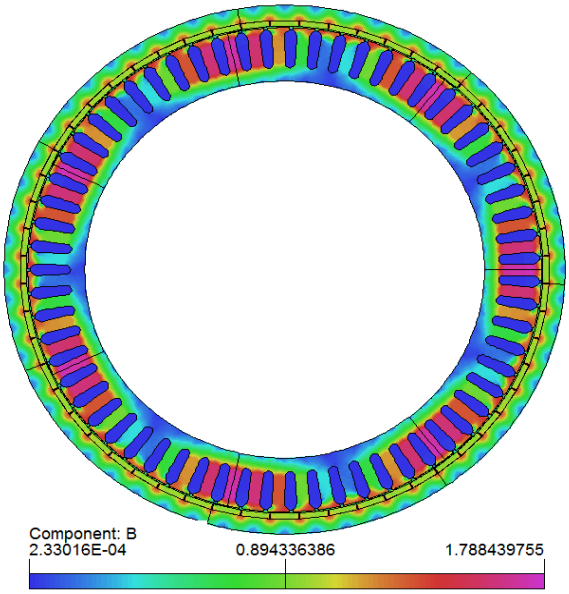

Fig. 180 Geometry modeled in FEM and magnetic flux density distribution at T=11.6 Nm and n=105 rpm.

Then the efficiency map of the HUB motor was obtained by using the same technique for Fig. 99 - Flux linkages of the motor were derived first for the torque calculation and corresponding current demands. Then copper losses were determined from the currents and measured resistances (no AC effect considered). Iron losses were calculated by using Bertotti's model and quadratic fitting with FEM simulations. The effect of harmonics induced by the modulation of the inverter was ignored in the simulations. Consequently, the result is shown in Fig. 181.

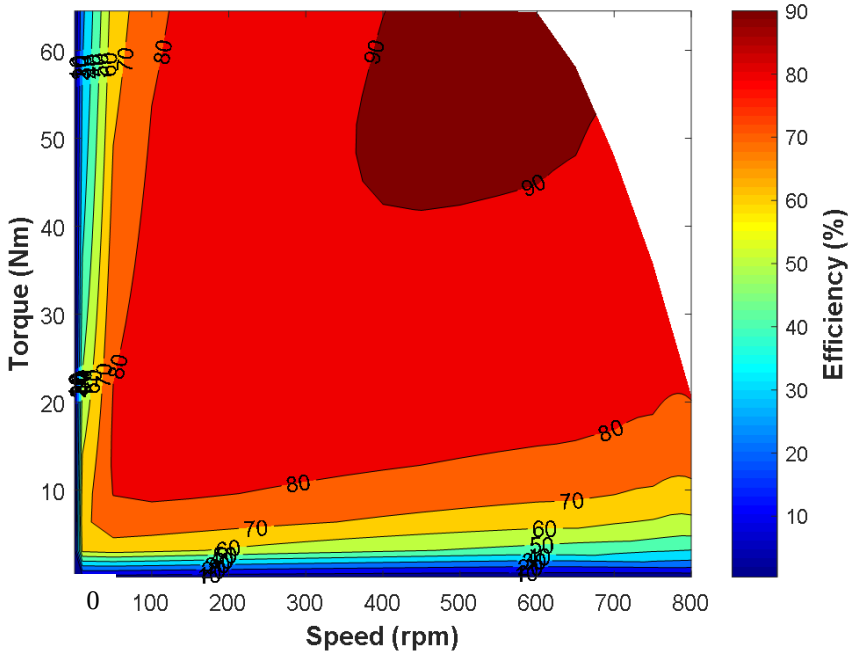

Fig. 181 Efficiency map of the HUB motor with origin magnets at room temperature

Next, measurements were carried out. The test bench set up is shown in Fig. 182. The DC power supply provides 72VDC voltage to the traction motor. The motor drive is a standard three-phase converter with hall sensor for position sensing. Two machines were assembled back to back. A resistive load was connected to the machine operating as a generator, and the value of the input power was measured by the power analyzer. The value of output power was derived by the torque and speed, where the torque is read by a torque transducer.

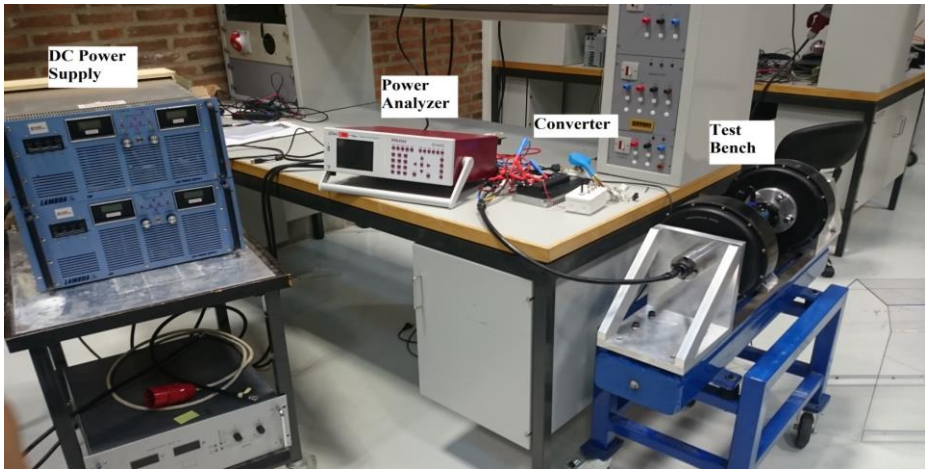

Fig. 182 Experiment set-up for efficiency measurement

The efficiency at different values of torque and speed were measured on the test bench. 57 operation points were taken in the range of 0 to 65 N.m and 0 to 700 rpm. The results are illustrated in Fig. 183.

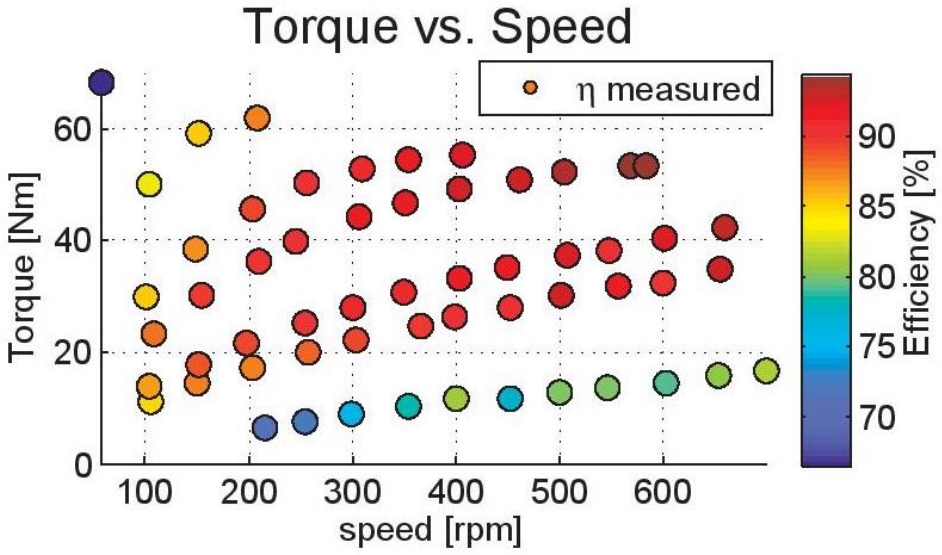

Fig. 183 Measured efficiency at different values of torque and speed

Then the comparisons could be made. With the same current input of these measured points, simulated torques and efficiencies could be extracted from the efficiency map. Fig. 184 shows the deviation in the simulated torque compared with measurements. The maximum deviation was estimated of approximately 17 %, while most of deviations were smaller than 5%. Fig. 185 shows the deviation in the calculation of the efficiency. The maximum deviation was approximately 9 %, while most of the deviations were smaller than 4%.

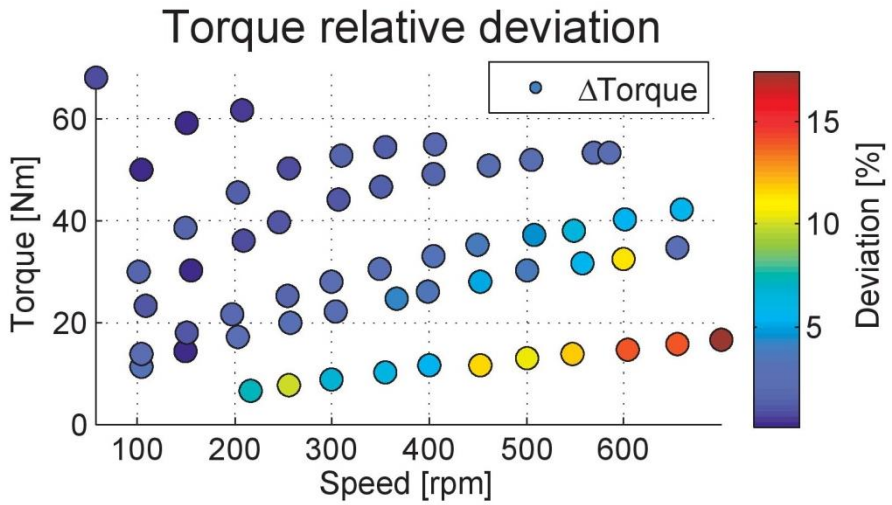

Fig. 184 Deviation in measured and calculated torque at different values of torque and speed

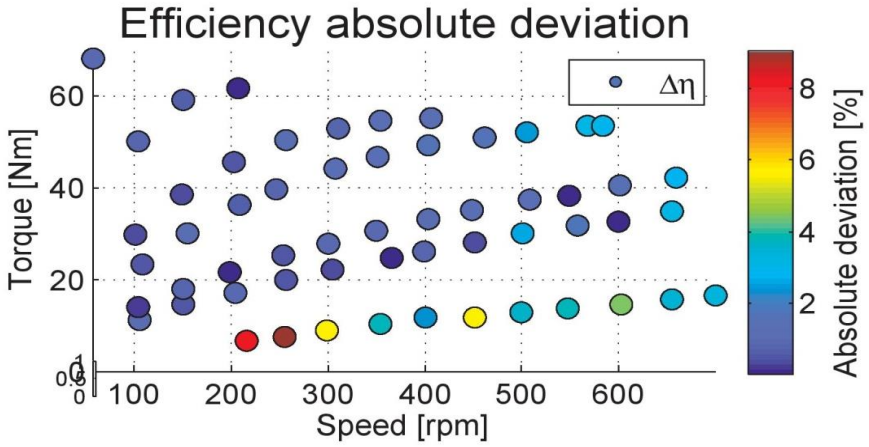

Fig. 185 Deviation in measured and calculated efficiency at different values of torque and speed

Various factors might be the source of such differences. In the torque case, the quality of the lamination might influence the performance of the machine regarding torque production. The deviations in the efficiency calculations might be due to the absence of the mechanical losses in the simulation results. In addition, simulations do not account for processes such as cutting, stacking, etc. that might diminish the quality of the laminations, thus increasing the losses. Additionally, errors in the measurements may influence the deviations between measured and simulated efficiencies.

In order to better understand the presence of deviations between measurements and calculations, a set of no load losses analysis was carried out. Mainly a decay test was performed on the HUB motor for investigation. The decay test consisted in running the machine solely by pulling the shaft and recording the back-EMF waveforms in an oscilloscope. A time decaying back- EMF wave-form was obtained, and the no-load losses P_{decay} (i.e. core losses, PM losses and mechanical losses) were obtained together with Eq. 103 [148],

$$P_{decay}(\omega_m) = -\omega_m J \frac{d\omega_m}{dt} \quad \text{Eq. 103}$$

where J is the inertia of the machine and ω_m is the mechanical angular speed. The inertia J was estimated with the main dimensions of the machine. The no-load losses as a function of the speed of the machine were approximated by quadratic curve fitting. Fig. 186 shows the decay test results, the calculated losses performed with FEM simulation and the measured no-load losses.

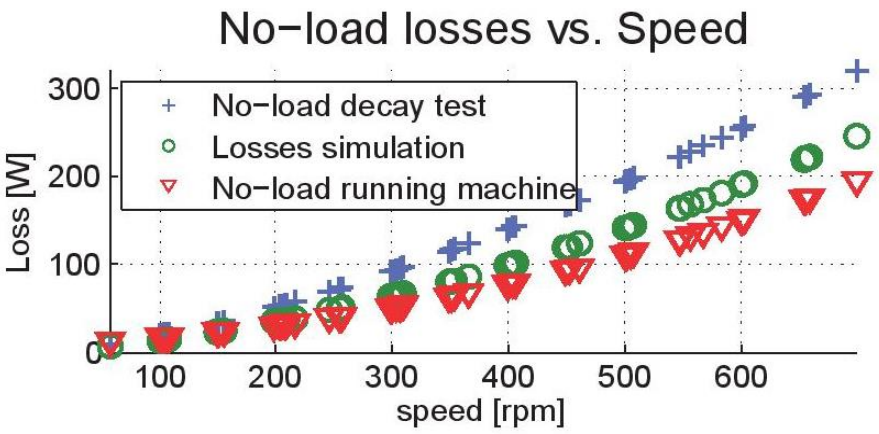

Fig. 186 Measured and calculated no-load losses in the original machine

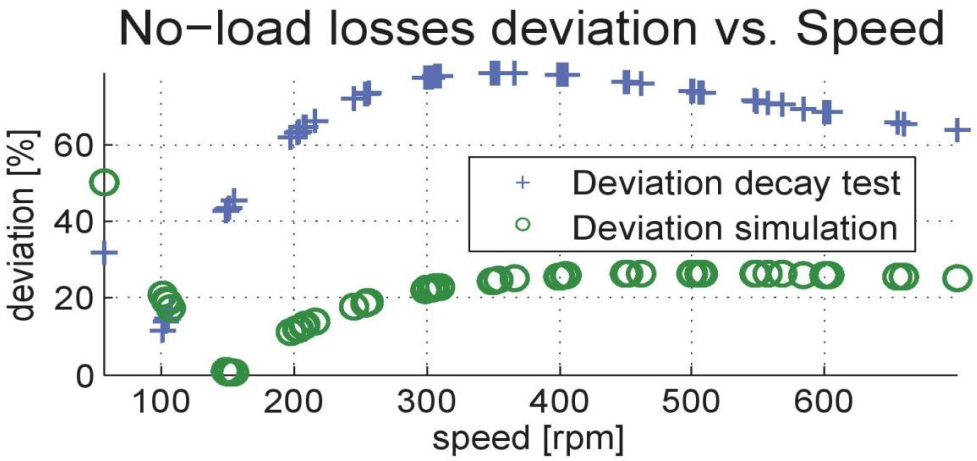

Fig. 187 Deviations in the no-load losses

The deviations between measured no-load running results and simulated results are shown in Fig. 187. The no-load losses P_0 with the machine running were determined with Eq. 104:

$$P_0 = P_m - P_0 - P_{Cu} \quad \text{Eq. 104}$$

where P_m is the input power measured with the power analyser and P_0 is the output power obtained with the measurements of torque and speed in the torque transducer. P_{Cu} is the copper losses. Note that P_0 contains the mechanical losses, core losses and PM losses.

The maximum deviation was estimated in approximately 50 %. The main source for this deviation would correspond to the portion of the mechanical and stray losses that are not included in the 2D FEM model. Additionally, the specific losses of the laminations in the actual machine remain unknown. Furthermore, as

mentioned before the processing of the laminations (i.e. cutting, stacking, etc.) is not accounted in the simulations. Regarding the deviations between measured no-load running results and the decay test results, Fig. 187 shows the largest deviations of approximately 79 %.

Based on Eq. 103 , another interference factor is the calculation of inertia *J*. In order to evaluate the sensitivity of the value of inertia *J* in the losses calculated with the decay test, *J* was modified by ±10 %. The results are shown in Fig. 188.

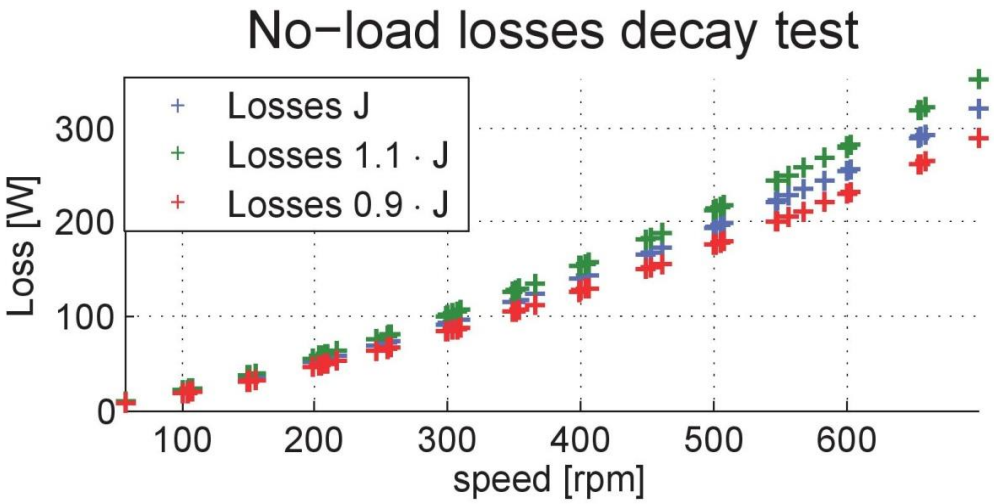

Fig. 188 Comparison of no-load losses with various values of inertia *J*

As shown in Fig. 188, the maximum deviation was estimated in 10 %. In this work, the calculation of *J* was performed both analytically and with the help of CAD software. The relative error between the two methods was approximately 3 %. The inertia calculated analytically was J_{ana} = 0.0899 kg·m^2. With CAD software, this value was estimated in J_{cad} = 0.0905 kg·m^2.

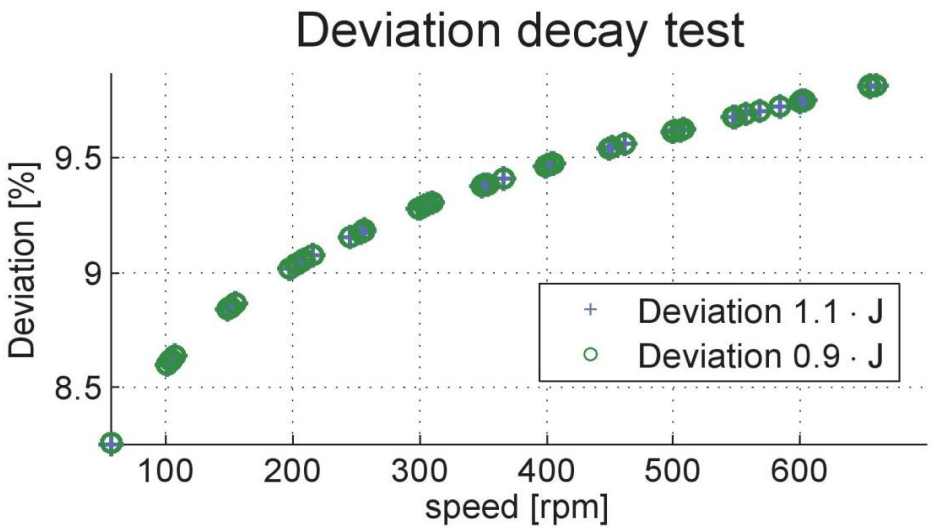

Fig. 189 Deviation of losses calculation with changing *J*

During the test with load in the machine, oscillations in the reading of torque were observed. In addition, an offset value was presented in the interface during the reading of torque value. Such offset was identified having a value of approximately 0.35 [N.m]. Here the goal is to identify the behavior of the measured losses accounting for such

deviations of the torque measurements. Hence, Eq. 104 was evaluated for the calculation of the no-load losses, accounting for the torque offset, by subtracting its value from the measurements. The results after applying quadratic curve fitting to the data are shown in Fig. 190, together with the decay test results and the losses results obtained with simulations.

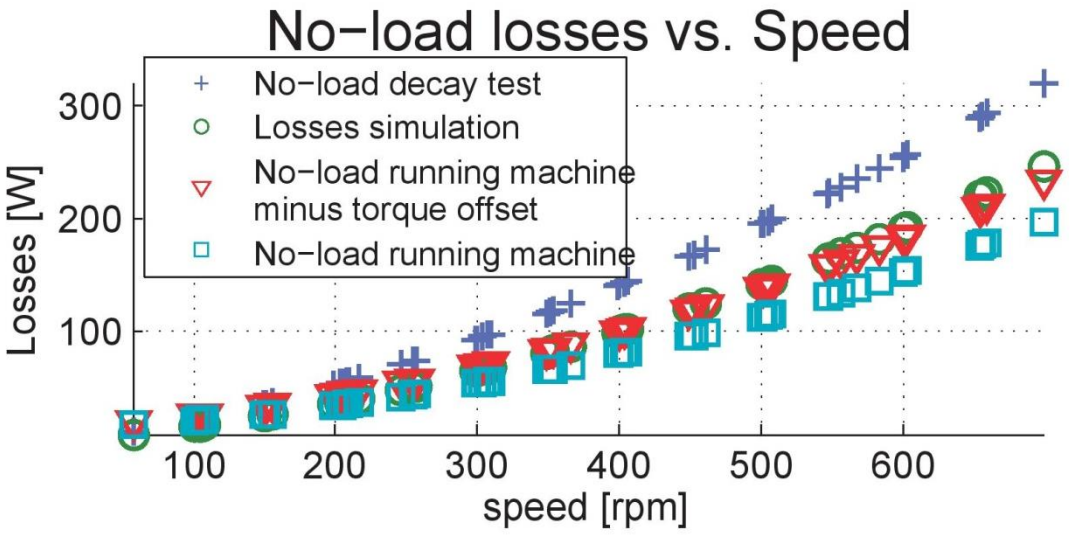

Fig. 190 No-load losses in the machine with torque offset

As it can be observed in Fig. 191, the subtraction of the torque offset from the measured values leads to the increment of the no-load losses. The maximum deviation between the decay test results and the measured no-load running result is of approximately 32 %, which shows that the calibration of the torque transducer might have a significant impact in the estimation of the no-load losses as in Eq. 104. In addition, the losses calculated in 2D FEM are still close or even higher than the measured values. This might be the indication that in the original machine, an electrical lamination of lower specific losses was used.

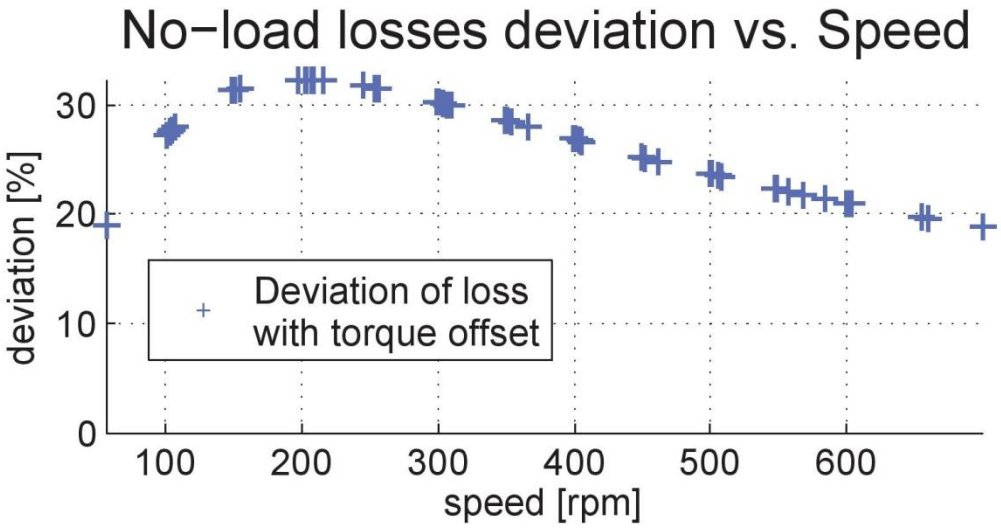

Fig. 191 Deviation in the no-load losses accounting for torque offset

Nevertheless, all the possibilities for causing deviations were analyzed. It is likely that the lack of iron lamination information and torque transducer accuracy contributes most of the deviation. However, due to the limited resources in the lab, this deviation cannot be avoided. Moreover, as most of the efficiency deviations are smaller than 4%, the results are considered as acceptable. Thus following works such as energy and index calculations can be continued.

4.3.2.2 Demonstration of energy index calculation

In the work of part (A), apart from the efficiency map calculation with virgin magnets, it is also necessary to do the efficiency map calculation with recycled magnets.

As mentioned in Section 4.3.1, if only recycled magnets are applied without the modification of the motor length or drive control, the performance of the E-machine can be degraded. As the HUB motor is a radial flux E-machine, thus the method of length increase is available for it.

As for the degree of the degradation of the recycled PM, research was been carried out. In [149]-[151], NdFeB PM scraps were recycled from various electronic sources, and recycled NdFeB PMs were re-fabricated by Hydrogen Decrepitation (HD) and HDDR processes. In this study, magnetic property of recycled magnet considered is around 0.96 T B_r. This is as per reference [149], where new magnet material had 1.36 T B_r, and recycled magnet had 1.08 T B_r, hence there was 20% reduction in the B_r. In this study virgin magnet has 1.2 T B_r, and taking 20% reduction for recycled magnet, the B_r evaluated is 0.96 T.

For the evaluation of machine performance with recycled magnets in sample motor, the methodology utilized is similar to performance calculated with virgin magnets as in Section 4.3.2.1. The dimensions of the motor were kept the same as with virgin magnets. Only the magnet properties were altered with recycled magnet properties i.e. having 0.96 T as B_r and increased length of the motor to achieve same torque as obtained with virgin magnets. The length of stator, rotor and magnets was increased from 40mm to 46mm, which was also nearly 20%. Due to the increase of the length, the magnets weight of the recycled magnets was increased from 0.7 kg to 0.81 kg. Henceforth, 2D FEM analysis was carried out to obtain the performances like back EMF, torque and iron losses. Performances had been evaluated with similar current values as used in tests and simulations during the study with virgin magnets in Section 4.3.2.1. Fig. 192 shows simulated torque vs. speed with corresponding efficiency values by virgin and recycled magnets. It can be observed that the torque values matched fairly well for virgin and recycled magnets. However, the efficiencies at certain points had increased with recycled magnets due to cumulative decrease of total losses, especially due to higher reduction of iron losses than the increase of copper losses.

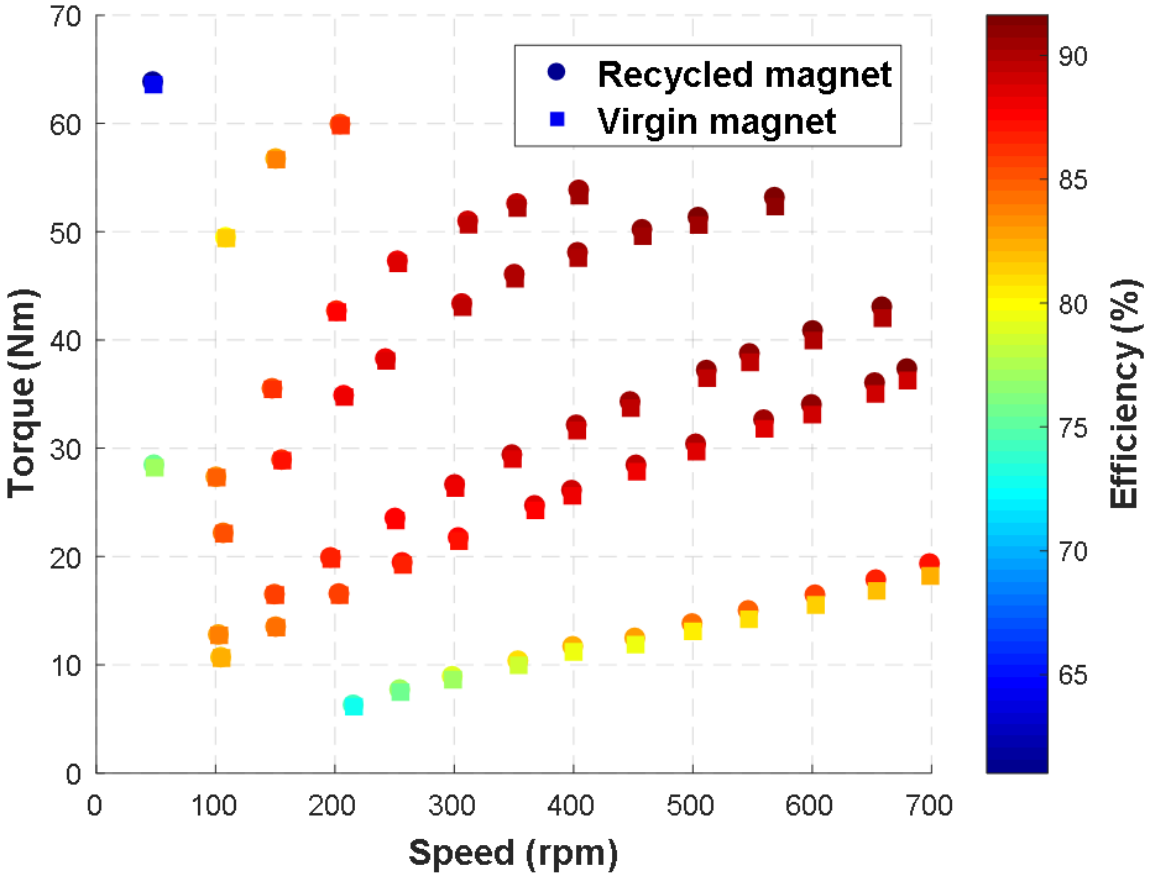

Fig. 192 Simulated torque vs. speed with corresponding efficiency values by virgin and recycled magnets

Then combined with Fig. 181, Fig. 193 illustrates the efficiency map of the HUB motor with recycled magnets. It can be found that not as people thought normally, the HUB motor with recycled magnets turned out to have lots of better efficiency regions than the original motor. These regions normally appeared in high torque region or high speed region. The reason might be that the original motor may not be fully optimized regarding the efficiency.

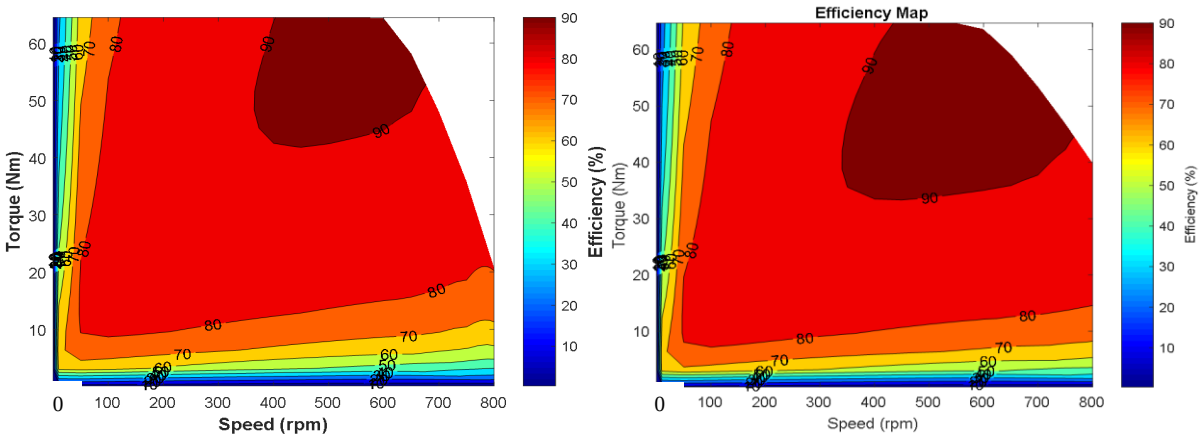

(a) (b)

Fig. 193 Efficiency maps of the HUB motor with (a) virgin magnets (b) recycled magnets at room temperature

Then, the torque and speed requirements for the motor can be derived by combining vehicle parameters and drive cycle. Here as the torque and power of the motor are relatively small, the target is set to drive a compact city car (segment A) with parameters listed in TABLE XL.

TABLE XL VEHICLE PARAMETERS FOR THE HUB MOTOR

Parameters	Value
Vehicle weight [kg]	920
Density of air [kg/m3]	1.225
Frontal area [m2]	1.85
Drag coefficient	0.4
Coefficient of rolling resistance	0.01
Tyre radius [m]	0.21

Also for the same reason, the drive cycle is decided to apply ECE-15, which is the urban driving part of NEDC. As for the high way driving part, the motor cannot reach that high speed and power (even with gearbox). Thus, the vehicle speed vs. time profile of ECE-15 is shown in Fig. 194. Then based on the car model in Fig. 195 and parameters in TABLE XL, the wheels torque vs. time profile is shown in Fig. 196.

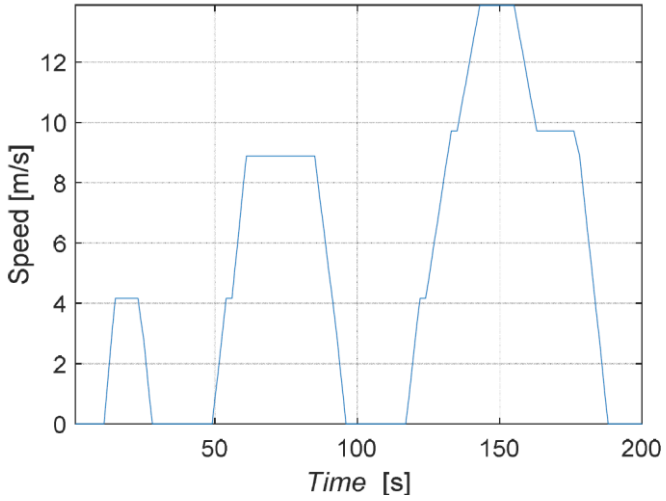

Fig. 194 Vehicle Speed vs. time profile of the ECE-15 drive cycle

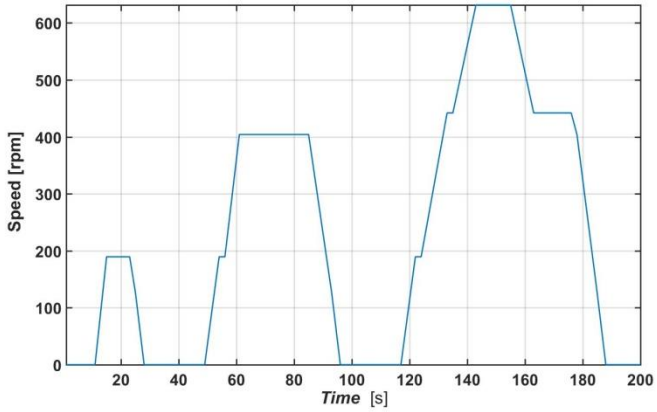

Fig. 195 Wheel Speed vs. time profile of the ECE-15 drive cycle

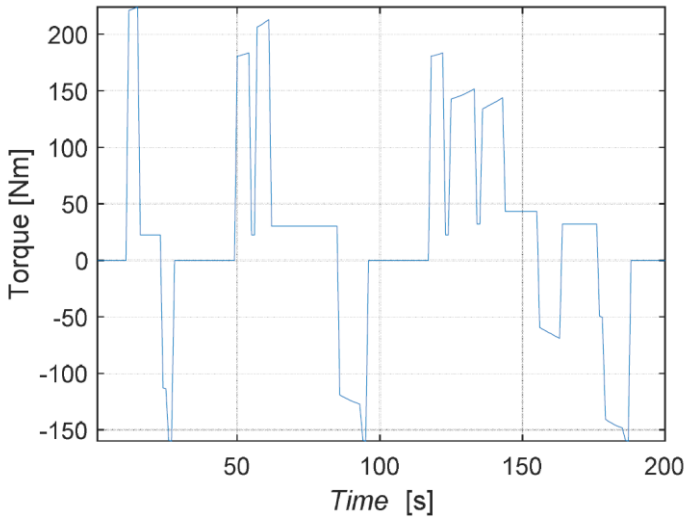

Fig. 196 Wheel torque vs. time profile for the specified vehicle and ECE-15

In typical EVs, E-machines are coupled to the wheels via transmission or speed reducer. Hence, E-machines gain relatively low speed but high torque and high efficiency. However, it can be observed in Fig. 195 that the required max wheel speed was larger than 600 rpm, which nearly approach the speed limit of the HUB motor. Thus, speed reducer cannot be used. From Fig. 196, the maximum torque required at wheels was around 220 Nm. As the maximum torque of a single motor was around 65 Nm. Four motors were assumed to be used in the vehicle with direct drive in-wheel configuration. The energy index finally could be calculated by input the torque, speed requirements to the efficiency maps.

In this case the regenerative braking and negative torque values were assumed to be zero in the energy calculations. From common senses, it is reasonable to assume the lifetime of the motor is 10 years with 2 hours daily operation. Thus the energy consumed by one motor during the life time could be derived. As a result, for the sample HUB motor with virgin magnets, the total energy consumption of a single motor was 3071 kWh while it was 2995 kWh for the motor with recycled magnets.

It is interesting to observe that the total energy consumption with recycled magnets were less than the energy consumption with virgin magnets. This result can be explained once the efficiency vs. time curve is plotted, as Fig. 197 indicates. It can be found that for most of the operation points, the efficiency with recycled magnet was higher than the efficiency with virgin magnets. Therefore, it can be deduced that the energy consumption depends on both drive cycle, i.e. operation points, as well as the machine design.

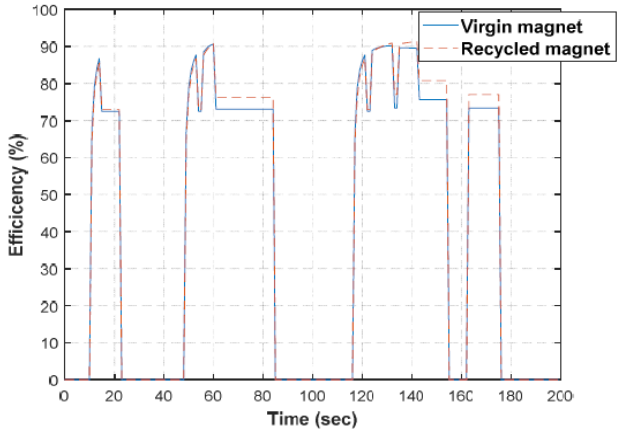

Fig. 197 Efficiency vs. time profile for virgin and recycled magnets

Finally, Eq. 102 was used to calculate the energy index. It is difficult to comment on the price of recycled magnets as it is subject to ongoing research studies. Hence a general representation of the index is tabulated in TABLE XLI, where energy cost index varies with the cost of virgin and recycled magnets (Be aware that the weight of virgin magnet is 0.7 kg and the weight of recycled magnet is 0.81 kg). Assuming the harmonized electricity price for Europe region as 0.22 €/kWh [152], thus the energy cost of one motor *Ec* with virgin magnet is € 676, *Ec* with recycled magnet is € 659.

Hence, it can be observed that as the PM material price varies for virgin and recycled magnets the index varies accordingly. The greener the index the better for economic benefit, and vice versa for the red index. The black dash line is the boundary between economic loss and profit regions. Above the dash line (or right side), it is profitable to apply recycled magnets; Below the dash line (or left side), it is deficit if recycled magnet applied. Similarly, hypothesis can be generated with variable energy costs for different grades of magnets and the index would indicate the cases which are economically more advantageous.

TABLE XLI ENERGY INDEX MATRIX WITH VARYING MAGNET COSTS

PM weight		Virgin magnet							
	0.7	PM price		30	50	70	90	110	130	150
			PM cost	21	35	49	63	77	91	105
0.81	kg	10	8.1	0.38	0.23	0.16	0.13	0.10	0.09	0.08
Recycled magnet		30	24.3	1.13	0.68	0.48	0.38	0.31	0.26	0.23
		50	40.5	1.88	1.13	0.81	0.63	0.51	0.43	0.38
		70	56.7	2.63	1.58	1.13	0.88	0.72	0.61	0.53
		90	72.9	3.39	2.03	1.45	1.13	0.92	0.78	0.68
		110	89.1	4.14	2.48	1.77	1.38	1.13	0.95	0.83

Other than the above cited advantages, with recycled magnets the motors have low environmental impact as compared to virgin magnets. The mining of rare earth materials has negative repercussions in terms of environmental and human conditions. The preparation of recycled magnets has lower implications on human labour aspects as no mining is required. Additionally, they have environmental benefits like reduction in air and water pollution. It can be argued that even for the preparation of recycled magnets a number of environmental hazards are possible like storage of hydrogen gas and its use in HD and HDDR process, and use of certain chemicals for separation of materials. But if both the circumstances are weighed together, the authors assume that mining would have higher negative impact than producing recycled magnets from scrap [153].

Therefore, the WIRE indexes worked for the sample PM motor. The methodologies were validated during the disassembly, simulation and experiments. The results could objectively reflect the state of the motor regarding the recyclability. Therefore, in the next section, WIRE indexes will be kept evaluating the newly designed 2-layer IPMSM.

4.4 Evaluating the bonded magnet IPMSM by WIRE

4.4.1 Recycling index for the bonded magnet IPMSM

First, the WIRE sheet was filled for the newly designed IPMSM with bonded NdFeB magnet. During the scoring, some sections need to be highlighted :

- The scoring was based on the ideal assembly and disassembly process of the IPMSM with bonded magnet.
- Therefore, the magnet injection molding with the rotor assembly together was considered. The same for PAM process.
- The disassembly utilizes the thermal treatment to take out magnets. During the treatment, it is necessary to have oxygen free environment.

Then statistic plots of the standard and cost of the IPMSM WIRE evaluation is shown in Fig. 198. Meanwhile the results are compared with the HUB motor, as the HUB motor is the baseline of comparison. The final recycling index of the HUB motor is 68.5%. The final recycling index of the IPMSM is 64.3%.

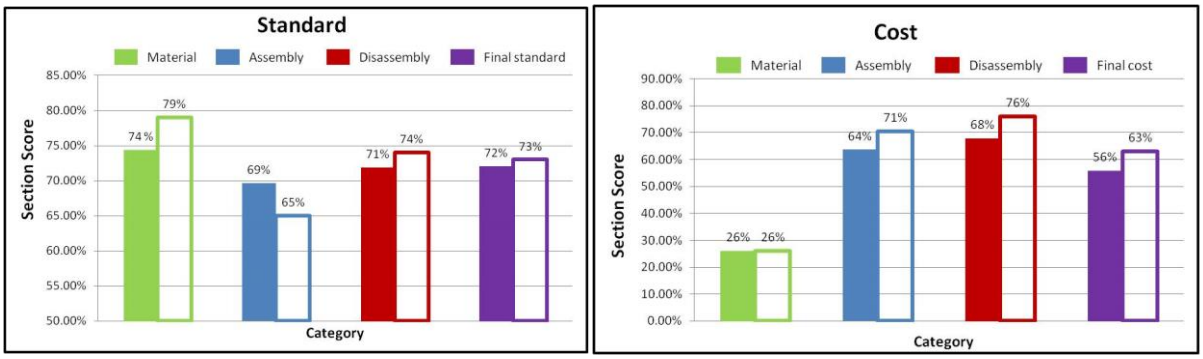

Fig. 198 Index distribution of the recycling index of the bonded magnet IPMSM (bars with solid color filled) and the HUB motor (bars without color filled)

It is found that the final scores of standard and cost of IPMSM are lower than the scores of the HUB motor. There are following reasons to explain the results

- Compared to sintered NdFeB, this bonded NdFeB magnet contains less rare earth element (e.g. No Dy). Therefore, regarding the material value, the IPMSM with bonded NdFeB is less important for recycling than the HUB motor.
- Currently the IPMSM needs quite complex non-standard processes for assembly and disassembly, such as injection molding, PAM and heating with oxygen free environment. Thus the IPMSM lost lots of points on the standard and cost of assembly and disassembly.
- Finally, the design of the table itself has some unbalanced issues. For instance, the material section occupied too small space in the cost evaluation part, as Fig. 199 shows. Thus the influence of the assembly and disassembly are much higher than the material value, while this is not true in practice.

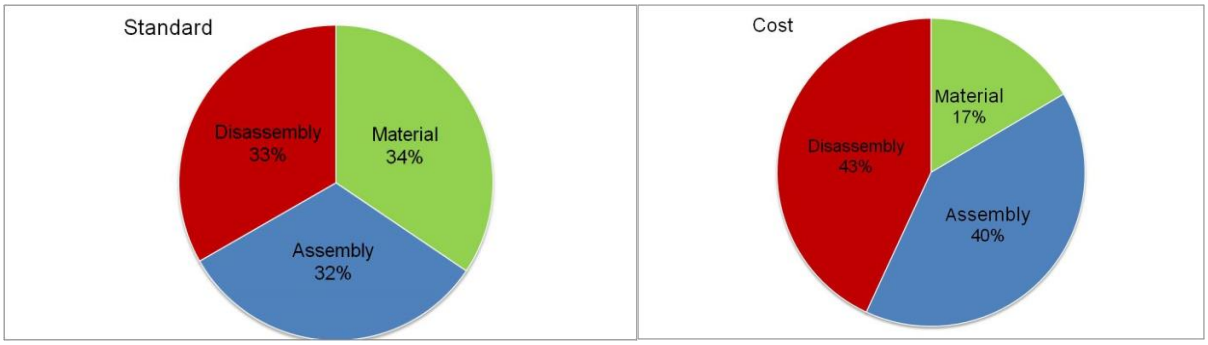

Fig. 199 Pie chart that reflects each section percentage regarding the total points

From the results it can be found that sometimes the innovation on the design can surprisingly degrade the recycling index, mainly due to various non-standard processes.

In a long term, if the assembly and disassembly processes for bonded magnets become standard, the score will be improved significantly. For instance, assuming the assembly standard score of bonded magnet is improved from 1 to 3; assembly cost score of bonded magnet is improved from 1 to 4; disassembly standard score of bonded magnet is improved from 2 to 3; Assembly cost score of bonded magnet is improved from 2 to 4; and finally some mechanical design is improved, such as the assembly cost score and importance of shaft changes - S:3 to 5, I:3 to 4. Then a promising result will be shown in Fig. 200.

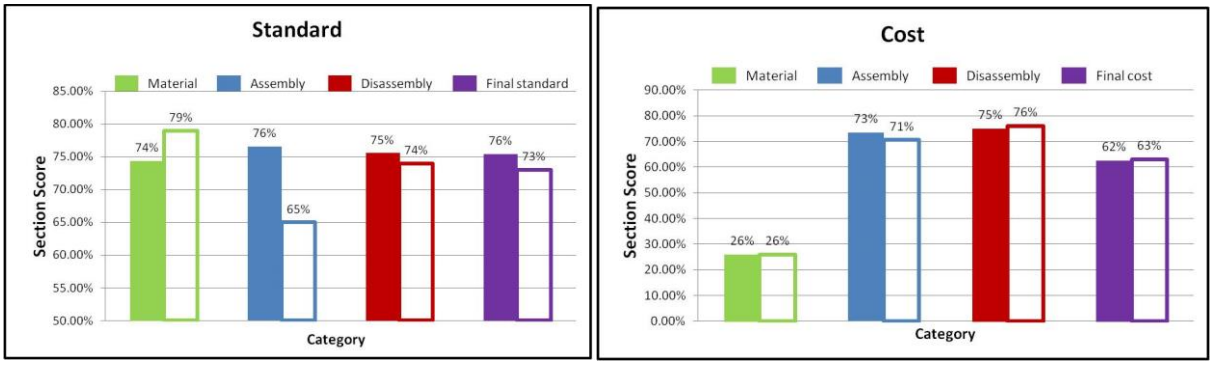

Fig. 200 Index distribution of the recycling index of the bonded magnet IPMSM with improved process (bars with solid color filled) and the HUB motor (bars without color filled)

After standardization, the standard points of the IPMSM turn to be higher than the HUB motor - Despite lower material value in IPMSM comparing to the HUB motor, the assembly of the IPMSM can easier than the HUB motor; the disassembly of IPMSM is also a slightly better than the HUB motor. The cost points of the IPMSM maintain the same level with the HUB motor, since the additional cost for the special processes are inevitable.

Nevertheless, the final index of the IPMSM after standardization is 69.2%, which is a little bit higher than the HUB motor index 68.5%. Therefore, the recyclability of a PM machine can be clearly quantified by the index. Moreover, by subdividing processes step by step, it can be clearly known the problems regarding recycling. Thus, people can customize their own scoring table and improve their own products.

4.4.2 Energy index of the IPMSM for EV application

4.4.2.1 Operation Points on Electrical Machines

Fig. 176 was still applied to the working flow of the energy index calculation. However, the details of the parameters are slightly changed. First, the performances of the electrical machine were from the IPMSM. Thus for the IPMSM with virgin bonded magnets, Fig. 144 about efficiency map at 80 °C was applied to the efficiency calculation.

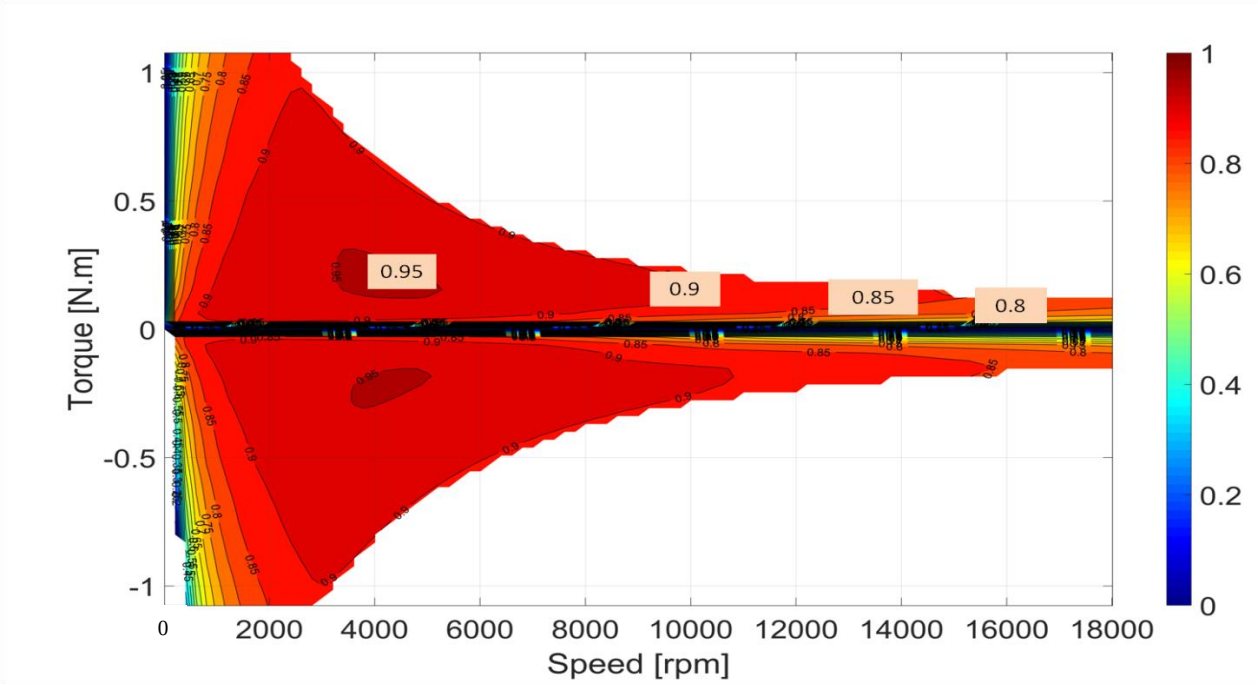

Fig.145 Efficiency of the 2-layer IPMSM @ 80 °C with AC copper loss and iron losses considering manufacturing impact

TABLE XLII VEHICLE PARAMETERS FOR THE IPMSM

Parameters	Value
Vehicle weight [kg]	500
Density of air [kg/m3]	1.25
Frontal area [m2]	1
Drag coefficient	0.3
Coefficient of rolling resistance	0.007
Tyre radius [m]	0.273

Second, WLTP drive cycle was implemented in order to fit the trend of the regulation. In this case, a speed reducer needed to be used to convert the high speed of the e-machine to high torque. Moreover, regarding only one E-machine was driven the car, the car has to be a light one. Thus, TABLE XLII illustrates the parameters of the car from [154].

Apart from the information in TABLE XLII, a gear ratio for the speed reducer also needed to be chosen. Here two gear ratios were selected for comparison: 4 and 10. If gear ratio 4 is selected, the WLTP operation points about torque & speed for the e-machine is shown in Fig. 201. This time there were negative torque values. Thus the regenerative breaking was taken into account.

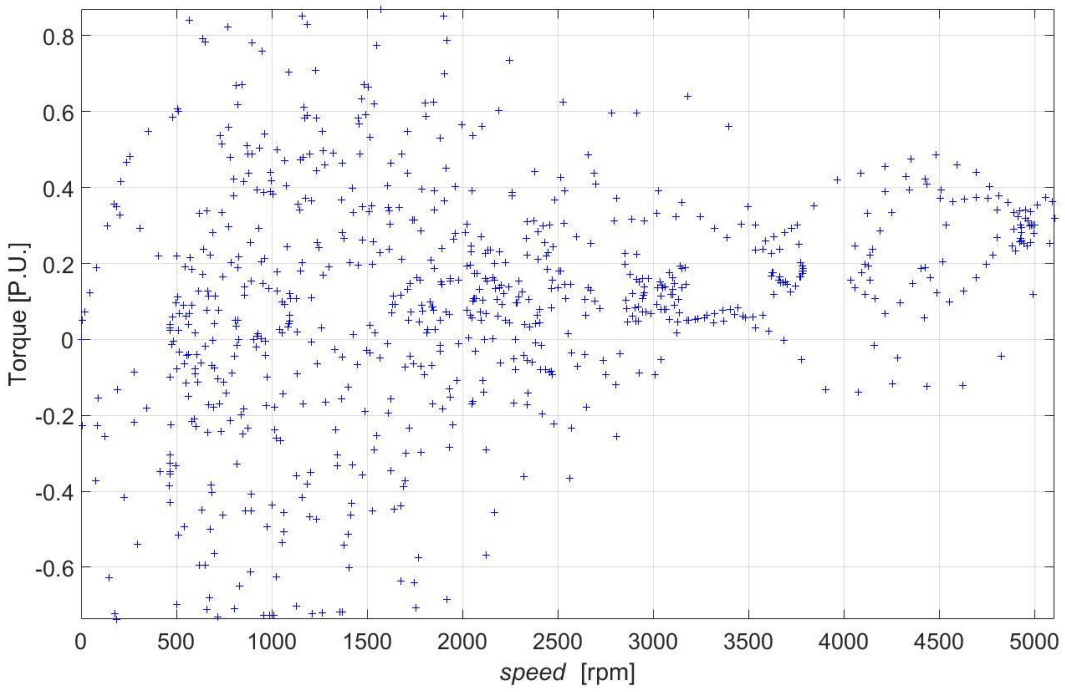

Fig. 201 WLTP operation points about torque vs. speed for the e-machine with gear ratio 4

Fig. 201 shows that the maximum torque was around 0.8 per unit value. The maximum speed was around 5000 rpm. Thus all the operation points were covered in the torque & speed envelope of the IPMSM. Finally, the calculated energy per cycle (kWh/30min) is 1.05. Convert to energy per kilometer (kWh/km), the value is 0.0451.

4.4.2.2 Performances of recycled magnet machine

Apart from the efficiency map calculation with virgin magnets, the efficiency map calculation with recycled magnets needed to be calculated afterwards. As discussed in Chapter 2.1, the quality of the recycled bonded magnets can be well maintained in a certain way, as shown in Fig. 51 and [87]. This means the BH curves of the virgin magnets and recycled magnets are basically the same. Naturally in this case no degradation of performances occurs on the recycled magnet machine.

However, for the worst case assumptions, NdFeB magnets degradation taken from [149]-[151] applied. Thus, 20% remanence flux reduction for the recycled NdFeB magnet was taken into account, the BH curves of the recycled magnet are shown in Fig. 202 (b). Thus, the recycled BH curves replaced the virgin BH curves in the simulation.

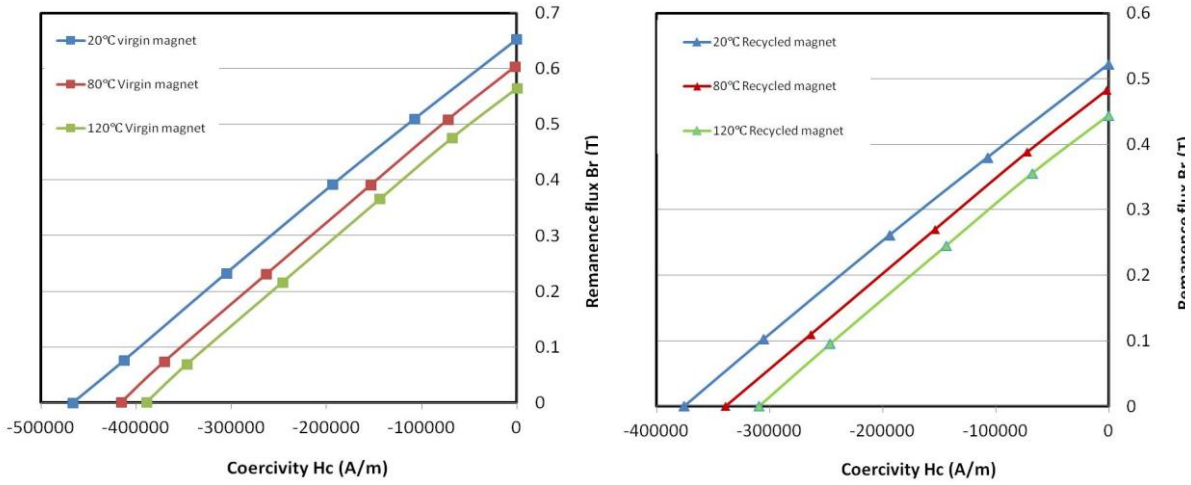

(a) (b)

Fig. 202 Implemented NdFeB bonded - type magnet B-H curves with different temperatures, (a) virign magnet (b) recycled magnet (20% degraded).

Next, as mentioned in Section 4.3.1, corresponding modification on the motor length or drive control needs to be made for the compensation. Here the modification on drive control was made. It was found that by increasing max current input by only 10%, the same max torque can be achieved for the recycled magnet machine compared to virgin magnet machine. The torque comparison is illustrated in Fig. 203.

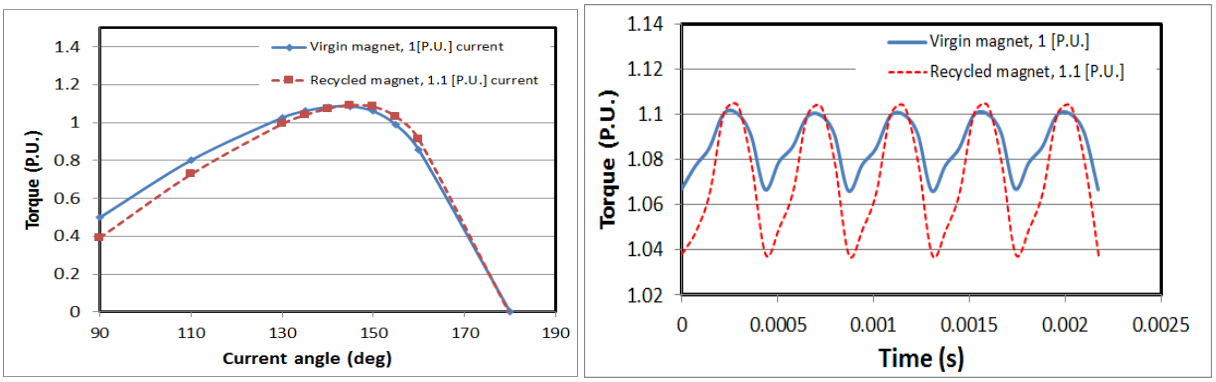

Fig. 203 Torque performances comparison between the IPMSMs with virgin magnet and recycled magnet respectively (a) Torque vs. current angle curves @80 °C (b) torque ripple curves @ 80 °C around 140 ° current angle. Torque ripple rate of the virgin magnet machine equals 3.2%, the recycled magnet machine equals 6.2%.

It was found that the torque angle curves of virgin magnet machine and recycled magnet machine are nearly overlapped. The max torque current angle for is 145° for both virgin magnet machine and recycled magnet machine. Fig. 203 (b) shows the comparison of the torque ripples. Here the current angle is set as 140°, since this angle has a good compromise between torque and torque ripple rate. It is found that the torque ripple rate of the recycled magnet machine is larger than the virgin magnet machine, but within an acceptable level.

Fig. 204 indicates the efficiencies of the two machines during the entire WLTP drive cycle. It shows that for most of the operation points, the efficiency with recycled magnet was lower than the efficiency with virgin magnets. Therefore, the final energy consumptions of the recycled magnet machine were expected to be higher than virgin magnet machine.

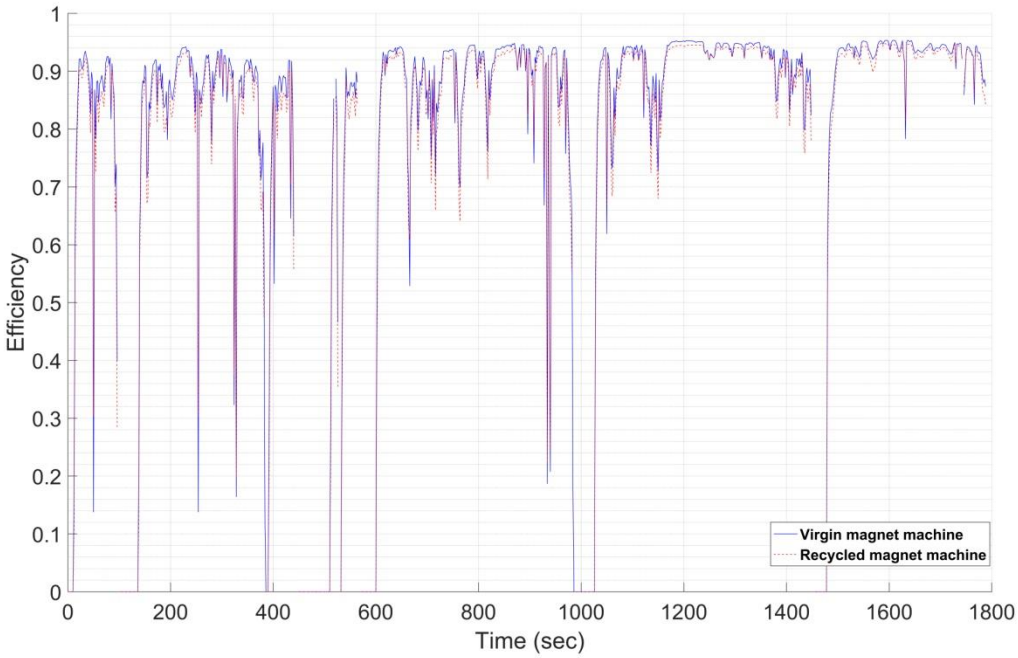

Fig. 204 Efficiency vs. time profile for virgin and recycled magnet machines

4.4.2.3 Energy consumption results and index calculation

Finally, with the accumulation of each step, the total energy consumptions of the virgin and recycled magnet machines can be compared. The results are shown in TABLE XLIII. Here the energy calculation of gear ratio 10 just followed the same procedure. However, it can be found that the recycled magnet machine with gear ratio 10 had no results. This is due to the fact that some operation points with low torque but high speed exceeded the torque speed envelope of the recycled magnet machine (The envelop of the recycled magnet machine has shrunk compared to the virgin magnet machine).

TABLE XLIII WLTP TOTAL ENERGY CONSUMPTIONS OF ELECTRICAL MACHINES WITH VIRGIN AND RECYCLED MAGNETS RESPECTIVELY, AND WITH DIFFERENT GEAR RATIOS

	Gear ratio	Cycle energy (kWh, 30mins)	Energy per km
Virgin magnet	4	1.05	0.0451
	10	1.06	0.0456
Recycled magnet	4	1.07	0.0460
	10	-	-

From TABLE XLIII, it can be found that the increase of energy consumptions of the virgin magnet machines with gear ratio 4 is only 1.9%, which is barely negligible.

Finally, results of *part (C) Index of energy calculation* can be derived. Again assuming the lifetime of the motor is 10 years with 2 hours daily operation. Thus the energy consumed by one motor with gear ratio 4 in the life time could be derived. As a result, for the virgin magnet machine, the total energy consumption was 15330 kWh. For the recycled magnet machine, the total energy consumption of a single motor was 15622 kWh. Finally, Eq. 102 was used to calculate the energy index. Again assuming the harmonized electricity price for Europe region as 0.22

€/kWh [149], the energy cost of one motor *Ec* with virgin magnet is € 3373; *Ec* with recycled magnet is € 3437. Then by using similar tool with TABLE XLI, TABLE XLIV of energy index matrix can be obtained. Just this time the weight of the magnet did not change.

TABLE XLIV ENERGY INDEX MATRIX WITH VARYING MAGNET COSTS FOR THE EV APPLICATION

PM weight		Virgin magnet							
	0.8	PM price		30	50	70	90	110	130	150
			PM cost	24	40	56	72	88	104	120
0.8	kg	10	8	0.34	0.20	0.15	0.11	0.09	0.08	0.07
Recylced magnet		30	24	1.02	0.61	0.44	0.34	0.28	0.24	0.20
		50	40	1.70	1.02	0.73	0.57	0.46	0.39	0.34
		70	56	2.38	1.43	1.03	0.79	0.65	0.55	0.48
		90	72	3.06	1.83	1.31	1.02	0.83	0.71	0.61
		110	88	3.74	2.24	1.60	1.25	1.02	0.86	0.75

Hence, it can be observed that to make the recycled magnet machine economically benefit in the life cycle, the cost of recycled magnet at least needs to be identical with the virgin magnet.

4.4.3 Energy index of the IPMSM for HEV application

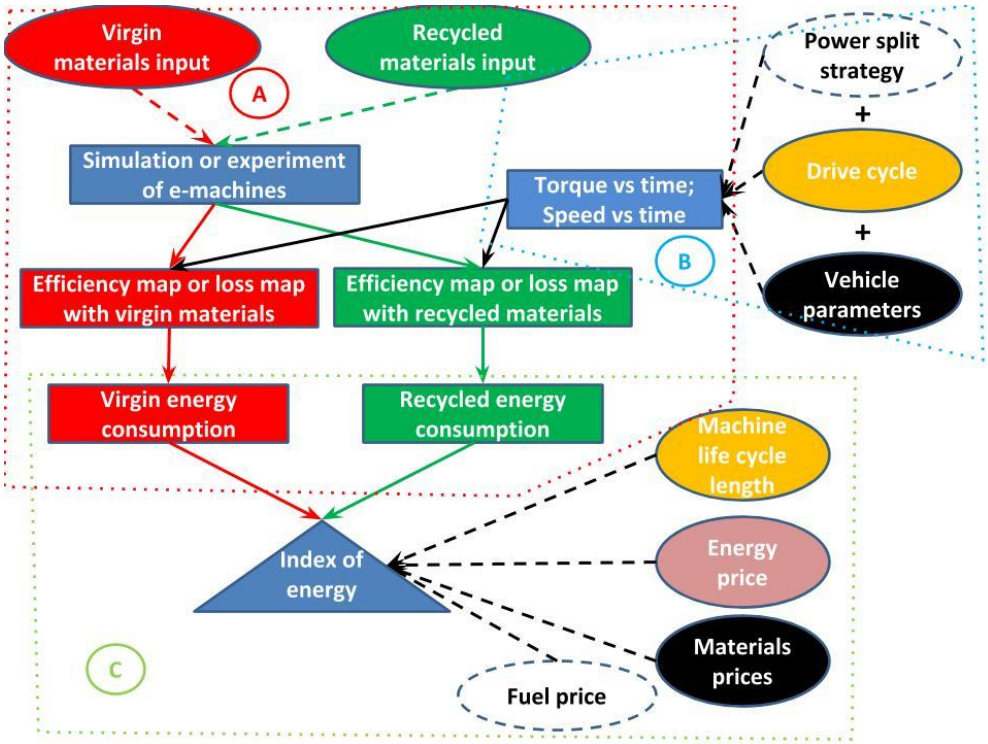

Fig. 205 Index of energy calculation flow diagram for HEV (A) Machine performances (B) Torque and speed requirements (C) Index of energy calculation

The energy index calculation for HEV applications are slightly different with EV applications. As can be seen from Fig. 205, two more factors are involved- *Fuel price* and *Power split strategy*. For the user phases of HEVs, the energy consumption is a mixed of fuel (gasoline or diesel) and electricity. However, depends on the configuration of the HEV, the percentage of this mixture can be different. For the mild hybrid electric vehicle, the only consumption is the fuel, as the electricity is also converted from the fuel. While for Plug-in hybrid electric vehicle, the consumptions are both fuel and electricity. As this thesis aims to mild hybrid application, only the fuel consumption is concerned. Apart from that, *Power split strategy (or torque split)* also affects the results. Because the operation points of the HEV drive cycle involves both ICE and E-machine. How much energy can be saved not only depending on the power and efficiency of the E-machine, but also on the power distribution management between ICE and E-machine for the maximum operation efficiency benefit. This section main focuses on how the IPMSM can be efficiently operated on the mild hybrid platform, with virgin and recycled magnets respectively. Meanwhile, the power split strategy is briefly introduced.

4.4.3.1 Comparisons between virgin and recycled magnet machines

In Fig. 205, the work of part **(A) Machine performances calculation** is similar to EV application. Again, by taking into account the worst case scenario - 20% remanence flux reduction for the recycled NdFeB magnet, the same BH curves of the recycled magnet with Fig. 202. (b) were applied. Then the modification on drive control was made again, which is still 10% increase on current, the torque comparison is illustrated in Fig. 206. The difference is that the E-machine is running under 120 °C.

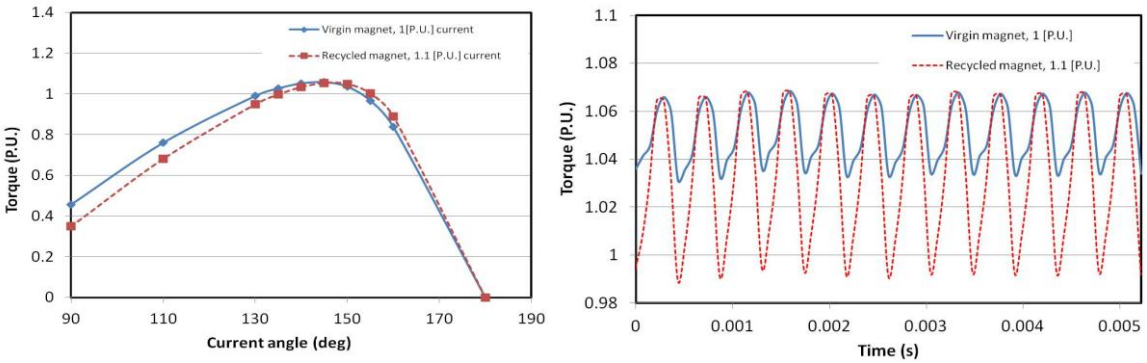

(a) (b)

Fig. 206 Torque performances comparison between the IPMSMs with virgin magnet and recycled magnet respectively (a) Torque vs. current angle curves @120 °C (b) torque ripple curves @ 120 °C around 140° current angle. Torque ripple rate of the virgin magnet machine equals 3.5 %, the recycled magnet machine equals 7.6%.

The maximum torque speed envelopes of these two machines are shown in Fig. 207. A serious concern about the recycled magnet machine is the reduced power. In fact, as shown Fig. 207, by using recycled magnets, high speed power is reduced. However, the reduction is still in an acceptable range.

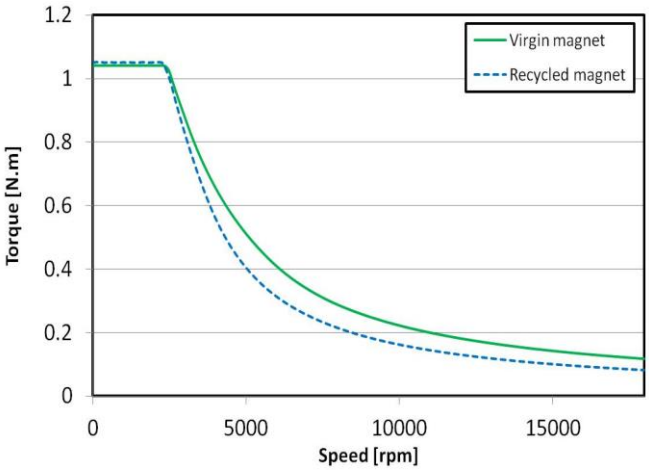

Fig. 207 Maximum torque envelopes of the machines

The efficiency comparisons are shown in Fig. 208 and Fig. 209. For the most of the low speed area, the efficiency of the recycled magnet machine is lower, as illustrated in Fig. 209. Those areas are depicted with yellow and green colors. However, at high speeds, the recycled magnet machine becomes more efficient; those areas are depicted by blue and cyan colors.

Some other concerns such as mechanical and thermal states can be overcome. As the radial plane topology was kept identical for the recycled magnet machine, the virgin and recycled magnet machines are mechanically identical, regarding the rotor principal stress for instance; there was a large margin for the constant load thermal state. Thus even though there is a slightly increase on the input current for the recycled magnet machine, the thermal state is still acceptable.

Therefore, because of the changes in power and efficiency, the energy management strategy needs to be adjusted. The operation points of the machines should be different to mitigate the fuel consumption impact. In order to better understand this phenomenon, hybrid powertrain configurations and their control law will be introduced in the next section.

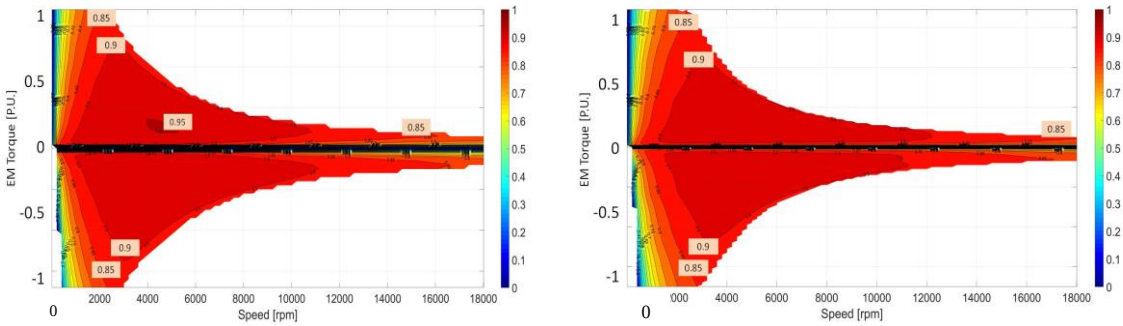

(a) (b)

Fig. 208 Efficiency map of the IPMSM @ 120 °C (a) with virgin magnet (b) with recycled magnet

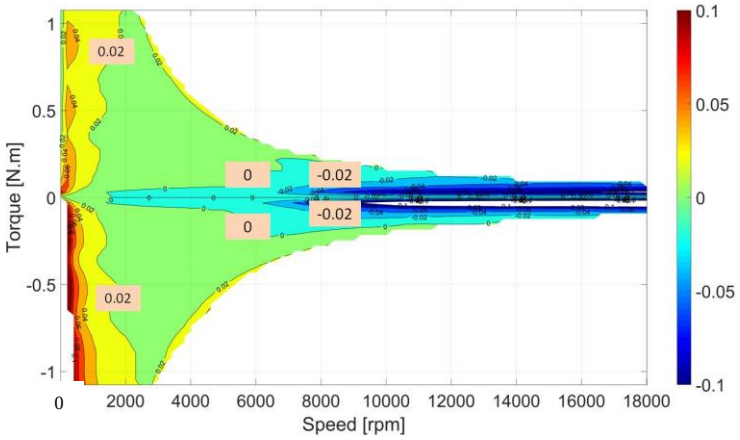

Fig. 209 Efficiency difference between IPMSMs with virgin magnet and with recycled magnet ("virgin"-"recycled")

4.4.3.2 Energy management strategy

As studied in chapter 1.4, there are mainly 5 different parallel hybrid configurations, which are denoted as P0 – P4. For this study, two configurations are implemented, which are P2 offline and P0P4. It needs to be highlighted that for P0P4 configuration, two machines are combined - a P0 machine which is only used as ICE starter and generator, and a P4 machine which still the main machine for emission reduction.

The control strategy is indispensable not only for the power distribution management but also for the optimal design of HEV. To be able to compare different vehicles systems (different electric motor for example), controllers should insure that these systems operate optimally or close to optimally [155].

The optimization of energy management control is based on optimal control theory. In the application of this theory to the problem of minimizing a hybrid vehicle consumption, Eq. 105 and Eq. 106 are used:

$$J(u) = \int_0^T L(x(t), u(t), t)dt + \phi(x(T), T) \qquad \text{Eq. 105}$$

$$\dot{x}(t) = f(x, u, t) \qquad \text{Eq. 106}$$

Where

- t denotes time, T denotes final time,
- $x(t)$ represents the state variable of State of Charge (SoC),
- $u(t)$ represents our command,
- $L(x, u, t)$ represents the instantaneous ICE consumption,
- $f(x, u, t)$ represents the SoC variation
- $\phi(x(T))$ represent a constraint on our final state (ISO-SoC constraint).
- $J(u)$ is aimed to minimize fuel consumption with respect of constraint ϕ.

According to the theories, with appropriate simplification on state constraints, our command should minimize Hamiltonian (H) which expressed as Eq. 107 for each instant t.

$$H(x,u,t,p) = L(x,u,t) + \lambda(t).f(x,u,t) \quad \text{Eq. 107}$$

Therefore, our command can be derived by Eq. 108:

$$u^*(t) = \underset{u}{argmin}\, H(x,u,t,p) \quad \text{Eq. 108}$$

Besides, in Eq. 107 λ can be known through Eq. 109

$$\dot{\lambda}(t) = -\frac{\partial H}{\partial x} \quad \text{Eq. 109}$$

and its initial value is set to reach ϕ [156].

The core idea of this theory is that the "shadow cost" which using energy from the battery represents, needs to be accounted for. For example, if the fuel consumption is lowered at a given time using energy from the battery to assist torque, this energy will not be used at another stage where it might have yielded more fuel consumption reduction. That is why the electric energy cannot be considered as "free" - using it might "cost" the system further fuel consumption reduction, that is why "shadow cost" is been used. Therefore, to be able to 'minimize consumption online', in other words 'minimizing consumption at each instant', the Hamiltonian should be minimized instead. However, the question of what is the value of λ is left unresolved. In order to perfectly obtain that, the speed and torque profile in the future needs to be known to select a λ that would respect state variables constraints.

For the simulations, it was preferred to use a realistic command instead of an optimal command. As explained before, an optimal command relies on knowing in advance the speed and torque profile of the vehicle. Obviously this is unrealistic in real life driving. Instead the strategy used relies on an heuristic approach on determining λ. It assumes that the driving conditions evolve slowly enough that if you can have a proper λ for the near past, this λ should be also suitable for the near future.

TABLE XLV EFFICIENCY OF OTHER KEY POWERTRAIN COMPONENTS

Efficiency	Percentage
Battery	95
DCDC	94
ACDC	96.5
Reducer	98

The fuel consumption results for virgin and recycled electric machines, based on NEDC and WLTP speed profiles, are analyzed in this section as well as the operating points for the two machines. The vehicle model is a segment

D vehicle with a 1.6 L gasoline engine and a manual transmission. An additional mass of 60kg is added to conventional vehicle mass which represents the mass of the electric motor, the power electronics and the 48V battery. The battery capacity is 20 Ah. At the end of simulation, the battery state of charge is identical to the initial state. Apart from the electrical machine, the efficiencies of other powertrain components are assumed as constant values, as TABLE XLV listed. The temperature of the electric machine is 120 C° for both cases P0P4 and P2 off-line. The mapping of total losses only includes the machine losses.

4.4.3.3 Operation Points on Electrical Machines

The machines with virgin magnets and recycled magnets are both simulated at P4 and P2 off-line positions of mild hybrid system respectively. Then based on the control strategy of section 4.4.3.2, an optimal operation behavior of each machine for energy saving can be obtained, which is part (B) in the work of Fig. 205. For instance, the NEDC energy repartition of each machine in each system is shown in Fig. 210 - white dotted line, black continuous line and black dotted line denote torque speed curves under 36V, 48V and 52V respectively, due to the variation of the State of Charge (SoC) of the battery. Four operation modes were illustrated - ZEV, boost, regenerative braking and generation modes. Thus, some interesting distinctive can be found on each operation strategy.

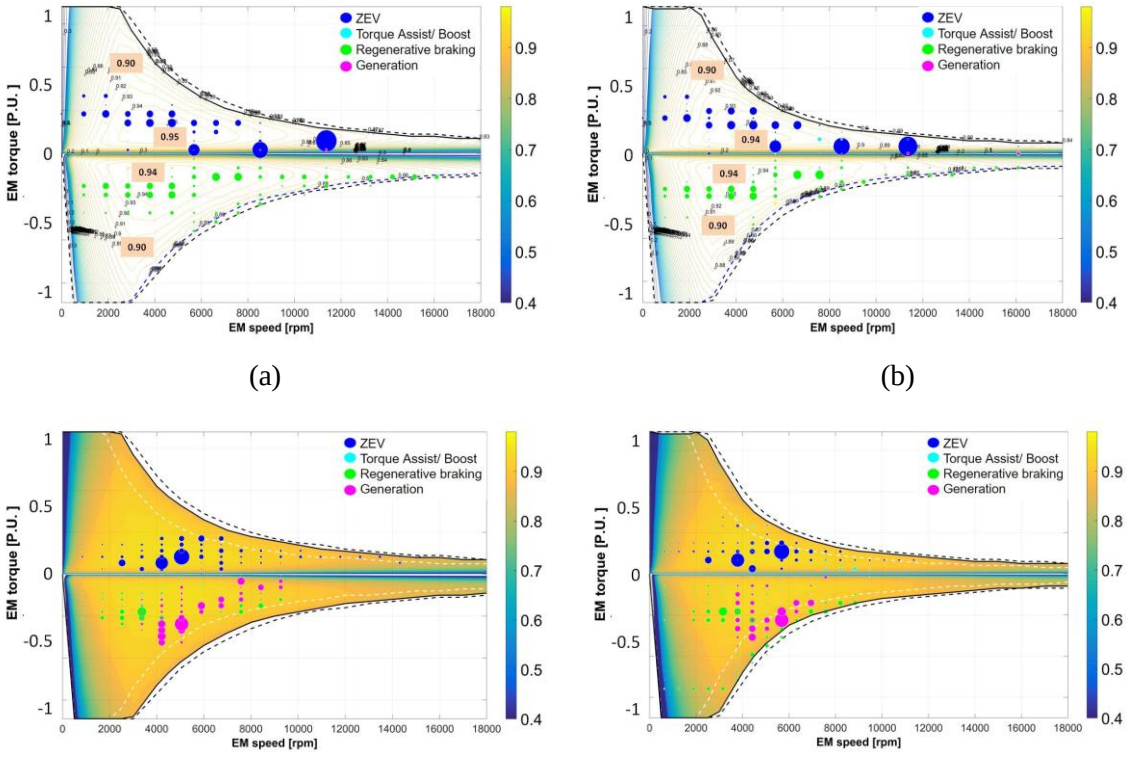

Fig. 210 Energy repartition of the machine operating points for NEDC (a) P4 with virgin magnets (b) P4 with recycled magnets (c) P2 with virgin magnets (d) P2 with recycled magnets @ 120 °C

Fig. 210 (a) and (b) show the operating points of P4 position for both virgin and recycled magnets respectively. The energetic repartition was similar in both cases, the only difference was the maximum power while recuperation phases. The machine with recycled magnet had less recuperation energy than the virgin one and that impacts the fuel consumption. Fig. 210 (c) and (d) show the operating points of P2 position for both virgin and recycled magnets respectively. In this case the energy repartition started to illustrate differences. The recycled magnet machine tended to have more ZEV and generation modes at high speed than the virgin magnet machine. Comparing P2 and P4 configurations, it can be found the ZEV mode of P4 frequently appeared in the high speed

zone. However, the ZEV mode of P2 was evenly distributed in medium speed zone. Besides, P2 has much more generation mode than P4. However, it seems that P4 can better utilize the regenerative braking than P2.

Similar simulations can be done with WLTP, as Fig. 211 presented. It can be observed that the energetic repartition between recycled and virgin magnet machines was similar, no matter what configuration it was. However, the main difference was still the maximum power during the recuperation phases, the machine with recycled magnet gain less recuperation energy than the virgin one, but this is not remarkable. On the other hand, comparing P4 and P2 configurations, the operation patterns are quite different. P4 can be mainly divided into three operation zones – high torque zone, mainly for ZEV mode; low torque zone, mainly for boost mode; braking zone, just for regenerative braking. However, P2 can be mainly divided into four operation zones – high torque medium speed zone, mainly for boost mode; medium torque zone, mainly for ZEV; strong braking low speed zone, mainly for regenerative braking; weak braking high speed zone, mainly for generation mode.

Compared to NEDC, the energetic repartition of WLTP is much evenly distributed inside the complete EM torque envelopes. Thus from the machine optimization point of view, it is hard to utilize the represent points method [154] to optimize the efficiency of the E-machine in WLTP.

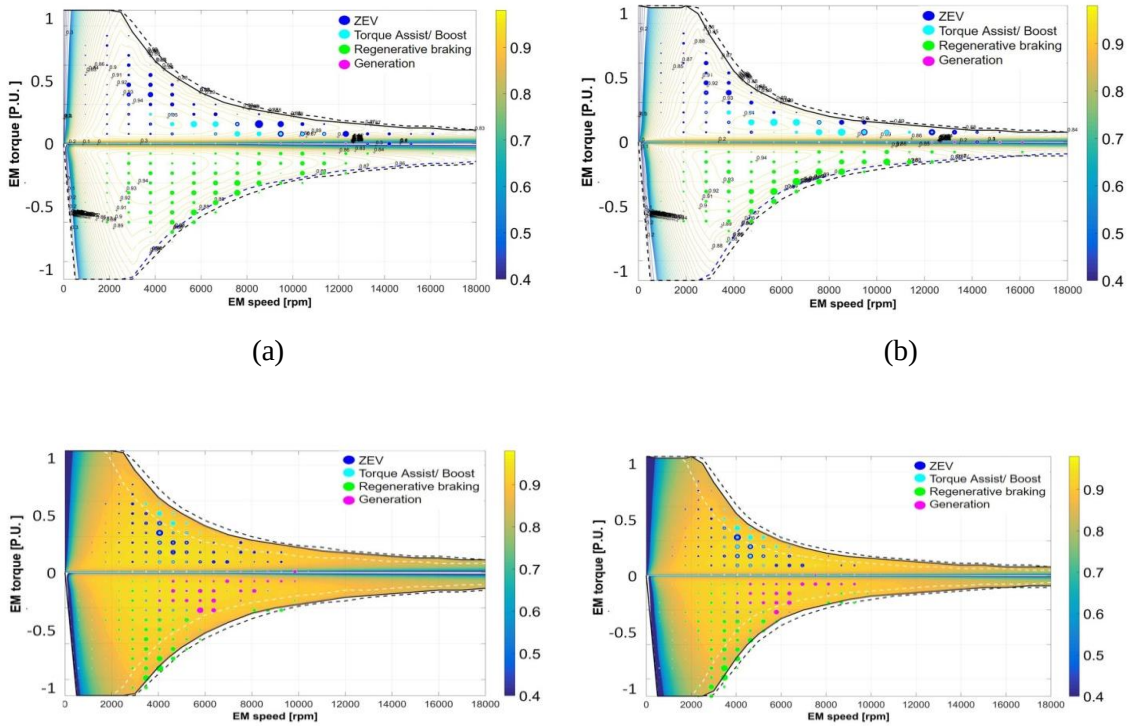

Fig. 211 Energy repartition of the machine operating points for WLTP (a) P4 with virgin magnets (b) P4 with recycled magnets (c) P2 with virgin magnets (d) P2 with recycled magnets @ 120 °C

4.4.3.4 Emission reduction results and index calculation

TABLE XLVI and Fig. 212 show the simulation results for the fuel consumption. Due to dynamic speed profile of WLTP, the fuel consumption is higher than NEDC. In WLTP cycle, the simulation results show that the powertrain hybridization allows ~ 17% of fuel saving compared to the baseline. The electric motor with virgin magnets has better efficiency and higher maximal power, this explains why the reduction of fuel consumption is higher with virgin magnets. In WLTP, the mean vehicle speed is approximately 46.5 km/h, clearly higher than NEDC's 34 km/h. On WLTP we can see that the P2 architecture is at an advantage, this is mainly due to the E-

machine being able to take profit from the gearbox: staying at moderate speed spares us the losses from high speeds. This enables for the most efficient areas of the E-machine to be privileged and it increases the regenerative power (E-machine maximum power is reached around 1/5th of its maximum speed).

TABLE XLVI CO2 EMISSION RESULTS (PER UNIT) OF P0P4 AND P2 MILD HYBRID CONFIGURATIONS

Configurations	WLTP		NEDC	
	Consumption (L/100km)	Gain (%)	Consumption (L/100km)	Gain (%)
Conventional	6.74	N/A	5.69	N/A
P0P4 virgin	5.57	17.4	4.17	26.7
P0P4 recycled	5.66	16	4.32	24
P2 offline virgin	5.57	17.4	4.4	26.2
P2 offline recycled	5.62	16.6	4.26	25.8

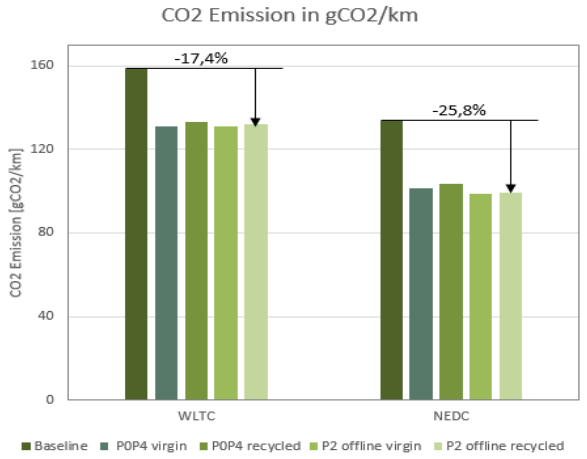

Fig. 212 Final gains of CO2 emission of P4 and P2 configurations with virgin and recycled magnets respectively on WLTC and NEDC

The graphic in Fig. 213 shows the recovered energy of each architecture on WLTP. It demonstrates the high efficiency of P2 architecture. It can be also remarked that the gain difference between virgin and recycled machine is higher in P0P4. Even that recycled electric machine has less losses at high speed as shown in Fig. 213, the impact of the drop of maximal power at high speed remains dominant on the fuel consumption in P0P4 architecture.

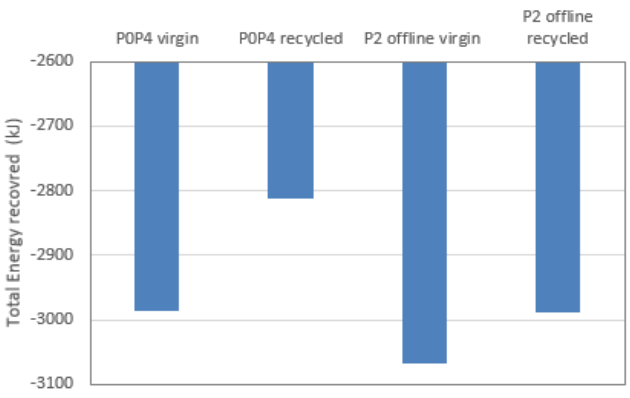

Fig. 213 Recuperation energies of P4 and P2 configurations with virgin and recycled magnets respectively on WLTP

Finally, energy index can be derived based on the final fuel consumptions of P2 configuration, the index matrix is shown in TABLE XLVII. It is interesting to find that with the same E-machine, Table (HEV) and Table (EV) show the same results. Thus, as long as the recycled magnet has the same cost with the virgin magnet, the recycle strategy can be profit. Last but not the least, it was figured out that the total cost of P2 configuration is 13% cheaper than P0P4 configuration. Thus by all dimensions, P2 with recycled magnet machine turns out to be the best solution.

TABLE XLVII ENERGY INDEX MATRIX WITH VARYING MAGNET COSTS FOR THE HEV APPLICATION

PM weight		Virgin magnet							
	0.8	PM price		30	50	70	90	110	130	150
			PM cost	24	40	56	72	88	104	120
0.8	kg	10	8	0.34	0.20	0.14	0.11	0.09	0.08	0.07
Recycled magnet		30	24	1.01	0.61	0.43	0.34	0.28	0.23	0.20
		50	40	1.68	1.01	0.72	0.56	0.46	0.39	0.34
		70	56	2.35	1.41	1.01	0.78	0.64	0.54	0.47
		90	72	3.03	1.82	1.30	1.01	0.83	0.70	0.61
		110	88	3.70	2.22	1.59	1.23	1.01	0.85	0.74

4.5 Conclusion

In order to evaluate the recyclability of PM electrical machines, WIRE method was developed. WIRE evaluates a PM E-machine from the phases of production, recycling and user. The production/recycling phases were evaluated by a scoring table involving standard, cost of materials and processing steps. The user phase was evaluated by changes of the energy consumption of the e-machine(s) over a drive cycle, due to the using of recycled PMs.

WIRE method was first evaluated on a commercialized HUB motor. Then WIRE was used to evaluate the newly designed IPMSM. It was found the production/recycling phases of the IPMSM had the potential to be higher than the HUB motor. For the user phase, the effects of using recycled magnets can be equivalent to the virgin magnets. In fact, the assumptions of recycle magnet were pessimistic because a full recycled magnet was assumed with the worst properties. Better results will be obtained once magnets are made from a mix of 30% recycle and 70%virgin powders.

Chapter 5 –Conclusion and future work

With the increasing demand of rare earth permanent magnets, as well as shortage of rare earth mining in Europe, it is necessary to recycle the rare earth permanent magnets. It can be foreseen that the traction electrical machines used on EVs and HEVs will be the main sources for rare earth PM recycling.

There are mainly three paths for rare earth PMs recycling – direct reuse, direct recycling and indirect recycling of the rare earth PMs. Direct reuse path has potential to be the most economical ways of recycling amount these three paths. Direct reuse means magnets can be easily extracted from an e- machine, which indicates the e-machine can be easily disassembled. Also the e-machine can implement the recycled magnets without significant performances degradation. As there are many different types of machines, specific direct reuse strategy needs to be developed for specific e-machines. Generally, there are 4 strategies to realize PM direct reusing - Complete magnet reusing, Modular magnet pole design, Magnet powder reusing and Modularity design.

Radial flux PM E-machines are the most conventional PM e-machines. They are widely used in (H)EVs. There are mainly two groups: SPMSM and IPMSM. SPMSM can implement the PM reuse strategies of complete magnet reusing or modular magnet pole design. IPMSM can comply the PMs reuse strategy of magnet powder reusing. Then, the possibility of applying SPMSMs and IPMSMs on small EVs or mild hybrid EV was investigated in terms of their performances. The designs of these machines were studied based on FEM simulations.

Designs of SPMSM were thoroughly examined. Different pole, slot and turn number combinations were tried out. Optimizations on split ratio and magnet poles were carried out. Several critical thermal conditions were analyzed. It was figured out that all the SPMSM designs could not achieve the requirements, due to the weak flux weakening capability, risk of coil overheating and ordinary efficiency. An IPMSM design with 5 pole pairs and 60 slots was selected to be compared with SPMSM designs, it was found that the IPMSM could overcome all the problems SPMSM encountered. Meanwhile, the magnet can be well protected, no expensive sleeve needed to be used on the rotor.

Then magnet powder reusing concept was applied on the IPMSM designs. A kind of bonded magnet made by HDDR anisotropic magnet powder and PPS binder was applied to the rotor of IPMSM. This bonded magnet has the performances in between traditional sintered NdFeB magnets and Ferrite magnets. Most importantly, it is possible to be melted down and reused again without significant performance degradation. The IPMSM was further optimized by trying 1, 2 and 3 magnet layers in the rotor. The rotor parameters that optimized included magnet layer span, shape, position, as well as the shaping of the rotor surface. After a thorough optimization, it was concluded that 2-layer rotor IPMSM is the best choice for the application, in terms of the performances as well as manufacture difficulty.

Based on the new IPMSM design with bonded magnets, a mock-up was fabricated. Unfortunately, the performance of the bonded magnets used for prototyping was not ideal. The measured remanence flux density was found to be 35% lower than that predicted by the supplier's original specifications. Nevertheless, new simulations have been carried out on the basis of the measured magnetic characteristics of the bonded magnets used. Serial reference tests at different temperatures were performed, such as no-load tests, short-circuit tests and load tests, for both generator and motor modes. Back-EMF, short circuit currents, torque and efficiency were measured during these tests. It has been found that the difference between the simulation results and the measurement results remained at an acceptable level. Thus, the simulation results were verified.

Apart from new design ideas of electrical machines, another goal is to evaluate e-machines with respect to the recyclability. Two indexes were introduced and used to evaluate the recyclability in terms of the production/recycle phases and user phase. Together they are called WIRE method. By using WIRE, the recyclability between different machines can be comparable, even with different dimension or power.

WIRE was first validated on a commercial PM HUB motor, which is a typical SPMSM with outer rotor. The HUB motor was disassembled for evaluating the WIRE index of production and recycle phases. Then an identical HUB motor was used for efficiency benchmark. Finite Element Method (FEM) results were validated by experiment methods with torque and efficiency measurements. Afterwards the energy consumptions of the machines with virgin magnets and recycled magnets were derived respectively. Hence, the second WIRE index of user phase could be evaluated. Finally, the validated WIRE methods were applied to the newly designed IPMSM with bonded magnets. The calculated efficiency maps were used to derive the energy index for both EV and HEV applications. It was found that by assuming 20% remanence flux density degradation on recycled magnets, the energy consumptions of the e-machine with recycled magnets for both HEV and EV applications had only small degradation, which can be totally acceptable. Furthermore, by taking into account the whole life cycle cost of rare earth mining and magnet production, it is very promising to gain environment benefit if the direct reuse strategy of rare earth PMs is implemented.

Future works

The analyses above are mainly served for the basic machine designs theories in this thesis. For each section, some topics were excluded, since they are either out of the scope, or not mature on analytical formulas. However, they still need to be highlighted to explain some phenomenon, and also for the interest of future studies.

Regarding the winding factor, there are many special ways to improve the winding factors or reduce sub-harmonics, such as using unequal teeth size [96], or different turns per coil [115]. However, due to the standardization of manufacturing, these special methods were not considered in the machine designs for mass production. Finally, many end winding details are excluded, especially for the insulation influence to the end winding length calculation.

As the thesis is more focused on machine ontology design than control, transient states are excluded for the Park transformation. Besides, many cross coupling items, such as mutual inductances between *dq* phases, or between dual phase-sets for dual-three phase winding, were ignored. Details can be found in [116]-[120].

For the section of efficiency, iron loss was still largely simplified. For instance, the manufacture impacts to the iron loss have not gone into details [107]. The influence of dc-bias magnetic field is barely considered, due to the compromised iron loss model implemented. Also, the influence of temperature to the iron loss is ignored, as the influence normally is small. Finally, the skin effect is ignored in the iron sheet, since this impact is only concerned for ultra-high speed machines. These details can be found in [121]. Besides, magnet eddy current losses were not discussed, since this will not be a serious concern for machines using distributed winding or bonded magnets.

Another important topic that was excluded is the influence of the motor drive. The drives for brushless DC electrical machines use Pulse-Width-Modulated (PWM) schemes. However, there are many different modulation methods, such as full-wave PWM, Sine-triangle PWM (SPWM) and Space Vector PMM (SVPWM). Each control method brings unique impacts to the machine performances, such as torque and efficiency. Moreover, the switch frequency of PWM also has significant impact to the losses. For instance, with higher switching frequencies, time harmonics in the current are lower, which results in lower iron losses and torque ripple, as well as lower noise and vibration. These details can be found in [121]-[127].

For multi-physics studies, the bidirectional coupling between electromagnetic field and mechanics was ignored. The Computational Fluid Dynamics (CFD) analysis of cooling watering flaw and wind flow are out of our scope.

Finally, WIRE method can be refined by including more processes steps with more specific norms. User phase results can be improved by using real road test data and real recycled magnet prices. It will more reasonable if the full chain of life cycle assessment from “mining” to “wheel” can be taken into account in WIRE.

Chapitre 6 - Résumé français

6. 1 Introduction

Aujourd'hui, notre planète est confrontée au changement climatique, en raison des gaz à effet de serre provenant de l'activité humaine. Il est impératif de réduire les émissions de CO_2 des véhicules routiers. L'une des stratégies les plus prometteuses pour réduire les émissions de CO_2 des automobiles consiste à utiliser des véhicules fonctionnant à partir de sources d'énergie non conventionnelles, également appelés véhicules à énergie nouvelle. Ces véhicules inclut divers sous-groupes. La partie la plus importante concerne les véhicules électriques (VÉ) et hybrides électriques (VÉH). Les VÉ et les VÉH peuvent être alimentés par une batterie au lithium ou par une pile à combustible. Cependant, quels que soient leurs sources et leurs dispositifs de stockage d'énergie, les VÉ et VÉH ont besoin de machines électriques pour réaliser la conversion d'énergie électromécanique. Par conséquent, les machines électriques sont, dans leur ensemble, des composants très importants des chaînes de propulsion des véhicules électriques.

Valeo est un leader dans le domaine de l'industrialisation de machines électriques pour l'automobile. Cette entreprise possède l'une des plus grandes parts de marché dans le domaine de la R&D, de la production et de la commercialisation de démarreurs et d'alternateurs et dispose d'une grande. Capacité de produire, en série, un nombre significatif de ces machines. Valeo occupé un tiers de la part de marché de l'alternateur électriques en 2018 et a également l'ambition d'être un des leaders sur le marché des chaînes de propulsion de VÉ et VÉH. L'entreprise Valeo a donc comme priorité de développer et produire des machines électriques performantes pour ce type d'application. Ceci implique la nécessité de répondre à des critères de performances élevés en termes de densité de couple et de rendement. Dans ce contexte, les machines électriques à aimants permanents sont parmi les meilleures candidates. Bien que la masse en aimants permanents soit relativement faible par rapport à la masse totale de la machine, le coût dû à ces aimants peut représenter jusqu'à la moitié du coût total d'une machine comprenant ce type de matériau. Par conséquent, pour que le coût d'une machine soit aussi bas que possible, il est essentiel d'étudier le coût des aimants permanents. Les aimants permanents ont évolué au cours du temps : découverts initialement via les ferrites et les AlNiCo, ils ont évolué, par la suite, grâce à des avancées scientifiques majeures en jouant sur la composition et le processus de fabrication. Par conséquent, de nos jours, les aimants permanents terres rares utilisés dans les machines électriques de traction automobile sont essentiellement constitués d'éléments terres rares dans une grande proportion (jusqu'à 32%). La densité d'énergie magnétique des aimants terres rares est beaucoup plus importante que celle des aimants ferrites. L'aimant permanent à base de terres rares à la densité d'énergie la plus forte a été inventé en 1982 : il s'agit de l'aimant Néodyme-Fer-Bore ($Nd_2Fe_{14}B$), ou simplement dénommé par l'acronyme NdFeB. La densité d'énergie des aimants NdFeB peut être deux fois supérieure à celles des aimants terres rares à base de Samarium Cobalt (SmCo). Généralement, afin d'améliorer la stabilité en température des propriétés magnétiques ainsi que le champ coercitive (résistance) à la désaimantation, une petite quantité d'éléments terres rares lourds, comme le Dysprosium (Dy) ou le Terbium (Tb) est ajoutée à l'alliage aimant permanent terres rares NdFeB.

Par conséquent, en raison de la supériorité des propriétés magnétiques des aimants NdFeB, les machines électriques à aimant NdFeB sont particulièrement utilisées dans les secteurs industriels technologiquement avancés comme l'industrie des disques durs informatiques (Hard Disk Drive), celle des éoliennes, des véhicules électriques (VÉ et VÉH), etc. Cependant, cette forte demande en terres rares implique de sérieux problèmes d'approvisionnement, particulièrement pour le marché européen. Plus précisément, ce sont les éléments terres rares tels que le Néodyme (Nd), le Dy et le Tb qui sont confrontés à ces difficultés. En 2011, le marché mondial des matériaux terres rares a connu une crise qui s'est manifestée par une montée en flèche de leur cours. Lors des jours les plus critiques de cette crise, le prix du Nd était environ 6 fois plus important que celui en 2010, soit équivalent à 10 fois le prix de l'or ! Une crainte persiste que ce scénario ne se reproduise à nouveau dans un avenir proche. Outre le problème dû au coût élevé et variable des terres rares, l'extraction minière de ces matériaux n'est pas un processus écologiquement durable. Les aimants SmCo ne peuvent pas être, non plus, une alternative aux aimants NdFeB car l'approvisionnement en Cobalt (Co) est également sujet à des difficultés. La plus grande partie du Cobalt est extraite en République Démocratique du Congo (RDC) et l'industrie minière y connaît de graves difficultés à cause de l'instabilité politique et économique dans cette région.

Il est donc impératif de trouver une nouvelle façon d'utiliser les terres rares, voire de les remplacer. Pour l'Europe, il existe différentes solutions pour lutter contre les risques d'approvisionnement en terres rares :

1. La prospection de nouveaux gisements miniers de terres rares en Europe
2. Le développement d'aimants sans terres rares tout en ciblant les performances des aimants NdFeB
3. Le recyclage des aimants terres rares.

La première solution en est encore au stade précoce de l'exploration géologique. En outre, il est impossible de mettre en exploitation une nouvelle mine dans un aussi court laps de temps. La deuxième solution est une technologie de niche qui n'est pas encore utilisée à grande échelle. Comme chaque aimant terres rares de nouvelle génération comme les NdFeB contient du Néodyme, il paraît intéressant d'étudier la troisième solution. Le sujet du recyclage des terres rares implique différentes questions. Tout d'abord, les sources de recyclage des terres rares peuvent être multiples : des résidus de séparation lors de phase d'enrichissement du minerai ou des produits en fin de vie contenant des terres rares. De plus, il existe de nombreux procédés techniques pour recycler les terres rares qui dépendent du type de terres rares en question. Étant donné que l'industrie automobile s'oriente de plus en plus vers les véhicules électriques et hybrides électriques, elle deviendra probablement le principal consommateur d'aimants terres rares. **DEMETER est l'acronyme anglais pour le groupe européen de formation universitaire pour la conception et le recyclage de moteurs et de générateurs électriques à aimants permanents terres rares pour les véhicules tout-électriques et hybrides électriques. DEMETER** est un projet enregistré par l'union européenne. Son objectif était étudier les trois voies possible pour le recyclage des aimants permanents à base de terres rares présents dans les moteurs électriques : la **réutilisation directe,** le **recyclage direct** et **le recyclage indirect.** Valeo est l'un des principaux partenaires industriels de ce projet. Cette entreprise s'intéresse principalement à **la réutilisation directe des aimants permanents**. Concrètement, l'objectif est de rechercher un moyen facile de retirer les aimants des moteurs et des alternateurs en fin de vie. Ensuite, il faudra trouver un moyen de les utiliser à nouveau dans de nouveaux moteurs/alternateurs. A l'inverse de la réutilisation directe qui ne nécessiterait pas de processus complexe, les deux autres méthodes (recyclage direct et indirect) utilisent des procédés physiques et/ou chimiques complexes. En plus de leur complexité technologique, ces filières de recyclage direct et indirect sont d'autant plus longues et coûteuses par rapport à la réutilisation directe. Ainsi, une fois que le processus de réutilisation directe des aimants sera maitrisé, il s'agira du moyen le plus économique de recycler les aimants. Les travaux de doctorat qui sont présentés dans cette thèse ont été financés par l'union européenne et supervisés par l'entreprise Valeo à Créteil et le laboratoire G2Elab à Grenoble. Cette thèse se concentre principalement sur les machines électriques à flux radial à aimants permanents qui sont les machines électriques les plus utilisées de nos jours. Les applications visées sont les véhicules hybrides électriques à niveau d'hybridation douce (*Mild Hybrid*) ou les petits VÉ. Le dimensionnement de ce moteur innovant doit non seulement être recyclable du point de vue des aimants permanents mais doit également répondre à tous les critères exigeants du cahier des charges.

6. 2 Conception de la machine

Lorsqu'on fait référence aux machines électriques à aimants permanents, on parle conventionnellement des machines synchrones à aimants permanents (MSAP) à flux radial. Deux catégories de MSAP sont habituellement distinguées : les machines synchrones à aimants permanents montées en surface (MSAPS) et les machines synchrones à aimants permanents insérés ou enterrés (MSAPI). Les stators de ces deux types de machines électriques sont normalement similaires. En effet, les principales différences concernent leurs rotors. Comme le nom de ce type de machines l'indique, les aimants d'une MSAPS se trouvent à la surface du rotor. Il est donc facile d'accéder aux aimants. Leur positionnement facilite également leur démontage. Cependant, le couple d'une machine à aimants en surface est entièrement produit par l'intermédiaire des aimants permanents. Ainsi, la quantité nécessaire en aimants permanents pour une telle machine est élevée. Les MSAPS présentent également des inconvénients tels qu'une faible capacité de défluxage et un risque de désaimantation. De plus, l'utilisation de la colle est indispensable pour la fixation des aimants sur le rotor. Enfin, un manchon mécanique, à la fois solide et léger, en fibre de carbone ou en métal, doit être emmanché sur le rotor pour retenir les aimants si la machine fonctionne à très grande vitesse. Par conséquent, du fait du manchon, l'entrefer magnétique est plus grand et le coût de fabrication est augmenté. Les machines synchrones à aimants permanents insérés (MSAPI) les aimants sont placées à l'intérieur du circuit magnétique du rotor et sont de ce fait plus protégé. Le couple d'une MSAPI est généré par l'intermédiaire des aimants mais aussi de la réluctance du rotor liée à sa saillance magnétique. De ce fait, la quantité d'aimants nécessaire à une MSAPI est normalement réduite par rapport à une MSAPS. Les machines à aimants insérés ont une bonne capacité de défluxage et le fait qu'ils soient enterrés permet de réduire le risque de désaimantation, de protéger leur surface de la corrosion et d'empêcher leur décollement par effet centrifuge à haute vitesse. De ce fait, le manchon mécanique n'est plus nécessaire à un dimensionnement

mécanique robuste de rotor. Cependant, les aimants frittés sont traditionnellement segmentés pour être collés à l'intérieur du rotor. Par conséquent, la colle, la force d'attraction magnétique et la segmentation rendent difficile le démontage des aimants pour leur réutilisation. Un autre point important est la possible nécessité de donner une forme différente à l'aimant lors de sa réutilisation dans un nouveau dimensionnement de machine. Cette nouvelle forme de l'aimant à chaque réutilisation doit être rendue possible dès la phase initiale de la conception.

En raison des spécifications exigeante pour les machines électriques dans applications VE et VEH, telles que performances, coût, fiabilité et production en série, il est probable que dans le groupe des machines électriques à flux radial, seules les MSAPS et les MSAPI conviennent. Par conséquent, cette thèse a pour but d'étudier et de proposer un ou plusieurs dimensionnements de machines MSAPS et MSAPI qui satisfassent aux cahiers des charges exigeants des applications véhicules électriques et également au concept de la réutilisation et le récyclaces des aimants à base de terres rares.

Premièrement, les MSAPS ont été étudiées. Nous avons décidé d'utiliser un bobinage distribué plutôt qu'un bobinage concentré sur dent. Afin de faire ce choix, nous avons comparé les harmoniques dus à la réaction d'induit et les coefficients de bobinage. Nous avons opté pour un bobinage double-triphasé afin d'augmenter la densité de puissance. Des modules de convertisseurs électroniques de puissance standards sont utilisés. Les matériaux pour le paquet de tôles ferromagnétiques et le cuivre composant les bobines ont également été fixés pour toute l'étude. Un grade d'aimant permanent NdFeB fritté a été choisi. Les dimensions extérieures de la machine ont été contraintes afin de limiter l'encombrement maximal alloué à l'ensemble. Enfin, en tenant compte de l'épaisseur de la frette de maintien des aimants emmanchée sur le rotor, l'entrefer minimum a été fixé à 2 mm. Ainsi, l'optimisation a pu être menée avec les contraintes susmentionnées. Des modèles numériques éléments finis électromagnétiques 2D et 3D ont été utilisés pour l'optimisation. Nous avons pu obtenir une machine aux performances (couple, puissance, rendement) optimales grâce à une étude paramétrique sur les variables de dimensionnement comme le nombre de pôles, le nombre de spires, le nombre d'encoches ainsi que le rayon du rotor et la forme des aimants. Plusieurs MSAPS optimales ont été retenues. De plus, la désaimantation et la tenue thermique ont été validées par une méthode simple et rapide. Sur la base de tous les résultats obtenus à l'issue de l'optimisation, nous avons conclu que la MSAPS (60,10) à 60 encoches et 10 pôles (5 paires de pôles) représentait le meilleur optimum.

TABLEAU I. SOMMAIRE DES AVANTAGES ET DES INCONVÉNIENTS DE 3 MACHINES À AIMANTS EN SURFACE ET UNE MACHINE À AIMANTS INSÉRÉS

Type de machine (Nb. encoches, Nb. pôles)	Couple	Puissance	Désaimantation	Rendement	Tenue thermique	Quantité d'aimant
MSAPS (48,8) pas diamétral	√	√	√	X	X	-
MSAPS (48,8) pas raccourci	√	-	-	-	X	X
MSAPS (60,10)	√	X	√	√	X	√
MSAPI (60,10)	√	-	√	√	-	-

* √ Satisfaisant ; X Non-satisfaisant ; - Assez satisfaisant

Deuxièmement, une machine synchrone à aimants permanent insérés (MSAPI) à 60 encoches et 10 pôles a été dimensionnée afin de la comparer à la machine à aimants en surface précédemment conçue. Les mêmes matériaux magnétiques ont été choisis. Des contraintes dimensionnelles identiques ont été adoptées. Puisqu'il n'y a pas de manchon pour la MSAPI, l'entrefer minimum a été réduit à 0,5 mm. Après une deuxième optimisation, nous avons constaté que les performances de la machine à aimants enterrés étaient meilleures que celles de la machine à aimants en surface, comme le montre le Tableau 1.

Cependant, avec la méthode d'assemblage usuelle, les aimants ne peuvent toujours pas être réutilisés. Pour la conception de la machine à aimants insérés (MSAPI), nous avons utilisé un aimant lié. Cet aimant a été fabriqué par l'association d'une poudre anisotrope de NdFeB obtenue par un procédé de recombinaison par désorpronation Désorption à hydrogène (*HDDR, Hydrogenation Desproportionation-Desorption Recombination*) avec un liant Sulfide (PPS). Ainsi, la densité d'énergie magnétique de l'aimant lié au NdFeB est supérieure à celle des ferrites, mais inférieure à celle des aimants frittés NdFeB. L'aimant lié est directement assemblé au fer rotorique par moulage par injection. L'aimantation de l'aimant lié est réalisée simultanément. Par conséquent, l'assemblage de la machine avec des aimants liés est plus facile que l'assemblage avec des aimants frittés. En outre, quelle que soit la forme des aimants, la méthode d'assemblage reste identique. Le démontage des aimants est également plus facile. En effet, pour les aimants liés, il n'y a pas de colle et la force d'attraction magnétique est moins forte que celle de l'aimant NdFeB fritté traditionnel. Ceci a pour conséquence que les aimants peuvent être facilement expulsés du rotor. Par ailleurs, aucune segmentation n'est nécessaire pour les aimants liés en raison de leur résistivité électrique élevée. Dans le contexte d'un procédé de recyclage en série des rotors à aimants liés, ces derniers pourraient être chauffés afin de faire fondre les aimants liés et les extraire ensuite facilement. Après avoir retiré les aimants, ils peuvent être mélangés à des aimants vierges dans une proportion 70% d'aimants vierges, 30% d'aimants recyclés pour fabriquer de nouveaux aimants liés sans modification notable des performances magnétiques de l'aimant. En somme, l'ensemble du processus de recyclage est relativement facile et écologiquement durable.

Ainsi, sur la base de ce nouveau concept, une machine à aimants enterrés (MSAPI) de type NdFeB liés a été dimensionnée. En prenant en compte quelques légères modifications sur les contraintes et en utilisant un couplage triangle pour chacun des deux systèmes triphasés, les performances de la MSAPI dimensionnée répondent aux spécifications en performances du cahier des charges, sans désaimantation et avec une bonne tenue thermique. Le rendement le plus élevé obtenu est supérieur à 95%, même en ajoutant aux pertes certains effets mineurs tels que les pertes cuivre AC et l'impact de la fabrication des tôles laminées sur les pertes fer. Par conséquent, un prototype de MSAPI avec des aimants liés a été fabriqué sur la base du dimensionnement proposé. La figure 1 montre le rotor de la machine prototypée. Pour ce prototype, les aimants liés n'ont pas injecté car le procédé n'était disponible. Ils ont été usinés dans la masse et placés dans les cavités allouées.

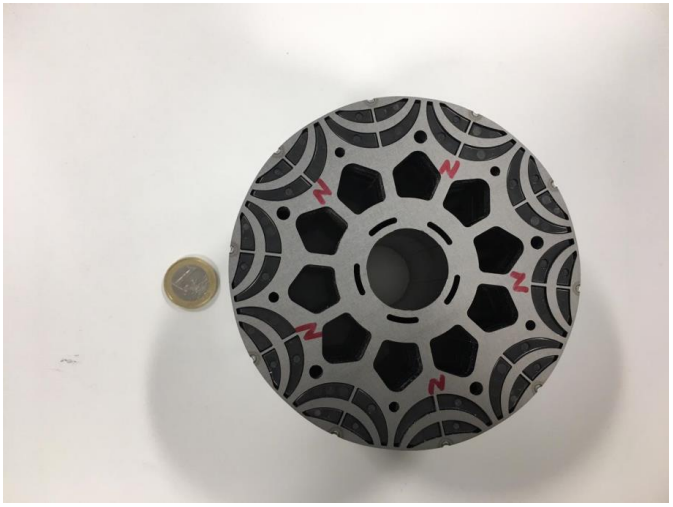

Fig. 1 Photo du rotor du prototype de la MSAPI avec les aimants permanents NdFeB liés

Cependant, les performances des aimants liés utilisés dans le prototype se sont révélés moins bons que ceux escomptés. La densité de flux de rémanence mesurée s'est révélée 35% inférieure à celle annoncée par les spécifications d'origine du fournisseur. Des nouvelles simulations ont alors été réalisées sur la base des ces

nouvelles caractéristiques magnétiques mesurées des aimants. De nombreux essais de référence ont été à réalisés différentes températures évaluer les performances de cette machine que ce soit, à vide, en court-circuit ou encore en charge et que ce soit en pour les modes générateur ou mode moteur. Les forces contre-électromotrices, les courants de court-circuit, le couple et le rendement ont été mesurés au cours de ces tests. Il a été constaté que la différence entre les résultats de simulations et les résultats des mesures reste à un niveau acceptable permettant ainsi de valider les résultats de simulation.

6. 3 Evaluation de la recyclabilité

Dans cette thèse, en plus des propositions de dimensionnements innovants, l'objectif est d'évaluer les machines électriques du point de vue de leur recyclabilité. Pour être définie comme recyclable, la machine électrique doit répondre aux deux conditions suivantes :

- La machine peut être facilement désassemblée et ses matériaux constitutifs peuvent être facilement recyclés
- La machine utilise des matériaux recyclés sans, ou avec peu de, dégradation de ses performances

Aujourd'hui, il n'existe pas d'outil pour évaluer la recyclabilité des machines électriques. Aucune expérience n'a été conduite jusqu'à présent pour effectuer une étude comparative en considérant cet aspect. En se basant sur les deux critères qui définissent la recyclabilité, nous présentons, dans cette thèse, deux méthodes pour analyser et évaluer le recyclage des machines électriques à aimants permanents pour les véhicules électriques :

- La première méthode évalue la recyclabilité des processus de production et de recyclage de la machine à aimants permanents. Ceci concerne son assemblage, son désassemblage et la mise en place d'une ligne pilote en vue d'une extension pour une application série.
- La seconde méthode évalue la recyclabilité de la phase d'utilisation de la machine. Principalement, nous évaluons l'impact de l'utilisation de matériaux recyclés (dans ce cas uniquement les aimants permanent) sur la consommation d'énergie d'une machine électrique sur la totalité de son cycle d'utilisation.

Les résultats de ces deux méthodes sont chiffrés par l'intermédiaire de deux indices. Ces derniers peuvent être regroupés sous le terme WIRE (*Weighted Index of Recycling and Energy* – index Pondéré de recyclage et de consommation énergétique). Grâce aux indices WIRE, la recyclabilité de deux machines non identiques peut être comparée, même si leur dimensionnement et leurs performances (puissance, couple, rendement, etc.) sont différentes.

Dans cette thèse, les indices WIRE ont d'abord été introduits puis validés sur un moteur roue à aimants permanents commercial utilisé dans une petite voiture de golf. Le moteur roue a été désassemblé pour évaluer l'indice WIRE concernant les processus de production et de recyclage. Ensuite, un moteur roue identique a été utilisé pour réaliser une analyse comparative sur les rendements. Les résultats obtenus par simulation éléments finis ont été validés avec des relevés expérimentaux de couple et de rendement. Ensuite, les consommations d'énergie des machines à aimants vierges et à aimants recyclés ont été calculées. Ainsi le deuxième indice WIRE concernant la phase d'utilisation a pu être évalué. Enfin, la méthode d'évaluation WIRE a été appliquée à la machine synchrone à aimants permanents liés insérés (MSAPI) dimensionnée. Les cartographies de rendement obtenues ont été utilisées pour calculer les indices énergétiques relatifs aux applications véhicules électriques et véhicules hybrides électriques. D'après certaines études de littérature connexes, on suppose une diminution de 20% de la densité de flux rémanent (Br) de l'aimant recyclé (ce qui est très pessimiste si on considère un aimant non pas réalisé totalement à partir poudres recyclés mais par un mélange de 50% de poudres d'aimant vierges et 50% de poudres). Avec cette hypothèse, la consommation d'énergie de la machine électrique avec les aimants recyclés pour les applications véhicules électriques connait une augmentation faible mais acceptable. Une partie des résultats est présentée dans le Tableau 2. Cependant, en prenant en compte le coût total du cycle de vie depuis l'extraction minière des terres rares à la production des aimants, la réutilisation des aimants et leur recyclage apparait comme une piste prometteuse pouvant avoir un effet bénéfique sur l'environnement.

TABLEAU 2 RÉSULTATS DES ÉMISSONS DE CO2 (VALEURS P.U) DES ARCHITECTURES À NIVEAU D'HYBRIDATION DOUCE A ET B

Configuration hybridation douce		CO2 (CO2 g / km)			
		WLTP		NEDC	
		consommation (L/100km)	Réduction (%)	consommation (L/100km)	Réduction (%)
Référence		6.74	N / A	5.69	N / A
1	A avec aimants vierges	5.57	17.4	4.17	26.7
2	A avec aimants recyclés	5.66	16	4.32	24
3	B avec aimants vierges	5.57	17.4	4.4	26.2
4	B avec aimants recyclés	5.62	16.6	4.26	25.8

Appendix

1. Harmonics and torque ripples

1.1 Three phase torque ripple

Besides constant torque value, the quality of torque is also important. This can be measured by the cogging torque and torque ripples. Cogging torque is a variation of the torque given by the permeance variation along the air gap at 0 current. The variation of permeance is due to the stator slot opening. Therefore, the constant torque part of cogging torque is zero.

It is more important to pay attention to the torque ripple, as it is the torque pulsation during the load condition. Normally it is essential to keep the ratio of torque ripple to inertia as low as possible, especially at low speed, in order to keep the rotation speed constant. Also if the machine is coupled with other sensitive equipment, like gearbox or clutch, a low torque ripple is also required to control noise and vibration.

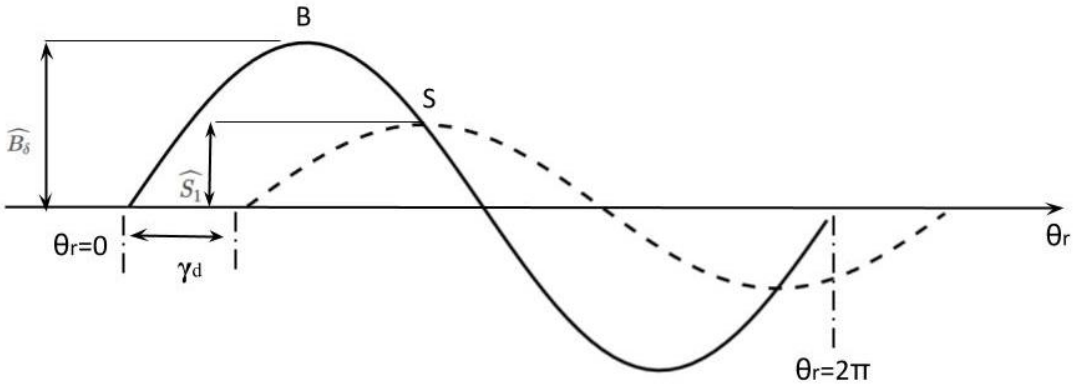

Fig. 1 Sinusoidal waveforms of airgap flux density and current loading with phase shift.

Thus, taking a three phase SPMSM for example, torque ripple will be analyzed by mathematics. First, assuming that I_a, I_b, I_c are the currents of three phases *A*, *B* and *C*. With balanced phase currents, a synthesis current I_m can be derived by Eq. 1.

$$I_m = \frac{2}{3}(i_a.e^{j.0} + i_b.e^{j.120} + i_c.e^{j.240}) = \widehat{I_m}\angle\gamma_\alpha \quad \text{Eq. 1}$$

Where the amplitude of $\widehat{I_m}$ is kept the same with original amplitude of three-phase current. The angle γ_α is the angle between I_m and phase *A*. Assuming the angular position of phase *A* is 0, and regarding γ_d still as the angle between current waveform I_m and the airgap flux density B_δ as Fig. 1 shows. γ_α can be disassembled to Eq. 2,

$$\gamma_\alpha = \omega_s t + \gamma_d \quad \text{Eq. 2}$$

where $\omega_s$is the electrical angular speed. I_a, I_b and I_c can also be used to synthesis a stator magnetic potential (MMF) M_s, as expression Eq. 3 shows.

$$M_s = n(\theta_s)I_a + n\left(\theta_s - \frac{2\pi}{3}\right)I_b + n\left(\theta_s + \frac{2\pi}{3}\right)I_c \quad \text{Eq. 3}$$

θ_s is the electrical angular position of stator reference frame. *n* is a winding function. It can be expressed as Eq. 4,

$$n = \sum_{v=1,2,3\ldots} n_v cos(v\theta_s), \quad \text{Eq. 4}$$
$$n_v = \frac{4}{\pi v}.\frac{Q_s}{6p}.N_s$$

where n_v is the amplitude of *v-th* stator harmonic. Here assume winding function is a square wave. Q_s is still total slot number, N_s is still the number of conductors per slot. Thus, Eq. 3 can be expended to Eq. 5.

$$\begin{aligned} M_{sv}(\theta_s, t) = 0.5\widehat{M_{sv}}[cos(v\theta_s - \omega_s t) + cos\left(v\theta_s - \omega_s t - \frac{v-1}{v}\frac{2\pi}{3}\right) \\ + cos\left(v\theta_s - \omega_s t - \frac{v-1}{v}\frac{4\pi}{3}\right)] \\ +0.5\widehat{M_{sv}}[cos(v\theta_s + \omega_s t) + cos\left(v\theta_s + \omega_s t - \frac{v+1}{v}\frac{2\pi}{3}\right) + cos\left(v\theta_s - \omega_s t - \frac{v+1}{v}\frac{4\pi}{3}\right)], \\ \widehat{M_{sv}} = \widehat{I_m}.n_v \end{aligned} \quad \text{Eq. 5}$$

It is found that for different harmonic orders, the rotation direction of the waves is different, as Eq. 6 shows.

$$\begin{aligned} &M_{sv}(\theta_s) = 1.5\widehat{M_{sv}}cos(v\theta_s - \gamma_\alpha), \text{ when v=6k+1, k=0,1,2; forward rotating} \\ &M_{sv}(\theta_s) = 1.5\widehat{M_{sv}}cos(v\theta_s + \gamma_\alpha), \text{ when v=6k-1, k=0,1,2; backwards rotating} \\ &M_{sv}(\theta_s) = 0, \text{ when v=6k+3, k=0,1,2} \end{aligned} \quad \text{Eq. 6}$$

Thus, the total stator magnetic potential M_s can be expressed as Eq. 7.

$$M_s(\theta_s) = \sum_{v=1,7,13,..} 1.5\widehat{M_{sv}}\, cos(v\theta_s - \omega_s t - \gamma_d) + \sum_{v=5,11,17,\ldots} 1.5\widehat{M_{sv}}\, cos(v\theta_s + \omega_s t + \gamma_d) \quad \text{Eq. 7}$$

Next, as the relationship between magnetic potential M_s and current loading is expressed as Eq. 8.

$$S = \frac{dM(\theta_s)}{d(\theta_s)} \Big/ \frac{(D_{in} - \delta)}{2} \quad \text{Eq. 8}$$

The sum of all current loading harmonics $S_s$can be calculated by Eq. 9.

$$\begin{aligned} S_s(\theta_s) &= -\frac{\sum_{v=1,7,13,..} 1.5v.\widehat{M_{sv}}\, sin(v\theta_s - \omega_s t - \gamma_d) + \sum_{v=5,11,17,\ldots} 1.5v.\widehat{M_{sv}}\, sin(v\theta_s + \omega_s t + \gamma_d)}{\frac{(D_{in} - \delta)}{2}} \\ &= -\frac{2}{p}N_s \frac{\sum_{v=1,7,13,..} \widehat{I_m}\, sin(v\theta_s - \omega_s t - \gamma_d) + \sum_{v=5,11,17,\ldots} \widehat{I_m}\, sin(v\theta_s + \omega_s t + \gamma_d)}{\left(\pi\frac{(D_{in} - \delta)}{Q_s}\right)} \\ &= -\widehat{S_s}[\sum_{v=1,7,13,..} sin(v\theta_s - \omega_s t - \gamma_d) + \sum_{v=5,11,17,\ldots} sin(v\theta_s + \omega_s t + \gamma_d)], \end{aligned} \quad \text{Eq. 9}$$

$$\widehat{S_s} = \frac{2}{p} N_s \frac{\widehat{I_m}}{(\pi \frac{(D_{in} - \delta)}{Q_s})} = \frac{2}{p} \widehat{S_1}$$

With all the parameters above, and based on Eq. 10, the torque calculation on stator reference frame can be written as Eq. 11.

$$T = \frac{(D_{in}-\delta)}{2} . p. \int_{\theta_r=0}^{2\pi} \frac{(D_{in}-\delta)}{2p} . L. \widehat{S_1}. \widehat{B_\delta}. k_{w1}. sin\ \theta_r. sin(\theta_r - \gamma_d) d\theta_r \text{ [N.m]} \quad \text{Eq. 10}$$

$$T = \frac{(D_{in} - \delta)}{2} . p. \int_{\theta_s=0}^{2\pi} \frac{(D_{in} - \delta)}{2p} . L. S_s(\theta_s). B_{\delta s}(\theta_s). d\theta_s \quad \text{Eq. 11}$$

Thus, the only parameter left unknown is the airgap flux density with all harmonics. The flux density can be derived from the sum of stator and rotor magnetic potentials, as Eq .12 indicates,

$$\begin{aligned} T &= \frac{(D_{in} - \delta)^2}{4} . L \int_{\theta_s=0}^{2\pi} S_s(\theta_s). \mu_0. \frac{-M_s(\theta_s) + M_r(\theta_s)}{\delta} d\theta_s \\ &= \frac{\mu_0}{\delta} \frac{(D - \delta)^2}{4} . L[\int_{\theta_s=0}^{2\pi} -S_s(\theta_s). M_s(\theta_s) d\theta_r + \int_{\theta_s=0}^{2\pi} S_s(\theta_s). M_r(\theta_s). d\theta_s] \\ &= k_T \int_{\theta_s=0}^{2\pi} -S_s(\theta_s). M_s(\theta_s) d\theta_r + k_T \int_{\theta_s=0}^{2\pi} S_s(\theta_s). M_r(\theta_s). d\theta_s, \\ k_T &= \frac{\mu_0}{\delta} \frac{(D_{in} - \delta)^2}{4} . L \end{aligned} \quad \text{Eq. 12}$$

where M_r is the magnetic potential from the rotor. k_T is the constant of coefficient of torque. Therefore, for the first part of the equation, Substitute Eq. 7 and Eq. 9, it can be calculated by Eq. 13.

$$\begin{aligned} &\int_{\theta_s=0}^{2\pi} -S_s(\theta_s). M_s(\theta_s) d\theta_r \\ &= \widehat{S_s}. \int_{\theta_s=0}^{2\pi} \left[\sum_{v=1,7,13\ldots} \widehat{M_{sv}} sin(v\theta_s - \gamma_\alpha) cos(v\theta_s - \gamma_\alpha) \right. \\ &\left. + \sum_{v=5,11,17..} \widehat{M_{sv}}. sin(v\theta_s + \alpha) cos(v\theta_s + \gamma_\alpha) \right] d\theta_s \end{aligned} \quad \text{Eq. 13}$$

$$=0.5\widehat{S_s}. \int_{\theta_s=0}^{2\pi} [\sum_{v=1,7,13\ldots} \widehat{M_{sv}} sin(2v\theta_s - 2\gamma_\alpha) + \sum_{v=5,11,17..} \widehat{M_{sv}} sin(2v\theta_s + 2\gamma_\alpha)] d\theta_s = 0$$

Thus the first part of Eq. 12 is zero, only the second part was kept. This indicates that torque ripple is only generated by the interaction of stator and rotor harmonics. Hence, rotor magnetic potential M_r needs to be derived. The waveform of M_r is even symmetric on the d-axis. Thus, it has no even harmonic from the knowledge of Fourier function. Then M_r can be expressed as Eq. 14.

$$M_r(\theta_s) = \sum_{v=2n+1, n=0,1,2} \widehat{M_r} \frac{1}{v} cos(v\theta_s - v\omega_s t) \quad \text{Eq. 14}$$

$\widehat{M_r}$ is the amplitude of magnetic potential. For a typical SPMSM, the flux is square wave, the magnet is full pole span, and the airgap thickness is constant. Then $\widehat{M_r}$ can be express as Eq. 15.

$$\widehat{M_r} = \frac{4}{\pi}.\frac{B_\delta}{v}.\frac{\delta}{\mu_0} = \frac{4}{\pi}.B_r.\frac{\delta}{\mu_0}.\frac{h}{h+\delta} \quad \text{Eq. 15}$$

where B_r is the remanence flux density of a PM, h is the height of the PM. Thus Eq. 12 can be continuously calculated as Eq. 16.

$$\begin{gathered} T = k_T \int_{\theta_s=0}^{2\pi} S_s(\theta_s).M_r(\theta_s).d\theta_s \\ =-k_T.\widehat{S_s}.\widehat{M_{rv}} \int_{\theta_s=0}^{2\pi}[\sum_{v=1,7,13\ldots}\frac{1}{v}.sin(v\theta_s-\omega_s t-\gamma_d).cos(v\theta_s-v\omega_s t)+\sum_{v=5,11,17\ldots}\frac{1}{v}.sin(v\theta_s+\omega_s t+ \\ \gamma_d).cos(v\theta_s-v\omega_s t)]\,d\theta_s, \\ k_T.\widehat{S_s}.\widehat{M_r} = \frac{(D_{in}-\delta)^2}{\pi}.L.\frac{h}{h+\delta}.B_r.\widehat{S_1} \end{gathered} \quad \text{Eq. 16}$$

For the first part of the bracket in the integral calculation, it can be separately calculated by Eq. 17.

$$\begin{gathered} \int_{\theta_s=0}^{2\pi} \sum_{v=1,7,13..} \frac{1}{v}.\sin(v\theta_s-\omega_s t-\gamma_d).\cos(v\theta_s-v\omega_s t)\,d\theta_s \\ = 0.5[\int_{\theta_s=0}^{2\pi} \sum_{v=1,7,13..} \frac{1}{v}.\sin\big((v-1)\omega_s t-\gamma_d\big)\,d\theta_s \\ + \int_{\theta_s=0}^{2\pi} \sum_{v=1,7,13..} \frac{1}{v}.\sin(2v\theta_s-(v+1)\omega_s t-\gamma_d)\,d\theta_s] \\ =0.5\int_{\theta_s=0}^{2\pi}\sum_{v=1,7,13..}\frac{1}{v}.\sin\big((v-1)\omega_s t-\gamma_d\big)\,d\theta_s \end{gathered} \quad \text{Eq. 17}$$

While for the second part of the bracket, the result is shown in Eq. 18.

$$\begin{gathered} \int_{\theta_s=0}^{2\pi} \sum_{v=5,11,17\ldots} \frac{1}{v}.\sin(v\theta_s+\omega_s t+\gamma_d).\cos(v\theta_s-v\omega_s t)\,d\theta_s \\ = 0.5[\int_{\theta_s=0}^{2\pi} \sum_{v=5,11,17\ldots} \frac{1}{v}.\sin\big((v+1)\omega_s t+\gamma_d\big)\,d\theta_s \\ + \int_{\theta_s=0}^{2\pi} \sum_{v=5,11,17\ldots} \frac{1}{v}.\sin(2v\theta_s-(v-1)\omega_s t+\gamma_d)\,d\theta_s] \\ =0.5\int_{\theta_s=0}^{2\pi}\sum_{v=5,11,17\ldots}\frac{1}{v}.\sin\big((v+1)\omega_s t+\gamma_d\big)\,d\theta_s \end{gathered} \quad \text{Eq. 18}$$

Therefore, the torque from Eq. 16 can be rewritten as Eq. 19.

$$T=-\frac{(D-\delta)^2}{2\pi}.L.\frac{h}{h+\delta}.B_r.\widehat{S_1}\int_{\theta_s=0}^{2\pi}[\sum_{v=1,7,13..}\frac{1}{v}.sin\left((v-1)\omega_s t-\gamma_d\right)+\sum_{v=5,11,17\ldots}\frac{1}{v}.sin\left((v+1)\omega_s t+\gamma_d\right)]\,d\theta_s \quad \text{Eq. 19}$$

Thus, it can be found that either when *v=6k+1*, or *v=6k-1, k=1,2,3…,* the torque harmonic wave speed is always *6k* multiple of the rotor angular speed.

Constant torque can be derived when *v=1*. Thus fundamental and harmonic components can be separated, as Eq. 20 shows.

$$T=(D-\delta)^2.L.\frac{h}{h+\delta}.B_r.\widehat{S_1}.sin(\gamma_d)$$
$$-(D-\delta)^2.L.\frac{h}{h+\delta}.B_r.\widehat{S_1}.\sum_{v=6k\pm1,\ k=1,2,3\ldots}\frac{1}{v}.sin\big((6k)\omega_s t\mp\gamma_d\big) \quad \text{Eq. 20}$$

Therefore, from Eq. 20, it can be observed that the constant torque part has similar structure with Eq. 21. The differences on constant coefficients are due to the different current and airgap flux waveforms used.

$$T=\pi.\frac{(D_{in}-\delta)^2}{4}.L.\widehat{S_1}.\widehat{B_\delta}.k_{w1}.sin(\gamma_d)\ \text{[N.m]} \quad \text{Eq. 21}$$

For the torque ripple part, it is found that the time harmonics are in multiple of six only. Only stator and rotor harmonics with *6k±1* order contribute to the torque ripple. Thus, the ratio of torque ripple to the constant torque can be express as Eq. 22.

$$\frac{T_{ripple}}{T_1}=\frac{1}{sin(\gamma_d)}\sum_{v=6k\pm1,\ k=1,2,3\ldots}\frac{1}{v}.sin\big((6k)\omega_s t\mp\gamma_d\big) \quad \text{Eq. 22}$$

Therefore, assuming that $\gamma_d=90^o$, and only harmonics with *5, 7-th* orders are considered in the torque ripple, then the torque ripple ratio will be calculated as Eq. 23.

$$\frac{T_{ripple}}{T_1}=\frac{1}{1}.\left(\frac{1}{5}-\frac{1}{7}\right)\approx 5.7\% \quad \text{Eq. 23}$$

Torque ripple ratio changes with angle γ_d. For another extreme case, $\gamma_d=180^o$, constant torque equals to zero, thus no torque ripple ratio.

Eq. 22 has only considered the harmonics from the winding and magnet. The harmonics produced by stator slots are ignored. Besides, the equation is only suit for a typical three-phase SPMSM with simple distributed winding. For more complicated designs such as with special shape of magnets, unequal airgap length or concentrated winding their torque ripple equations will be much more complicated. In addition, as the rotor magnetic potential of IPMSM is quite different with SPMSM, Eq. 22 is neither appropriate to the IPMSM torque ripple calculation.

1.2 Dual three phase torque ripple

The aforementioned torque derivation is only for a machine with one set of three phase winding. The torque ripple of a machine with dual three phase winding can be calculated in a similar way. For the first phase set, considering all harmonics, the current loading S_{s1}can be expressed as Eq. 9. With similar format, the second phase set with θ_d phase shift can be expressed as Eq. 24.

$$S_{s2}=-\widehat{S_s}[\sum_{v=1,7,13,..}sin(v\theta_s-(\omega_s t-\theta_d)-\gamma_d)+\sum_{v=5,11,17,...}sin(v\theta_s+(\omega_s t-\theta_d)+\gamma_d)] \quad \text{Eq. 24}$$

Using Eq. 9 and Eq. 24 to derive the torque of each phase set respectively, Eq. 20 is still available for the first phase set. The torque of phase set 1 denotes T_1. While the torque of phase set 2 can be expressed with similar format, as Eq. 25 shows.

$$\begin{aligned} T_2 &= (D-\delta)^2.L.\frac{h}{h+\delta}.B_r.\widehat{S_1}.\sin(\gamma_d) \\ &-(D-\delta)^2.L.\frac{h}{h+\delta}.B_r.\widehat{S_1}.\sum_{v=6k\pm1,\ k=1,2,3\ldots}\frac{1}{v}.\sin\big((6k)(\omega_s t-\theta_d)\mp\gamma_d\big) \end{aligned} \quad \text{Eq. 25}$$

Thus, the total torque T can be expressed as Eq. 26.

$$\begin{aligned} T &= T_1+T_2 \\ &= 2.(D-\delta)^2.L.\frac{h}{h+\delta}.B_r.\widehat{S_1}.sin(\gamma_d) \\ &-(D-\delta)^2.L.\frac{h}{h+\delta}.B_r.\widehat{S_1}.[\sum_{v=6k\pm1,\ k=1,2,3\ldots}\frac{1}{v}.sin\big((6k)\omega_s t\mp\gamma_d\big) \\ &+\sum_{v=6k\pm1,\ k=1,2,3\ldots}\frac{1}{v}.sin\big((6k)(\omega_s t-\theta_d)\mp\gamma_d\big)] \end{aligned} \quad \text{Eq. 26}$$

Thus, it can be found that for the constant torque part, the total torque is simply the sum of two torques from two phase sets. This conclusion is aligned with the results of park transformation from Eq. 68. While, for the torque ripple part, it is related to angle θ_d.

If θ_d is zero, then the torque ripple generated by both phase sets are totally identical, including the amplitude and phase shift. Thus the amplitude of the total torque ripple is two times of single phase set. However, as constant torque is also double times of single phase set, the torque ripple ratio thus remains unchanged. If θ_d equals $\frac{\pi}{6}$, then the ripple part of Eq. 25 can be written as Eq. 27.

$$\begin{aligned} T_{ripple} &= K.\Bigg[\sum_{v=6k\pm1,\ k=1,2,3\ldots}\frac{1}{v}.sin\big((6k)\omega_s t\mp\gamma_d\big) \\ &+\sum_{v=6k\pm1,\ k=1,2,3\ldots}\frac{1}{v}.sin\left((6k)\left(\omega_s t-\frac{\pi}{6}\right)\mp\gamma_d\right)\Bigg] \\ &=K.\,2\sum_{v=6k\pm1,\ k=2,4,6\ldots}\frac{1}{v}.sin\big((6k)\omega_s t\mp\gamma_d\big) \\ &=2K.\sum_{v=12k\pm1,\ k=1,2,3\ldots}\frac{1}{v}.sin\big((12k)\omega_s t\mp\gamma_d\big) \end{aligned} \quad \text{Eq. 27}$$

It can be found that torque ripple harmonics with *6k, k=1,3,5…* multiple of the rotor angular speed are totally eliminated. Which means only harmonics with *12k, k=1,2,3…* multiple of the rotor angular speed exist. From Eq. 23 it can be found that the torque ripple ratio caused by 6th harmonics is 5.7% at least. While as Eq. 28 shows, with the elimination of 6th harmonics, the torque ripple ratio caused by 12th harmonics is only 1.4%. Thus compared to three-phase winding or dual-three phase winding with $\theta_d = 0$, theoretically the torque ripple ratio is reduced by 75% by applying dual-three phase winding with $\theta_d = 30^o$.

$$\frac{T_{ripple}}{T_1}=\frac{2}{2}.\left(\frac{1}{11}-\frac{1}{13}\right)\approx 1.4\% \quad \text{Eq. 28}$$

For other θ_d values, none of them can obtain less torque ripple than $\theta_d = 30^o$, regardless of slot effect and other non-linear behaviors.

Thus from the calculations of both three phase and dual three phase windings, it can be found dual three phase winding has less torque ripple ratio than three phase winding.

2. FEM model validation

It is necessary to validate the FEM model obtained with the analytical methods in Chapter 2 Section 2.2. Thus, a standard three-phase SPMSM is taken as a reference for comparisons between analytical model and FEM model. The analytical model is built by an online tool called *EMETOR KTH* [129]. *EMETOR KTH* is completely based on analytical equations of PM electrical machines. Their analytical methods are essentially consistent with the analytical methods introduced in Section 2 (Details can be checked in [129], "Help →Models"). Typical three-phase SPMSMs can be modeled by this tool. A 2D FEM model for the SPMSM is built by JMAG. A configuration for this reference SPMSM is given by Table I. It needs to be highlighted that the requirement for slot current density is only for the current with constant operation. The current amplitude is around half of the current with max average torque.

Table I REQUIREMENTS AND SPECIFICATIONS FOR A THREE-PHASE SPMSM

Requirements	Abbreviation	Unit	Value
Outer diameter	D_o	mm	150
Axial length	L	mm	60
Current limitations for drive unit	I_{max}	Arms	230
Corner speed	Ω_c	rpm	1500
Max average torque	T_m	N.m	56
Constant operation torque	T_c	N.m	28
Mechanical speed tolerance	Ω_m	rpm	21000
Slot current density limit (for water cooling)	J_{slot}	Arms/mm²	15
DC supply voltage	V_{DC}	V	96
Temperature of stator and rotor		℃	80
Rotor type			Inner
Pole pair number	p		4

2.1 A three phase PM machine model built by analytical method

An analytical model is built first. In *EMETOR KTH*, the default iron sheet has infinite permeability without saturation. The remanence flux density of PM is constant at certain temperature. Here at 80 ℃, Br=1.14T. The winding is prescribed as distributed winding. For the first model, no fractional pitch (or short pitch) is used. Then

based on the input requirements of *EMETOR KTH*, parameters in Table II are entered to construct the analytical model.

Table II INPUT PARAMETERS VALUES FOR THE SPMSM MODEL BUILT BY EMETOR KTH

Input parameters	Abbreviation	Unit	Value
Number of stator slots/pole/phase	*SPP*		2
Rotor outer diameter	D_r	mm	76.6
Shaft diameter	D_{sha}	mm	36
Magnet thickness	h	mm	3
Magnet coverage angle	θ_{mag}	El.deg	178
Airgap length	δ	mm	2
Stator tooth width	W_{th}	mm	3.7
Stator slot height	h_{slot}	mm	23
Stator slot opening/slot width	k_{ow}	p.u	0.5
Slot wedge height	h_{wed}	mm	1
Slot filling factor	k_{fill}		0.45
AC phase voltage	V_{AC}	Vrms	33.3

It needs to be highlighted that AC voltage is the [RMS] value of the phase voltage. It can be derived from DC voltage and the modulation factor, as Eq. 1 shows.

$$V_{AC} = \frac{V_{DC} k_m}{\sqrt{3}.\sqrt{2}} \quad \text{Eq. 1}$$

The airgap length is commonly 0.5 mm. However, in the model, the airgap length needs to include the real airgap length plus a sleeve thickness as mentioned in Section 2.6. Assumes that the sleeve is made by carbon fibers, and the sleeve tolerates the same max stress with what in [111]. Then by using Eq. 2,

$$\delta_c = \rho_m \Omega^2 r_m^2 \quad \text{Eq. 2}$$

and combining machine information in [111], the sleeve thickness of the SPMSM can be derived by Eq. 3,

$$h_{sleeve} = h_{so} \frac{[\Omega_m.(D_r+2h)]^2}{(\Omega_o.D_{ro})^2} \quad \text{Eq. 3}$$

where h_{so}, Ω_o and D_{ro} are the sleeve thickness, maximum rotation speed and rotor outer diameter (include magnet height) from [111] respectively. h_{so}=5 mm, $\Omega_o = 60$ krpm, $D_{ro} = 27$ mm. Thus with Eq. 3, the sleeve thickness is around 1.5mm. The airgap thickness in the model then becomes 2 mm.

With the input parameters, *EMETOR KTH* can automatically derive other geometry parameters and turn number by analytical equations. The results are shown in Table III. There are some preset conditions in the embedded

model. For instance, the teeth width is constant; only random wound windings with round conductor can be applied. For each conductor, no insulation or coating is considered. Thus, the slot filling factor that set as 0.45 is reasonable.

Table III DERIVED PARAMETERS VALUES FOR THE SPMSM MODEL BUILT BY EMETOR KTH

Derived parameters	Abbreviation	Unit	Value
Total number of stator slots	n_s		48
Inner stator diameter	D_{in}	mm	86.6
Stator slot pitch		mm	5.7
Stator yoke height	h_{yoke}	mm	8.7
Inner stator slot width	w_{slin}	mm	2.1
Outer stator slot width	w_{slo}	mm	5
Slot area	A_{slot}	mm^2	77.9
Slot opening width	w_{open}	mm	1
Magnet coverage	c_{mag}	%	98.9
Number of turns per slot	N_{slot}		4
Number of turns per phase	N_{ph}		8
Conductor diameter	D_{con}	mm	3.34
Total conductor area per slot	A_{Cu}	mm^2	35

With the parameters in Table II and Table III, the geometry of the machine can be depicted as Fig. 1.

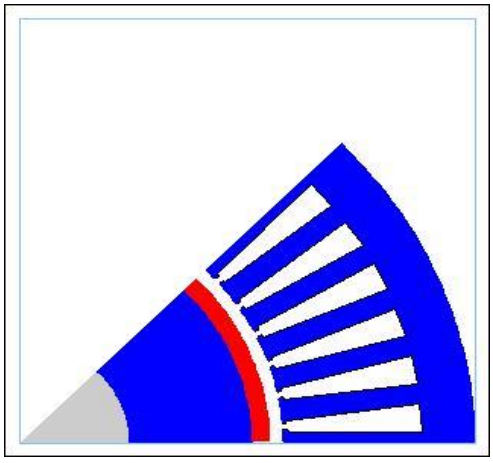

Fig. 1 1/8 cross section of the reference SPMSM by EMETOR KTH

The performances of the machine thus can be derived by the analytical model. The calculation results are shown in Table IV, Fig. 2 and Fig. 3 respectively.

Table IV PERFORMANCES OF SPMSM MODEL DERIVED BY EMETOR KTH

Performance	Abbreviation	Unit	Value
Slot current density	J_{slot}	Arms/mm2	12.5
Phase current	I_{ph}	Arms	219
Winding factor	k_{w1}		0.966
Average torque	T	N.m	56
Torque ripple ratio	$\frac{T_{ripple}}{T_1}$	%	9.7

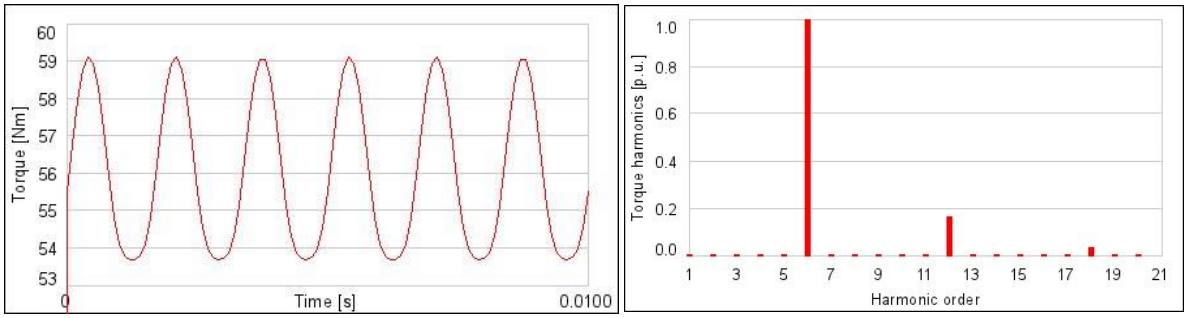

(a) (b)

Fig. 2 *EMETOR KTH* results of (a) Max torque pulsation; (b) Spectrum of the torque pulsation;

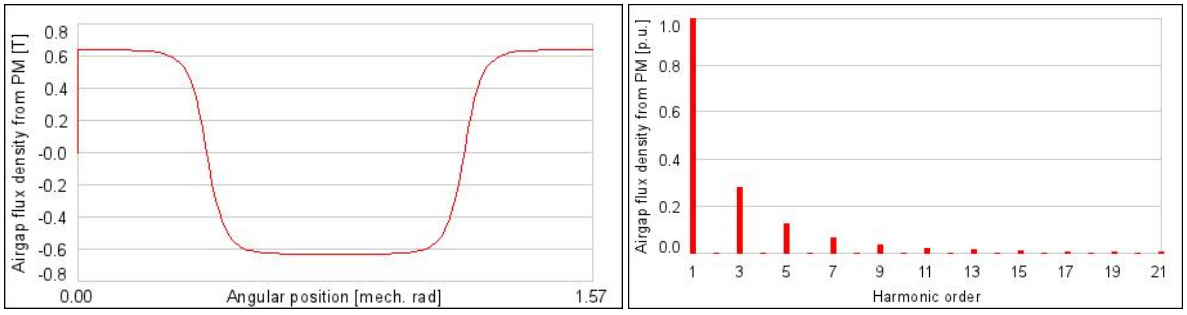

(a) (b)

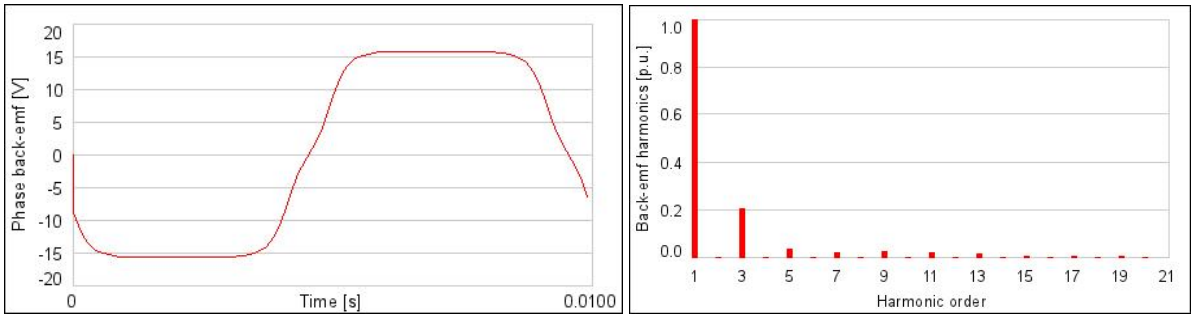

(c) (d)

Fig. 3 *EMETOR KTH* results of (a)Waveform of airgap flux density during open circuit operation; (b) Spectrum of airgap flux density during open circuit operation; (c)Waveform of one phase back-EMF @1500 rpm; (b) Spectrum of one phase back-EMF @1500 rpm;

It can be found that the slot current density with constant operation is in the range of water cooling capability. To achieve the max torque, the phase current only needs 95% of the phase current limit, thanks to the infinite permeability of the iron material. As *SPP = 2*, $y_{sp}=6$, submitting them into Eq. 4, the winding factor is 0.966.

$$k_{w1} = \frac{1}{q} . \frac{sin\frac{\pi}{6}}{sin\frac{\pi}{6q}} . sin\frac{y_{sp}.\pi}{6q} \quad \text{Eq. 4}$$

From the observation of torque ripple spectrum in Fig. 2 (b), it is clear that the 6th order harmonic is the main contributor to the torque ripple. This result is consistent with the conclusion in Appendix 1.2.

Besides, from Fig. 3, the harmonic orders are very consistent between waveforms of airgap flux density and Back-EMF. Thus, it can be concluded the main harmonics on Back-EMF are mainly from the magnet. Thus, one of the ways to reduce these harmonics is to make the airgap flux density wave more sinusoidal. It can be also observed that at 1500 rpm, the max amplitude of Back-EMF is only around 16 V. This is actually much lower than input voltage limit. In fact, for the load condition, the d-axis inductance also contributes to part of the EMF. Thus when torque reaches 56 N at 1500 rpm, the voltage nearly reaches the limit.

2.2 A similar three phase PM machine model built by FEM

Then a FEM model is built. In JMAG, the non-linear material properties can be set. Key material properties are shown in Table V, the B-H curve of the iron material is shown in Fig. 4.

Table V MATERIAL CHARACTERISTICS OF EACH COMPONENT

Machine component	Material	Properties
Iron cores (rotor, stator)	M270-35A	1.65 T, 5000 A/m
Magnets	NdFeB	Remanence flux density @ 80 °C:1.14T Remanence temp coefficient: -0.1% /°C Coercivity @80 °C: 1.5e6 A/m Electrical conductivity: 0.67 MS/m
Windings	Copper	Electrical Conductivity: 5.96×10^7 S/m

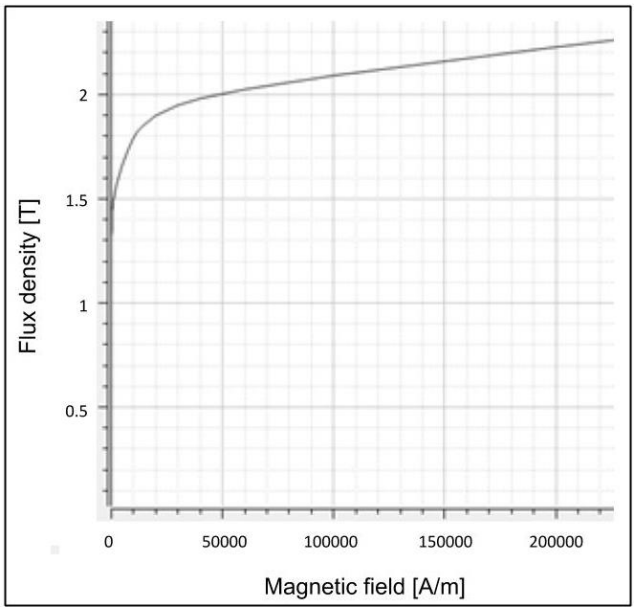

Fig. 4 B-H curve of the iron material used in JMAG

Then considering the saturation effect, the stator tooth is designed as a trapezoid shape instead of a rectangle shape with constant width. Stator slot also has parallel sides. Hence, rectangular conductor is more suit for this parallel slot than round conductors. So for this FEM model, the filling factor is increased.

Except the points above, other configurations in FEM model are the same with the analytical model. For instance, distributed winding without short pitch is also applied; each slot has 4 turns. Stator and rotor sizes are the same with analytical model; magnet coverage and height are the same. The magnetization direction of the magnet is in parallel as Fig. 5 shows.

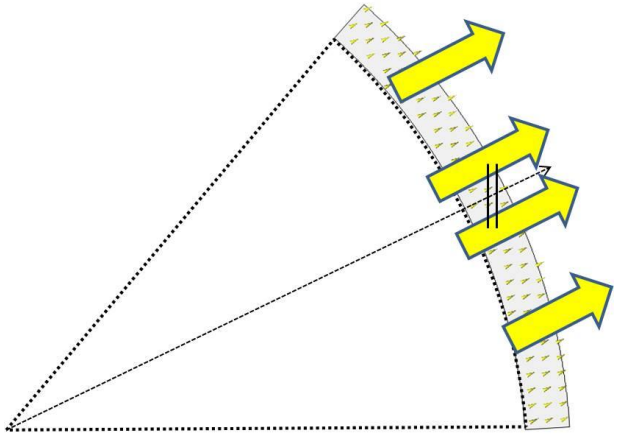

Fig. 5 Parallel magnetization of a magnet of the SPMSM. The Yellow arrow represents the magnetization direction. All the arrows are paralleled to the dash arrow that in the middle of the sector.

The cross section of $1/8^{th}$ of the machine is shown in Fig. 6.

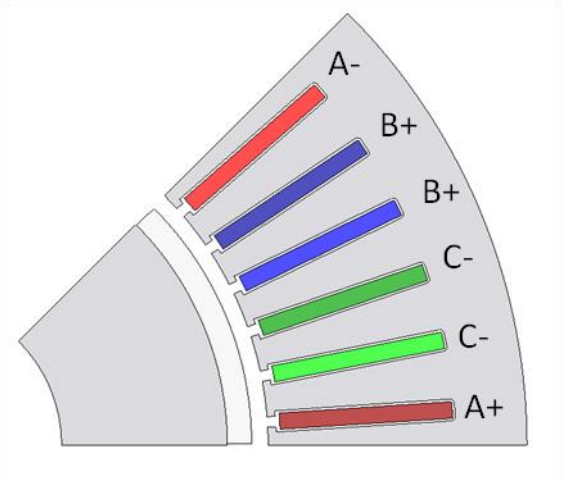

Fig. 6 1/8 cross section of the reference SPMSM by JMAG

The following works are mesh and solver settings in the software. An example of the mesh setting is shown Fig, 7.

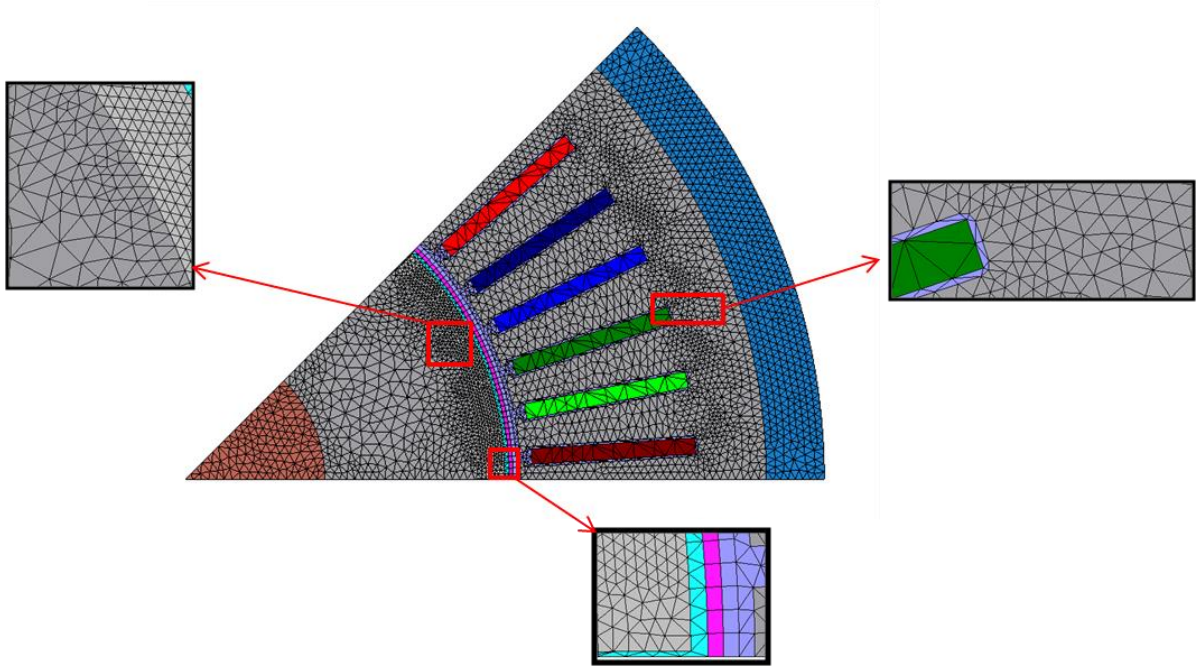

Fig. 7 Meshing setting of the reference SPMSM by JMAG

In Fig. 7, triangle mesh type is used for the 2D model. Three regions need to be given special attention. First, the airgap mesh has 4 layers in radial direction. The two layers that are adjacent to the rotor (cyan and pink) also rotate with the rotor. While the other two layers adjacent to the stator (purple) are fixed. In circumferential direction, the mesh is divided every one degree, 45 segments in total. Thus, the tiny variation of airgap flux density can be grasped. Second, as the flux change on magnet might be significant, the magnet mesh size is set as 0.5 mm. It is also for the preparation of demagnetization study. Finally, in the corner area of the stator slot, adaptive mesh feature is used. It is showed that the closer it is to the corner, the denser the mesh is. Thus, the cutting edge effect

with sudden flux change can be grasped. Besides, some meshes are set on the outside air area of the machine (shaft mesh in brown, mesh of stator outside in blue) in order to take into account the leakage flux. A statistic shows that the total elements number is 7253. Meshes with normalized quality that larger than 0.5 occupy 92% of total mesh. These are considered reasonable for PC calculation.

The main setups for solver are study time steps and number of step. To be consistent with mesh setting, it is decided that the solver needs to solve every one degree of the rotation. As the rotation speed is 1500 rpm and thus the study step is 0.11 ms. The total number of steps is set to 90, which indicates a rotor revolution over 1 pole pair. Thus the full cycle of the current, voltage and torque can be captured. Besides, as the electrical frequency is 100Hz, based on Shannon's sampling law, combined with solver frequency $f=1/0.11\approx 9.1$kHz, up to 45^{th} order harmonics can be captured in FFT analysis, which is 45 kHz. This analysis also applies to torque ripple harmonic spectrum.

In JMAG, a lump circuit can be coupled with the FEM model, as Fig. 8 shows. Ampere's circuit law indicates flux density is directly link to the current. All the electromagnetic performances of steady state can be thus derived by the current. Thus, in the circuit, only sinusoidal current sources are applied. However in reality, the power supply is always voltage source with proper control loop. This will bring some unwanted harmonics in the current waveform. Since our focus is on the machine performances itself, voltage simulation is out of the scope.

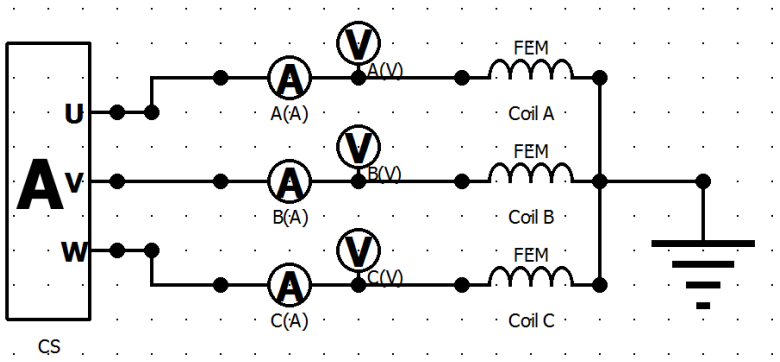

Fig. 8 The lump circuit that coupled with the FEM model of SPMSM in JMAG

The number of turns per coil denotes turns per phase. The current amplitude and the current angle can be set up in a current source. The definition of current angle is the lead angle between the current vector and d-axis positive direction. Thus, for SPMSMs, without the reluctance part, the current angle with the max torque is 90°. Finally, the initial rotor position is set as 0°. Thus the d-axis of rotor is aligned with the α-axis of stator. All the details of input parameters can be found in Table VI. The Flux density distribution of the full load operation is shown in Fig. 9. It can be seen a tooth and a part of stator yoke is fairly saturated, which may cause a reduction of the torque.

Table VI INPUT PARAMETERS VALUES FOR THE SPMSM MODEL BUILT BY JMAG

Input parameters	Abbreviation	Unit	Value
Number of stator slots/pole/phase	SPP		2
Rotor outer diameter	D_O	mm	76.6
Shaft diameter	D_{sha}	mm	36
Magnet thickness	h	mm	3
Magnet coverage angle	θ_{mag}	El.deg	178
Airgap length	δ	mm	2
Inner stator diameter	D_{in}	mm	86.6
Inner stator tooth width	W_{thin}	mm	3.8
Outer stator tooth width	W_{tho}	mm	5.8
Stator yoke height	h_{yoke}	mm	8.7
Stator slot pitch	y_{sp}		6
Stator slot height	h_{slot}	mm	23
stator slot width	w_{sl}	mm	2.6
Stator slot opening	k_{ow}	p.u	0.5
Slot wedge height	h_{wed}	mm	1
Total number of stator slots	n_s		48
Slot opening width	w_{open}	mm	1.3
Slot area	A_{slot}	mm2	59.8
Number of turns per slot	N_{slot}		4
Number of turns per phase	N		8
Conductor height	h_{con}	mm	5.3
Conductor width	w_{con}	mm	2
coating thickness	$w_{coating}$	mm	0.085
Total conductor copper area per slot	A_{cu}	mm2	37.44
Filling factor	k_{fill}		0.63

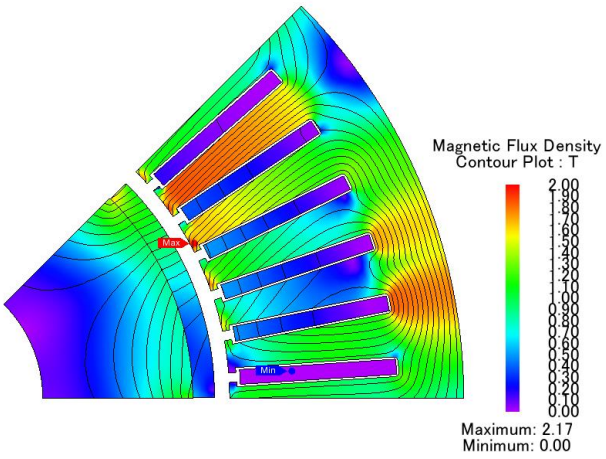

Fig. 9 The flux density distribution and flux line of the reference SPMSM with max torque (full load) operation

Then with the information above, the performance of SPMSM derived from JMAG can be found in Table VII, Fig. 10 and Fig. 11.

Table VII PERFORMANCES OF THE SPMSM MODEL DERIVED BY JMAG

Performance	Abbreviation	Unit	Value
Slot current density	J_{slot}	Arms/mm^2	12.1
Phase current	I_{ph}	Arms	226
Max average torque	T_m	N.m	56
Torque ripple	$\frac{T_{ripple}}{T_1}$	%	9.2

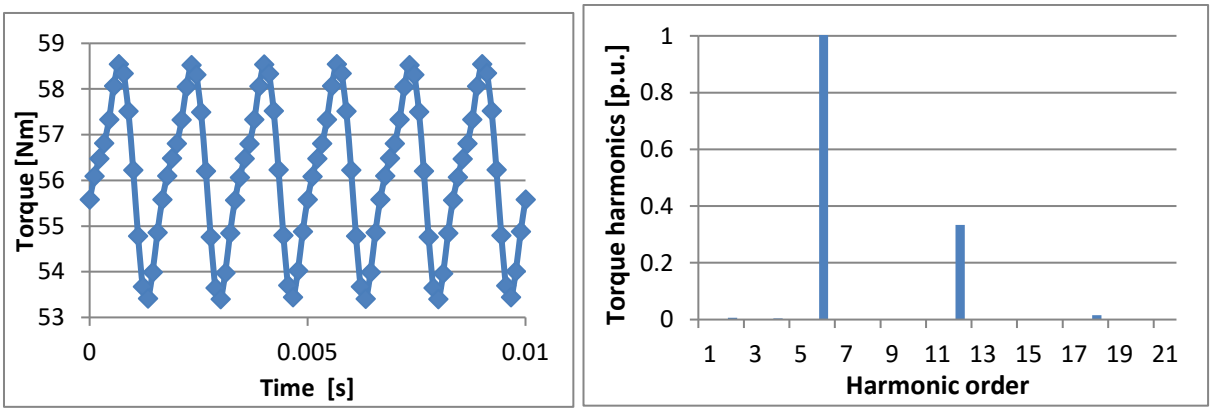

(a) (b)

Fig. 10 JMAG results of (a) Max torque pulsation; (b) Spectrum of the torque pulsation;

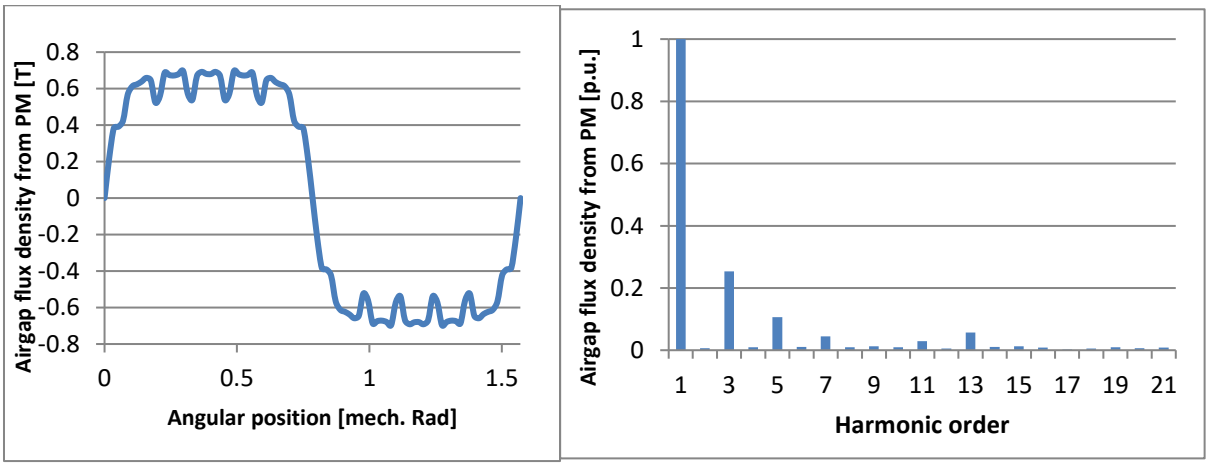

(a) (b)

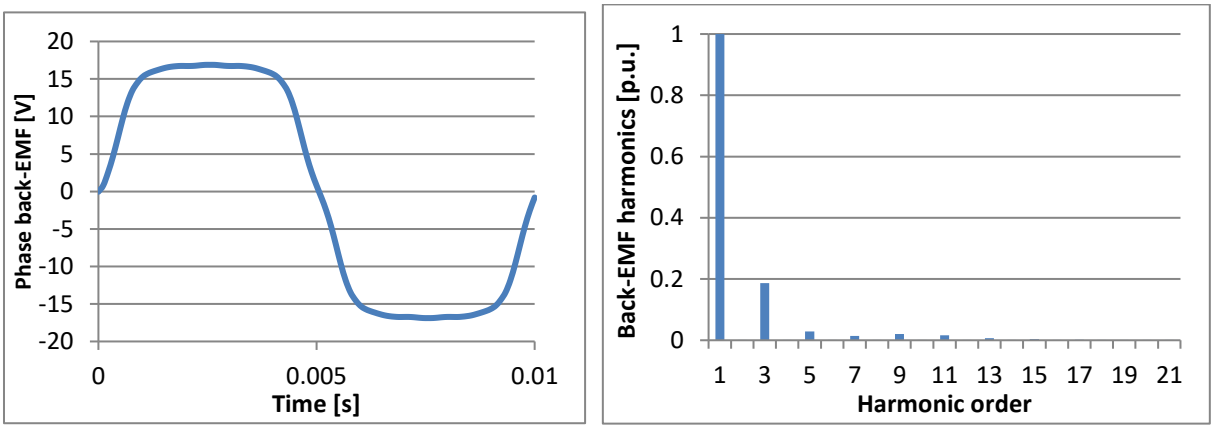

(c) (d)

Fig. 11 JMAG results of (a)Waveform of airgap flux density during open circuit operation; (b) Spectrum of airgap flux density during open circuit operation; (c)Waveform of one phase back-EMF @1500 rpm; (d) Spectrum of one phase back-EMF @1500 rpm;

It can be found that to achieve the max torque, the phase current needs 98% of the phase current limit, which is a little bit higher than the current amplitude in *EMETOR KTH*. This can be explained by the effect of the saturation of the iron material.

The torque ripple ratio is close to the result of *EMETOR KTH*. The ripple spectrum in Fig. 10 (b) is similar to Fig. 2 (b), 6th order harmonic still dominates the torque ripple.

A quite obvious difference can be found in Fig. 11 (a) and (b), where 13th order harmonic appears, which results in tiny pulsation on the airgap flux density. It is believed that the stator slot openings bring this harmonic into the airgap flux. However, the spectrum of back-EMF is still similar to Fig. 3 (d). No 13th harmonic reflects in the back-EMF wave. This can be explained by the filter effect of the wide airgap, high frequency harmonic cannot go through the airgap. Besides, the max amplitude of Back-EMF is still close to the result of *EMETOR KTH*. Thus, it can be concluded that the results derived from the FEM model are consistent with the results of analytical model.

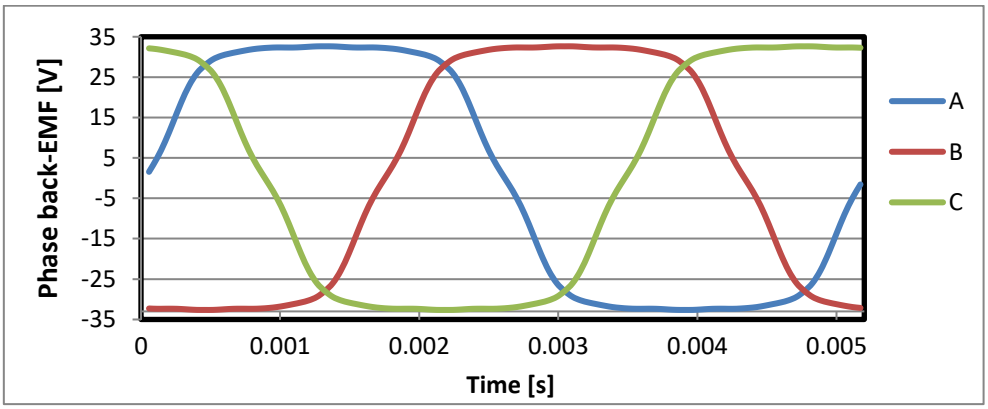

Fig. 12 Waveforms of three phases back-EMF @2900 rpm

When the machine is running at 2900 rpm without load, the back-EMF waveform is shown in Fig. 12. It can be found the amplitude of Back-EMF is around 33 V, which hit the voltage limit of the drive. This speed thus is called base speed.

2.3 A dual- three phase PM machine model built by FEM

After the validation of the FEM model, a dual-three phase FEM model can be built in JMAG to validate the conclusion in analytical method. Thus, a model with dual-three phases electrical circuit is shown in Fig. 13. In the circuit, CS1 and CS2 represent current sources of two phase sets. CS1 always leads CS2 30º. For instance, if the current angle of CS1 equals 0º, the current angle of CS2 thus equals to -30º. The coil settings in the electrical circuit are consistent with the settings in the right FEM model.

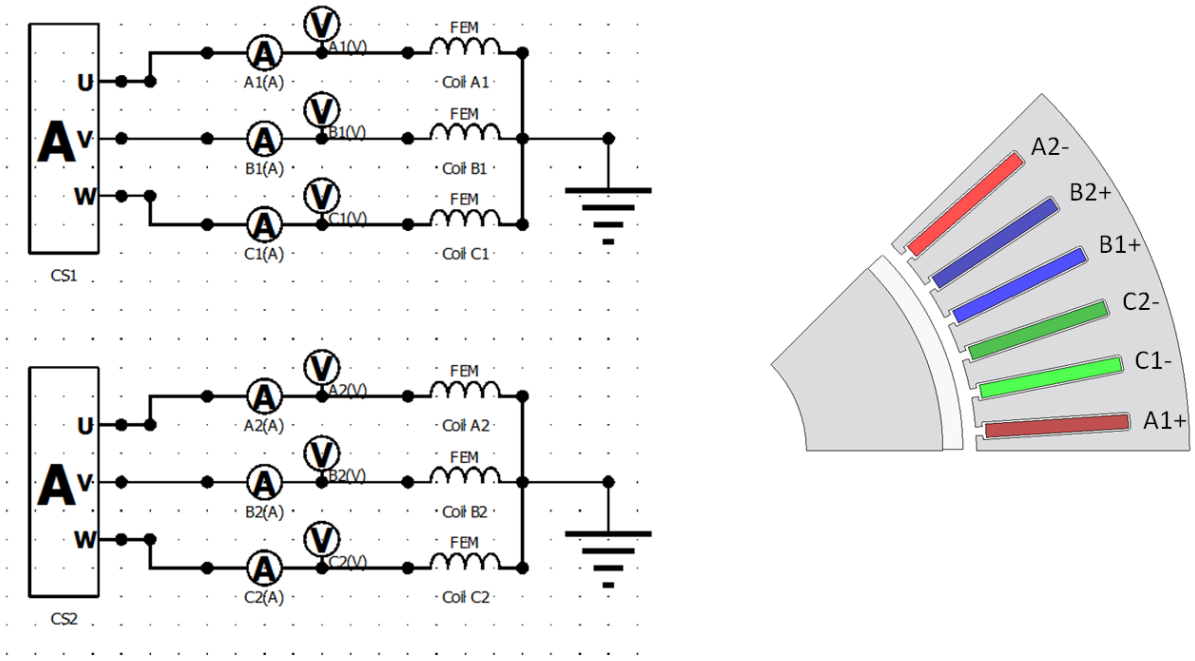

Fig. 13 1/8 cross section of the dual three-phase SPMSM and its coupling electrical circuit

Set the current angle CS1 as 0º, and align the rotor d-axis with the stator alpha-axis, which is around 3.75º, the max torque can be obtained. The Flux density distribution of the full load operation is shown in Fig. 14. It can be observed that the flux density distribution is similar to Fig. 9. However, the saturation level of the teeth and the stator yoke is a bit mitigated. This may contribute an increase of torque.

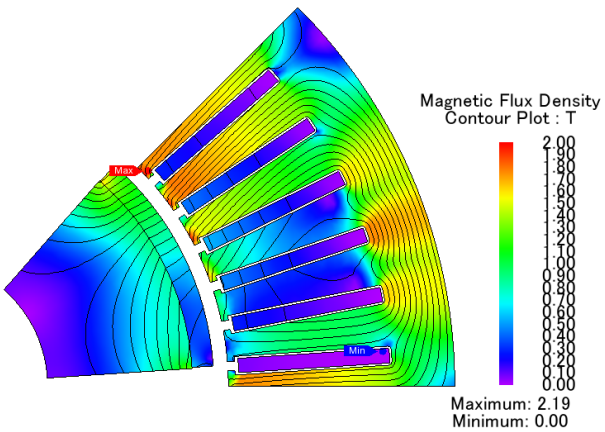

Fig. 14 The flux density distribution and flux line of the dual-three phase SPMSM with max torque (full load) operation

With the information above, the performance of SPMSM derived from JMAG can be found in Table VII, Fig. 15 and Fig. 16.

Table VIII PERFORMANCES OF SPMSM MODEL DERIVED BY JMAG

Performance	Abbreviation	Unit	Value
Slot current density	J_{slot}	Arms/mm^2	12.1
Phase current	I_{ph}	Arms	212
Max average torque	T_m	N.m	56
Torque ripple	$\frac{T_{ripple}}{T_1}$	%	3.7

First it can found that to achieve 56N.m, only 92% current is needed, which is 6% less than for the reference three phases SPMSM. The additional torque part may be due to mitigation of the saturation and the increased winding factor (the winding factor is 1 for dual-three phases). Besides, as analyzed in Section 2.2, the 6th harmonic is totally eliminated in dual-three phases winding. This is totally proved in the model. From Fig. 15 (b), only 12th order harmonic remains in the torque ripple, and the torque ripple ratio is reduced to 3.7%. The waveforms of Back-EMF still have not much change, except the amplitude which is only around 8 V, due to the half turn number per phase. This can be also observed in Fig. 17, when the machine is running at 2900 rpm. Thus, it can be concluded that the voltage limit of the motor drive for dual-three phase winding only needs to be half of what drives three phase winding. Besides, from Back-EMF waveforms, the phase shift between two phase sets can be clearly observed.

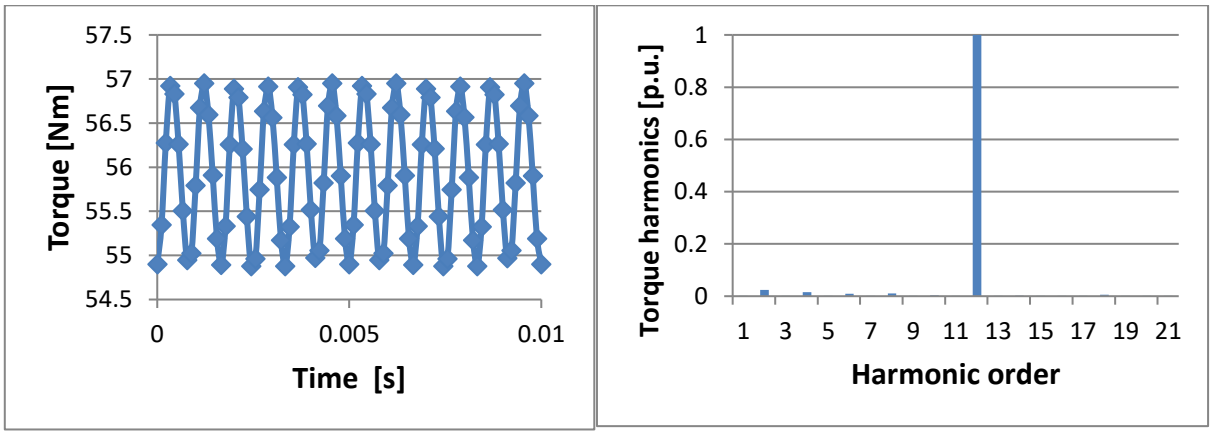

(a) (b)

Fig. 15 (a) Max torque pulsation; (b) Spectrum of the torque pulsation;

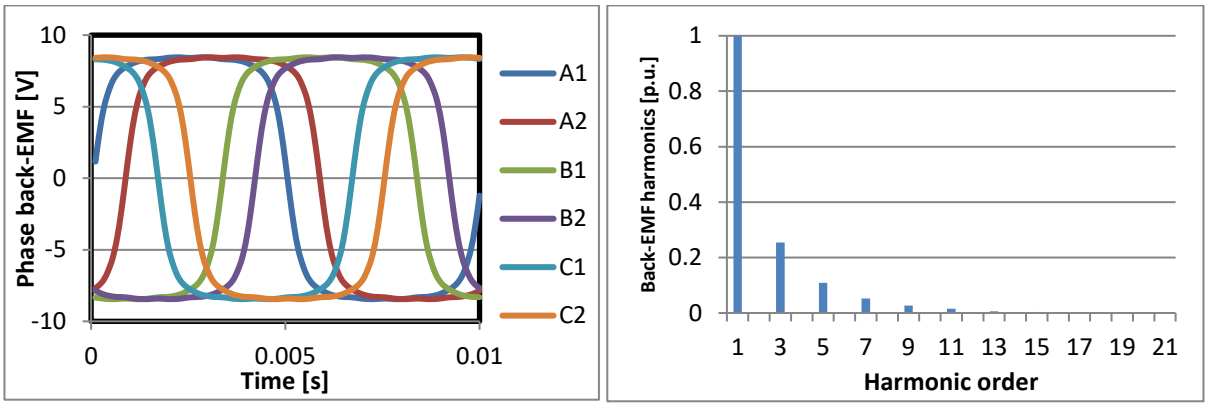

(a) (b)

Fig. 16 (a)Waveform of six phase back-EMF @1500 rpm; (b) Spectrum of phase A1 back-EMF @1500 rpm;

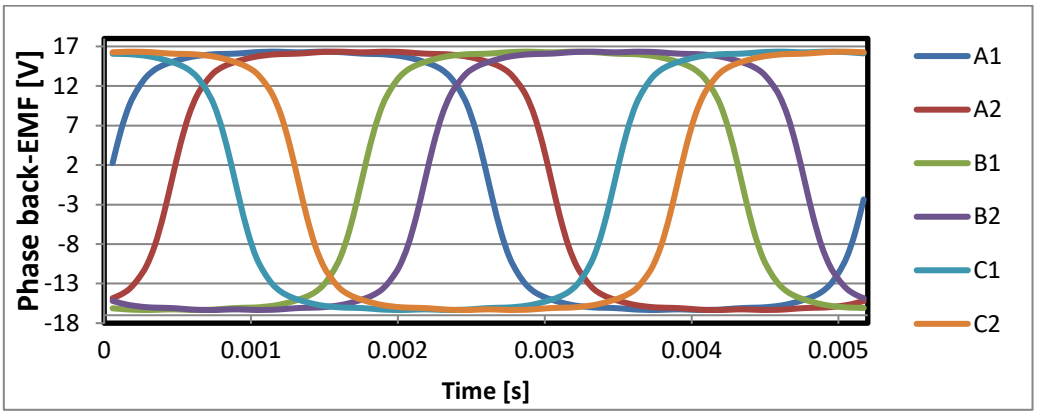

Fig. 17 Waveforms of the dual-three phases back-EMF @2900 rpm

Therefore, all the analytical conclusions are validated by FEM models. It can be concluded that FEM method is accurate and reliable. However, the premise is that all the study and mesh settings about the model need to be correct. In addition, FEM model can even take into account many non-linear and miscellaneous effects, which is almost impossible for analytical method. For 2D FEM models, the construction and solving speeds are sufficiently high. Therefore, for the following research, only FEM methods are used for machine design and analysis.

2.4 3D FEM model setup

In JMAG, compared to 2D simulation, 3D simulation needs some special setups –

1. Symmetry. The symmetry not only can be applied on radial surface, but also on axial direction. In order to reduce the finite element number, only half axial length needs to be created. Then ‘symmetry boundary’ in the condition can be applied. Finally, in the ‘study properties’ setting, ‘Conversion’ - ‘other than periodic boundary’ should be set as ‘2’.
2. Mesh. The mesh generation method could apply ‘Extruded mesh’, instead of ‘Semi-Auto mesh’, in order to reduce the element number.
3. End coil. The coil length needs to be longer than stator core length, for the setting of symmetry. In all 3D models, 20 mm extension was used on the coil.
4. High speed solver. Just a reminder that high speed solver can be enabled to accelerate 3D simulation. The setting is hided in study properties - ‘Nonlinear’ section.

3. Copper loss calculation (interlock with temperature)

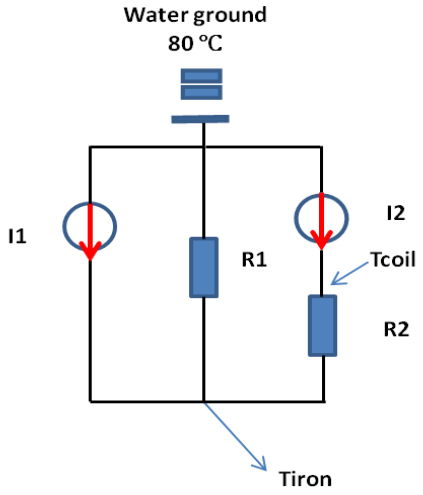

Fig. 1 Simplified stator thermal circuit

Still based on the same thermal circuit Fig, the coil temperature T_{coil} can be express as Eq. 1

$$T_{coil} = R_2 I_2 + T_{iron} \quad \text{Eq. 1}$$

Where Tiron can be derived by Eq. 2

$$T_{iron} = (I_1 + I_2)R_1 + T_{water} \quad \text{Eq. 2}$$

I1, R1 and R2 are constant values. The problem is I2, the copper loss, change with the coil temperature T_{coil}, which can be expressed as Eq. 3

$$I_2 = 6 * I^2 R * (1 + 0.004 * (T_{coil} - 20)) \quad \text{Eq. 3}$$

Where *I* denotes the RMS current for the thermal condition; R denotes the phase resistance at 20 °C. Thus, Eq. 1 and Eq. 3 together is an iterative calculation. In this case, excel can be used with the function "Enable iterative calculation". For the thermal studies in chapters 2 and 3, the setting was always "Maximum iterations" =100, "Maximum changes" =0.001.

4. *WIRE scoring table*

TABLE I. WIRE SCORING TABLE FOR THE HUB MOTOR

MOTOR ID	Hub motor for in-wheel application										
Component/ Parts			Standard				Cost				WIRE SCORE
		Remarks	Score	Imp.	F.S.	Remarks	Score	Imp.	F.S.	Remarks	
Materials											
- Stator											
	Lamination	segmented stator	5	5	25	Standard SiFe lamination(0.5mm)	1	5	5	6642(g)	30
	Copper	AWG 24	5	5	25	Copper strand circular	2	1	2	1189(g)	27
- Rotor											0
	Steel R	MS steel	5	5	25	Solid iron	1	4	4	3675(g)	29
	Magnets	NdFeB-rect shape	5	4	20	Sintered standard shape magnet with coating	5	1	5	711(g)	25
-Shaft											0
	Shaft	Steel	4	5	20	shaft with hole for wires	1	2	2		22
-Endshileds											0
	Drive Side	aluminium die cast	2	5	10	prepare new die	1	2	2		12
	Non-Drive side	aluminium die cast	2	5	10	prepare new die	1	2	2		12
Section sum				34	135			17	22		157
Section scores					79%				26%		
Assembly											
- Stator											0
	Lamination S	segmented stator	2	3	6	new design, bcoz of rivet 1pt less, no welding	3	3	9	Hard process with standard tools(punching machine)	20
	Copper winding	AWG 24	3	3	9	manual insertion, independent of method of insertion and less varnish	3	3	9	Hard process by hand with standard tools	12
- Rotor											0

	Steel R	MS steel	5	3	15	solid rotor	5	3	15	Easy to assemble with standard tools/process	40
	Magnets with glue	NdFeB-rect shape	2	5	10	magnetized 56 magnets ORSPM	3	3	9	Complex process with standard tools	18
-Shaft											0
	Shaft	Steel	4	3	12	press fit but with hole	4	3	12	Low as not critical for recycle	45
-Endshileds											0
	Drive Side	aluminium die cast	4	3	12	For assembly okay	4	3	12		36
	Non-Drive side	aluminium die cast	4	3	12		4	3	12		36
- Assembly of rotor and stator			4	3	12	Stong forces and outer rotor so complex	4	3	12	careful assembly process, green not to change	18
											0
Wires	Lead wires		2	1	2	insertion through hole	3	3	9		18
	Sensor wires		2	1	2	insertion through hole	3	3	9		15
Sensing assembly	Sensors	Linear latch type	2	1	2	putting sensor on stator	3	3	9		12
Section sum				29	94			33	117		270
Section scores					65%				71%		
Disassembly											
- End shields											
	Drive side Bearing		2	3	6	One was too hard	3	3	9	first one hard to take	12
	Non-Drive side bearing		3	3	9	other little okay to disassemble	4	3	12	second one little easy	16
- Separation of rotor and stator			4	4	16	High forces	4	4	16		12
											0
- Stator											0
	Lamination S	segmented stator	4	3	12	rivet and way to assemble the 2 plates, welding unknown	4	3	12	Easy to take out with standard tools/process	24
	Copper winding	AWG 24	4	3	12	Low varnish	4	4	16	Easy to take out with standard tools/process(Low varnish)	36
- Rotor											0
	Steel R	MS steel	5	3	15	solid hollow rotor	5	3	15	Easy to take out without tool	45

	Magnets	NdFeB-rect shape	3	5	15	taking out easy as O ring	3	5	15	Hard process to take out with standard tools	21
-Shaft											0
	Shaft	Steel	5	3	15		4	3	12		40
Section sum				27	100			28	107		270
Section scores					74%				76%		
Final scores					73%				63%		68.5%

Reference

[1] U.S. Environmental Protection Agency, www.epa.gov.

[2] Internal combustion engine, https://en.wikipedia.org/wiki/Internal_combustion_engine#Energy_efficiency

[3] S. Arnoud, S. Thomas, P. Walter, B. Markus, "Integrated fuels and vehicles roadmap to 2030+", Roland Berger, April 2016.

[4] Bloomberg NEF, Electric Vehicle Outlook 2017

[5] Global and China Automotive Electric Motor Industry Report, 2016-2020, http://www.researchinchina.com/htmls/report/2016/10329.html

[6] M. Yilmaz, "Limitations/capabilities of electric machine technologies and modeling approaches for electric motor design and analysis in plug-in electric vehicle applications," Renewable and Sustainable Energy Reviews, vol. 52, p. 80-99, 2015

[7] J. D. Widmer, R. Martin and M. Kimiabeigi, "Electric vehicle traction motors without rare earth magnets," Sustainable Materials and Technologies, vol. 3, pp. 7-13, 2015.

[8] Magnet, https://en.wikipedia.org/wiki/Magnet

[9] O. Gutfleisch, M. A. Willard, E. Bruck, C. H. Chen, S. G. Sankar, J. Liu, "Magnetic materials and devices for the 21st century: stronger, lighter, and more energy efficient," Advanced materials, vol. 23, no. 7, pp. 821-842, 2011.

[10] https://en.wikipedia.org/wiki/Rare_earth_element

[11] K. Binnemans, P. T. Jones, B. Blanpain, T. V. Gerven, Y. Yang, A. Walton and M. Buchert, "Recycling of rare earths: a critical review," Journal of Cleaner Production, vol.51, pp. 1-22, 2013.

[12] K. Binnemans, P. T. Jones, T. Müller, L. Yurramendi, "Rare Earths and the Balance Problem: How to Deal with Changing Markets," Journal of Sustainable Metallurgy, pp. 1-21, 2018.

[13] European Commission, Directorate-General for Internal Market, Industry, Entrepreneurship and SMEs (2017) Study on the review of the list of Critical Raw Materials: executive summary.

[14] Asian Metal, http://www.asianmetal.com/

[15] E. Alonso, A. M. Sherman, T. J. Wallington, M. P. Everson, F. R. Field, R. Roth, R. E. Kirchainm, "Evaluating rare earth element availability: a case with revolutionary demand from clean technologies," Environ. Sci. Technol, vol. 46, no. 6, pp. 3406-3414, 2012.

[16] Bloomberg, "Rare Earth Metals Electrified by China's Illegal Mining Clean-Up," https://www.bloomberg.com/news/articles/2017-09-07/rare-earth-metals-electrified-by-china-s-illegal-mining-clean-up, September, 2017

[17] C. Hurst, "China's Rare Earth Elements Industry: What Can the West Learn?" Institute for the Analysis of Global Security Washington DC, 2010.

[18] "Never Mind the Mines. In Congo, There's Cobalt Under the House," https://www.bloomberg.com/news/features/2018-03-28/never-mind-the-mines-in-congo-there-s-cobalt-under-the-house

[19] E. Balomenos, P. Davris, E. Deady, J. Yang, D. Panias, B. Friedrich, ... & I. Paspaliaris, The EURARE project: Development of a sustainable exploitation scheme for Europe's Rare Earth Ore deposits. Johnson Matthey Technology Review, vol. 61, no. 2, pp.142-153, 2017

[20] Toyota develops new magnet for electric motors aiming to reduce use of critical rare-earth element by up to 50%, "https://newsroom.toyota.eu/toyota-develops-new-magnet-for-electric-motors-aiming-to-reduce-use-of-critical-rare-earth-element-by-up-to-50/"

[21] Y. Yang, A. Walton, R. Sheridan,et al, " REE recovery from end-of-life NdFeB permanent magnet scrap: a critical review," Journal of Sustainable Metallurgy, vol. 3, no 1, pp. 122-149, 2017

[22] European Training Network for the Design and Recycling of Rare-Earth Permanent Magnet Motors and Generators in Hybrid and Full Electric Vehicles (ETN-DEMETER), http://etn-demeter.eu/project/, EU Horizon 2020.

[23] T. Elwert, D. Goldmann, F. Römer, M. Buchert, C. Merz, D. Schueler, J. Sutter, "Current developments and challenges in the recycling of key components of (hybrid) electric vehicles," Recycling, vol. 1, no 1, pp. 25-60, 2015.

[24] N.A. Rowson, "Policy Brief - Processing options and future possibilities for sustainable recycling of Hybrid Electric Vehicles and Internal Combustion Engine vehicles at vehicle recycling sites," EU-EREAN/DEMETER, 2017

[25] "Mild Hybrid Electric Vehicle (MHEV) – architectures," https://x-engineer.org/automotive-engineering/vehicle/hybrid/mild-hybrid-electric-vehicle-mhev-architectures/

[26] S. Hanley, "Mercedes To Add 48 Volt Mild Hybrid System to 2017 S Class," https://gas2.org/2016/06/13/mercedes-add-48-volt-mild-hybrid-system-2017-s-class/

[27] B. McKay, "48V Architectures for Enabling High Efficiency," https://www.theicct.org/sites/default/files/Panel%202%20-%20Brian%20McKay_48V.pdf , Powertrain technology & Innovation, Continental AG, Sep, 2016

[28] Etelligentdrive, "Think electric, think Magna," http://electrification.magna.com/wp-content/uploads/2017/11/A_MPT_eDrive_Brochure_EN_221117.pdf, Magna.

[29] H. Sorger, "The tailored engine & powertrain for 48V," https://futurepowertrains.co.uk/wp-content/uploads/2017/12/Helfried-Sorger.pdf , AVL List GmbH, Future powertrain conference, Birmingham, Feb, 2018.

[30] L. Kumar, S. Jain, "Electric propulsion system for electric vehicular technology: A review," Renewable and Sustainable Energy Reviews, vol. 29, pp. 924-940, 2014.

[31] S. E. de Lucena, "A survey on electric and hybrid electric vehicle technology," Electric Vehicles-The Benefits and Barriers, IntechOpen, 2011.

[32] M. Yilmaz, “Limitations/capabilities of electric machine technologies and modeling approaches for electric motor design and analysis in plug-in electric vehicle applications,” Renewable and Sustainable Energy Reviews, vol. 52, pp. 80-99, 2015.

[33] L. Gang, J. Zhu, Y. Guo, “Multidisciplinary design optimization methods for electrical machines and drive systems,” Heidelberg : Springer, 2016.

[34] D. G. Dorrell, A. M. Knight, M, Popescu, L. Evans, D. A. Staton, “Comparison of different motor design drives for hybrid electric vehicles,” Energy Conversion Congress and Exposition (ECCE), IEEE, pp. 3352-3359, 2010.

[35] Renault, “2015 - R240 electric motor manufacturing at the Renault Cléon plant,” https://media.group.renault.com/global/en-gb/renault/media/videos/21211876/2015-fabrication-du-moteur-electrique-r-240-a-lusine-renault-de-cleon1.

[36] A.Chiba, K. Kiyota, N. Hoshi, M. Takemoto, S. Ogasawara, “Development of a rare-earth-free SR motor with high torque density for hybrid vehicles,” IEEE Transactions on Energy Conversion, vol. 30, no 1, pp. 175-182, 2015.

[37] S. Kozuka, N. Tanabe, J. Asama, A. Chiba, “Basic characteristics of 150,000 r/min switched reluctance motor drive,” Power and Energy Society General Meeting-Conversion and Delivery of Electrical Energy in the 21st Century, IEEE, pp. 1-4, 2008.

[38] K. Kiyota, T. Kakishima, A. Chiba, “Estimation and comparison of the windage loss of a 60 kW Switched Reluctance Motor for hybrid electric vehicles,” Power Electronics Conference (IPEC-Hiroshima 2014-ECCE-ASIA), IEEE, pp. 3513-3518, 2014.

[39] F. N. Isaac, A. A. Arkadan, A. El-Antably, “Characterization of axially laminated anisotropic-rotor synchronous reluctance motors,” IEEE Transactions on Energy Conversion, vol. 14, no 3, pp. 506-511, 1999.

[40] F. Leonardi, P. J. McCleer, A. Elantably, “Rotors for synchronous reluctance traction motors: a comparative study,” Industry Applications Conference, Thirty-Fourth IAS Annual Meeting. Conference Record of the IEEE, pp. 835-839, 1999.

[41] R. M. Rajabi, Y. Liu, C. Monnay, P.Tenca, “Modular rotor for synchronous reluctance machine,” World, U.S. Patent, 20120146448A1, Sep, 14, 2009

[42] J. Kolehmainen, “Synchronous reluctance motor with form blocked rotorm: IEEE Transactions on Energy Conversion, vol. 25, no 2, pp. 450-456, 2010.

[43] S. Morimoto, S. Masayuki, T. Yoji, "Performance of PM assisted synchronous reluctance motor for high efficiency and wide constant power operation," Industry Applications Conference, vol. 1, pp. 509-514, 2000.

[44] N. Bianchi, S. Bolognani, D. Bon, M. D. Pre, “Rotor flux-barrier design for torque ripple reduction in synchronous reluctance and PM-assisted synchronous reluctance motors,” IEEE Transactions on Industry Applications, vol. 45, no 3, pp. 921-928, 2009.

[45] MotorBrain project, http://www.motorbrain.eu/, 2011-2014.

[46] Z. Q. Zhu, “Switched flux permanent magnet machines—Innovation continues,” Electrical Machines and Systems (ICEMS), IEEE, pp. 1-10, 2011

[47] H. Yang, H. Lin, Z. Q. Zhu, “Recent Advances in Variable Flux Memory Machines for Traction Applications: A Review,” CES Transactions on Electrical Machines and Systems, vol. 2, no 1, pp. 34-50, 2018.

[48] S. E. Rauch, L. J. Johnson, “Design principles of flux-switch alternators. Transactions of the American Institute of Electrical Engineers. Part III: Power Apparatus and Systems,” vol. 74, no 3, pp. 1261-1268, 1955.

[49] A. Jack, B. Mecrow, P. Dickinson, “Iron loss in machines with powdered iron stators,” in International Conference on Electric Machines and Drives (IEMD), pp. 48–50, 1999.

[50] K. Hioki, A. Hattori, T. Iriyama, “Development of Dy-Free Hot-Deformed Nd-Fe-B Magnets by Optimizing Chemical Composition and Microstructure,” Journal of the Magnetics Society of Japan, vol. 38, no 3-1, pp. 79-82, 2014.

[51] X. Tang, H. Sepehri-Amin, T. Ohkubo, K. Hono, “Suppression of non-oriented grains in Nd-Fe-B hot-deformed magnets by Nb doping. Scripta Materialia,” vol. 147, pp. 108-113, 2018.

[52] Shin-etsu, “New alloying process by grain boundary diffusion,” http://www.shinetsu-rare-earth-magnet.jp/e/rd/grain.html, 2007.

[53] Techtalk, "Grain Boundary Diffusion (GBD) Technology of Sintered NdFeB Magnet," http://www.magnet-sdm.com/2017/08/31/grain-boundary-diffusion-gbd-technology-of-sintered-ndfeb-magnet/ , SDM Magnetics

[54] W. F. Li, T. Ohkubo, K. Hono, M. Sagawa, “The origin of coercivity decrease in fine grained Nd–Fe–B sintered magnets. Journal of Magnetism and Magnetic Materials,” vol. 321, no 8, pp. 1100-1105, 2009.

[55] C. R. Saha, “Modelling theory and applications of the electromagnetic vibrational generator,” Sustainable Energy Harvesting Technologies-Past, Present and Future, IntechOpen, 2011.

[56] B. M. Ma, J. W. Herchenroeder, B. Smith, M. Suda, D. N. Brown, Z. Chen, “Recent development in bonded NdFeB magnets. Journal of magnetism and magnetic materials,” 2002, vol. 239, no 1-3, pp. 418-423.

[57] Y.Honkura,"The development of Dy free MAGFINE and its applications to motors", Symposium on "current research trends in magnetic materials“, Dec. 2013.

[58] R. Lee, E. Brewer, N. Schaffel, “Processing of neodymium-iron-boron melt-spun ribbons to fully dense magnets,” IEEE Transactions on Magnetics, vol. 21, no 5, pp. 1958-1963, 1985.

[59] Y.Ying-chang, Z. Xiao-dong, K. Lin-shu, P. Qi, H. Yong-tian, H. Shuang, Y. Liu, G. Sen-lin, “Structural and magnetic properties of nitride compounds of the type R2Fe17Nx, R2Fe14BNx and RTiFe11Nx,” Journal of the Less Common Metals, vol. 170, no 1, pp. 37-44, 1991.

[60] Y. Hirayama, T. Miyake, K. Hono, “Rare-earth lean hard magnet compound NdFe12 N,” JOM, vol. 67, no 6, pp. 1344-1349, 2015.

[61] Y. Hirayama, Y. K. Takahashi, S. Hirosawa, K. Hono, “NdFe12Nx hard-magnetic compound with high magnetization and anisotropy field. Scripta Materialia,” vol. 95, pp. 70-72, 2015.

[62] U. Bast, F. Treffer, C. Thürigen, T. Elwert, F. Marscheider-Weidemann, “Recycling von Komponenten und strategischen Metallen aus elektrischen Fahrantrieben,” Recycling und Rohstoffe, Bd, vol 5, 2014.

[63] T. Klier, F. Risch, J. Franke, “Disassembly, recycling, and reuse of magnet material of electric drives,” Assembly and Manufacturing (ISAM), IEEE International Symposium, pp. 88-90, 2013.

[64] J. Franke, B. Hofmann, J. Tremel, A. Meyer, “Innovative Methods for Automated Assembly and Fixation of Permanent Magnets in Electrical Machines,” Procedia CIRP, Elsevier, vol. 26, pp. 724-728, 2015.

[65] J. Tremel, B. Hofmann, F. Risch, “Handling and fixation of permanent magnets, “Advanced Materials Research, vol. 769, pp. 3-10, 2013.

[66] E. Joseph, J. Tremel, B. Hofmann, A. Meyer, Jö. Franke, S. Eschrich, “Automated magnet assembly for large PM synchronous machines with integrated permanent magnets,” Electric Drives Production Conference (EDPC), 3rd International, pp. 1-6, 2013.

[67] A. K. Jha, L. Garbuio, A. Kedous-Lebouc, J. P. Yonnet, J. M. Dubus, “Design and comparison of outer rotor bonded magnets Halbach motor with different topologies,” In Electrical Machines, Drives and Power Systems, ELMA, 15th IEEE.International Conference, pp. 6-10, June, 2017.

[68] A. K. Jha, A. Kedous-Lebouc, L. Garbuio, J. P. Yonnet, J. M. Dubus, “FEA based analysis on effect of slot pole combination on motor torque and magnet eddy current loss with bonded NdFeB Halbach rotor,” In Electrical Machines and Systems (ICEMS),20th International Conference, IEEE, pp. 1-5, 2017.

[69] Z. Li, A. Kedous-Lebouc, J. Dubus, L. Garbuio, S. Personnaz, “Reuse and Recycle Strategies of Rare Earth Permanent Magnets for PM Electrical Machines –an overview study”, 3eme Symposium de Génie Electrique(SGE), Nancy, France, 2018.

[70] S. Högberg, J. Holboll, N. Mijatovic, B. B. Jensen, F. B. Bendixen, “Direct Reuse of Rare Earth Permanent Magnets-Coating Integrity,” vol. 53, no. 4, p. 1-9, IEEE Transactions on Magnetics, IEEE, 2016.

[71] S. Högberg, T. S. Pedersen, B. B. Jensen, N. Mijatovic, J. Holboll, “Direct Reuse of Rare Earth Permanent Magnets - Wind Turbine Generator Case Study,” Electrical Machines (ICEM), 2016 XXII International Conference on. IEEE, pp. 1625-1629, 2016.

[72] P. Kjeldsteen, A. Sørensen, F. B. Bendixen, “(WO2010066251) A PERMANENT MAGNET ROTOR FOR A MACHINE, A METHOD FOR MANUFACTURING A PERMANENT MAGNET ROTOR AND A MANUFACTURING SYSTEM,” GRUNDFOS MANAGEMENT A/S, 2010, https://patentscope.wipo.int/search/en/detail.jsf?docId=WO2010066251&recNum=1&tab=Drawings&maxRec=&office=&prevFilter=&sortOption=&queryString=

[73] S. Högberg, F. B. Bendixen, N. Mijatovic, B. B. Jensen, J. Holb, “Influence of demagnetization-temperature on magnetic performance of recycled Nd-Fe-B magnets,” Electric Machines & Drives Conference (IEMDC), IEEE International, pp. 1242-1246, May 2015.

[74] Environmental initiatives - Denmark: Re-use of pre-consumed magnetic materials, https://www.grundfos.com/about-us/sustainability-responsibility/green-at-heart/environmental-initiatives.html, Grundfos.

[75] I. Stamenkovic, N. Schofield, N. Milivojevic, M. Krishnamurthy, A. Emadi, “A novel modular permanent-magnet electric machine design,” IECON'09, 35th Annual Conference of IEEE, Industrial Electronics, pp 997-1002, 2009.

[76] S. T. Lundmark, M. Alatalo, “A segmented claw-pole motor for traction applications considering recycling aspects,” Ecological Vehicles and Renewable Energies (EVER), 8th International Conference and Exhibition, IEEE, pp 1-6, 2013.

[77] M. Alatalo, S. T. Lundmark, E. A. Grunditz, “Electric Machine Design for Traction Applications Considering Recycling Aspects -Review and New Solution,” IECON 2011-37th Annual Conference on IEEE Industrial Electronics Society, pp. 1836-1841.

[78] Z. Q. Zhu, Y. X. Li, “Modularity Techniques in High Performance Permanent Magnet Machines and Applications,” CES Transactions on Electrical Machines and Systems 2, no. 1, pp93-103, 2018.

[79] M. Kimiabeigi, R. S. Sheridan, J. D. Widmer, A. Walton, M. Farr, B. Scholes, I. R. Harris, “ Production and Application of HPMS Recycled Bonded Permanent Magnets for a Traction Motor Application,” IEEE Transactions on Industrial Electronics 65, no. 5, pp. 3795-3804, 2018.

[80] J. D. McFarland, T. M. Jahns, A. M. EL-Refaie, P. B. Reddy, “Effect of magnet properties on power density and flux-weakening performance of high-speed interior permanent magnet synchronous machines,” Energy Conversion Congress and Exposition (ECCE), IEEE, pp. 4218-4225, 2014.

[81] A. Pouramin, R. Dutta, M. F. Rahman, “Preliminary study on differences in the performance characteristics of concentrated and distributed winding IPM machines with different rotor topologies,” Energy Conversion Congress and Exposition (ECCE), IEEE, pp. 3565-3570, 2017.

[82] M. Kimiabeigi, R. Long, J. D. Widmer, Y. Gao, “ Comparative Assessment of Single Piece and Fir-Tree-Based Spoke Type Rotor Designs for Low-Cost Electric Vehicle Application,” IEEE Trans. Energy Convers, vol. 32, no 2, pp. 486-494, 2017.

[83] Shrink fiber sleeve – Innovative bandage solution for brushless motors, http://www.politubes.it/cms/238-shrink-fiber-tubes-a-soluzione-innnovativa-di-bendaggio-per-motori-brushless?language_code=ENG Politubes.

[84] A. Negahdari, H. A. Toliyat, “Post-assembly magnetization of rare-earth permanent magnet materials in permanent magnet assisted synchronous reluctance motors,” In Electric Machines and Drives Conference (IEMDC), IEEE, pp. 1-6, 2017.

[85] Techtalk, " Introduction of Anisotropic Bonded Magnet," http://www.magnet-sdm.com/2018/07/23/introduction-anisotropic-bonded-magnet/, SDM Magnetics.

[86] Direction of the Magnetic Force: The Right Hand Rule, http://oer2go.org/mods/en-boundless/www.boundless.com/physics/textbooks/boundless-physics-textbook/magnetism-21/magnetic-force-on-a-moving-electric-charge-157/direction-of-the-magnetic-force-the-right-hand-rule-553-10931/images/right-hand-rule-5b9e3411-cd3e-4be5-8162-23b2de96d856/index.html.

[87] H. Matsuoka, “Proposal of Dy-free Nd anisotropic bonded magnet and its new applied motors”, 22th Magnetic Application Technology Symposium, A3-2-20, 2014.

[88] Ron, "ZERO MOTORCYCLES, HERE’S THE THE HISTORY OF THEIR TECH", 2018, http://electricmotorcycle.com/zero-motorcycles-tech/

[89] S. Meier, “ Theoretical design of surface-mounted permanent magnet motors with field-weakening capability,” Master Thesis. Royal Institute of Technology Department of Electrical Engineering Electrical Machines and Power Electronics Stockholm, 2002.

[90] Chandur Sadarngani, “ Electrical machines -Design and Analysis of Induction and Permanent Magnet Motors,” Division of Electrical Machines and Power Electronics, School of Electrical Engineering, Royal Institute of Technology, Stockholm, 2016.

[91] F. Magnussen, H. Lendenmann, “Parasitic effects in PM machines with concentrated windings, ” IEEE transactions on industry applications, vol. 43, no 5, pp. 1223-1232, 2007.

[92] J. Pyrhonen, T. Jokinen, V. Hrabovcova, “Design of rotating electrical machines,” pp.283, John Wiley & Sons, 2013.

[93] J. F. Gieras, “Advancements in electric machines,” pp.102, Springer Science & Business Media, 2008.

[94] A. M. El-Refaie, “Fractional-slot concentrated-windings synchronous permanent magnet machines: Opportunities and challenges,” IEEE Transactions on industrial Electronics, vol. 57, no 1, pp. 107-121, 2010.

[95] F. Magnussen, C. Sadarangani, “Winding factors and Joule losses of permanent magnet machines with concentrated windings,” In : Electric Machines and Drives Conference, IEMDC'03. IEEE International, pp. 333-339, 2003.

[96] F. Libert, “Design, optimization and comparison of permanent magnet motors for a low-speed direct-driven mixer,” Licentiate Thesis, Royal Institute of Technology, TRITA-ETS-2004-12, ISSN-1650-674x, Stockholm, 2004.

[97] Electric motor winding calculator, https://www.emetor.com/windings/, 2018 Emetor AB.

[98] M. Popescu, J. Goss, D. A. Staton, D. Hawkins, Y. C. Chong, A. Boglietti, “Electrical Vehicles—Practical Solutions for Power Traction Motor Systems,” IEEE Transactions on Industry Applications, vol. 54, no 3, pp. 2751-2762, 2018.

[99] A. O. Di Tommaso, F. Genduso, R. Miceli, C. Nevoloso, “Procedure for the calculation of maximum slot filling factors in electrical machines,” In : Ecological Vehicles and Renewable Energies (EVER), 12th International Conference on. IEEE, pp. 1-8, 2017.

[100] M. C. Kulan, N. J. Baker, J. D. Widmer, “Design of a high fill factor permanent magnet integrated starter generator with compressed stator windings,” In : Electrical Machines (ICEM), XXII International Conference on. IEEE, pp. 1513-1519, 2016.

[101] W. C. Duesterhoeft, M. W. Schulz, E. Clarke, “Determination of instantaneous currents and voltages by means of alpha, beta, and zero components,” Transactions of the American Institute of Electrical Engineers, vol. 2, no 70, pp. 1248-1255, 1951.

[102] Magnetic materials - Part 2: Methods of measurement of the magnetic properties of electrical steel strip and sheet by means of an Epstein frame, International Standard IEC 60404-2:2008. https://webstore.iec.ch/publication/2064

[103] H. E. Tacca, C. Sullivan, “Extended steinmetz equation,” 2002.

[104] F. Fiorillo, “Characterization and measurement of magnetic materials,” Academic Press, 2004.

[105] “Estimating iron loss in opera-2d,” in Opera-2d User Guide, Oxfordshire, UK: Cobham Technical Services, 2012.

[106] F. Preisach, “Über die magnetische Nachwirkung,” Zeitschrift für Physik, vol. 94, no. 5, pp. 277–302, 1935.

[107] A. Krings, “Iron losses in electrical machines-Influence of material properties, manufacturing processes, and inverter operation,” doctoral dissertation, KTH Royal Institute of Technology, 2014.

[108] C. Sadarangani, “Electrical machines: Design and Analysis of induction and permanent magnet motors,” Division of Electrical Machines and Power Electronics, School of Electrical Engineering, Royal Inst. of Technology, 2006.

[109] H. C. Karmaker, “Stray losses in large synchronous machines,” IEEE transactions on energy conversion, vol. 7, no 1, pp. 148-153, 1992.

[110] B. Aslan, E. Semail, J. Legranger, “Analytical model of magnet eddy-current volume losses in multi-phase PM machines with concentrated winding.” In : Energy Conversion Congress and Exposition (ECCE), IEEE, pp. 3371-3378, 2012.

[111] R. Benlamine, T. Hamiti, F. Vangraefschèpe, and D. Lhotellier, “Electromagnetic, mechanical and thermal analysis of a high-speed surface-mounted PM machine for automotive application. In Electrical Machines,” XXII International Conference (ICEM), pp. 1662-1667, IEEE. 2016.

[112] A. Foggia, J. E. Torlay, C. Corenwinder, A. Audoli, J. Herigault, “Circulating current analysis in the parallel-connected windings of synchronous generators under abnormal operating conditions,” In : Electric Machines and Drives, 1999. International Conference IEMD'99. IEEE, pp. 634-636, 1999.

[113] M. Popescu, D. G. Dorrell, “Proximity losses in the windings of high speed brushless permanent magnet AC motors with single tooth windings and parallel paths,” IEEE Transactions on Magnetics, vol. 49, no 7, pp. 3913-3916, 2013.

[114] D. Bauer, P. Mamuschkin, H. C. Reuss, E. Nolle, “Influence of parallel wire placement on the AC copper losses in electrical machines,” In : Electric Machines & Drives Conference (IEMDC), IEEE International. IEEE, pp. 1247-1253, 2015.

[115] G. Dajaku, W. Xie, D. Gerling, “Reduction of low space harmonics for the fractional slot concentrated windings using a novel stator design,” IEEE Transactions on Magnetics, vol. 50, no 5, pp. 1-12, 2014.

[116] Y. Zhao, T. A. Lipo, “Space vector PWM control of dual three-phase induction machine using vector space decomposition,” IEEE Transactions on industry applications, 1995, vol. 31, no 5, p. 1100-1109.

[117] T. J. E. Miller, M. I. McGilp, “Analysis of multi-phase permanent-magnet synchronous machines,” In : Electrical Machines and Systems, ICEMS International Conference on. IEEE, pp. 1-6, 2009.

[118] J. Karttunen, S. Kallio, P. Peltoniemi, P. Silventoinen, O. Pyrhonen, “Dual three-phase permanent magnet synchronous machine supplied by two independent voltage source inverters,” Proc. Int. SPEEDAM, pp. 741-747, 2012.

[119] J. Karttunen, S. Kallio, P. Peltoniemi, P. Silventoinen, O. Pyrhönen, "Decoupled vector control scheme for dual three-phase permanent magnet synchronous machines," IEEE Transactions on Industrial Electronics, vol. 61, no 5, pp. 2185-2196, 2014.

[120] Y. Hu, Z. Q. Zhu, M. Odavic, "Comparison of two-individual current control and vector space decomposition control for dual three-phase PMSM," IEEE Transactions on Industry Applications, vol. 53, no 5, pp. 4483-4492, 2017.

[121] J. Millinger, O. Wallmark, J. Soulard, High-Frequency Characterization of Losses in Fully Assembled Stators of Slotless PM Motors. IEEE Transactions on Industry Applications, vol. 54, no 3, pp. 2265-2275, 2018.

[122] H. Kaihara, N. Takahashi, M. Nakano, M. Kawabe, T. Nomiyama, A. Shiozaki, D. Miyagi, "Effect of carrier frequency and circuit resistance on iron loss of electrical steel sheet under single-phase full-bridge PWM inverter excitation," IEEE Transactions on Magnetics, vol. 48, no 11, pp. 3454-3457, 2012.

[123] A. Boehm, I. Hahn, "Influence of pulse width modulation (PWM) on the iron losses of electrical steel," In : Power Electronics Conference (IPEC-Hiroshima 2014-ECCE-ASIA), International. IEEE, pp. 283-288, 2014.

[124] A. G. Gonzalez, J. Millinger, J. Soulard, "Magnet losses in inverter-fed two-pole PM machines," In : Electrical Machines (ICEM), XXII International Conference on. IEEE, pp. 1854-1860, 2016.

[125] I. Husain, M. Ehsani, "Torque ripple minimization in switched reluctance motor drives by PWM current control," IEEE transactions on power electronics, vol. 11, no 1, p. 83-88, 1996.

[126] L. Mingji, G. Hanjin, S. Meihong, "Ripple torque analysis and simulation of BLDC motor with different PWM modes," In : Power Electronics and Motion Control Conference (IPEMC), 7th International. IEEE, pp. 973-977, 2012.

[127] J. Fang, H. Li, B. Han, "Torque ripple reduction in BLDC torque motor with nonideal back EMF," IEEE transactions on power electronics, vol. 27, no 11, pp. 4630-4637, 2012.

[128] Jamg-Designer, https://www.jmag-international.com/products/jmag-designer/

[129] Emetor KTH, http://184.106.195.250/emetor.php

[130] A. M. El-Refaie, M. R. Shah, R. Qu, J. M. Kern, "Effect of number of phases on losses in conducting sleeves of surface PM machine rotors equipped with fractional-slot concentrated windings," IEEE Transactions on Industry Applications, vol. 44, no 5, pp. 1522-1532, 2008.

[131] M. R. Shah, A. M. El-Refaie, "Eddy-current loss minimization in conducting sleeves of surface PM machine rotors with fractional-slot concentrated armature windings by optimal axial segmentation and copper cladding," IEEE Transactions on Industry Applications, vol. 45, no 2, p. 720-728, 2009.

[132] Y. Pang, Z. Q. Zhu, D. Howe, "Analytical determination of optimal split ratio for permanent magnet brushless motors," IEE Proceedings-Electric Power Applications, vol. 153, no 1, pp. 7-13, 2006.

[133] J. Goss, R. Wrobel, P. Mellor, D. Staton, "The design of AC permanent magnet motors for electric vehicles: A design methodology," In Electric Machines & Drives Conference (IEMDC), pp. 871-878, IEEE International, May 2013.

[134] R. Islam, I. Husain, A. Fardoun, K. McLaughlin, "Permanent-Magnet Synchronous Motor Magnet Designs With Skewing for Torque Ripple and Cogging Torque Reduction," IEEE Trans. Ind. Appl., vol. 45, no. 1, pp. 152-160, Jan/Feb, 2009.

[135] W. Q. Chu, Z. Q. Zhu, "Investigation of Torque Ripples in Permanent Magnet Synchronous Machines With Skewing," IEEE Trans. Magn., vol. 49, no. 3, pp. 1211-1220, Mar, 2013.

[136] K. I. Laskaris, A. G. Kladas, "Permanent-magnet shape optimization effects on synchronous motor performance." IEEE Transactions on Industrial Electronics, vol. 58, no 9, p. 3776-3783, 2011.

[137] Z. S. Du, T. A. Lipo, "High torque density and low torque ripple surface permanent magnet machines with sinusoidal plus third harmonic shaped magnets," In : Electric Machines and Drives Conference (IEMDC), 2017 IEEE International, pp. 1-8, 2017.

[138] B. Aslan, E. Semail, J. Legranger, "General Analytical Model of Magnet Average Eddy-Current Volume Losses for Comparison of Multiphase PM Machines With Concentrated Winding." IEEE Transactions on Energy Conversion, vol. 29, no 1, pp. 72-83, 2014.

[139] S. Tizianel, N. Novello, "Permanent magnet demagnetization process considering the inclination of the demag field," IEEE Transactions on Magnetics 52, no. 8, pp. 1-7, 2016.

[140] P. Peng, H. Xiong, J. Zhang, W. Li, F. Leonardi, C. Rong, M.W. Degner, F. Liang, L. Zhu, "Effects of external field orientation on permanent magnet demagnetization," IEEE Transactions on Industry Applications 53, no. 4, pp. 3438-3446, 2017.

[141] "Issue 4 Material Modeling and Powerful Analysis Capabilities that Contribute to Limit Design," JMAG Technical Report, https://www.jmag-international.com/technicalreport/04/

[142] T. Matsuo, D. Shimode, Y. Terada, M. Shimasaki, "Application of stop and play models to the representation of magnetic characteristics of silicon steel sheet," IEEE transactions on magnetics, vol. 39, no 3, pp. 1361-1364, 2003

[143] K. Narita, T. Asanuma, K. Semba, H. Sano, T. Yamada, K. Aiso, K. Akatsu, "An accurate iron loss evaluation method based on finite element analysis for switched reluctance motors," In : Energy Conversion Congress and Exposition (ECCE), IEEE, pp. 4413-4417, 2015.

[144] T. A. Burress, C. L. Coomer, S. L. Campbell, L. E. Seiber, L. D. Marlino, R. H. Staunton, J. P. Cunningham, "Evaluation of the 2007 Toyota Camry hybrid synergy drive system," Oak Ridge National Laboratory (ORNL), Oak Ridge, TN, 2008.

[145] F. Gillon, P. Brochet, "Screening and response surface method applied to the numerical optimization of electromagnetic devices," IEEE transactions on magnetics, vol. 36, no 4, pp. 1163-1167, 2000.

[146] C. Tang, W. L. Soong, T. M. Jahns, N. Ertugrul, "Analysis of iron loss in interior PM machines with distributed windings under deep field weakening," IEEE Transactions on Industry Applications, vol.51, No. 5, pp. 3761-3772, 2015.

[147] "DIFFÉRENCES ENTRE LES CYCLES NEDC ET WLTC / WLTP, " http://www.fiches-auto.fr/articles-auto/consommation/s-1980-differences-entre-les-cycles-nedc-et-wltp.php

[148] A. Fitzgerald, C. Kingsley, and S. Umans, "Parameter determination from no-load and block-rotor tests," in Electric Machinery, 6th ed. New York, US: McGraw-Hill, 2003, ch. 6.

[149] R .S. Sheridan, A. J. Williams, I. R. Harris, and A. Walton, "Improved HDDR processing route for production of anisotropic powder from sintered NdFeB type magnets," Journal of Magnetism and Magnetic Materials, vol. 350, pp. 114-118, Jan. 2014.

[150] R. S. Sheridan, R. Sillitoe, M. Zakotnik, I. R. Harris, and A. J. Williams, "Anisotropic powder from sintered NdFeB magnets by the HDDR processing route," Journal of Magnetism and Magnetic Materials, vol. 324, no. 1, pp. 63-67, Jan. 2012.

[151] M. Zakotnik, I. R. Harris, and A. J. Williams, "Multiple recycling of NdFeB-type sintered magnets," Journal of Alloys and Compounds, vol. 469, no. 1-2, pp. 314-321, Feb. 2009.

[152] Electricity price statistics, http://ec.europa.eu/eurostat/statisticsexplained/ index.php/Electricity_price_statistics

[153] H. Jin, P. Afiuny, S. Dove, G. Furlan, M. Zakotnik, Y. Yih, and J. W。 Sutherland, “Life Cycle Assessment of Neodymium-Iron-Boron Magnet-to-Magnet Recycling for Electric Vehicle Motors,” Environ. Sci. Technol. Journal, 52 (6), pp 3796–3802, 2018.

[154] P. Lazari, J. Wang, and L. Chen, "A Computationally Efficient Design Technique for Electric-Vehicle Traction Machines," IEEE Trans. on Industry Applications, vol. 50, no. 5, pp. 3203-3213, Sep.-Oct. 2014.

[155] N. Kim, S. Cha, H. Peng, “Optimal control of hybrid electric vehicles based on Pontryagin's minimum principle,” IEEE Transactions on Control Systems Technology, 2011, vol. 19, no 5, pp. 1279-1287.

[156] D. Sinoquet, G. Rousseau, Y. Milhau, “Design optimization and optimal control for hybrid vehicles. Optimization and Engineering,” vol. 12, no 1-2, pp. 199-213, 2011.

Publication

1. **Z. Li**, A. Kedous-Lebouc, R. Fratila, J. Legranger, J. Dubus, A. Ikram, "Investigation on surface mounted PM machines with magnet recycling concept for hybrid electrical vehicle applications," International Conference on Electrical Machines and Systems (ICEMS 2017), Sydney(Australia), 10-14 August 2017
2. A. Jha, **Z. Li**, A. Garcia, P. Upadhayay, P. O. Rasmussen, A. Kedous- Lebouc, L. Garbuio, "Weighted Index of Recycling and Energy (WIRE) Cost for Motors in Electric Vehicles," International Symposium on Power Electronics, Electrical Drives, Automation and Motion (SPEEDAM), Amalfi (Italy), 20-22 June, 2018.
3. A. Garcia, A. Jha, **Z. Li**, P. Upadhayay, P. O. Rasmussen, "Validation of Efficiency Maps of an Outer Rotor Surface Mounted Permanent Magnet Machine for Evaluation of Recyclability of Magnets," International Magnetic Conference (INTERMAG). IEEE, 2018. pp. 1-6.
4. **Z. Li**, A. Kedous-Lebouc, J. Dubus, L. Garbuio, S. Personnaz, "Reuse and Recycle Strategies of Rare Earth Permanent Magnets for Electrical Machines –an overview study," Nancy(France), 3ème Symposium de Génie Electrique (SGE), 3-5 July, 2018.
5. P. Upadhayay, A. G. Garcia, **Z. Li**, A. Jha, P. O. Rasmussen, A. Kedous-Lebouc, J. Mipo, "Evaluation of Energy Cost Index for an Electric Vehicle Motor over a particular Drive Cycle with Recycled Magnet Concept," XXIIIrd International Conference on Electrical Machines (ICEM), 3-6 September, 2018
6. **Z. Li**, A. Kedous-Lebouc, J. Dubus, J. Legranger, R. Fratila, "Investigation on IPMSM machines with Dy-free magnets and magnets recycling concept for hybrid electrical vehicle applications," International conferences on magnetism: the IEEE International Magnetics Conference and the Conference on Magnetism and Magnetic Materials (MMM-INTERMAG). Washington DC (US), 14-18 January 2019
7. **Z. Li**, A. Kedous-Lebouc, J. M. Dubus, L. Garbuio, S. Personnaz, "Reuse and Recycle Strategies of Rare Earth Permanent Magnets for PM Electrical Machines-an overview study," Eur. Phys. J. Appl. Phys. 86, 20901 (2019).